

## Remote Sensing for Wind Energy

**Pena Diaz, Alfredo; Hasager, Charlotte Bay**

*Publication date:*  
2011

*Document Version*  
Publisher's PDF, also known as Version of record

[Link back to DTU Orbit](#)

*Citation (APA):*  
Peña, A., & Hasager, C. B. (Eds.) (2011). Remote Sensing for Wind Energy. Risø National Laboratory for Sustainable Energy, Technical University of Denmark. (Risø-I; No. 3184(EN)).

## DTU Library

Technical Information Center of Denmark

---

### General rights

Copyright and moral rights for the publications made accessible in the public portal are retained by the authors and/or other copyright owners and it is a condition of accessing publications that users recognise and abide by the legal requirements associated with these rights.

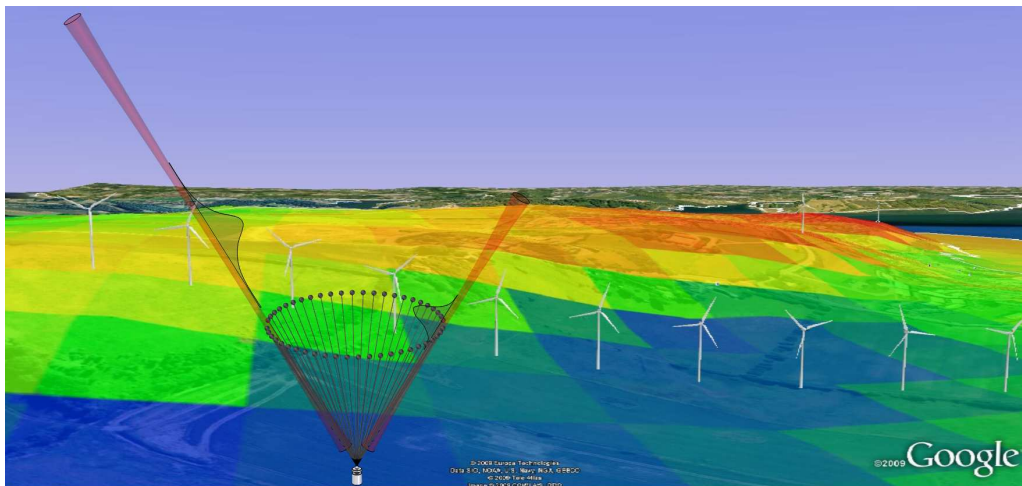
- Users may download and print one copy of any publication from the public portal for the purpose of private study or research.
- You may not further distribute the material or use it for any profit-making activity or commercial gain
- You may freely distribute the URL identifying the publication in the public portal

If you believe that this document breaches copyright please contact us providing details, and we will remove access to the work immediately and investigate your claim.

Risø-I-3184(EN)

# Remote Sensing for Wind Energy

Alfredo Peña and Charlotte B. Hasager (Eds)



Risø DTU  
National Laboratory for Sustainable Energy



Risø National Laboratory for Sustainable Energy,  
Technical University of Denmark, Roskilde, Denmark

May 2011

# Remote Sensing for Wind Energy

Jan Anger  
Merete Badger  
Ferhat Bingöl  
Oliver Bischoff  
Jean-Pierre Cariou  
Stefan Emeis  
Julia Gottschall  
Michael Harris  
Charlotte B. Hasager  
Martin Hofsäß  
Martin Kühn  
Jakob Mann  
Torben Mikkelsen  
Frank Monaldo  
Alfredo Peña  
Andreas Rettenmeier  
Ameya Sathe  
Fabio Scanzani  
David Schlipf  
Donald Thompson  
Juan José Trujillo  
Rozenn Wagner

Edited by:  
Alfredo Peña and Charlotte B. Hasager  
*Wind Energy Division, Risø DTU, Roskilde, Denmark*

# Contents

<b>Preface</b>	<b>6</b>
<b>1 Remote Sensing of Wind</b>	<b>7</b>
1.1 Ground-based remote sensing for today's wind energy research . . . . .	7
1.2 Part I: Remote sensing of wind by sound (sodars) . . . . .	7
1.3 Part II: RS of wind by light (lidars) . . . . .	13
Notation . . . . .	20
References . . . . .	20
<b>2 Atmospheric turbulence</b>	<b>21</b>
2.1 Introduction . . . . .	21
2.2 Definitions . . . . .	22
2.3 Rapid distortion theory . . . . .	23
2.4 Fitting spectra to observations . . . . .	28
2.5 Model spectra over the ocean and flat land . . . . .	31
2.6 Comparison with the spectral tensor model . . . . .	34
2.7 Wind field simulation . . . . .	36
Notation . . . . .	38
References . . . . .	39
<b>3 Introduction to continuous-wave Doppler lidar</b>	<b>41</b>
3.1 Introduction . . . . .	41
3.2 Basic principles of lidar operation and system description . . . . .	42
3.3 Lidar measurement process: Assumptions . . . . .	45
3.4 End-to-end measurement process for CW Doppler lidar . . . . .	47
3.5 Uncertainty analysis . . . . .	54
3.6 Calibration, validation and traceability . . . . .	58
3.7 Summary, state of the art, and future developments . . . . .	60
Notation . . . . .	62
References . . . . .	62
<b>4 Pulsed lidars</b>	<b>65</b>
4.1 Introduction . . . . .	65
4.2 End-to-end description of pulsed lidar measurement process . . . . .	66
4.3 Lidar performances . . . . .	74
4.4 Conclusions and perspectives . . . . .	78
Notation . . . . .	80
References . . . . .	81
<b>5 What can remote sensing contribute to power curve measurements?</b>	<b>82</b>
5.1 Introduction . . . . .	82
5.2 Power performance and wind shear . . . . .	82
5.3 Wind speed profiles . . . . .	87
5.4 Equivalent wind speed . . . . .	89
5.5 Summary . . . . .	94
Notation . . . . .	95
References . . . . .	96

<b>6</b>	<b>Lidars and wind profiles</b>	<b>97</b>
6.1	Introduction . . . . .	97
6.2	Wind profile theory . . . . .	98
6.3	Comparison with observations at great heights . . . . .	100
6.4	Summary . . . . .	104
	Notation . . . . .	105
	References . . . . .	105
<b>7</b>	<b>Complex terrain and lidars</b>	<b>107</b>
7.1	Introduction . . . . .	107
7.2	Lidars . . . . .	107
7.3	Challenges and Known Issues . . . . .	112
7.4	Experimental studies . . . . .	114
7.5	Conclusions . . . . .	119
	Notation . . . . .	122
	References . . . . .	124
<b>8</b>	<b>Nacelle wind lidar</b>	<b>126</b>
8.1	Summary . . . . .	126
8.2	Introduction . . . . .	126
8.3	The units of the LiDAR system . . . . .	126
8.4	Scan pattern . . . . .	128
8.5	CNR . . . . .	129
8.6	Wind field reconstruction . . . . .	131
8.7	“Visited” test sites of the SWE Scanner . . . . .	132
8.8	Measurement campaigns and some results . . . . .	135
8.9	Outlook & Conclusions . . . . .	136
	Notation . . . . .	137
	References . . . . .	137
<b>9</b>	<b>Lidars and wind turbine control</b>	<b>139</b>
9.1	Introduction . . . . .	139
9.2	Measuring wind fields with lidar . . . . .	139
9.3	Prediction of wind fields . . . . .	141
9.4	Improving control . . . . .	142
	Notation . . . . .	147
	References . . . . .	147
<b>10</b>	<b>Turbulence measurements by wind lidars</b>	<b>148</b>
10.1	Introduction . . . . .	148
10.2	Theory . . . . .	149
10.3	Comparison of models with the measurements . . . . .	155
10.4	Discussion . . . . .	161
10.5	Conclusion . . . . .	163
10.6	Future Perspectives . . . . .	163
	Notation . . . . .	164
	References . . . . .	164
<b>11</b>	<b>Precision (and accuracy) for lidars –</b>	
	<b>Basics of a standardized testing of lidar profilers</b>	<b>167</b>
11.1	Traceability for lidar measurements . . . . .	167
11.2	General concept of verification scheme . . . . .	167
	References . . . . .	168

<b>12 Derivation of the mixing-layer height by remote sensing including RASS</b>	<b>169</b>
12.1 Introduction . . . . .	169
12.2 Mixing-layer height . . . . .	169
12.3 Boundary-layer height . . . . .	181
12.4 Summary . . . . .	182
Notation . . . . .	182
References . . . . .	183
<b>13 SAR for wind energy</b>	<b>186</b>
13.1 Introduction . . . . .	186
13.2 Background . . . . .	186
13.3 Ocean wind retrievals from SAR . . . . .	188
13.4 Meteorological applications of SAR wind fields . . . . .	191
13.5 Wind energy applications of SAR wind fields . . . . .	194
13.6 Future advances in ocean wind mapping from SAR . . . . .	197
Notation . . . . .	198
References . . . . .	199

# Preface

---

The Remote Sensing in Wind Energy Compendium provides a description of several topics and it is our hope that students and others interested will learn from it. The idea behind this compendium began in year 2008 at Risø DTU during the first PhD Summer School: Remote Sensing in Wind Energy. Thus it is closely linked to the PhD Summer Schools where state-of-the-art is presented during the lecture sessions. The advantage of the compendium is to supplement with in-depth, article style information. Thus we strive to provide link from the lectures, field demonstrations, and hands-on exercises to theory. The compendium will allow alumni to trace back details after the course and benefit from the collection of information. This is the second edition of the compendium, after a very successful and demanded first one, and we warmly acknowledge all the contributing authors for their work in the writing of the compendium, and we also acknowledge all our colleagues in the Meteorology and Test and Measurements Programs from the Wind Energy Division at Risø DTU in the PhD Summer Schools. We hope to continue adding more topics in future editions and to update and improve as necessary, to provide a truly state-of-the-art compendium available for people involved in Remote Sensing in Wind Energy.

# 1 Remote Sensing of Wind

**Torben Mikkelsen**

*Wind Energy Division, Risø DTU, Roskilde, Denmark*

---

## 1.1 Ground-based remote sensing for today's wind energy research

Wind turbines are being installed at an ever increasing rate today, on and offshore, in hilly and forested areas and in complex mountainous terrain. At the same time, as the wind turbines become bigger and bigger, they reach higher and higher into the atmosphere but also into hitherto unknown wind and turbulence regimes.

The traditional method for accredited measurements for wind energy is to mount calibrated cup anemometers on tall met masts. But as turbines grow in height, high meteorology masts and instrumentation becomes more and more cumbersome and expensive correspondingly. Costs for installation of tall instrumented met towers increase approximately with mast height to the third power and licensing permits can be time consuming to obtain.

With hub heights above 100 m and rotor planes nowadays reaching diameters of 120 m or more on today's 5 MW turbines, the wind speed distribution over the rotor planes will no longer be representatively measured from a single hub height measurement point, but will also require a multi-height measurement strategy with measurements ranging in heights between 50–200 m, for the purpose of capturing the simultaneous wind distribution over the entire wind turbine rotor.

### Wind remote sensing (RS) methodologies

A simple way to remotely determine the wind speed is by observing marked cloud drift aloft from the ground on a sunny day. More quantitative and accurate remote sensing measurement techniques for wind energy applications include nowadays sound and light wave propagation and backscatter detection based instruments such as sodar, lidar and satellite-based sea surface wave scatterometry.

Today's quest within RS research for wind energy is to find useful replacement alternatives for expensive and cumbersome meteorology mast erection and installations. However, accuracy is of particular importance for site and resource assessments irrespectively of terrain, on or offshore, and measurement errors much in excess of 1% cannot be tolerated neither by banks nor by project developers, as 1% uncertainty in mean wind speed results in 3% uncertainty in mean wind power.

## 1.2 Part I: Remote sensing of wind by sound (sodars)

Sodar (sound detection and ranging) is based on probing the atmosphere by sound propagation, lidar (light detection and ranging) is based on probing the atmosphere by electromagnetic radiation (microwaves or laser light) and satellite RS is based on microwave scatterometry on the sea surface and synthetic aperture radar (SAR) methods. The first two (sodar and lidar) are direct measurements of wind speed based on Doppler shift, whereas the satellite scatterometry are based on proxy-empirical calibration methods. First, a description of the background and the state-of-the-art sodar is addressed. Second, the corresponding development and application lidar RS technology is addressed.

Wind turbines operate within the so-called atmospheric boundary layer, which is char-





*Figure 1:* Commercial available sodars being inter-compared during the WISE 2004 experiment: An array of sodars (and one lidar) during inter-comparison and testing against the tall met towers (up to 168 m above ground) equipped with calibrated cup anemometers at several heights. Venue: The Test station for large wind turbines, Høvsøre, Denmark

acterized by relatively high turbulence levels. Turbulence is here created from the strong wind shear due to the proximity of the Earth's surface. The wind speed at the ground is always zero, both on and offshore.

Sodar is a RS methodology for measurements of the wind speed and direction aloft at various heights in the atmosphere. Sodars are ground-based instruments that transmit a sequence of short bursts of sound waves at audible frequencies (2000–4000 Hz) upward in three different inclined directions into the atmosphere.

The sodar measurement technology was well established and in operational use for decades by now, starting in the 1980's where they served environmental protection issues and has been extensively applied to atmospheric research for environmental protection air pollution prediction measures well before the present burst in wind energy research and application. In Germany for example, sodars have been commissioned on several nuclear installations to replaced tall meteorological towers and serve now as operational monitoring devises of the local wind speed, direction and atmospheric stability.

As the sound waves from a sodar propagate forward a small fraction of the transmitted sound energy is scattered and reflected in all directions from temperature differences and turbulence in the atmosphere. A very small fraction of this scattered energy reaches back into the sodar's detector, which in principle is a directional-sensitive microphone.

The height at which the wind speed is measured is usually determined by the time delay in the backscatter from the transmitted pulse. Under standard atmospheric conditions with sound propagation speed of about  $340 \text{ m s}^{-1}$  backscatter from a sodar measurement at 170 m height above the ground will reach back into the detector after 1 s delay time.

The wind speed component in the transmitted beam direction is subsequently determined from the Doppler shift observed as frequency difference between the transmitted frequency and the frequency of the received backscattered sound wave. By combining the measured wind speed components obtained in this way from three differently inclined sound path directions, e.g. from one vertical and two inclined sound paths, the three-dimensional wind vector including wind speed and direction and tilt can be measured by sodar from preset heights from the ground and up to the limit determined by the sodar's lowest acceptable Carrier-to-Noise (C/N) ratios.

The above description is for a mono-static system, where transmitter and receivers are

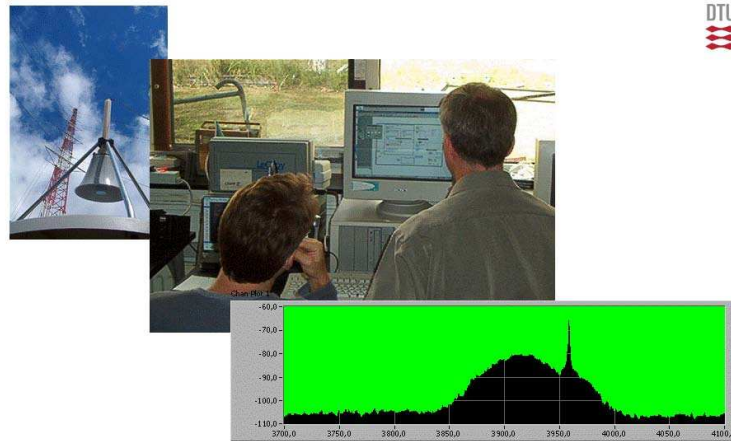


*Figure 2:* Calibration, laboratory work, and real-time Doppler spectrum obtained at Risø DTU with the experimental bi-static CW sodar “Heimdall” (Mikkelsen et al., 2007). Upper panel: Combined acoustic horn and parabola antenna for high-yield (+30 dB gain) backscatter receiving of sound waves. Middle panel: Two researchers at the Risø DTU Laboratory while testing of the bi-static sodar. Lower panel: A real-time obtainable continuous Doppler spectrum Heimdall bi-static sodar from wind measurements at 60 m above Risø DTU

co-located on the ground. But alternative configurations, e.g. in the form of so-called bi-static sodar configurations exist as well, where the transmitter and receivers are separated e.g. 100–200 meters on the ground.

Bi-static configurations have significant C/N-ratio advantages over mono-static configurations for wind energy applications. Received backscatter in a bi-static configuration is not limited to direct ( $180^\circ$ ) backscatter from temperature (density) fluctuations only, but enables also backscatter contributions from the atmospheric turbulence. And the higher the wind speed the more turbulence.

As a consequence significant improvements of the C/N- ratios can be obtained from a so-called “bi-static configuration”, in which the transmitter and the receiver are separated from one another on the ground. This becomes in particular relevant during strong wind situations, where the background noise level increases with the wind speed.

A particular configuration considered for wind energy applications is therefore the bi-static continuous wave (CW) sodar configuration. Alternatively to the range gating in a pulsed system, the range to the wind speed measurement in a CW system can be determined by well-defined overlapping transmission and receiving antenna functions. At Risø DTU we have build and investigated such a sodar system for wind energy applications.

## RS applications within Wind Energy

Remote sensed wind speed measurements are needed to supplement and extend tall met mast measurements, on and offshore, and within research to evaluate various wind flow models and wind atlases for a number of purposes, including:

1. Wind resource assessments
2. Wind park development projects
3. Power curve measurements
4. Bankability
5. Wind model and wind resource (wind atlas) uncertainty evaluation

The common denominator in most of these issues is high accuracy, and with a demand for reproducible certainty to more than 99% of what can be achieved with a corresponding calibrated cup anemometer. A significant source for uncertainty with RS instrumentation relative to a cup anemometer, and for sodars in particular, is the remote instrument's relative big measurement volumes. A sodar measuring the wind speed from say 100 m height probes a total sampling volume of more than 1000 m<sup>3</sup>, whereas a cup anemometer is essentially a point measurement device in this connection. In addition the sodar's measured wind components are displaced in space and time, which makes the interpretation of measured turbulence by a sodar impaired. In addition the huge sampling volumes will be putting restrictions on measurements in non-uniform flow regimes such as found near forest edges, on offshore platforms, and over hilly or complex terrain.

Sodar's RS is also in demand for direct turbine control integration, wind power optimization and turbine mounted gust warning systems, but here the demand on accuracy and reliability is correspondingly high. Today, sodars are typically used to measure 10-min averaged vertical profiles in the height interval between, say 20 and 200 m above the ground, of the following quantities:

- Mean wind speed
- Mean wind directions (including azimuth and tilt)
- Turbulence (all three wind components: longitudinal, transverse and vertical)

Albeit significant inherent scatter persists in sodar measured mean wind speed and direction data average mean wind speed compare relatively well (in most cases to within  $\pm 3\%$ ) to that of a corresponding cup anemometer measured wind speed, cf. the slopes of the scatter plots in Figure 3.

However, the correlation coefficients between sodar and cup anemometer data is, depending on measurement height and atmospheric stability, relative poor as compared to a cup-to cup anemometer correlation, where the two cups are separated by  $\sim 100$  m (typically less than 0.95) and reflects, among other issues, that a mono-static sodar measures the wind speed over a huge volume whereas the cup anemometer represents a point measurement. In addition, increased scatter will occur as a result of beam-bending due to the relative big wind speed to propagation speed of the sound pulses. Also notable is that sodars are able to make only a single 3D vector speed measurement about once per 6–10 s. A slow sampling rate also makes the mean prediction of a 10-min averaged quantity uncertain, due to limited independent sampling counts. In his note "Statistical analysis of poor sample statistics", Kristiansen (2010) has shown that "counting" uncertainty in terms of relative "standard deviation of the sample variance" in a small sample can give rise to a  $\sim 10\%$  relative uncertainty when averaged quantities are drawn from a set of only 100 independent samples.

It is also seen from the sodar vs. cup anemometer data in Figure 3 that difficulties with the C/N ratio can occur when wind speeds exceed approximately 15 m s<sup>-1</sup>, which by the way is a nominal wind speed for a wind turbine. This is due to high background noise and the loss of backscatter in neutrally stratified high wind speed regions.

Recently relative good agreements over forested areas have nevertheless been seen (< 1% discrepancy) between sodar and cup anemometer mean turbulence intensity has been reported by Gustafsson (2008). However, turbulence intensity, which is the stream wise turbulence component relative to the mean wind speed, is in a 10-min averaged quantity dominated, particularly in forested areas, by the most energy containing eddies, which in this case will be larger than the sodar's sampling volumes and therefore be well represented in the statistics. However, the smaller scales including turbulent eddies with wind gusts must be anticipated to be present also on the scales smaller than a mono-static ground based sodar will be able to capture.

While sodars appears to be able to measure accurately both the mean winds speed and the turbulence intensities at a turbines hub height it was found more difficult to use a

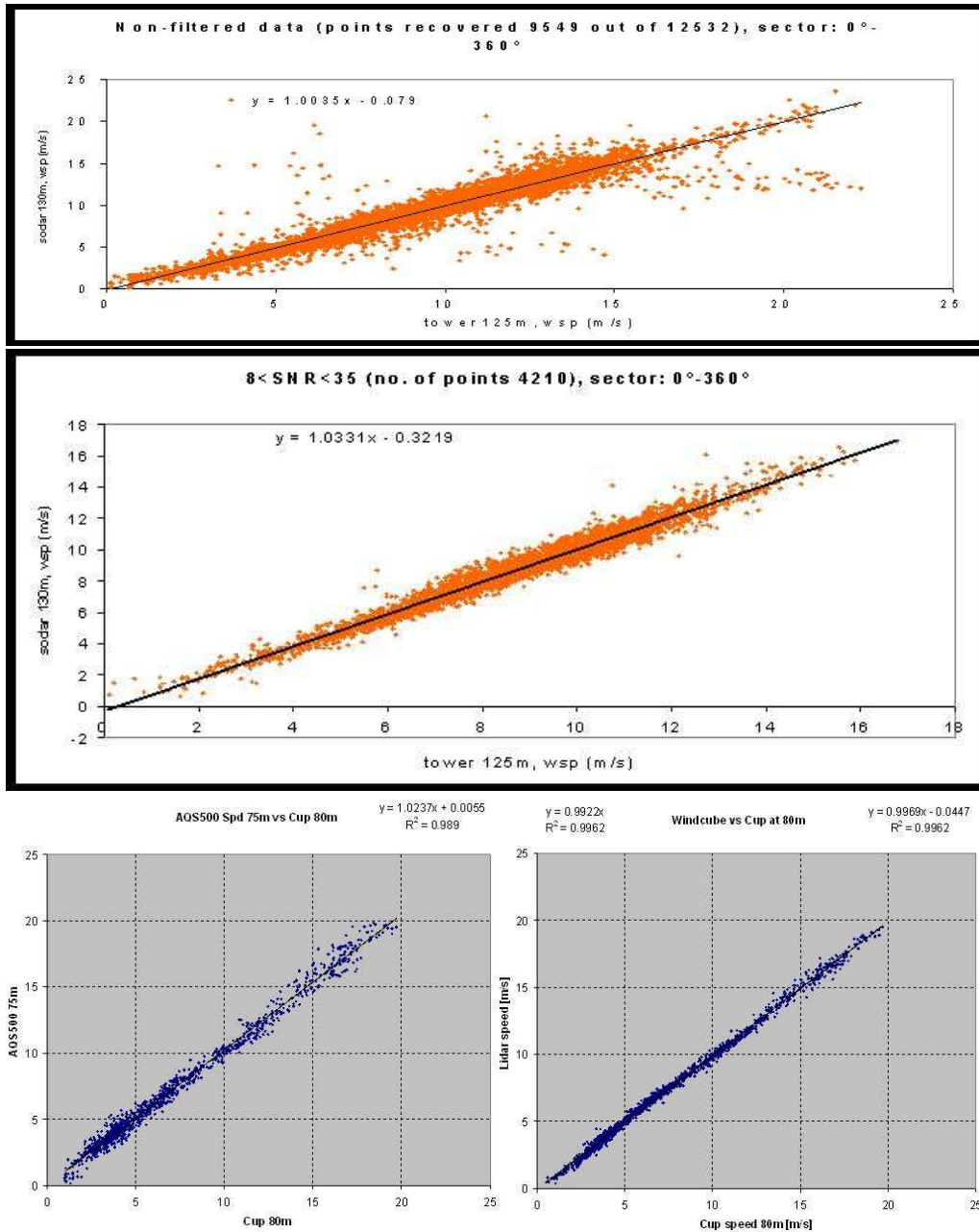


Figure 3: Example of scatter plots from sodar vs. cup anemometer data. The upper graph presents unscreened sodar wind speed data plotted against corresponding high-quality cup anemometer data measured at the Risø DTU met tower at 125 m. A data availability corresponding to 76% (9549 10-min averaged wind speeds) was obtained during this particular sodar vs cup anemometer inter-comparison test of almost three month duration (12532 10-min periods). The middle data graph shows the same data set after screening of the sodar data for high C/N-ratios. The scatter is significantly reduced, but so is also the data availability which with only 4210 data points has been reduced to almost 34%. The bottom panel shows (left) simultaneous measured sodar vs cup scatter plot at 75 m height (0.989) and (right) lidar vs the same cup for the same data period. The lidar measurements at 80 m are seen to exhibit less scatter and high correlation coefficient (0.996)

sodar for accurate measurements over the entire rotor plane due to low C/N ratio (Wagner et al., 2008). There are several sodar manufactures on the wind RS market today including for example Remtech, Atmospheric Systems Corporation (formerly Aerovironment), Metek, Scintec, Second Wind Inc. and Swedish AQ System to mention the most dominant. All but one base their sodar technology on mono-static phased array antenna configurations except AQ System sodars which are build on three solid dish parabolas offering a somewhat bigger antenna directivity (12° opening angle). However, only a couple of today’s sodar manufacturers address directly the high accuracy demanding wind energy market.

The EU WISE project addressed and evaluated commercial sodars for wind energy (deNoord et al., 2005) and concluded then that neither of the commercial sodars were particularly close to be able to substituting standard measuring masts. In conclusion the WISE project stated that general purpose commercial sodars were unreliable, especially in case of bad weather or high background noise

### Recent developments

A few improvements seem to have emerged since 2005. Particularly for the few sodars that addresses the wind energy market. Replacement of the phased arrays by parabola dish seems to have contributed to the sodars overall C/N performance. Also better and improved signal processing is apparently applied today. However, it is my personal belief that we won’t see any significant quantum leap in sodar performance until sodars for wind energy applications are build on bi-static configurations. Research and development along these lines are in progress, and researchers and test engineers at Risø DTU are looking forward to see and to test possible future bi-static configured sodars especially designed to meet the high accuracy demands set within wind energy RS.

Table 1: Pros & Cons of sodars

Pros	Cons
Portable	Low duty cycle (1 pulse transmitted every 3 s, and up to 6–10 s lapse times before all three wind components have been sampled)
Build on well developed and well-proven audio-frequency “low tech” technology	Limited by low S/N- ratio at: 1) high wind speed conditions 2) during neutrally stratified conditions
Sodars are relatively cheap (priced down to some 25% of a corresponding wind lidar)	Prone to solid reflections from the surroundings (including wind turbines)
Low power consumption (one solar powered version uses less than 10 W)	Prone to high background environmental noise
Sound backscatter: Relatively high yield (backscattered power at the detector of the order of $10^{-10}$ W)	Low wavelength/aperture ratio (1:10) results in undefined broad antenna beams Prone to beam bending with wind speed of the order of 5% or higher of the speed of sound Huge measurement and sample volumes Signal processing limited by pulsed sodars relative long data acquisition times (sampling time per pulse of the order of 1 s)

Table 2: Accuracy with sodars during neutral conditions

Slope mean wind speed vs. calibrated cup anemometers	$\pm 3\%$
Correlation coefficients [at 125 m, neutral stratification]	0.9–0.95
Mean turbulence intensity[at 80 m]	< 1% error

### Summary of sodars

Most of today commercially available sodars are still build on “pre wind energy era” antenna design and processing technology, which do not in particular address nor support the high accuracy demands required within wind energy and resource assessment studies of today. The consequence is that most – if not all – of the available sodars today still exhibit insufficient accuracy to be accepted by the wind energy industry and society as an accurate RS tool for precise and “bankable” wind energy investigations.

Although some improvements seem to have occurred in accuracy since our first 2005 WISE sodar investigation, it is still not this author’s belief that sodars as they come will be able to meet the high accuracy demands of the wind energy society in the future unless a major quantum jump can be demonstrated in their overall performance at high wind speed, neutral atmospheric stratification, and at present wind turbine hub heights (> 100 m).

At Risø DTU we see two venues for further research along which improved accuracy of sodars may happen: One is to switch to fully bi-static pulsed or CW based sodar configurations, however cumbersome, and the other is to take advantage of the immense, fast and cheap embeddable processing power set to our disposal from the information technology industry today, and apply these for enhanced on-line real time signal processing.

## 1.3 Part II: RS of wind by light (lidars)

### Introduction to lidars

The motivation and demand in the wind energy market for wind lidars are similar to those of wind sodars. At a continuously increasing rate today wind turbines are being installed on, offshore, in hilly and forested areas, and even in complex or mountainous terrain. At the same time, as the turbines gets bigger and more powerful, they also reach higher and higher into the atmospheric flow, and thereby also into hitherto unknown wind and turbulence regimes – on as well as offshore.

The industry’s traditional method for performing accredited and traceable measurements of power performance is to mount a single accurately calibrated cup anemometer at hub height two to four rotor diameters upwind in front of the turbines on a tall meteorological mast. IEC 61400-12-1 describes the accepted standard for power performance verification (power curve measurement) and prescribes measurements of power production correlated with wind speed measurements from a cup anemometer located at hub height in front of the wind turbine 2–4 rotor diameters upstream.

With turbines becoming bigger correspondingly high meteorology masts equipped with wind speed instrumentation becomes progressing more cumbersome and expensive to install, especially in mountainous and complex terrain. As wind turbines rotor planes reaches 120 m in diameter or more it is evident that the incoming wind field over the entire rotor planes is not measured representatively from a single cup anemometer mounted at hub height.

Accurate measurements of the inflow of today’s huge wind turbines will require multi-point multi-height wind measurements within the entire rotor plane, to characterize the wind speed and wind shear over the entire rotor plane. Research activities addressing detailed rotor plane inflow and wakes is ongoing at Risø DTU in connection with the

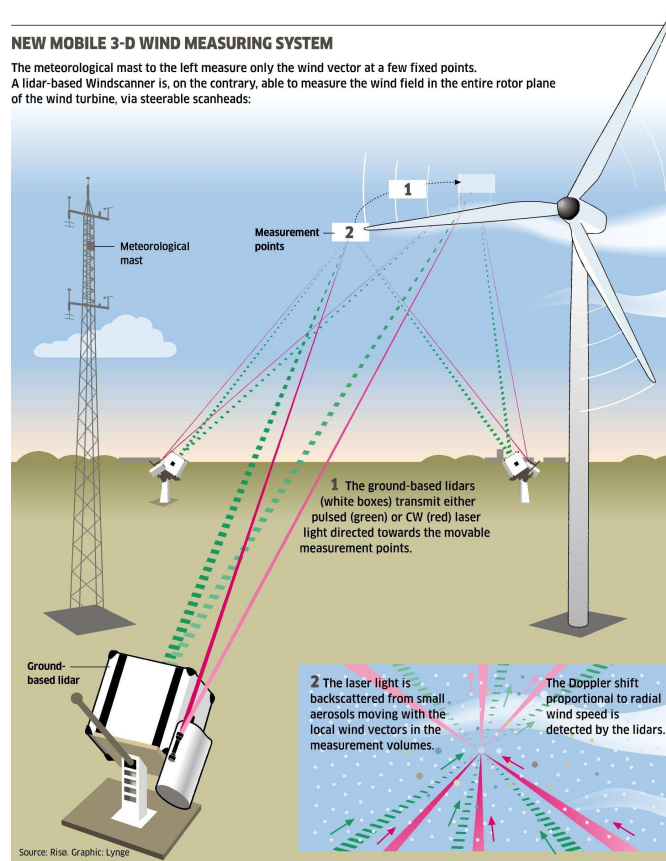


Figure 4: Windscanners in operation – CW and pulsed wind lidars engaged in measurements of the wind and turbulence fields around a spinning wind turbine (See Windscanner.dk for more details)

establishment of new research infrastructure based on wind lidars, see Windscanner.dk and Mikkelsen (2008).

### Wind RS methodologies

RS measurement methodologies for wind energy applications are today commercially available and encompass various measurement techniques that include sound based sodars, laser based lidars and satellite borne scatterometry. The application range for wind measurements are also plentiful, and encompass for example:

1. Wind turbine power performance verification – Establishment of new RS based measurement standards for the replacement of in-situ reference met masts. Work within the IEC is at the moment aiming at establishment of a new international IEC-standard for remote sensed wind measurements, as e.g. obtained by lidars, for power curve measurements.
2. Wind energy resource measurements – The global wind resources are now being mapped globally on shore, off shore, over hilly and in mountainous terrain, etc. Here also, high accuracy is of uttermost importance for accurate site and resource assessments. Measurement errors in excess of 1% are unacceptable by project developers and investment banks.
3. Wind turbine control – RS lidar instruments that are directly integrated into the wind turbines hub or spinner or even into the blades are also seen as a forthcoming RS measurement technology that can help improve the wind turbines power performance

and possibly also diminish fatigue wear from extreme gusts and wind shear via active steering the wind turbines individual blade pitch or, to come one day maybe, its trailing edge flaps.

Researchers at Risø DTU have during decades now followed and contributed to the development of improved instrumentation for RS of wind. Starting out already in the 60's with more general boundary-layer meteorological investigations of flow and diffusion our present research and experimental developments within the meteorology and test and measurement programs at Risø DTU has recently become more and more directed towards applications within wind energy. Wind lidars and lidar-based wind profilers, their measurement principles, their measurement performances, and also their possible future integration within wind turbines themselves are here addressed.

## Wind lidars

Measuring wind with a wind lidar means to probe the atmospheric flow from the ground by use of light beams. A wind lidar is wind measurement devise able to detect the Doppler shifts in backscattered light. The Doppler shift is proportional to the wind speed in the beam direction in the wind lidar's adjustable measurement volumes.

Lidars, like sodars, provide a ground-based RS measurement methodology for measuring the winds at various ranges, angles and heights aloft. Wind lidars work by transmitting electromagnetic radiation (light) from a laser with a well-defined wavelength in the near infrared band around  $1.5 \mu\text{m}$ . They detect a small frequency shift in the very weak backscattered light, a Doppler shift that results from the backscattering of light from the many small aerosols suspended and moving with the air aloft.

From a meteorological point of view wind turbine are "obstacles" within the lowest part of the atmospheric boundary layer, that is, the part of the atmosphere best characterize by high wind shear, strong wind veers, and with the highest levels of turbulence.

A wind profiler is a ground-based wind lidar transmitting a continuous beam or a sequence of pulsed radiation in three or more different inclined directions. A wind profiler determines the radial wind speeds in multiple directions above its position on the ground. It does so also by determining the Doppler shifts in the detected backscattered radiation along each beam direction. Wind lidars, like sodars, therefore have both transmitting and receiving antennas, which most wind profilers today combine into a single optical telescope. The three-dimensional wind vector as function of height by measuring the radial wind speeds in three or more beam directions above the lidar. In practice, the transmitting and receiving radiation are combined in a single telescope and the beam is then steered in different directions via a rotating wedges or turning mirrors.

Wind lidars in the market for vertical mean and turbulence profile measurements are available based on two different measurement principles:

1. Continuous wave (CW) lidars
2. Pulsed lidars

Several wind lidars addressing the wind energy market are commercial available today. CW-based wind lidars are manufactured by Natural Powers (ZephIR) and OPDI Technologies & DTU Fotonik (WINDAR) while Coherent Technologies Inc. (Wind tracer), Leosphere (WindCube), CatchtheWindInc (Vindicator) and Sgurr Energy (Galion) manufacture pulsed lidars for the time being.

The technology imbedded in today's CW and pulsed wind lidar systems have been spurred from the telecommunication  $1.5 \mu\text{m}$  fiber and laser technology revolution in the 90's. There are however, some principally differences between CW and pulsed lidar's temporal and spatial resolution, properties that have influence on the different lidar types ability to measure and resolve the mean wind and turbulence characteristics of the atmospheric boundary layer wind field.





*Figure 5:* Two CW wind lidars belonging to the Windscanner.dk research facility being inter-compared and tested up against the tall meteorological masts at Høvsøre, Risø DTU.

The CW lidar focuses a continuous transmitted laser beam at a preset measurement height and there determines, also continuously, the Doppler shift in the detected backscatter also from that particular height. When wind measurements from more than a single height are required, the CW lidar adjusts its telescope to focus on the next measurement height. The measurement ranges (measurement heights) as well as the spatial resolution of a CW lidar measurement is controlled by the focal properties of the telescope. The shorter the measurement distance, and the bigger the aperture (lens), the better defined is a CW lidar's range definition and its radial measurement confinement. A CW lidar resolves the wind profile along its beam in a similar manner as a photographer controls the focal depth in a big sport or bird telescope.

The focal depth of any telescope, however, increases proportional to the square of the distance to the focus or measurement point. This optical property limits a CW lidar build with e.g. standard 3" optics to measurement heights below, say 150 m.

A pulsed lidar on the other hand transmits a sequence of many short pulses, typical 30 m in effective length, and then it detects the Doppler shift in the backscattered light from each pulse as they propagate with the speed of light. While a CW lidar measures from one height at a time a pulsed lidar measures wind speeds from several range-gated distances simultaneously, typically at up to 10 range gates at a time.

The pulsed lidar's spatial resolution, in contrast to the CW lidar, is independent of the measurement range. The pulse width and the distance the pulse travels while the lidar samples the detected backscatter control its resolution. The spatial resolution in the beam direction obtainable with the 1.5  $\mu\text{m}$  wavelength pulsed lidar in the market today are of the order of 30–40 m.

In addition, while a CW lidar's upper measurement distance is limited progressing unconfined measurement volume at long distances, a pulsed lidar's maximum measurement range is limited by deteriorating C/N-ratios in measurements from far distances (height).

Moreover, while a CW lidar equipped with a 1 W 1.5  $\mu\text{m}$  eye-safe laser has been tested able to sample and process up to 500 wind speed measurements per second, a corresponding powered pulsed lidar can handle only 2–4 wind speed samples per second.



Figure 6: CW wind lidars (ZephIRs) under testing at Høvsøre, Risø DTU

Each of these samples, however, then on the contrary contain wind speeds from up to 10 range gates (ranges) measured simultaneously.

**CW vs pulsed lidars** Overall, CW lidar features high spatial resolution in the near range and very fast data acquisition rates, features that are well suitable for turbulence measurements. Today's commercial available CW lidar profilers measure radial wind speeds at ranges up to  $\sim 200$  m and wind vectors at heights up to 150 m.

The pulsed lidar configuration on the other hand features lower but always constant spatial resolution properties (30–40 m) at all ranges. They are also inherently slower in their data acquisition rate, but then they measure wind speeds at multiple heights simultaneously, and they hold also potential for reaching longer ranges (heights) than corresponding powered CW lidars. At the test site in Høvsøre Risø DTU, commercial available pulsed wind lidar profiles have regularly measured the wind vector profiles up to 300 m height.

### Wind profiling

A wind “profiler” measures 10-min averaged quantities of the vertical wind speed profile, the vertical direction profile, and the vertical turbulence profiles, by combining a series of radial measured wind speed components from several, and at least three, different beam directions, into a three-dimensional wind vector. CW-based wind lidars, e.g. the ZephIR, measure the vertical wind profile at five consecutive heights, selectable in the range from, say 10 to 150 m height. Pulsed lidars, e.g. the WindCube or the Galion, measure correspondingly the vertical wind profile simultaneously at several (of the order of 10) heights, in the height interval from 40– $\sim 300$  m, the upper bound depending on the amount of aerosols in the air.

True for all wind profilers in the wind energy market, however, CW and pulsed lidars irrespectively, is that they rely during combining measured radial wind speeds into a single wind vector on the assumption that the flow over the wind lidar is strictly homogeneous. Homogeneous wind flow means that the air stream is unaffected and not influenced by hills, valleys, other wind turbine wakes, or near-by buildings within their volume of air scanned above the lidar.

For this reason, neither lidar nor sodar based wind profilers will be able measure correctly over sites located in hilly or complex terrain where the wind field is affected



*Figure 7:* Pulsed wind lidars (six WLS7 WindCubes) and one Galion (far back) during testing at Høvsøre, Risø DTU

by the near-presence of hills or upwind turbines. Easily, up to  $\sim 10\%$  measurement errors can be observed between wind speeds measured by a lidar and a mast-mounted cup anemometer co-located to take wind profile measurements from the on top of a hill. Research is therefore ongoing in order to correct wind lidar based profile measurements for flow distortion e.g. induced by terrain effects (Bingöl et al., 2008).

### **Lidar accuracy**

Inherently, lidars can remotely measure the wind speeds aloft with much higher accuracy than a sodar. This is due to the nature of light, which propagates  $\sim 1$  million times faster than a sound pulse, and because a lidar’s antenna aperture size compared to the wavelength, i.e. “lens diameter-to-wavelength ratio” in a lidar is about 1000 times bigger than practically obtainable with a sodar. This result in superior beam control and also in much higher data sampling rates.

At Risø DTU’s test site at Høvsøre, testing and calibration of wind lidar is now daily routine and is performed by inter-comparing and correlating lidar-measured wind speeds with wind speeds from calibrated cup anemometers in our 119-m freely exposed tall reference met mast. During “fair weather conditions”, 10-min averaged wind speeds from lidars and the cups are in-situ intercompared and correlated. Linear regression coefficients with both CW and pulsed lidars could be obtained in the range of  $\sim 0.99 - 1.00$ , and correlation coefficients as high as  $\sim 0.99$  (Wagner et al., 2009).

“Fair weather” means here that lidar data are screened for periods with rain, fog, mist and low-hanging clouds and mist layers. Usually this only removes a few per cent of the data. All lidars, CW and pulsed included, rely during determination of the wind speed from Doppler shift measurements on the assumption that the aerosols in the measurement volumes are homogeneously distributed and follow the mean wind flow.

Sodars for that matter, can under ideal conditions perform almost similarly well with respect to mean wind speed (linear regression coefficients as high as  $\sim 0.99$  has been reported above). The observed scatter, however, as compared to a lidar, is bigger. Correlation coefficients observed while testing of sodars at Risø DTU’s 125 m tall met mast at wind energy relevant neutrally stratified strong wind conditions ( $> 10 \text{ m s}^{-1}$ ) has so far not been observed to exceed the 0.90 level.

## Wind lidar applications for wind energy

Wind lidar manufactures today address the market for replacement of tall reference meteorology mast installations at the moment required for accredited and bankable wind resource measurements and for ground-based wind turbine performance measurements. Lidar manufactures also offer their wind lidars as instruments for evaluation of model-based wind resource estimation, on and offshore (numerical wind atlases).

Wind lidars in the market today offer the wind energy industry with RS instruments, for:

- Wind speed, wind direction and turbulence profiling.
- Wind resource assessments, on and offshore.
- Wind turbine performance testing (power curves).
- Wind resource assessment via horizontal scanning over complex terrain.

**Further developments** Furthermore, new and improved wind lidar data and measurement technologies are under development for RS-based power performance measurements from the ground but also directly from the wind turbines. A conically scanning wind lidar (Control-ZephIR) has during the summer 2009 been tested in a operating NM80 2.3 MW wind turbine located at Tjæreborg Enge, Denmark, with the purpose to investigate the use of wind lidars integrated directly into the wind turbine hubs, blades or spinners. The intention is to improve the wind turbine's performance by use of upstream approaching wind speed measurements from inside the turbines rotor plane as an active input to the wind turbines active control systems. Wind lidars for turbine yaw control are already nowadays on the market (Vindicator) and new and smaller wind lidars are in the near-future envisioned to become integrated as "standard" on wind turbines to provide upstream lead time wind data to the turbines control system, e.g. for:

- Enhanced wind turbine yaw control.
- Lead-time control for individual pitch control.
- Protection against fatigue from extreme wind shear and wind gusts.
- Prolonging the wind turbines longevity.
- Improving the wind turbine productivity.

## Summary of lidar

Since the wind lidar era started at Risø DTU in 2004 new wind lidars have emerged on the wind energy market, spurred by the telecom technology revolution of the 90's. Today, wind lidars, continuous and pulsed, and properly calibrated, aligned, installed and maintained, and their volume-averaged wind measurements properly interpreted, are indeed very precise wind measuring devices, capable of matching the wind industry's needs today and in the future for precise and reproducible wind profile measurements and resource assessments.

Before, however, lidar measured wind measurements can become fully certified and accredited to industry standards, new and revised IEC lidar standards have first to be set and come into effect. It is important, however, here also to apprehend the very different nature of the previous standards point measurements as obtained from a mast-mounted cup anemometer and a volume-averaged wind vectors as obtainable from a profiling wind lidar.

Although the first generations of wind lidars, CW and pulsed, indeed had many difficulties with reliability, this era now seems to have been improved beyond their first children growth pains. Today's wind lidars offer realistic and mobile alternatives to the

installation of tall meteorological masts for many wind resource estimation assessment studies, on and offshore. The near future will inevitably also show turbine mounted wind lidars fully integrated with the wind turbines control systems for improving the wind turbines productivity and longevity.

## Notation

CW	continuous wave
C/N	carrier-to-noise
lidar	light detection and ranging
RS	remote sensing
SAR	synthetic aperture radar
sodar	sound detection and ranging

## References

- Bingöl F., Mann J., and Foussekis D. (2008) Lidar error estimation with WAsP engineering. *IOP Conf. Series: Earth and Environ. Sci.* 1:012058
- de Noord M. et al. (2005) Sodar power performance measurements, WISE WP5.
- Gustafsson D. (2008) Remote wind speed sensing for site assessment and normal year correction – The use of sodar technology, with special focus on forest conditions. Master of Science Thesis in Energy Technology, KTH, Stockholm.
- Mikkelsen T., Jørgensen H. E., and Kristiansen L. (2007) The Bi-static sodar “Heimdall” – you blow, I listen. Risø-R-1424(EN), Roskilde
- Mikkelsen T., Courtney M., Antoniou I., and Mann J. (2008) Wind scanner: A full-scale laser facility for wind and turbulence measurements around large wind turbines. *Proc. of the European Wind Energy Conf.*, Brussels
- Wagner R. and Courtney M. (2009) Multi-MW wind turbine power curve measurements using remote sensing instruments – the first Høvsøre campaign. Risø-R-1679(EN), Roskilde
- Wagner R., Jørgensen H. E., Poulsen U., Madsen H. A., Larsen T., Antoniou I., and Thesberg L. (2008) Wind characteristic measurements for large wind turbines power curve. *Proc. of the European Wind Energy Conf.*, Brussels
- Kristiansen L. (2010) My own perception of basic statistics. *Available on request from Torben Mikkelsen*, Roskilde

# 2 Atmospheric turbulence

Jakob Mann

Wind Energy Division, Risø DTU, Roskilde, Denmark

---

## 2.1 Introduction

For many civil engineering structures, including wind turbines, dynamic wind loading caused by the atmospheric turbulence is a serious concern for the designer. Gust loading on streamlines bridge decks requires knowledge of the vertical wind field fluctuations not only in one point, but also how the fluctuations are correlated in space Simiu and Scanlan (1996); Larose and Mann (1998). Also the horizontal components may be of importance in bridge aerodynamics. For dynamical load calculations on a wind turbine, for example at an off-shore location knowledge of all three wind components and their spatial correlations are needed because the gusts are ‘sampled’ in a complicated way by the sweeping blades. Yet other structures such as tension leg platforms used for extracting oil on deep waters are sensitive to slow variation in the direction of the wind. Thus various engineering structures are sensitive to various components of wind fluctuations at a wide range of frequencies and also to the spatial correlations of these fluctuations.

The spatial structure of turbulence is also important in order to understand how remote sensing instruments such as lidars measure in a turbulent flow fields. That is because the lidar’s sampling volume is rather extended and thus very far from the almost point-like measurements of a ultra-sonic anemometer. The description of how lidars measure turbulence may be found in Mann et al. (2009) for a pulsed lidar, or in Sjöholm et al. (2009) for a continuous wave (cw) lidar.

The purpose of this contribution is to model the *spectral tensor* of neutral atmospheric surface layer turbulence. The spectral tensor contains all information on spectra, cross-spectra and coherences, which usually are the input requested by wind engineers. We also want to devise a general algorithm to simulate three-dimensional fields of all three components of the wind velocity fluctuations. Such simulations are particular useful for time domain simulations of gust loading of wind turbines and other structures.

In section 2.3 rapid distortion theory (RDT) is used to estimate the tendency of shear to make turbulence anisotropic. RDT is a linearization of the Navier–Stokes equations and has as such limited applicability. The influence of the non-linearity is modeled by postulating some limit as to how much shear is allowed to make the turbulence anisotropic. This modelling uses the concept of eddy lifetime. Despite the various assumptions and postulates the tensor model only contains three adjustable parameters: a length scale describing the size of the energy containing eddies, a non-dimensional number used in the parametrization of eddy lifetime, and the third parameter is a measure of the energy dissipation.

These three parameters are estimated by comparing the model to measurements over the sea in section 2.4. In section 2.5 the model is compared to various widely used wind engineering spectral formulations. Finally, in section 2.7 the spectral tensor is used in a numerical algorithm to simulate three-dimensional fields of all three components of the wind vector. This is done by recasting the Fourier representation of the wind field in the discrete wave-vector space, i.e. as a trigonometric series, where the statistics of the random coefficients are determined by the spectral tensor. The method is considerably simpler, faster and in some aspects more physical than many other currently used simulation algorithms. The method is now used in bridge aerodynamics and in load calculations on wind turbines.

Much of the material presented here has previously been reported in Mann (1994, 1998),

and more details on many aspects may be found in these papers. Newer comparison with neutral atmospheric data taken from Risø's test station Høvsøre may be found in Peña et al. (2010) and comparison under different atmospheric stabilities are under way.

## 2.2 Definitions

The atmospheric turbulent velocity field is denoted by  $\tilde{\mathbf{u}}(\mathbf{x})$ , where  $\mathbf{x} = (x, y, z)$  is a right-handed coordinate system with the  $x$ -axis in the direction of the mean wind field and  $z$  as the vertical axis. The fluctuations around the mean wind,  $\mathbf{u}(\mathbf{x}) = (u_1, u_2, u_3) = (u, v, w) = \tilde{\mathbf{u}}(\mathbf{x}) - (U(z), 0, 0)$ , are assumed to be homogeneous in space, which is often the case in the horizontal directions but is only a crude approximation in the vertical. Since turbulence over the sea at high wind speeds is primarily shear-generated, the mean wind field is allowed to vary as a function of  $z$ . Because of homogeneity, the covariance tensor

$$R_{ij}(\mathbf{r}) = \langle u_i(\mathbf{x})u_j(\mathbf{x} + \mathbf{r}) \rangle \quad (1)$$

is only a function of the separation vector  $\mathbf{r}$  ( $\langle \ \rangle$  denotes ensemble averaging).

We shall use *Taylor's frozen turbulence hypothesis* to interpret time series as 'space series' and to serve as a 'dispersion relation' between frequency and wave number (Panofsky and Dutton, 1984). Therefore, we can suppress the time argument in  $\mathbf{u}$ .

We only aim at modelling the second order statistics of turbulence, such as variances, cross-spectra, etc. For simulation purposes the velocity field is otherwise assumed to be Gaussian (see section 2.7). It is still not clear how much influence the statistics of third order, such as skewness, has on load calculations.

All second order statistics can be derived from the covariance tensor or its Fourier transform, the spectral tensor:

$$\Phi_{ij}(\mathbf{k}) = \frac{1}{(2\pi)^3} \int R_{ij}(\mathbf{r}) \exp(-i\mathbf{k} \cdot \mathbf{r}) d\mathbf{r}, \quad (2)$$

where  $\int d\mathbf{r} \equiv \int_{-\infty}^{\infty} \int_{-\infty}^{\infty} \int_{-\infty}^{\infty} dr_1 dr_2 dr_3$ . The spectral tensor is the basis of the Fourier simulation in section 2.7.

The stochastic velocity field can be represented in terms of a generalized stochastic Fourier-Stieltjes integral:

$$\mathbf{u}(\mathbf{x}) = \int e^{i\mathbf{k} \cdot \mathbf{x}} d\mathbf{Z}(\mathbf{k}), \quad (3)$$

where the integration is over all wave number space. The orthogonal process  $\mathbf{Z}$  is connected to the spectral tensor by

$$\langle dZ_i^*(\mathbf{k}) dZ_j(\mathbf{k}) \rangle = \Phi_{ij}(\mathbf{k}) dk_1 dk_2 dk_3, \quad (4)$$

which is valid for infinitely small  $dk_i$  and where  $*$  denotes complex conjugation (Batchelor, 1953).

Is it very difficult to measure the spectral tensor directly. Instead cross-spectra, defined as

$$\chi_{ij}(k_1, \Delta y, \Delta z) = \frac{1}{2\pi} \int_{-\infty}^{\infty} R_{ij}(x, \Delta y, \Delta z) e^{-ik_1 x} dx \quad (5)$$

are often measured, say by two instruments separated by  $\Delta y$  in the horizontal direction perpendicular to the wind and  $\Delta z$  in the vertical, and are used in practical applications. The connection between the components of the spectral tensor and the cross-spectra is

$$\chi_{ij}(k_1, \Delta y, \Delta z) = \int_{-\infty}^{\infty} \int_{-\infty}^{\infty} \Phi_{ij}(\mathbf{k}) e^{i(k_2 \Delta y + k_3 \Delta z)} dk_2 dk_3. \quad (6)$$

When the two indices  $i$  and  $j$  are the same and  $\Delta y = \Delta z = 0$  Eq. (6) becomes the one-point spectrum  $F_i(k_1) = \chi_{ii}(k_1, 0, 0)$ . This definition implies that spectra are *two-sided*, i.e. we get the variance by integrating from  $-\infty$  to  $\infty$ . This convention is used throughout this chapter.

To distinguish between spectra as functions of wave number  $k_1$  ( $= 2\pi f/U$ ) and frequency  $f$  we use  $F$  for the former and  $S$  for the latter, i.e.  $S_i(f)df = F_i(k)dk$ . The *coherence* is defined as

$$\text{coh}_{ij}(k_1, \Delta y, \Delta x) = \frac{|\chi_{ij}(k_1, \Delta y, \Delta z)|^2}{F_i(k_1)F_j(k_1)}, \quad (7)$$

which can be interpreted as a normalized cross-spectrum.

## 2.3 Rapid distortion theory

The incompressible Navier-Stokes equation may be written as

$$\frac{D\mathbf{u}}{Dt} + \mathbf{u} \cdot \nabla \mathbf{U} = -\frac{1}{\rho} \nabla p + \text{non-lin. and viscous terms}, \quad (8)$$

where  $p$  is the pressure, and  $D/Dt \equiv \partial/\partial t + \mathbf{U} \cdot \nabla$  is the ‘average Lagrangian derivative.’ Assuming a linear shear ( $\nabla \mathbf{U}$  constant), taking the curl, and dropping the non-linear and viscous terms we get

$$\frac{D\boldsymbol{\omega}}{Dt} = \boldsymbol{\Omega} \cdot \nabla \mathbf{u} + \boldsymbol{\omega} \cdot \nabla \mathbf{U}, \quad (9)$$

where  $\boldsymbol{\Omega}$  and  $\boldsymbol{\omega}$  are the mean and the fluctuating part of the vorticity. It is not at all clear that this linearization is permissible. For example, it can be shown that if the curl of Eq. (8) is used to estimate the change in mean square vorticity the non-linear terms will dominate the linear. However, Hunt and Carruthers (1990) argue that when used for the calculation of the response of velocity fluctuations ( $\mathbf{u}$  or  $R_{ij}$ ) to a sudden application of a large scale shearing or straining motion the linearization Eq. (9) is valid.

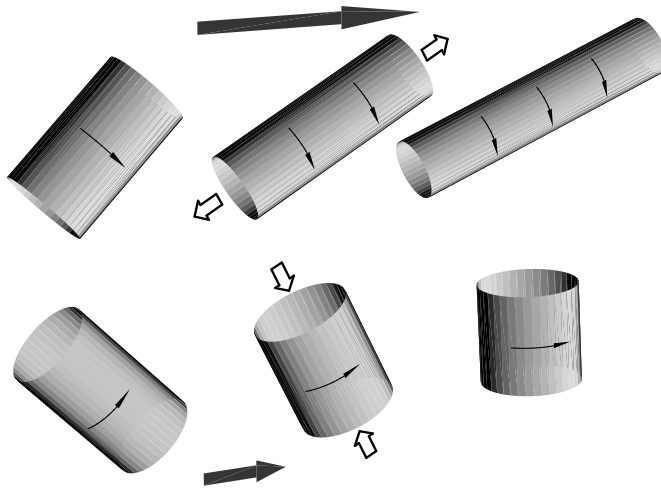


*Figure 8:* Interpretation of the interplay of shear and turbulence: Two differently oriented eddies are followed over three successive times. Shear stretches (along the axis of rotation) and speeds up the upper eddy while the lower eddy is compressed and slowed down.

Physically, the last term on the right hand side of Eq. (9) may be interpreted as the stretching of vorticity by the mean shear (see Figure 8). The first term is a distortion of the mean vorticity by velocity fluctuations.

In order to solve Eq. (9) we have to Fourier transform the equation. In order to do so, it is important to notice that wave fronts are advected by the mean flow i.e.

$$\frac{d\mathbf{k}}{dt} = -(\nabla \mathbf{U})\mathbf{k}. \quad (10)$$



The solution to this wave front advection equation is

$$\mathbf{k}(t) = \exp(-\nabla U t) \mathbf{k}_0 \quad (11)$$

where  $\exp$  means the matrix exponential.

For a general linear  $U$  Eq. (9) does not have analytic solution. However, for many simple situations such as unidirectional shear, non-rotational stretching or compression, etc. such solutions exists (Townsend, 1980).

To get the velocity field from the vorticity we shall express  $dZ$  in terms of  $d\Omega$ , which is the Fourier transform of  $\boldsymbol{\omega}$  defined in parallel to Eq. (3):

$$\boldsymbol{\omega} = \nabla \times \mathbf{u} \Rightarrow d\Omega = i\mathbf{k} \times dZ \Rightarrow -i\mathbf{k} \times d\Omega = \mathbf{k} \times (\mathbf{k} \times dZ). \quad (12)$$

Because of the general identity  $\mathbf{A} \times (\mathbf{B} \times \mathbf{C}) = \mathbf{B}(\mathbf{A} \cdot \mathbf{C}) - \mathbf{C}(\mathbf{A} \cdot \mathbf{B})$  and that  $\mathbf{k} \cdot dZ = 0$  we get

$$-i\mathbf{k} \times d\Omega = -k^2 dZ \Rightarrow dZ = i \frac{\mathbf{k} \times d\Omega}{k^2}. \quad (13)$$

We shall re-derive (3.11) in Mann (1994), i.e. set up the equations of motion for

$$\nabla U = \begin{pmatrix} 0 & 0 & 0 \\ 0 & 0 & 0 \\ \frac{dU}{dz} & 0 & 0 \end{pmatrix}. \quad (14)$$

In this case

$$\mathbf{k}(t) = \exp(-\nabla U t) \mathbf{k}_0 = \begin{pmatrix} 1 & 0 & 0 \\ 0 & 1 & 0 \\ -\frac{dU}{dz} t & 0 & 1 \end{pmatrix} \mathbf{k}_0, \quad (15)$$

in accordance with (3.13) of Mann (1994), and  $\boldsymbol{\Omega} = (0, dU/dz, 0)$ . The equations of motion Eq. (9) becomes

$$\frac{D\mathbf{k} \times dZ}{D\beta} = k_2 dZ + \begin{pmatrix} d\Omega_3 \\ 0 \\ 0 \end{pmatrix}. \quad (16)$$

Taking the cross product with  $\mathbf{k}$  and adding  $\dot{\mathbf{k}} \times (\mathbf{k} \times dZ)$  on both sides we get

$$\begin{aligned} -\frac{Dk^2 dZ}{D\beta} &= \frac{D\mathbf{k}}{D\beta} \times (\mathbf{k} \times dZ) + \mathbf{k} \times \frac{D\mathbf{k} \times dZ}{D\beta} \\ &= \frac{D\mathbf{k}}{D\beta} \times (\mathbf{k} \times dZ) + k_2 \mathbf{k} \times dZ + \begin{pmatrix} 0 \\ k_3 \\ -k_2 \end{pmatrix} d\Omega_3. \end{aligned} \quad (17)$$

Writing this more explicitly we get

$$\frac{Dk^2 dZ}{D\beta} = \begin{pmatrix} (k_1^2 - k_2^2 - k_3^2) dZ_3 - 2k_1 k_3 dZ_1 \\ 2k_1 (k_2 dZ_3 - k_3 dZ_2) \\ 0 \end{pmatrix} \quad (18)$$

and using  $Dk^2/D\beta = -2k_1 k_3$  from Eq. (15) this can be shown to be equivalent to (3.11) in Mann (1994).

The differential equations Eq. (18) are easily solved given the initial conditions  $\mathbf{k}(0) = \mathbf{k}_0 = (k_1, k_2, k_3)$  and  $d\mathbf{Z}(\mathbf{k}_0, 0)$ . Instead of time,  $t$ , we shall use the non-dimensional time,  $\beta$ , defined as

$$\beta = \frac{dU}{dz} t. \quad (19)$$

The solution to Eq. (18) is

$$d\mathbf{Z}(\mathbf{k}, \beta) = \begin{bmatrix} 1 & 0 & \zeta_1 \\ 0 & 1 & \zeta_2 \\ 0 & 0 & k_0^2/k^2 \end{bmatrix} d\mathbf{Z}(\mathbf{k}_0, 0), \quad (20)$$

where

$$\zeta_1 = \left[ C_1 - \frac{k_2}{k_1} C_2 \right] \quad , \quad \zeta_2 = \left[ \frac{k_2}{k_1} C_1 + C_2 \right] \quad (21)$$

with

$$C_1 = \frac{\beta k_1^2 (k_0^2 - 2k_{30}^2 + \beta k_1 k_{30})}{k^2 (k_1^2 + k_2^2)} \quad (22)$$

and

$$C_2 = \frac{k_2 k_0^2}{(k_1^2 + k_2^2)^{\frac{3}{2}}} \arctan \left[ \frac{\beta k_1 (k_1^2 + k_2^2)^{\frac{1}{2}}}{k_0^2 - k_{30} k_1 \beta} \right]. \quad (23)$$

Eqs. (15) and (20) give the temporal evolution of individual Fourier modes.

### RDT and surface layer turbulence

In this section we first discuss the connection between RDT and stationary surface-layer turbulence, then the key concept of eddy lifetime, and finally we combine the different parts to obtain the spectral tensor model. The theory in the previous section describes how turbulence react to a sudden and fast application of a linear shear. It is natural to ask what this has to do with turbulence in the surface layer over the ocean.

If the initial conditions can be represented by the isotropic von Kármán tensor,

$$\Phi_{ij}(\mathbf{k}) = \frac{E(k)}{4\pi k^4} (\delta_{ij} k^2 - k_i k_j), \quad (24)$$

with the energy spectrum

$$E(k) = \alpha \varepsilon^{\frac{2}{3}} L^{\frac{5}{3}} \frac{(Lk)^4}{(1 + (Lk)^2)^{\frac{17}{6}}}, \quad (25)$$

then the tensor  $\Phi_{ij}(\mathbf{k}, t)$  will become more and more ‘anisotropic’ with time.

The linearization implied by RDT is unrealistic, and at some point (in time) the stretched eddies will break up. We postulate that eddies of linear dimension  $\approx |\mathbf{k}|^{-1}$  (or more precisely the Fourier modes) are stretched by the shear over a time which is proportional to their lifetime. The lifetime  $\tau$  is

$$\tau(k) \propto \varepsilon^{-\frac{1}{3}} k^{-\frac{2}{3}} \quad (26)$$

pertaining, at least in the inertial subrange, to eddies with wave vector magnitude  $k = |\mathbf{k}|$  (Landau & Lifshitz 1987, § 33).

The basic *postulate* is that the *stationary* spectral tensor

$$\Phi_{ij}(\mathbf{k}) \equiv \Phi_{ij}(\mathbf{k}, \tau(k)) \quad (27)$$

describes the surface layer turbulence well. The combination of RDT and scale dependent eddy lifetimes has previously been used by Derbyshire and Hunt (1993).

Maxey (1982) has described a similar model with the exception that the lifetime  $\tau$  was assumed to be constant for all wavevectors. ( $\tau dU/dz$  is called ‘the equilibrium value of the effective distortion strain’ by Maxey.) Maxey’s model gives a reasonable, but not perfect, description of the ratios between  $\sigma_u^2$ ,  $\sigma_v^2$ ,  $\sigma_w^2$  and  $\langle uw \rangle$  for turbulent shear flows. There are, however, two grave drawbacks when the model of Maxey (1982) is used to calculate spectra:

1. The  $uw$ -cross-spectrum in the inertial subrange decays as  $k_1^{-\frac{5}{3}}$  whereas Wyngaard & Coté (1972) observe and give scaling arguments for  $k_1^{-\frac{7}{3}}$ .
2. For typical values of the effective distortion strain the model predicts  $F_u/F_w \approx 7$  in the inertial subrange whereas it should be  $F_u/F_w = \frac{3}{4}$ .

The models presented here do not suffer from these shortcomings.

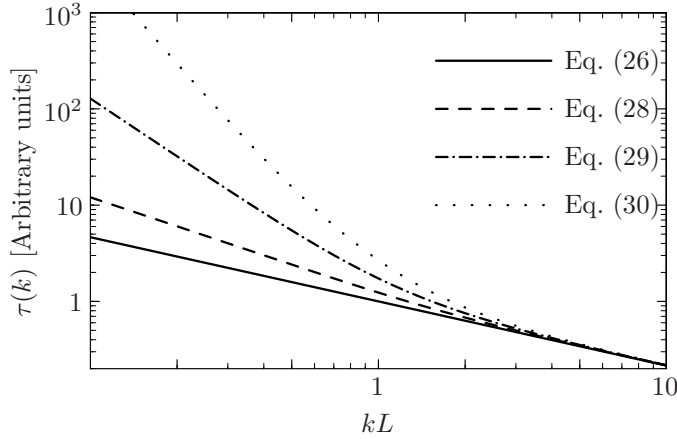


Figure 9: Eddy lifetimes as functions of the magnitude of the wave vector. The lifetimes given by Eq. (28) give the most realistic results.

### Eddy lifetimes

At scales larger than the inertial subrange Eq. (26) is not necessarily valid. We construct an alternative model for the ‘eddy lifetime’ assuming that the destruction of an eddy with size  $k^{-1}$  is mainly due to eddies comparable to or smaller than  $k^{-1}$ . The characteristic velocity of these eddies may be written as  $(\int_k^\infty E(p)dp)^{\frac{1}{2}}$ , and we simply assume the lifetime to be proportional to the size  $k^{-1}$  divided by this velocity:

$$\begin{aligned} \tau(k) &\propto k^{-1} \left( \int_k^\infty E(p)dp \right)^{-\frac{1}{2}} \\ &\propto k^{-\frac{2}{3}} \left[ {}_2F_1 \left( \frac{1}{3}, \frac{17}{6}; \frac{4}{3}; -(kL)^{-2} \right) \right]^{-\frac{1}{2}} \propto \begin{cases} k^{-\frac{2}{3}} & \text{for } k \rightarrow \infty \\ k^{-1} & \text{for } k \rightarrow 0 \end{cases} \end{aligned} \quad (28)$$

where we have chosen  $E$  as the von Kármán energy spectrum Eq. (25) and where  ${}_2F_1$  is the hypergeometric function.

Comte-Bellot and Corrsin (1971) give another lifetime model which has the right asymptotic behaviour for  $k \rightarrow \infty$ , the ‘coherence-destroying diffusion time’ :

$$\begin{aligned} \tau_D(k) &\propto k^{-2} \left[ \int_k^\infty p^{-2} E(p)dp \right]^{-\frac{1}{2}} \\ &\propto k^{-\frac{2}{3}} \left[ {}_2F_1 \left( \frac{4}{3}, \frac{17}{6}; \frac{7}{3}; -(kL)^{-2} \right) \right]^{-\frac{1}{2}} \propto \begin{cases} k^{-\frac{2}{3}} & \text{for } k \rightarrow \infty \\ k^{-2} & \text{for } k \rightarrow 0 \end{cases} \end{aligned} \quad (29)$$

which was constructed as the square of the eddy size divided by a  $k$ -dependent ‘turbulent viscosity’.

Further, the inverse ‘eddy-damping rate’

$$\tau_E(k) \propto (k^3 E(k))^{-\frac{1}{2}} \propto \begin{cases} k^{-\frac{2}{3}} & \text{for } k \rightarrow \infty \\ k^{-\frac{7}{2}} & \text{for } k \rightarrow 0 \end{cases} \quad (30)$$

is used by Lesieur (1987) in eddy-damped quasi-normal theories of turbulence as a characteristic non-linear relaxation time.

All lifetime models are shown in Figure 9 normalized such that they coincide in the inertial subrange. It turns out that  $\sigma_u^2$  becomes infinite using Eq. (29) or (30), while Eq. (26) and (28) give reasonable results. It also turns out that the spectra calculated from Eq. (28) fit the data better than Eq. (26) for which reason Eq. (28) is used in the rest

of this chapter. Some support for Eq. (28) may be found in Panofsky, Larko, Lipschutz, Stone, Bradley, Bowen and Højstrup (1982) who measured eddy ‘response times’ of eddies in the neutral atmospheric surface-layer. Also Kristensen and Kirkegaard (1987) were in their theoretical model of the growth of a puff in a turbulent fluid compelled to use Eq. (28) rather than Eq. (29) or (30).

It is convenient to write Eq. (28) as

$$\tau(k) = \Gamma \left( \frac{dU}{dz} \right)^{-1} (kL)^{-\frac{2}{3}} \left[ {}_2F_1 \left( \frac{1}{3}, \frac{17}{6}; \frac{4}{3}; -(kL)^{-2} \right) \right]^{-\frac{1}{2}}, \quad (31)$$

where  $\Gamma$  is a parameter to be determined.<sup>1</sup>

It should be emphasized that at low wave numbers the assumptions made so far are not valid. F.ex. the assumptions of linear shear is only valid over small distances, i.e. for large  $k$ . Similarly, homogeneity is a dubious assumption for large vertical separations. Finally, despite talking about eddy lifetimes, there is no real modelling of the decay process, because there is no equation describing the non-linear transfer of energy among various wave vectors.

In an attempt to relax the assumption of vertical homogeneity Mann (1994) modelled the influence of the blocking of the surface in addition to shear. This gave slightly better coherence predictions than the present model, but greatly complicated the mathematics and had also other negative consequences.

### The uniform shear model

To make a stationary model we use Eqs. (31) and (27) discussed in the beginning of this section, i.e. we substitute  $t$  with  $\tau$  given by Eq. (31). For the 33-component we get

$$\Phi_{33}(\mathbf{k}) = \Phi_{33}^{\text{iso}}(\mathbf{k}_0) \frac{k_0^4}{k^4} = \frac{E(k_0)}{4\pi k^4} (k_1^2 + k_2^2), \quad (32)$$

where  $\Phi_{33}^{\text{iso}}$  refers to the isotropic von Kármán tensor and  $E$  to the energy spectrum Eq. (25). The other components become

$$\Phi_{11}(\mathbf{k}) = \frac{E(k_0)}{4\pi k_0^4} (k_0^2 - k_1^2 - 2k_1 k_{30} \zeta_1 + (k_1^2 + k_2^2) \zeta_1^2) \quad (33)$$

$$\Phi_{22}(\mathbf{k}) = \frac{E(k_0)}{4\pi k_0^4} (k_0^2 - k_2^2 - 2k_2 k_{30} \zeta_2 + (k_1^2 + k_2^2) \zeta_2^2) \quad (34)$$

$$\Phi_{12}(\mathbf{k}) = \frac{E(k_0)}{4\pi k_0^4} (-k_1 k_2 - k_1 k_{30} \zeta_2 - k_2 k_{30} \zeta_1 + (k_1^2 + k_2^2) \zeta_1 \zeta_2) \quad (35)$$

$$\Phi_{13}(\mathbf{k}) = \frac{E(k_0)}{4\pi k_0^2 k^2} (-k_1 k_{30} + (k_1^2 + k_2^2) \zeta_1) \quad (36)$$

and

$$\Phi_{23}(\mathbf{k}) = \frac{E(k_0)}{4\pi k_0^2 k^2} (-k_2 k_{30} + (k_1^2 + k_2^2) \zeta_2). \quad (37)$$

Eqs. (32)–(37) with Eq. (31) constitute the uniform shear model (US).

These equations have two differences from the expressions of Townsend (1976) for plane shearing of homogeneous turbulence. The first is the elimination of time by Eq. (31) and the second and related difference is that we do not use the turbulent viscosity of Townsend, which would make the decay time for all eddies equal, independent of their sizes.

---

<sup>1</sup>Keith Wilson has reformulated this expression in terms of the incomplete beta function.

## 2.4 Fitting spectra to observations

First the uncertainties on estimated spectra are discussed. These are either caused by variations in atmospheric stability, which persists even at high wind speeds ( $> 16 \text{ m s}^{-1}$ ) over water, or by statistical variations. Secondly, the measured neutral spectra are fitted to the spectral tensor model. Based on this fit the coherences are finally predicted and compared to the measurements.

### Uncertainties on spectra

Often spectra are averaged over, say,  $n$  consecutive frequencies or wave numbers to decrease the random error of the estimate. Alternatively, the time series could be divided into  $n$  segments of equal duration. Each segment is then Fourier transformed and the spectrum determined as the average of the absolute square of these Fourier transforms. For either definition the statistical uncertainty on spectral density  $F$  calculated from a stationary time series is (under the assumption that the time series is long compared to the time scale of the process)

$$\frac{\sigma(F)}{\langle F \rangle} = \frac{1}{n^{\frac{1}{2}}} \quad (38)$$

(Koopmans, 1974; Bendat and Piersol, 1986).

Figure 10 shows the result of an analysis of 14 two-hour time series from the Great Belt. The series have mean speeds  $U$  between 16 and 20  $\text{m s}^{-1}$  and the mean directions are within a narrow range around south where there is an uninterrupted fetch over water for at least 20 km.

Assuming the stability to be neutral, the variation of spectral densities should obey Eq. (38) and the standard deviation at the lowest wavenumbers should be around 25% and 5% at  $k_1 = 0.1 \text{ m}^{-1}$ . The observed rms variations are clearly larger, at least 50% at the lowest frequencies and maybe 20% at higher frequencies. Most noticeably, there are spectra with only 10% of the spectral density of the others.

This variation is due to the stability of the atmosphere not being neutral. The case with suppressed turbulence is slightly stable and has  $U = 16 \text{ m s}^{-1}$ . From the point of view of aerodynamic loads this may imply enhanced loads on a bridge deck. While the buffeting loads are smaller the loads from vortex shedding can be much larger. Usually vortex shedding from a bridge deck is suppressed or even destroyed by the turbulence in the atmosphere, but if turbulence is absent as in a stably stratified atmosphere (e.g. warm air flowing out over a cold sea) the vortex shedding might be strong. Stable stratification might also alter loads on off-shore wind turbines because of increased shear.

Unstable stratification also alters the spectrum. Though none of the spectra from the Great Belt are obtained under very unstable situations, an analysis of unstable, high-wind spectra on the west coast of Norway indicate that the spectra are mainly enhanced (by more than 100%) at *very* low frequencies ( $f < 0.02 \text{ Hz}$ ). These might be relevant for various off-shore production units (Mann, 1992).

### Spectral fitting and prediction of coherences

In order to conduct simultaneous measurements of spectra and coherence over the sea a 70 m high mast was erected 40 m from an existing mast on the easterly spit of Sprogø, an island in the midst of the Great Belt separating the two Danish islands Funen and Zealand. A 15 m long horizontal boom was mounted symmetrically at the top of the new mast so that the whole construction has the form of a letter “T”. A Kaijo-Denki DAT-300 omni-directional sonic anemometer was installed at each end of the boom and at the top of the old mast, providing 15.0, 32.5 and 47.5 m horizontal separations between the three co-linear instruments. The mast array is shown in Figure 12. More details about

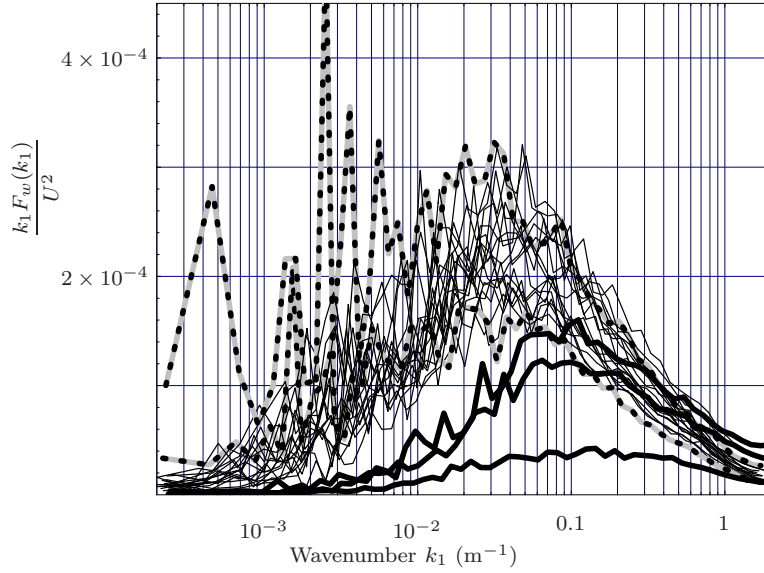


Figure 10: Spectra of  $w$  from the Great Belt Coherence Experiment. Mean wind speeds are between  $16$  and  $20 \text{ m s}^{-1}$  and directions are in a narrow interval around the South. Dashed spectra have slightly unstable stratification, gray have stable, and the thin have neutral.

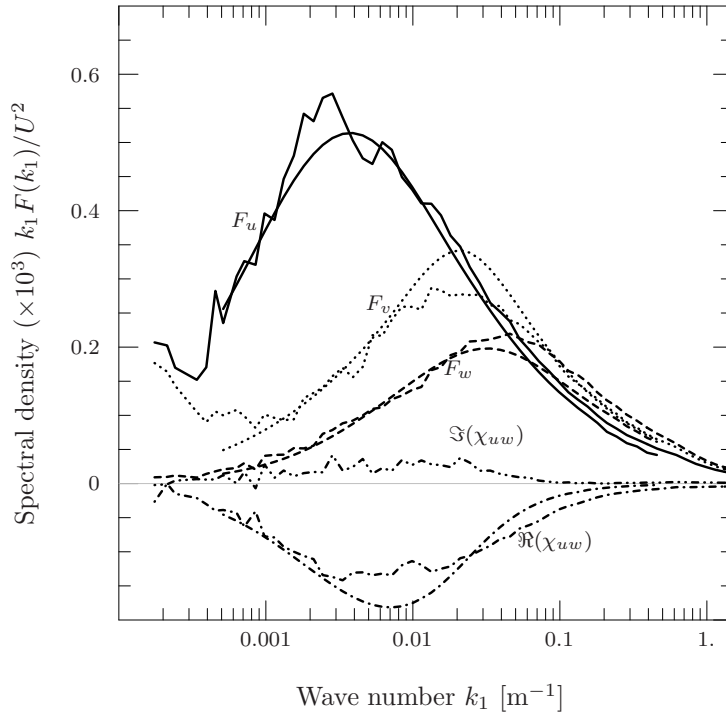


Figure 11: Average  $u$ -,  $v$ -,  $w$ -, and cross-spectra of all the *neutral* runs present in Figure 10. The ragged curves are measurements while the smooth are the model spectra. The model has zero imaginary part of the cross-spectrum (quadrature spectrum).

the experiment including correction for flow distortion by the sonic anemometers may be found in Mann et al. (1991).

The measured spectra shown in Figure 11 are an average of 16 *neutral* two hour runs with wind speeds between  $16$  and  $20 \text{ m s}^{-1}$ . The smooth curves are model spectra derived from the spectral tensor model with the parameters  $\Gamma = 3.2$ ,  $L = 61 \text{ m}$ , and  $\alpha \varepsilon^{2/3} / U^2 =$

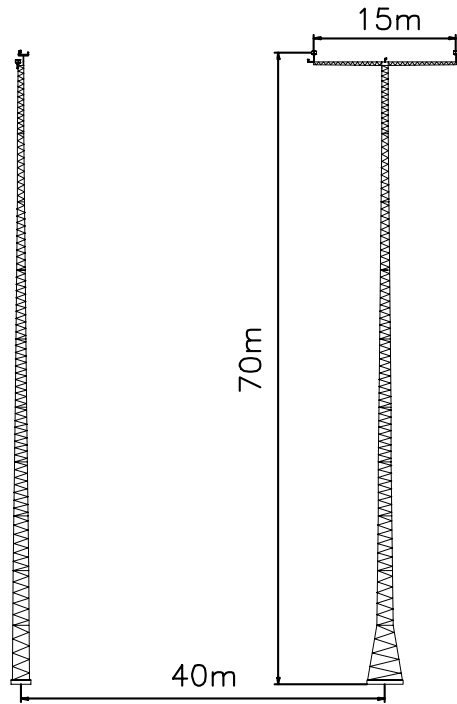


Figure 12: The mast array on Sprogø viewed from SSE. The tiny dots at the top of the masts are the omni-directional sonic anemometers.

$1.810^{-4} \text{ m}^{-2/3}$ , which are taken from Mann (1994), who used fewer two hour runs but slightly higher wind speeds.

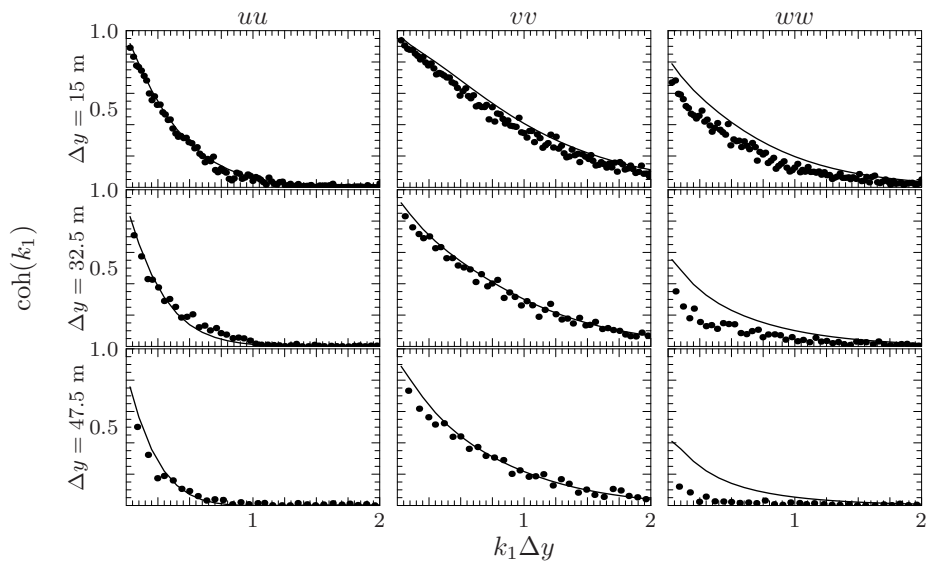


Figure 13: The dots are measured coherences from the same set of data as used for Figure 11 for various horizontal separations  $\Delta y$  and for all three velocity components. The lines are the coherences predicted by the model.

These parameters are in turn used to predict the coherences as shown in Figure 13. As seen from this figure the predictions agree well with the measurements except for the  $w$  coherence, especially at the largest separation.

## 2.5 Model spectra over the ocean and flat land

Here we compare the tensor model of section 2.3 to spectra and coherences from the literature. We will not give an exhaustive review of spectral models but select a few modern models which the author believes is used in wind engineering. The purpose is to estimate the parameters  $\Gamma$ ,  $L$  and  $\alpha\varepsilon^{2/3}$  for a given mean wind speed  $U$  and height above the water surface  $z$ .

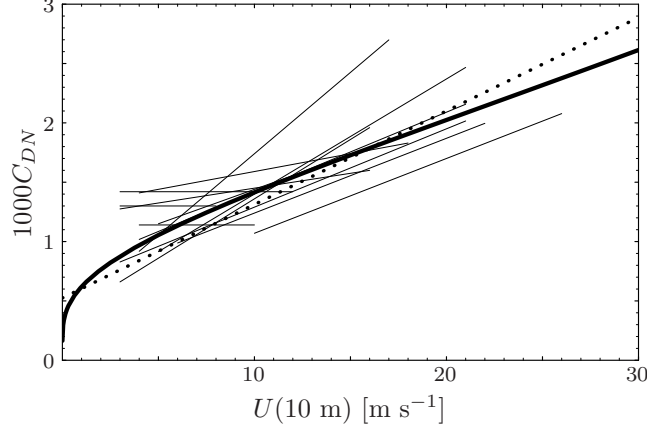


Figure 14: The neutral drag coefficient  $C_{DN}$  as a function of mean wind speed at  $z = 10$  m. The broad line is from Charnock's relation Eqs. (41) and (39). The thin lines are empirical relations from Geernaert (1987) and the dotted line is from NDP (1998), see Eq. (50).

The logarithmic mean wind profile defines the roughness length:

$$U(z) = \frac{u_*}{\kappa} \ln(z/z_0), \quad (39)$$

where  $u_* \equiv (-\langle uw \rangle)_{z \rightarrow 0}^{1/2}$  is the friction velocity and  $\kappa = 0.40$  the von Kármán constant (Landau and Lifshitz, 1987; Panofsky and Dutton, 1984).

ESDU International (1982) gives a slightly more accurate wind profile:

$$U(z) = \frac{u_*}{\kappa} (\ln(z/z_0) + 34.5fz/u_*) \quad (40)$$

with the Coriolis parameter  $f \equiv 2\Omega \sin \phi$ , where  $\Omega$  is the angular velocity in  $\text{rad s}^{-1}$  of the Earth and  $\phi$  the geographical latitude. The profile Eq. (40) is valid up to  $z = 300$  m, below 30 m Eq. (39) is a good approximation to Eq. (40). Throughout this comparison we use  $f = 10^{-4} \text{ s}^{-1}$ .

Charnock (1955) argued that over the sea the roughness length is related to  $g = 9.8 \text{ m s}^{-2}$  the acceleration due to gravity and the friction velocity by

$$z_0 = A \frac{u_*^2}{g} \quad (41)$$

where  $A$ , the Charnock constant, must be determined experimentally. On basis of an extensive literature study of ocean data Garratt (1977) found that the best fit of Eq. (41) is  $A = 0.0144$ . A slightly newer value is given by ESDU International (1982):

$$A = 0.0167, \quad (42)$$

which will be used here. Over the ocean the neutral drag coefficient

$$C_{DN} = \left( \frac{u_*}{U(10 \text{ m})} \right)^2 \quad (43)$$

increases monotonically with  $U$  as can be seen by solving Eqs. (41) and (39). This is shown in Figure 14 as a broad line together with several recent empirical relations. The figure gives a good impression of the uncertainty in estimates of drag coefficients. Among the



various reasons for this variability are atmospheric stability, surface currents, ‘wave age’, length of the fetch over water, and water depth (Garratt, 1977; Geernaert, 1987; Brown and Swail, 1991). The spectral density of velocity fluctuations is in general proportional to the drag coefficient so the uncertainty of the former is probably of the same order of the latter.

### Code and textbook spectra

*Surface layer scaling* is used in many spectral models, implying that length scales are proportional to  $z$  and that variances are proportional to  $u_*^2$ . Therefore, it is convenient to normalize the spectra with  $u_*^2$  and present them as functions of either  $n \equiv fz/U$  or  $k_1z$ . All spectra in this paper are ‘two-sided’ implying  $\int_{-\infty}^{\infty} S(f)df$  is equal to the variance<sup>2</sup>.

The spectra of Kaimal are (Kaimal et al., 1972; Kaimal and Finnigan, 1994)

$$\frac{fS_u(f)}{u_*^2} = \frac{k_1F_u(k_1)}{u_*^2} = \frac{52.5n}{(1+33n)^{5/3}}, \quad (44)$$

$$\frac{fS_v(f)}{u_*^2} = \frac{8.5n}{(1+9.5n)^{5/3}}, \quad (45)$$

and

$$\frac{fS_w(f)}{u_*^2} = \frac{1.05n}{1+5.3n^{5/3}}. \quad (46)$$

Kaimal’s spectra are based on measurements over flat homogeneous terrain in Kansas.

The spectra of Simiu and Scanlan (1996) have the same functional shapes as Kaimal’s but the numerical constants are different:

$$\frac{fS_u(f)}{u_*^2} = \frac{100n}{(1+50n)^{5/3}}, \quad (47)$$

$$\frac{fS_v(f)}{u_*^2} = \frac{7.5n}{(1+9.5n)^{5/3}}, \quad (48)$$

and

$$\frac{fS_w(f)}{u_*^2} = \frac{1.68n}{1+10n^{5/3}}. \quad (49)$$

*Deviations from surface layer scaling* are found in the model spectra from ESDU International (1985). Also the spectra of Norwegian Petroleum Directorate NDP (1998) and Højstrup, Larsen and Madsen (1990) do not obey surface layer scaling, but they are only limited to  $u$ -spectra.

The Engineering Science Data Unit (ESDU) wind profile, spectra and coherences (ESDU International, 1982, 1985 and 1986) are derived from many sources from all over the world during several decades. ESDU proposes that the turbulence intensities and length scales in the surface layer are dependent on mean wind speed. The argument is that the boundary layer depth increases with increasing wind speed implying larger scales of the turbulence. The other models, relying on surface layer scaling do not contain any information on the boundary layer depth and they contain no explicit reference to the mean wind speed. The equations of ESDU are, compared to all other spectral models discussed here, by far the most complicated. Therefore we shall not cite them explicitly. The most important input parameters are, as for the other spectral models, the height above the surface  $z$ , and the mean wind speed at some height. Of less important input is the Coriolis parameter which, as mentioned previously, is taken to be  $f = 10^{-4} \text{ s}^{-1}$ . The models we use are valid for the neutral atmosphere.

The  $u$ -spectrum of NDP (1998) applies to winds over oceans and assumes the drag coefficient to be

$$C_{DN} = 0.525 \times 10^{-3}(1 + 0.15U_{10}), \quad (50)$$

---

<sup>2</sup>The so-called ‘one-sided’ spectra, where  $\int_0^{\infty} S(f)df$  is equal to the variance, are probably more commonly used.

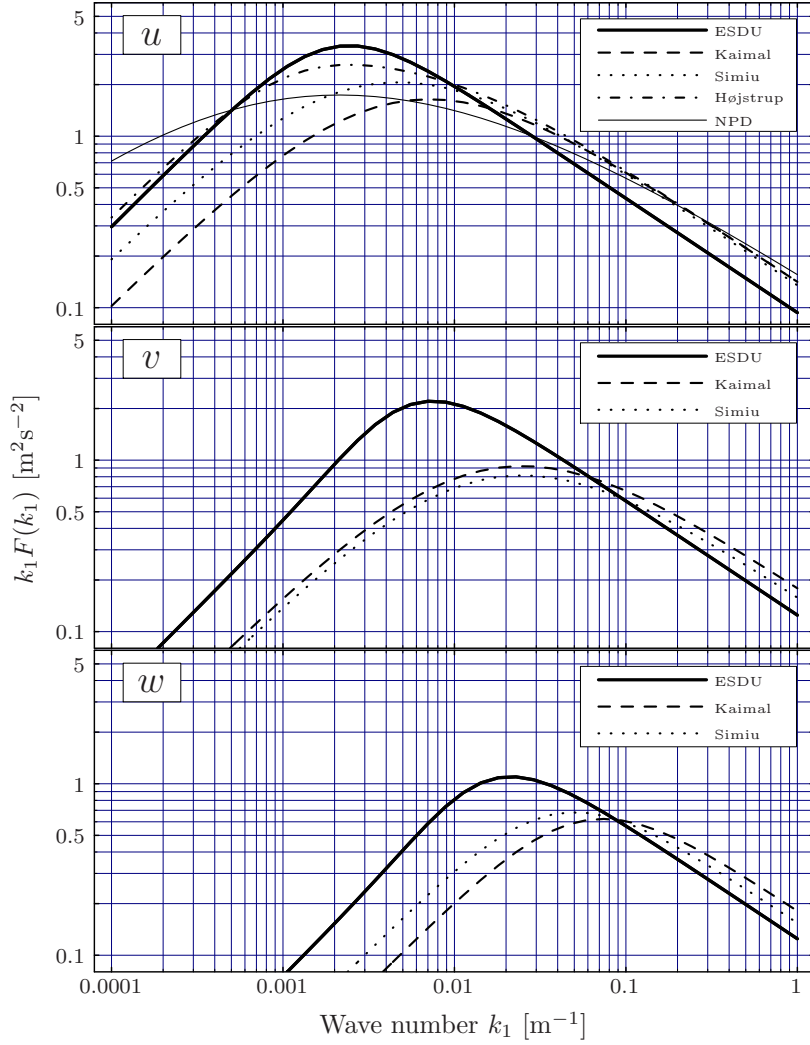


Figure 15: Comparison of spectral models. For the comparison  $z = 40$  m and  $U = 40$  m  $s^{-1}$  (over the sea) is chosen. For  $u$  (ESDU International, 1985), Eqs. (44), (47), (57), (53) are used. For  $v$  and  $w$  (ESDU International, 1985), Eqs. (45) and (48), and (ESDU International, 1985), Eqs. (46) and (49), respectively. Eq. (40) together with Eq. (41) gives  $u_* = 1.78$  m  $s^{-1}$  and  $z_0 = 0.0054$  m.

see Figure 14. Integrating  $dU/dz = u_*/(\kappa z) = \sqrt{C_{DN}}U_{10}/(\kappa z)$  Eq. (50) implies that

$$U(z) = U_{10} \left(1 + C \ln \frac{z}{10 \text{ m}}\right) \quad (51)$$

with

$$C = 0.0573(1 + 0.15U_{10})^{1/2} \quad (52)$$

where  $U_{10}$  has to be measured in meters per second. While discussing the NPD spectrum we also assume the unit of  $z$  to be meter,  $f$  is Hz and  $S_u$  is  $m^2 s^{-2} Hz^{-1}$ . The spectral density of the longitudinal wind component is

$$S_u(f) = \frac{160 \left(\frac{U_{10}}{10}\right)^2 \left(\frac{z}{10}\right)^{0.45}}{\left(1 + \tilde{f}^n\right)^{\frac{5}{3n}}} \quad (53)$$

with

$$\tilde{f} = 172f \left(\frac{z}{10}\right)^{2/3} \left(\frac{U_{10}}{10}\right)^{-3/4} \quad (54)$$

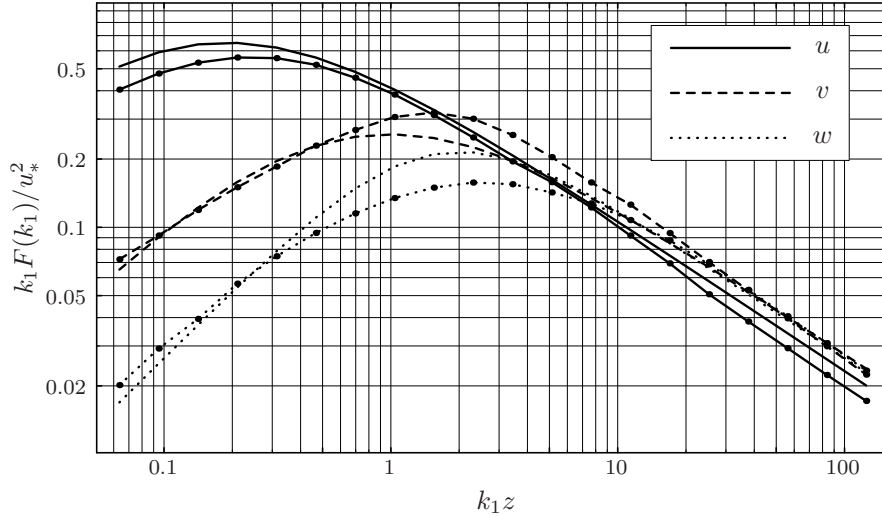


Figure 16: The ‘sheared spectral tensor’ of section 2.3 (curves with dots) fitted to the models by Simiu and Scanlan Eqs. (47)–(49). The result is given by Eq. (60).

and  $n = 0.468$ . This spectrum implies that the variance

$$\sigma_u^2 = 0.00309 \frac{U_{10}^{2.75}}{z^{0.217}} \quad (55)$$

will decrease with height and not constant as implied by surface layer scaling. Furthermore, the integral length scale

$$\text{length scale} \propto z^{2/3} U_{10}^{1/4} \quad (56)$$

will not be proportional with height but will grow somewhat slower and it will also increase a little with wind speed. This is not consistent with surface layer scaling where it under neutral conditions is constant with wind speed.

Højstrup et al. (1990) suggested that spectra at low frequencies do not obey surface layer scaling because the low frequency part scales with the height of the boundary layer, not  $z$ . To verify their model they used data selected for neutrality and high wind speeds ( $11 < U < 23 \text{ m s}^{-1}$ ) from both over sea and land sites in Denmark. The  $u$ -model is<sup>3</sup>

$$\frac{f S_u(f)}{u_*^2} = \left( \frac{2.5 n_t}{1 + 2.2 n_t^{5/3}} + \frac{52.5 n}{(1 + 33 n)^{5/3}} \right) \frac{1}{1 + 7.4 (z/A)^{2/3}} \quad (57)$$

where the ‘neutral length scale’  $A = 3000 \text{ m}$  and  $n_t = fA/U$ . The second term in the parenthesis is the Kaimal spectrum Eq. (44).

All spectral models are compared in Figure 15 for a specific choice of  $U$  and  $z$ . Generally, ESDU has larger length scales compared to those by Kaimal and by Simiu & Scanlan, which are similar. NPD and Højstrup support ESDU’s large  $u$ -scale. ESDU, though, has the most peaked spectra and, at high wave numbers, slightly lower spectral densities. All spectra agree fairly well at high wave numbers but have substantial scatter at low wave numbers.

## 2.6 Comparison with the spectral tensor model

Here we fit the spectral tensor of section 2.3 to models that describe all three component spectra, namely the ones by Kaimal, Simiu & Scanlan and ESDU.

We obtain the parameters  $\Gamma$ ,  $L$  and  $\alpha \varepsilon^{2/3}$  by making a simultaneous least squares fit to the  $u$ -,  $v$ - and  $w$ -model spectra for wave numbers in the range  $0.05 < k_1 L < 100$ . For

<sup>3</sup>Højstrup, Larsen and Madsen (1990) also gives a model for the  $v$  spectrum, but it was never compared with data, so it will not be discussed here.

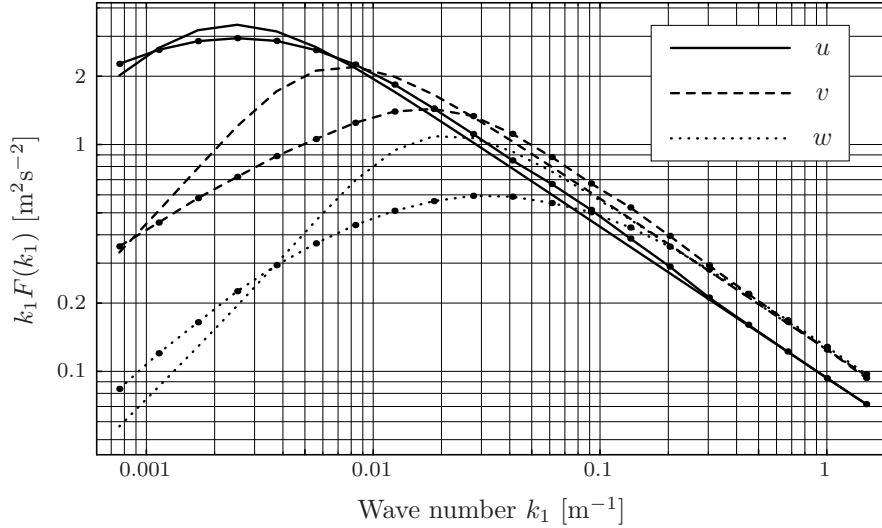


Figure 17: Example with  $z = 40$  m and  $U = 40$  m s<sup>-1</sup> of the fit of the spectral tensor model (curves with dots) to the ESDU models.

the Kaimal spectra we get

$$\begin{aligned}
 \Gamma &= 3.9 \\
 L &= 0.59z \\
 \alpha\varepsilon^{2/3} &= 3.2 \frac{u_*^2}{z^{2/3}},
 \end{aligned} \tag{58}$$

where the dependence on  $z$  is a consequence of surface layer scaling. For the Simiu & Scanlan spectra, where the fit is shown in Figure 16, we get

$$\begin{aligned}
 \Gamma &= 3.8 \\
 L &= 0.79z \\
 \alpha\varepsilon^{2/3} &= 2.8 \frac{u_*^2}{z^{2/3}}
 \end{aligned} \tag{59}$$

and for both models  $u_*$  can be obtained from Figure 14.

It is more complicated to get the parameters from the ESDU models because the spectra no longer depend on  $U$  and  $z$  in a simple way. For each set  $\{U, z\}$ , a fit to the tensor model has to be calculated. We do that on a mesh limited by  $10 < U < 80$  m s<sup>-1</sup>,  $5 < z < 300$  m over the sea. The result is shown in Figure 18. As an example of use of these graphs, suppose that the parameters for  $U(z = 80 \text{ m}) = 20$  m s<sup>-1</sup> are wanted. From the upper plot of Figure 18 we get  $L = 33$  m and  $\alpha\varepsilon^{2/3} = 0.1 \text{ m}^{4/3} \text{ s}^{-2}$ . The lower plot gives  $\Gamma = 4.5$ .

Table 3: Parameters of the spectral tensor derived from different sources for  $U(40 \text{ m}) = 40$  m s<sup>-1</sup> at sea.

	$\Gamma$	$L$ [m]	$\alpha\varepsilon^{2/3}$ [m <sup>4/3</sup> s <sup>-2</sup> ]
Great Belt	3.2	35	0.79
Kaimal	3.9	24	0.86
Simiu	3.8	31	0.76
ESDU	4.5	66	0.62

Another example is shown in Table 3 where the Great Belt data from Mann (1994) are extrapolated using neutral surface layer scaling to  $U(40 \text{ m}) = 40$  m s<sup>-1</sup>. The spectral fit for these values of  $U$  and  $z$  is shown in Figure 17.

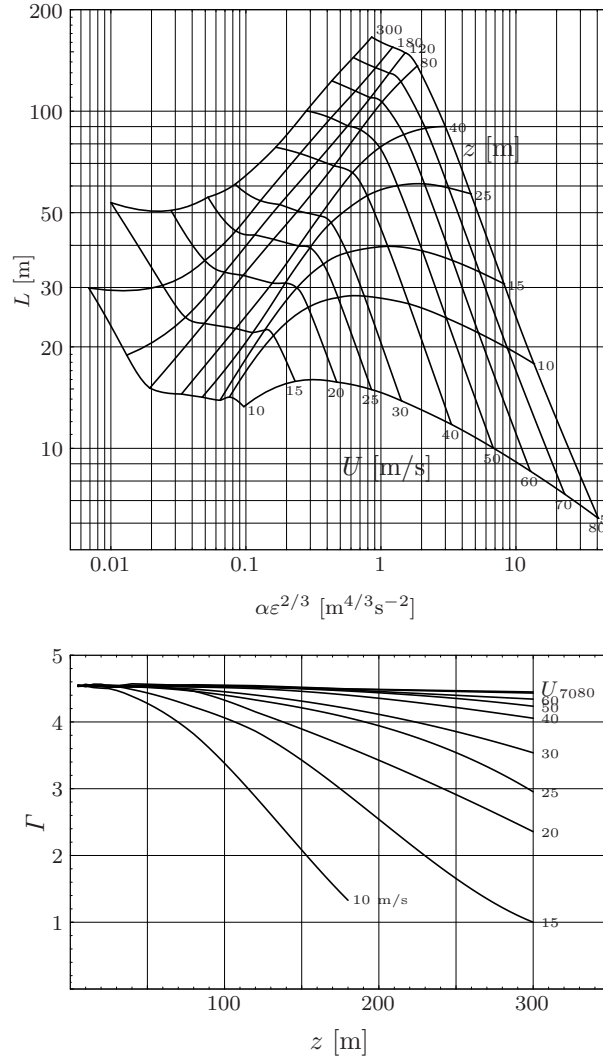


Figure 18: The parameters of the spectral tensor model derived from fits to the ESDU model spectra for turbulence over the sea. Given  $U$  and  $z$ , all three parameters can be extracted from these plots.

Literature coherences and coherences derived from the spectral tensor by Eqs. (6) and (7) are compared in Mann (1998). Generally, the agreement is good.

## 2.7 Wind field simulation

Having discussed the spectral tensor in relation to commonly used literature spectra we now describe how to simulate a velocity field  $\mathbf{u}(\mathbf{x})$ , which can be used for calculating loads on engineering structures. We approximate the integral Eq. (3) by a discrete Fourier series:

$$u_i(\mathbf{x}) = \sum_{\mathbf{k}} e^{i\mathbf{k}\cdot\mathbf{x}} C_{ij}(\mathbf{k}) n_j(\mathbf{k}), \quad (60)$$

where the  $l$ 'th component of  $\mathbf{x}$  is  $x_l = n\Delta L_l$  with  $n = 1, \dots, N_l$ . The symbol  $\sum_{\mathbf{k}}$  denotes the sum over all wave vectors  $\mathbf{k}$  with components  $k_i = m2\pi/L_i$ , with the integer  $m = -N_i/2, \dots, N_i/2$ ,  $n_j(\mathbf{k})$  are independent Gaussian stochastic complex variables with unit variance and  $C_{ij}(\mathbf{k})$  are coefficients to be determined. The great advantage of Eq. (60) is that, once the coefficients are known, it can be evaluated very fast by the fast Fourier transform (FFT) (Shinozuka and Deodatis, 1991).

Solving Eq. (60) we get approximately (Mann, 1998)

$$C_{ij}(\mathbf{k})n_j(\mathbf{k}) = \frac{1}{V(B)} \int_B u_i(\mathbf{x})e^{-i\mathbf{k}\cdot\mathbf{x}} d\mathbf{x}, \quad (61)$$

where  $V(B) = L_1L_2L_3$  is the volume of  $B$  and  $\int_B d\mathbf{x}$  means integration over the box  $B$ . From Eq. (61) it is easy to see that  $n_j(\mathbf{k})$  have to be Gaussian when  $u_i(\mathbf{x})$  is a Gaussian field. Many authors relax this constraint and let  $n_j(\mathbf{k})$  have random phase but a fixed absolute value (Shinozuka and Jan, 1972; Shinozuka and Deodatis, 1991, 1996). Using this approach every sample will get exactly the same variance and, given a wavenumber (or vector), the estimated power spectral density at this wavenumber will be the same for all realizations of the same process. This might be advantageous in some situations, but it is in contrast to power spectral density estimates of stationary time series which have 100% rms (Press et al., 1992; Bendat and Piersol, 1986). The difference between the two approaches is discussed in detail in Grigoriu (1993). In practice there is little difference and both models could be used. However, the Gaussian approach is usually easier to analyze theoretically and we shall stick to that here.

To find the coefficients  $C_{ij}(\mathbf{k})$  we calculate the covariance tensor of Eq. (61) obtaining

$$\begin{aligned} C_{ik}^*(\mathbf{k})C_{jk}(\mathbf{k}) &= \frac{1}{V^2(B)} \int_B \int_B \langle u_i(\mathbf{x})u_j(\mathbf{x}') \rangle e^{i\mathbf{k}\cdot\mathbf{x}} e^{-i\mathbf{k}\cdot\mathbf{x}'} d\mathbf{x}d\mathbf{x}' \\ &= \frac{1}{V^2(B)} \int \int R_{ij}(\mathbf{x} - \mathbf{x}') 1_B(\mathbf{x})1_B(\mathbf{x}') e^{i\mathbf{k}\cdot(\mathbf{x}-\mathbf{x}')} d\mathbf{x}d\mathbf{x}', \end{aligned} \quad (62)$$

where  $1_B(\mathbf{x}) = 1$  if  $\mathbf{x} \in B$  and 0 otherwise. Using the change of variables  $\mathbf{r} = \mathbf{x} - \mathbf{x}'$  and  $\mathbf{s} = \mathbf{x} + \mathbf{x}'$  having the Jacobian  $|\partial(\mathbf{r}, \mathbf{s})/\partial(\mathbf{x}, \mathbf{x}')| = 8$  we get

$$C_{ik}(\mathbf{k})C_{kj}(\mathbf{k}) = \frac{1}{8V^2(B)} \int R_{ij}(\mathbf{r})e^{-i\mathbf{k}\cdot\mathbf{r}} \int 1_B\left(\frac{\mathbf{s} + \mathbf{r}}{2}\right) 1_B\left(\frac{\mathbf{s} - \mathbf{r}}{2}\right) d\mathbf{s}d\mathbf{r} \quad (63)$$

The inner integration can be carried out according to

$$\int 1_B\left(\frac{\mathbf{s} + \mathbf{r}}{2}\right) 1_B\left(\frac{\mathbf{s} - \mathbf{r}}{2}\right) d\mathbf{s} = \begin{cases} \prod_{l=1}^3 2(L_l - |r_l|) & \text{for } |r_l| < L_l \text{ for all } l \\ 0 & \text{otherwise} \end{cases} \quad (64)$$

so, using the convolution theorem and noting that the Fourier transform of  $L - |r|$  (for  $|r| < L$  and else 0) is  $L^2 \text{sinc}^2(kL/2)$ , we get

$$C_{ik}^*(\mathbf{k})C_{jk}(\mathbf{k}) = \int \Phi_{ij}(\mathbf{k}') \prod_{l=1}^3 \text{sinc}^2\left(\frac{(k_l - k'_l)L_l}{2}\right) d\mathbf{k}', \quad (65)$$

where  $\text{sinc } x \equiv (\sin x)/x$ . For  $L_l \gg L$ , the  $\text{sinc}^2$ -function is ‘delta-function-like’, in the sense that it vanishes away from  $k_l$  much faster than any change in  $\Phi_{ij}$ , and the area beneath the  $\text{sinc}^2$ -curve is  $2\pi/L_l$ . Therefore, we get

$$C_{ik}^*(\mathbf{k})C_{jk}(\mathbf{k}) = \frac{(2\pi)^3}{V(B)} \Phi_{ij}(\mathbf{k}). \quad (66)$$

The solution to Eq. (66) is

$$C_{ij}(\mathbf{k}) = \frac{(2\pi)^{3/2}}{V(B)^{1/2}} A_{ij}(\mathbf{k}) = (\Delta k_1 \Delta k_2 \Delta k_3)^{1/2} A_{ij}(\mathbf{k}) \quad (67)$$

with  $A_{ik}^* A_{jk} = \Phi_{ij}$  and  $\Delta k_l = 2\pi/L_l$ . This result should be expected when comparing Eq. (3) to (60).

Two problems occur by simulating a field by the Fourier series Eq. (60) with the coefficients Eq. (67). The first is that for many applications the dimensions of the simulated box of turbulence need *not* to be much larger than the length scale of the turbulence model  $L$ . Therefore Eq. (66) may not be a good approximation to Eq. (65). The second

problem is that the simulated velocity field Eq. (60) is periodic in all three directions. Both problems have been addressed in Mann (1998).

The algorithms above simulate a three-dimensional vector field on a three-dimensional domain, but it can easily be modified to simulate one- or two-dimensional vectors in a 2- or 3-D domain (Mann, 1998). The algorithms are not needed for a one-dimensional domain, i.e. simulation of wind fluctuations in one point as a function of time.

The implementation of the model includes three steps:

1. Evaluate the coefficients  $C_{ij}(\mathbf{k})$ , either by Eq. (67) or a modification of this (Mann, 1998).
2. Simulate the Gaussian variable  $n_j(\mathbf{k})$  and multiply.
3. Calculate  $u_i(\mathbf{x})$  from Eq. (60) by FFT.

The time consumption in the first step is proportional to the total number of points  $N = N_1 N_2 N_3$  in the simulation. The required time to perform the FFT is  $O(N \log_2 N)$  (Press et al., 1992). In practice, simulating a three-dimensional field, used for load calculations on wind turbines, with millions of velocity vectors takes of the order of a few minutes on a modern pc.

## Notation

$A$	Charnock constant neutral length scale
$B$	box of e.g. turbulence
$\text{coh}_{ij}$	coherence or normalized cross-spectrum
$\text{cw}$	continuous wave
$C_{ij}$	coefficients for a discrete Fourier series
$C_{DN}$	neutral drag coefficient
$E(k)$	energy spectrum
ESDU	engineering science data unit
$f$	frequency Coriolis parameter
$F$	spectrum (function of wave number)
FFT	fast Fourier transform
$g$	gravitational acceleration
$i$	tensor index
$j$	tensor index
$k$	wave number/component
$\mathbf{k}$	wave vector
$L$	turbulence length scale or length of a volume
$m$	integer number
$n$	number of segments normalized frequency
$n_j(\mathbf{k})$	Gaussian variable
$n_t$	normalized neutral frequency
$N$	number of points
NPD	Norwegian Petroleum Directorate
$p$	pressure
$\mathbf{r}$	separation vector
$R_{ij}(r)$	covariance tensor
RDT	rapid distortion theory
$S$	spectrum (function of frequency)
$t$	time
$u$	longitudinal wind component
$\tilde{\mathbf{u}}(\mathbf{x})$	turbulent velocity field
$u_*$	friction velocity
$U$	mean wind speed

$U$	mean flow
US	uniform shear model
$v$	transversal wind component
$V(B)$	volume of the box $B$
$w$	vertical wind component
$x$	direction of the mean wind field
$\mathbf{x}$	coordinate system
$y$	transversal direction
$z$	vertical axis direction or height
$z_0$	roughness length
$Z$	orthogonal process
$\alpha\varepsilon$	energy dissipation measure
$\beta$	non-dimensional time
$\Gamma$	anisotropy parameter
$\delta$	Kronecker delta
$\kappa$	von Kármán constant
$\sigma_X$	standard deviation of a variable $X$
$\tau$	eddy lifetime
$\tau_D$	coherence-destroying diffusion time
$\tau_E$	eddy-damping rate
$\phi$	geographical latitude
$\Phi_{ij}(\mathbf{k})$	spectral tensor
$\chi_{ij}$	cross-spectra
$\omega$	fluctuating part of the vorticity
$\Omega$	angular velocity
$\mathbf{\Omega}$	mean part of the vorticity
$\partial$	partial derivate
$\nabla$	vector differential operator
$\langle X \rangle$	ensemble average of the variable $X$

## References

- Batchelor G. K. (1953) The theory of homogeneous turbulence, Cambridge University
- Bendat J. S. and Piersol A. G. (1986) Random data: Analysis and Measurement Procedures, 2 edn, Wiley-Interscience
- Brown R. D. and Swail, V. R. (1991) Over-water gust factors. *Ocean Engng.* **18**(4):363–394
- Charnock H. (1955) Wind stress on a water surface. *Q. J. Royal Meteorol. Soc.* **81**:639–640
- Comte-Bellot G. and Corrsin S. (1971) Simple Eulerian time correlation of full- and narrow-band velocity signals in grid generated, ‘isotropic’ turbulence. *J. Fluid Mech.* **48**:273–337
- Derbyshire S. H. and Hunt J. C. R. (1993) Structure of turbulence in stably stratified atmospheric boundary layers; comparison of large eddy simulations and theoretical models. *in* S. D. Moobs and J. C. King (eds), *Waves and Turbulence in Stably Stratified Flows*, Clarendon, Oxford, 23–59 pp
- ESDU International (1982) Characteristics of wind speed in the lower layers of the atmosphere near the ground: strong winds (neutral atmosphere), ESDU International, London
- ESDU International (1985) Characteristics of atmospheric turbulence near the ground. Part II: single point data for strong winds (neutral atmosphere), ESDU International, London
- Garratt J. R. (1977) Review of drag coefficients over oceans and continents, *Mon. Wea. Rev.* **105**:915–929
- Geernaert G. L. (1987) On the importance of the drag coefficient in air-sea interactions. *Dynamics Atmos. Oceans* **11**:19–38
- Grigoriu M. (1993) On the spectral representation method in simulation. *Prob. Eng. Mech.* **8**:75–90
- Højstrup J., Larsen S. E. and Madsen P. H. (1990) Power spectra of horizontal wind components in the neutral atmospheric boundary layer. *in* N. O. Jensen, L. Kristensen and S. E. Larsen (eds), *Ninth Symposium on Turbulence and Diffusion*, American Meteorological Society, 305–308 pp
- Hunt J. C. R. and Carruthers D. J. (1990) Rapid distortion theory and the ‘problems’ of turbulence. *J. Fluid Mech.* **212**:497–532
- Kaimal J. C. and Finnigan J. J. (1994) *Atmospheric Boundary Layer Flows, Their Structure and Measurement*, Oxford University Press, New York



- Kaimal J. C., Wyngaard J. C., Izumi Y. and Coté O. R. (1972) Spectral characteristics of surface-layer turbulence, *Q. J. R. Meteorol. Soc.* **98**:563–589
- Koopmans L. H. (1974) *The Spectral Analysis of Time Series*, Academic Press
- Kristensen L. and Kirkegaard P. (1987) Puff kinematics, Technical Report R-548, Risø National Laboratory
- Landau L. D. and Lifshitz E. M. (1987) *Fluid Mechanics*, Pergamon Press
- Larose G. L. and Mann J. (1998) Gust loading on streamlined bridge decks, *J. Fluids Structures* **12**(5):511–536
- Lesieur M. (1987) *Turbulence in fluids*, Martinus Nijhoff Publishers
- Mann J. (1992) Investigation of atmospheric low-frequency turbulence over the ocean, Technical Report I-634(EN), Risø National Laboratory, Roskilde
- Mann J. (1994) The spatial structure of neutral atmospheric surface-layer turbulence. *J. Fluid Mech.* **273**:141–168
- Mann J. (1998) Wind field simulation, *Prob. Engng. Mech.* **13**(4):269–282
- Mann J., Cariou J.-P., Courtney M. S., Parmentier R., Mikkelsen T., Wagner R., Lindelöw P., Sjöholm M. and Enevoldsen K. (2009) Comparison of 3D turbulence measurements using three staring wind lidars and a sonic anemometer. *Meteorol. Z.* **18**(2):135–140
- Mann J., Kristensen L. and Courtney M. S. (1991) The great belt coherence experiment – a study of atmospheric turbulence over water, Technical Report R-596, Risø National Laboratory, Roskilde
- Maxey M. R. (1982) Distortion of turbulence in flows with parallel streamlines. *J. Fluid Mech.* **124**:261–282
- NDP (1998) Acts, regulations and provisions for the petroleum activities, Vol. 2., Norwegian Petroleum Directorate
- Panofsky H. A. and Dutton J. A. (1984) *Atmospheric Turbulence*, John Wiley & Sons, New York
- Panofsky H. A., Larko D., Lipschutz R., Stone G., Bradley E. F., Bowen A. J. and Højstrup J. (1982) Spectra of velocity components over complex terrain. *Q. J. R. Meteorol. Soc.* **108**:215–230
- Peña A., Gryning S.-E., Mann J. and Hasager C. B. (2010) Length scales of the natural wind profile over homogeneous terrain *J. Appl. Meteor. Climat.* **49**:792–806
- Press W. H., Flannery B. P., Teukolsky S. A. and Vetterling W. T. (1992) *Numerical Recipes*, 2nd edn, Cambridge University Press
- Shinozuka M. and Deodatis G. (1991) Simulation of stochastic processes by spectral representation, *Appl. Mech. Rev.* **44**(4):191–203
- Shinozuka M. and Deodatis G. (1996) Simulation of multi-dimensional gaussian stochastic fields by spectral representation. *Appl. Mech. Rev.* **49**(1):29–53
- Shinozuka M. and Jan C.-M. (1972) Digital simulation of random processes and its applications. *J. Sound Vibration* **25**(1):111–128
- Simiu E. and Scanlan R. H. (1996) *Wind Effects on Structures*, 3. ed., John Wiley & Sons
- Sjöholm M., Mikkelsen T., Mann J., Enevoldsen K. and Courtney M. (2009) Time series analysis of continuous-wave coherent Doppler lidar wind measurements. *Meteorol. Z* **18**(3):281–287
- Townsend A. A. (1976) *The Structure of Turbulent Shear Flow*, 2nd edn, Cambridge University Press
- Townsend, A. A. (1980) The response of sheared turbulence to additional distortion. *J. Fluid Mech.* **98**:171–191

# 3 Introduction to continuous-wave Doppler lidar

**Michael Harris**

*Natural Power, The Old Barns, Fair Oaks Farm,  
Hollybush, Nr. Ledbury HR8 1EU, U.K.*

---

## 3.1 Introduction

Remote sensing offers the wind industry an attractive alternative or complement to the traditional methods for obtaining accurate wind measurements that involve the siting of tall masts. Laser anemometry (lidar) is now demonstrating its potential for resource assessment, power curve measurement, and turbine mounted deployment for advance wind speed detection. Widespread acceptance of lidar by the industry requires that this technique be extensively validated, aiming towards a certifiable and traceable measurement standard and formal accreditation of lidar methods for different applications in a range of terrain types. This chapter outlines the lidar measurement process and capabilities specifically for the case of continuous wave (CW) systems.

Wind lidar systems were first demonstrated in the 1970's (Jelalian, 1992) and have since been applied to a wide variety of applications including aviation and meteorology. Although applications to wind energy were explored in the 1980's (Hardesty and Weber, 1987; Vaughan and Forrester, 1989), the lidar systems that existed at that time were too large and expensive to achieve serious acceptance in the industry. The situation has now changed dramatically, with rapid growth of the wind industry coinciding with development of a new generation of lidars based on optical fibre and other components that emerged from the telecommunications boom of the 1990's. The first all-fibre lidars were demonstrated in the late 1990's, and a commercial prototype unit (ZephIR) was mounted on a turbine to demonstrate wind speed detection in front of the rotor plane in early 2003. A demonstration of ground-based wind profiling followed shortly afterwards. ZephIR is a CW coherent lidar system, and this approach was selected as a means to combine simplicity with high sensitivity at ranges relevant to wind energy, and hence achieve a robust, reliable system at relatively low cost. Following this pioneering work the pace of development has accelerated, with lidar increasingly becoming an established tool in the wind industry.

Section 3.2 provides an overview of lidar techniques and technology. Different types of lidar system are surveyed, and the generic physical principles underlying their operation are reviewed. The specific case examined in detail here is that of wind profiling by a ground-based conically-scanned continuous-wave (CW) lidar, rapidly becoming established as a powerful tool in the wind energy industry, and exemplified by the ZephIR lidar, developed by QinetiQ and Natural Power. A number of assumptions must be made in order to extract values of wind speed from raw lidar data; these are reviewed in section 3.3. The different steps that are required during the end-to-end measurement process in order to arrive at a value of wind speed are detailed in section 3.4. It is important to understand the potential sources of error and uncertainty, and these are reviewed and analysed in section 3.5. Section 3.6 examines the important requirement for lidar calibration and traceability. Finally, section 3.7 draws together some conclusions and a summary of the future outlook for lidar in wind energy.

## 3.2 Basic principles of lidar operation and system description

### Brief survey of lidar types

There are many different types of lidar (Jelalian, 1992) and these are capable of performing a diverse range of tasks (e.g. 3D imaging and range finding, gas species detection, remote measurement of vibrations). We concern ourselves here specifically with systems for the measurement of wind speed in the atmosphere (Zak, 2003). Such systems fall into two broad categories: coherent lidar and direct detection lidar. Coherent lidar measures Doppler shifts by comparing the frequency of backscattered radiation to that of a reference beam via a light beating process, whereas direct detection lidar (Chanin et al., 1989) performs its frequency-shift measurements by passing the light through an optical filter, such as a Fabry-Perot etalon. By operating in the ultra-violet, direct detection lidars can exploit molecular scattering processes, guaranteeing signal returns even in very clean air where there is an absence of scattering particles.

Coherent wind lidar systems can be categorised according to their emission waveform (pulsed or continuous), waveband (visible, near-IR, far-IR), and their transmit/receive geometry (monostatic or bistatic). These notes concentrate specifically on CW coherent monostatic lidar systems that operate in the telecommunications near-IR band around  $1.55 \mu\text{m}$  (Karlsson et al., 2000); at this wavelength reliable components including optical fibre are readily available. Such systems can route the light within the lidar via fibre cables (creating an “all-fibre lidar”), rather than use mirrors to direct the beams in free space. This confers an enormous design advantage, simplifying alignment and improving robustness. Pulsed all-fibre lidar has also been developed as reported in Pearson et al. (2002).

### Principles underlying anemometry by coherent laser radar (CLR)

The principle by which coherent lidar measures the velocity of a target is simple: a beam of coherent radiation illuminates the target, and a small fraction of the light is backscattered into a receiver. Motion of the target along the beam direction leads to a change in the light’s frequency via the Doppler shift: motion towards the lidar brings about a compression of the wave and an increase in its frequency (a “blue shift”), while movement away stretches the wave reducing its frequency (a red shift). This frequency shift is accurately measured by mixing the return signal with a portion of the original beam, and sensing the resulting beats at the difference frequency on a photodetector. Like the Doppler effect, the beat phenomenon is perhaps most familiar in the context of acoustics as, for example, when two closely (but not identically) tuned guitar strings are simultaneously plucked.

The essential features are readily seen in the simplified generic CLR depicted in Figure 19. In order to illustrate the concept this is drawn as a bistatic system, in which the transmit and receive optics are separate and distinct. In practice a monostatic geometry is more usual, in which the transmit and receive paths share common optics.

### Role of local oscillator and range selection by focus

The reference beam, or local oscillator (LO) plays a crucial role in the operation of a CLR (Sonnenschein and Horrigan, 1971). Firstly, it defines the region of space from which light must be scattered for detection of the beat signal; radiation from other sources (e.g. sunlight) is rejected both spatially and spectrally, so that CLR systems are usually completely immune to the effect of background light. The LO also provides a stable reference frequency to allow very precise velocity determination; as a consequence the Doppler shift measurement by a CLR system is inherently calibrated. Finally, the LO amplifies

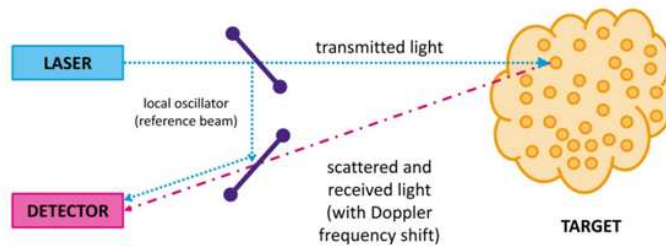


Figure 19: Generic bistatic lidar system. A small fraction of the transmitted light is tapped off by a beamsplitter to form a reference beam. This is superimposed at a second beamsplitter with the weak return scattered from moving particles. The detector picks up the resulting beat signal; this undergoes spectral analysis to determine particle velocity.

the signal via the beating process to allow operation at a sensitivity that approaches the shot-noise (or quantum) limit. This very high sensitivity permits the operation of CLR systems in an unseeded atmosphere, relying only on detection of weak backscattering from natural aerosols.

CW systems are the simplest form of lidar possessing the advantage of reduced complexity, and their performance can be tailored closely to the wind industry’s requirements. However, the overall trade-off between the pulsed and CW options for each specific application must take into account a number of factors including sensitivity, cost, velocity resolution, and maximum and minimum ranges. Unlike pulsed lidar systems, which use time of flight to discriminate between returns from different ranges, a CW lidar achieves operation at a given range by beam focusing. Wind profiling is achieved by focusing at a number of chosen ranges in turn; the rapid data rate permits 1 s “snapshots” of the flow across the scan disk at each measurement height. Focusing of the lidar beam brings about a Lorentzian spatial weighting function along the beam axis, with its peak located at the beam waist (Sonnenschein and Horrigan, 1971; Karlsson et al., 2000). This function has a half-width given by the Rayleigh range (the distance from the waist at which the beam area has doubled).

The beam diameter at the waist increases linearly with range while the Rayleigh range increases roughly as the square. Hence the effective probe volume varies as the 4th power of the focus range, and this strong dependence has some implications for the signal statistics at shorter ranges (Harris et al., 2001b). The minimum range for a CW lidar is very short with detection possible in principle at zero range, whereas a pulsed system is blinded while the pulse is leaving the transmitter leading to a minimum range of 10’s of metres, typically around 40–50 m.

### Doppler frequency analysis and signal processing

The stages of signal processing required for CLR wind signals are discussed in section 3.4. The detector output, containing the beat signal information embedded in broadband noise, is typically digitised by an analogue-to-digital converter (ADC). Spectral analysis (e.g. by fast Fourier transform methods) leads to the generation of Doppler spectra. It is usually necessary to average a number of these spectra in order to improve the signal-to-noise ratio (SNR), after which the Doppler peak stands clearly above a flat shot-noise floor. A value for the line-of-sight wind speed can then be computed via a velocity estimation algorithm. This might calculate, for example, the peak or centroid value of the Doppler signal.

## Wind profiling in conical scan mode

Since a single lidar measurement only provides the component of wind speed along the beam direction, it is necessary to scan the direction of the beam in order to generate a measurement of the wind speed vector. A conical or VAD (velocity-azimuth-display) scan pattern has been widely used (Banakh et al, 1993), see Figure 20; as the beam moves, it intercepts the wind at different angles, thereby building up a series of measurements around a disk of air from which the wind speed vector can be derived. In uniform flow, a plot of the measured line-of-sight wind speed ( $V_{LOS}$ ) versus scan azimuth angle ( $\phi$ ) takes the form of a cosine wave (rectified for a lidar system that cannot distinguish the sign of the Doppler shift). The peak Doppler shifts correspond to measurements when the azimuth scan angle aligns with the upwind and downwind directions. Doppler shifts close to zero are obtained when the azimuth angle is perpendicular to the flow.

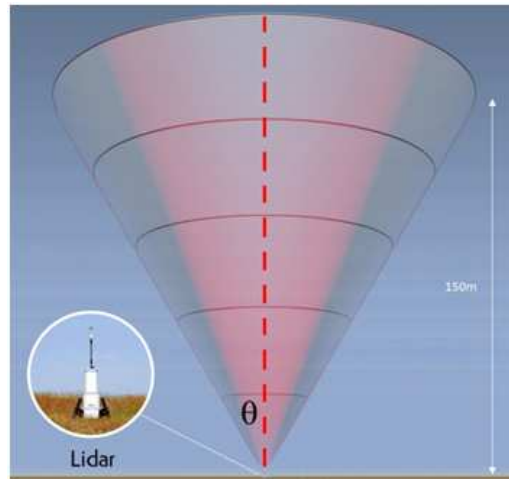


*Figure 20:* Conical scan pattern as used for lidar wind profiling. The cone half-angle ( $\theta$ ) is typically of order  $30^\circ$ . The lidar can operate successfully even when part of its scan is obscured, e.g. by an adjacent met mast. In order to build up a wind profile, the lidar operates in a repeating sequence during which all the heights are interrogated in series

## Pioneering a revolution: QinetiQ/Natural Power ZephIR lidar

Many different research groups have built and successfully deployed wind lidars over the past 30 years. However, commercial lidar products have until very recently been available from only a few companies. In 2003 the UK company QinetiQ (formerly the government-funded establishment RSRE, later DRA then DERA), launched the first commercial all-fibre lidar (“ZephIR<sup>TM</sup>”) which exploits decades of research in the coherent lidar area. QinetiQ began a programme to develop a commercial fibre-based lidar in 2001; its ZephIR product is now an established tool for wind profiling in the wind energy industry. Systems have been deployed successfully around the world in several demanding applications that illustrate the flexibility and robustness of the solution. Initial deployment of the ZephIR lidar (March 2003) was on the nacelle of a large (2.3 MW) wind turbine (Figure 21-left frame), remotely measuring for the first time the wind speed up to 200 m in front of the blades (Harris et al., 2006, 2007). The lidar consisted of a 19” rack unit containing laser source, detector and signal processing computer, situated in the base of the tower, connected via over 100 m of electrical and optical fibre cable to the transceiver head mounted on the top of the nacelle. The lidar system was installed and was fully operational after just a few hours, thus allowing a demonstration of advance warning of oncoming gusts and providing valuable experience in practical deployment issues.



*Figure 21:* Stages of evolution of the ZephIR lidar. The left-hand picture shows the lidar head mounted on the nacelle of a Nordex N-90 wind turbine (March 2003). The central picture shows prototype ground-based wind profiler at Risø wind energy test site, Høvsøre, Denmark. The right-hand picture shows a ZephIR production model deployed in the field

The system returned to QinetiQ Malvern having achieved several weeks of successful operation. It was then converted into a ground-based scanning unit for wind profiling (Figure 21-middle frame). The system was first trialled in December 2003, and soon after was used in numerous campaigns in the UK, Europe, and other parts of the world. Notably the system is still operational 7 years later! The experience gained through these trials has built confidence in the robustness and reliability of the core ZephIR design. In late 2004, work started on a production instrument (Figure 21-right frame), designed to perform autonomous wind profiling measurements at heights up to 200m (Smith et al., 2006), primarily for site surveys at proposed wind farm sites. Over eighty of these systems (February 2010) have performed more than 200 deployments in 25 countries in a wide variety of locations, including offshore. ZephIR is now marketed and developed for the wind industry by Natural Power, and its basic specifications are available via the web: <http://www.naturalpower.com/zephir-laser-anemometer>

### 3.3 Lidar measurement process: Assumptions

The following sections discuss generic CW lidar considerations (most of which apply equally to pulsed systems). Where appropriate, application to the ZephIR lidar is used to provide an illustrative example.

#### Behaviour of scattering particles

The lidar signals from which wind speeds are derived originate via backscattering of the beam by particles in the atmosphere. The constitution of these particles is generally unknown, but they are normally assumed to consist of dust, organic matter (e.g. pollen), soot, or water droplets. Knowledge of the particles' make-up is not a requirement for lidar wind speed measurement. The particles must provide sufficient signal for Doppler analysis and their motion must faithfully follow that of the wind flow. This latter assumption is very good, since viscous forces are dominant for such small particles. Larger particles for which this does not apply will rapidly fall to ground. Raindrops or snowflakes provide a strong contribution to the lidar signal. Their downward motion can lead to an error in the vertical component of wind speed (a parameter usually of lesser interest; such data can be easily identified and filtered), but the important horizontal component will be correct.

A further excellent assumption is that the return signal is dominated by light generated by single-scattering events. While it is possible for light to suffer multiple scattering in dense fog, it is assumed that any effect on the Doppler spectrum is negligible.

### **Uniformity of flow and backscatter**

A least-squares fitting to the azimuthal variation of line-of-sight wind speed allows the derivation of wind parameters from conical scan data. These parameters pertain to a significant volume of atmosphere – the signal originates from a disk whose diameter commonly exceeds 100 m, and whose depth along the beam direction can be over 10 m. Except in situations of strong shear, turbulence or highly complex terrain the wind speed is reasonably uniform throughout this sampled volume, and the best fit wind parameters are used to indicate the average values over the volume. In fact, ZephIR data itself can provide a straightforward check on wind field uniformity since conical scanning provides measurements at many different azimuth angles; where the assumptions have broken down, measurements with less certainty can be flagged.

The contribution to the lidar signal from different regions of the lidar probe volume is weighted by the value of the atmospheric backscatter coefficient  $\beta(\pi)$  at each point. The value of  $\beta(\pi)$  is typically constant to  $\sim 10\%$  throughout the probe volume (Banakh et al., 1993) except in conditions that lead to stable mist layers, or when the lidar beam intersects a low cloud base.

### **Beam positional accuracy**

Lidar scan angle and focus calibration are performed in the laboratory, and these must be correctly maintained throughout a period of deployment in the field. Obviously errors in the focus setting would result in wind speed measurement at the wrong height. Careful design eliminates the risk of uncertainty in the beam focus: thermal expansion, which could change the length of the transceiver telescope, can be compensated and the position of the focus mechanism can be automatically checked to provide information on any malfunction.

The lidar must be correctly set up, with the vertical and azimuthal orientation adjusted appropriately during installation. External to the lidar, it has been established that small-scale refractive-index atmospheric fluctuations will have negligible effect on the propagation of the lidar beam (Clifford and Wandzura, 1981; Lading et al., 1984).

### **Optical and electrical interference sources**

The lidar identifies the presence of a wind signal when the power density in the Doppler spectrum exceeds a threshold level. In the absence of any significant source of spurious signal, the only mechanism that can lead to such detection events is the backscatter of Doppler-shifted light into the lidar receiver. Optical interference is highly unlikely – even when the lidar points directly at the sun the spectral power density is insufficient to cause a problem, and interaction between two lidars placed side-by-side can be neglected including the possibility of interference from the beam emitted by an adjacent lidar. Careful screening eliminates the risk of spurious spectral features caused by electrical interference for any normal deployment.

### **Time-of-flight considerations**

The round-trip time for light interrogating the atmosphere at a height of 100 m is less than 1  $\mu\text{s}$ . On this timescale the ZephIR scanner moves the focused beam a distance of only 300  $\mu\text{m}$ , and the laser phase drifts by an insignificant amount. The polarisation state of the lidar output is similarly frozen on this timescale.

## 3.4 End-to-end measurement process for CW Doppler lidar

### Introduction

The measurement process can be split into a number of steps. This section describes these steps in turn, arriving at an overall end-to-end description of the wind speed measurement process for a CW coherent Doppler lidar wind profiler. Again, where appropriate, the ZephIR lidar is used as an example.

### Transmitter optics

The role of the transmitter is to provide a focused beam at a desired location. This location can be moved around in space with a combination of (i) changing the focus range and (ii) passing the beam through a scanning element such as a rotating prism (wedge). Wind profiling lidars conveniently employ a conical scan with its axis aligned vertically; the cone half-angle is commonly of order  $30^\circ$  (i.e. the beam elevation angle is  $\sim 60^\circ$ ).

In a monostatic CW system, a Doppler-shifted contribution to the signal is generated via light scattering from any moving part of the atmosphere that the beam illuminates. The contribution from any point is weighted by the square of the beam's intensity at that point (Harris et al., 2001a). Hence it can be shown that focusing of an ideal Gaussian beam (Siegman, 1986) gives rise to a spatial sensitivity along the beam direction that depends on the inverse of beam area; it follows that the sensitivity rises to a peak at the beam waist, and falls symmetrically on either side. There is also a spatial dependence of sensitivity transverse to the beam, but because the beam is very narrow this is of little interest and can be ignored. To a good approximation the axial weighting function for a CW monostatic coherent lidar is given by a Lorentzian function (Sonnenschein and Horrigan, 1971; Karlsson et al., 2000):

$$F = \frac{\Gamma/\pi}{\Delta^2 + \Gamma^2}, \quad (68)$$

where  $\Delta$  is the distance from the focus position along the beam direction, and  $\Gamma$  is the half-width of the weighting function to the -3 dB point, i.e. 50% of peak sensitivity. Note that  $F$  has been normalised such that its integral from  $-\infty$  to  $\infty$  gives unity. To another good approximation,  $\Gamma$  is given by:

$$\Gamma = \frac{\lambda R^2}{\pi A^2}, \quad (69)$$

where  $\lambda$  is the laser wavelength, here assumed to be the telecommunications wavelength  $\lambda \sim 1.55 \times 10^{-6}$  m,  $R$  is the distance of the beam focus from the lidar output lens, and  $A$  is the beam radius at the output lens. The beam intensity profile is assumed to be an axially-symmetric 2D Gaussian;  $A$  is calculated for the point at which the intensity has dropped to  $1/e^2$  of its value at the beam centre. For example, if  $A$  takes the value 20 mm then, at a focus range  $R$  of 100 m,  $\Gamma$  has a value of  $\sim 11$  m, or a probe length (to -3 dB points) of  $\sim 22$  m. For  $A = 28$  mm,  $\Gamma$  drops by a factor of  $\sim 2$  to give  $\Gamma \sim 5.5$  m. At a range  $R$  of 50 m, the width drops by a factor 4 ( $\Gamma = 2.7$  m for  $A = 20$  mm).

Figure 22 shows the behaviour of the theoretical sensitivity curves for the two example cases ( $A = 20$  mm, 28 mm) at several focus heights above ground level. In addition the theoretical curve corresponding to one of the calibration ranges has been plotted, with experimental calibration data for comparison. Section 3.6 contains more detail of the calibration processes. The minimum range is determined by the focusing capability of the transceiver optics, and for ZephIR it takes the value 10 m.



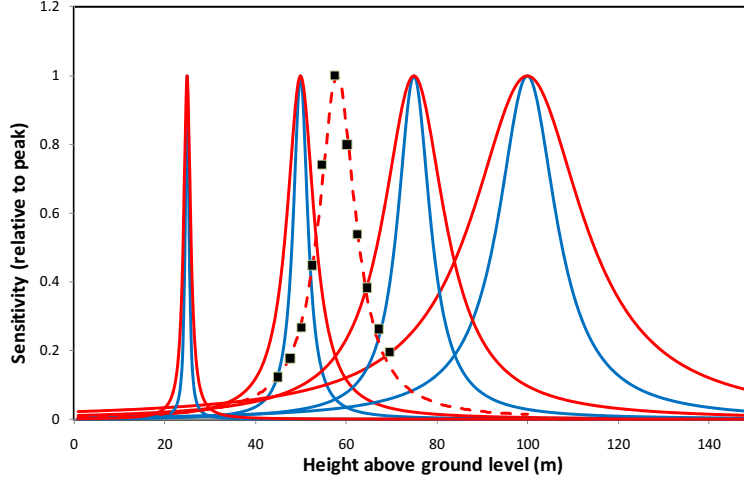


Figure 22: Theoretical lidar sensitivity curves at focus heights 25, 50, 75 and 100 m for the two cases listed above with  $A = 20$  mm and 28 mm, corresponding to respectively the original (red curve) and current (blue curve) ZephIR design. The peak is normalised to unity in each case; the absolute peak value decreases as the inverse of height squared, so that the area under each curve (representing the overall sensitivity) is always the same. This illustrates a useful feature of focused CW coherent lidar that in uniform scattering, the signal-to-noise ratio is independent of focus height. Data obtained in calibration measurements (black squares) at a calibration range  $R = 68$  m are in close agreement with the corresponding theoretical values (dashed curve) at the equivalent height 58 m ( $=68 \text{ m} \times \cos 30^\circ$ )

### Light scattering by aerosols

Coherent lidar measures the Doppler shift resulting from the component of target velocity along the beam (or line-of-sight) direction. Motion of the target transverse to the beam direction produces no net Doppler shift. Hence, for a lidar at  $(0,0,0)$  measuring at a specific location  $(x, y, z)$  where wind components are  $(u, v, w)$ , the lidar will detect a line-of-sight velocity given by the dot product of the wind vector  $(u, v, w)$  and the unit vector along the beam direction:

$$V_{\text{LOS}} = \left| (\mathbf{u} + \mathbf{v} + \mathbf{w}) \cdot \left( \frac{\mathbf{x} + \mathbf{y} + \mathbf{z}}{\sqrt{x^2 + y^2 + z^2}} \right) \right|, \quad (70)$$

where the modulus applies to systems that cannot distinguish the sign of the Doppler shift.

In the backscattering geometry considered here, the scattered light experiences a Doppler shift in frequency given by:

$$\delta\nu = \frac{2V_{\text{LOS}}\nu}{c} = \frac{2V_{\text{LOS}}}{\lambda}, \quad (71)$$

where  $c$  is the speed of light ( $2.998 \times 10^8 \text{ m s}^{-1}$ ) and  $\nu$  is the laser frequency.

Since the signal originates from a finite probe length, the overall return exhibits a spectrum of frequencies. This results from the contributions from different velocities (with strengths determined by the weighting function, Eq. 68) over all the space occupied by the lidar beam. Note that in the absence of additional information it is not possible to identify from what range each component of the spectrum has originated. Section 3.5 will outline how information from additional focus heights is used to identify and reject spectral components originating from strongly-scattering objects (e.g. clouds) situated well outside the probe length.

For a CW coherent system, the time-averaged optical signal power  $P_s$  backscattered

by the aerosols into the receiver is given to a good approximation by:

$$P_s = \pi P_T \beta(\pi) \lambda, \quad (72)$$

where  $P_T$  is the transmitted laser power. It is notable that Eq. (72) contains no dependence on either the focus range or the system aperture size. With a value of  $10^{-8}$  (mrad) $^{-1}$  for  $\beta(\pi)$  in clear boundary-layer air, a transmitted power  $P_T \sim 1$  W and  $\lambda \sim 1.5$   $\mu\text{m}$ , the received power  $P_s$  derived from Eq. (72) is only of order  $5 \times 10^{-14}$  W emphasising the need for high sensitivity.

### Receiver optics

In a monostatic system, the backscattered light returns through the transmission optics (the word transceiver is commonly used to denote this dual role). Any motion of the beam due to scanning over the timescale for the radiation to travel to the aerosols and back will result in misalignment of the receiver, but this is insignificant for the range of parameters considered here.

After entering the transceiver, optical means are used to isolate the return light, and this is passed to the next stages of the detection process.

### Light beating

In coherent laser radar, the incoming Doppler-shifted radiation is optically mixed with a reference LO beam. The mixing of two waves in this manner leads to the well-known ‘‘beat’’ phenomenon in which the resulting amplitude oscillates at the difference frequency. In lidar, the process conveniently ‘‘downmixes’’ the optical frequency of the Doppler shifted return at  $\sim 2 \times 10^{14}$  Hz to a more manageable signal in the MHz range. The efficiency of the beating process is optimised when the signal and LO beams overlap perfectly in space (i.e. they occupy identical spatial ‘‘modes’’). This condition is ensured when both beams propagate in the same single-mode optical fibre, assuming that they share the same polarisation state.

It is instructive to consider a simple classical description of the light beating process. Superposition of a LO field  $E_{\text{LO}} \cos(\omega_{\text{LO}} t)$  and a stable signal field  $E_s \cos(\omega_s t)$  results in a fluctuating detector output:

$$i(t) \propto (E_{\text{LO}} \cos(\omega_{\text{LO}} t) + E_s \cos(\omega_s t))^2. \quad (73)$$

This is conveniently separated into a ‘‘constant’’ term and a cross term oscillating at the difference frequency:

$$i(t) \propto (E_{\text{LO}}^2 + E_s^2) + 2E_{\text{LO}} E_s \cos |\omega_s - \omega_{\text{LO}}| t. \quad (74)$$

Since the optical power of the local oscillator beam typically exceeds that of the signal beam by many orders of magnitude, the first term is given by  $E_{\text{LO}}^2$  to a very good approximation, quantum fluctuations on which give rise to the shot noise floor of the instrument (section 3.6). For a system for which there is no frequency shift between the LO and transmitted beams, the measured Doppler shift is given simply by:

$$\delta\nu = 2\pi |\omega_s - \omega_{\text{LO}}| \quad (75)$$

from which the value of  $V_{\text{LOS}}$  is derived via Eq. (71). In practice a signal field originating from atmospheric scattering exhibits fluctuations in both its amplitude and phase (or frequency). The coherent detection process ensures that these properties are reproduced in the detector output so that, in the limit of high SNR, its spectral analysis gives a correct representation of the scattered light’s spectrum (Harris et al., 1994).

The coherent detection process described above is also commonly referred to as homodyne or heterodyne detection. A rigorous quantum-mechanical theoretical treatment of the detection process is given in Loudon (2000). Note that although the detection process is described as coherent, the backscattered radiation itself is incoherent in nature,

meaning that its phase is uncorrelated with that of either the transmitted beam or the local oscillator. The phase and intensity are typically subject to random fluctuations on a timescale that is related to the inverse of the signal bandwidth (see section 3.7).

### Photodetection

The beat signal is detected by directing the optically-mixed beam onto a photodetector which measures fluctuations in the light's intensity. In the telecommunications wavelength band around  $1.55 \mu\text{m}$ , reliable photodiodes are readily available that are well suited to this purpose. The photodiode converts the incident photons into photoelectrons, which generate a measurable current (or voltage) that is normally passed through further stages of amplification before digitisation. There are generally four contributions to the output of the photodetector module:

- Dark noise – this is the intrinsic wideband noise floor generated by the detector and amplifier combination in the absence of any incident light.
- Photon shot noise (Bleaney and Bleaney, 1976) (sometimes called quantum noise) – the random generation of photoelectrons by the incident LO beam leads to a wideband, spectrally flat (white) Gaussian noise source. The shot noise power spectral density increases in proportion to the optical power of the LO beam.
- Laser relative intensity noise (RIN) – intensity fluctuations that are in excess of shot noise, caused for example by relaxation oscillation (Siegman, 1986) of the laser output. For a RIN-dominated noise floor, the power spectral density increases as the square of LO power. Such oscillation is typically at relatively low frequency, peaking below 1 MHz, and hence only affects the sensitivity of the lidar at low line-of-sight wind speeds around  $1 \text{ m s}^{-1}$ . In some systems it is possible to cancel the RIN by use of a dual-channel balanced detector.
- Beat term resulting from the wind signal – this is the contribution that contains the information on Doppler shifts from which the wind speed is derived. Its power spectral density increases in proportion both to the LO power and the signal power.

The requirements for the detector are high quantum efficiency, sufficient bandwidth to cope with the maximum Doppler frequencies of interest, and for the shot noise contribution to significantly exceed that of dark noise. This latter requirement depends on a combination of the detector's intrinsic noise floor and the optical saturation threshold.

### Fourier analysis and lidar sensitivity

In order to extract the Doppler frequency information, it is necessary to perform a spectral analysis of the detector output. This is conveniently done digitally; an example of a typical signal processing procedure is described below and illustrated in Figure 23. An ADC with a sampling rate of 100 MHz permits spectral analysis up to a maximum frequency of 50 MHz, corresponding to a wind speed  $V_{\text{LOS}}$  of  $\sim 38.8 \text{ m s}^{-1}$  (Eq. (72), with  $\lambda = 1.55 \mu\text{m}$ ). A hardware low-pass filter with a cut-off frequency of 50 MHz, inserted between the detector and ADC, eliminates aliasing problems. Spectra are calculated by digital Fourier transform (DFT) methods; a 512 point DFT gives rise to 256 points in the output spectrum with a bin width of  $\sim 200 \text{ kHz}$ , corresponding to a line-of-sight velocity range of  $\sim 0.15 \text{ m s}^{-1}$ . Each DFT represents  $\sim 5 \mu\text{s}$  of data; successive DFTs are then calculated, and the resulting “voltage” spectra are squared in order to generate a power spectrum. These power spectra are then averaged to find a mean spectrum for the averaging period. The random fluctuation in the shot noise floor of the spectrum reduces as the square root of the number of averages: the sensitivity increases by this same factor. For 4000 averages, the measurement time amounts to  $\sim 20 \text{ ms}$  (or a data rate of  $\sim 50 \text{ Hz}$ ). This requires

that the processing is capable of 100% duty cycle, which is achieved in ZephIR with a fast Fourier transform (FFT) block within a field-programmable gate array (FPGA). It has been shown that a standard fast PC with no additional duties to perform can achieve a similar performance. It is possible to accommodate reasonable variations in any of the above parameters (sample rate, DFT size, number of averages) and maintain the 100% duty cycle.

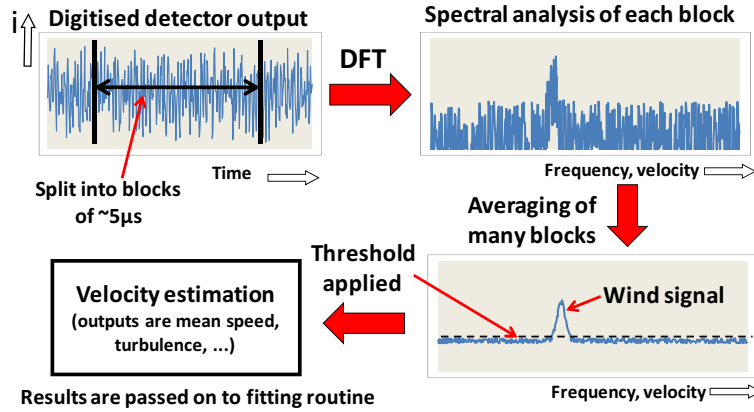


Figure 23: Stages in typical lidar signal processing: DFT analysis is carried out by a computer integrated into the lidar system. As an example, 4000 individual spectra might be averaged to achieve high sensitivity and measurable returns even in very clear air. This entire process takes only 20 ms, giving  $\sim 50$  measurements per second of line-of-sight wind velocity

The width of the Doppler spectrum is determined by three elements:

- Instrumental width: this corresponds closely to the  $\sim 200$  kHz bin width mentioned above.
- Transit-time broadening: during the conical scan, the beam passes through the aerosol particles in a timescale of  $\sim 10 - 15 \mu\text{s}$ , independent of the lidar focus setting. The corresponding broadening is again of order 200 kHz.
- Turbulence broadening: the probing of a significant volume results in a range of Doppler shifts from parts of the atmosphere that are moving at different speeds (see section 3.3). In general, this contribution increases with turbulence and shear, and occasionally there is more than one peak in the spectrum as a result.

The last of these usually dominates except under conditions of very uniform airflow. High system sensitivity is of crucial importance for a wind lidar reliant on weak backscatter from the atmosphere. The SNR<sup>4</sup> for a wind speed measurement by a CW CLR is given by:

$$\text{SNR} = \frac{\eta P_s}{(hc/\lambda) \Delta\nu [1 + D(\nu) + R(\nu)]}. \quad (76)$$

Here  $\eta$  is an efficiency term incorporating optical losses and photodetector sensitivity (typically  $\eta \sim 0.5$ , approaching the value 1.0 only for a “perfect” system),  $P_s$  is the input signal power, as defined in Eq. (72) and  $hc/\lambda$  is the light quantum energy, of order  $1.3 \times 10^{-19}$  J. The signal bandwidth  $\Delta\nu$  is determined by the three contributions listed above, and the term inside the square brackets denotes the various noise sources listed in section 3.6.  $D(\nu)$  and  $R(\nu)$  represent the power spectral density (at frequency  $\nu$ ) from dark noise and RIN respectively in units of the power spectral density of the local oscillator shot noise. Ideally  $D(\nu)$  and  $R(\nu)$  should both be  $\ll 1$  over the range

<sup>4</sup>In the lidar community, this is commonly, and more properly, referred to as the carrier-to-noise ratio (CNR)

of Doppler frequencies of principal interest, so that the shot noise is the dominant noise source.

The SNR as defined here is the power spectral density at the Doppler peak divided by that in the surrounding noise floor. The averaging of many spectra (described in the following sections) ensures that good performance can be obtained even when the SNR is well below unity. For example, an SNR of 0.1 will easily exceed a  $5\sigma$  threshold level (see next section) for an average of 4000 spectra. From the above it is possible to derive an approximate value of  $\beta(\pi)_{\min} \sim 10^{-9} \text{ (m srad)}^{-1}$  for the minimum detectable backscatter, assuming a transmitted intensity 1 W and a 20 ms measurement time.

### Velocity estimation

From the preceding sections it is apparent that each measurement of line-of-sight wind speed, obtained over a timescale of  $\sim 20$  ms, generates a Doppler spectrum consisting of one or more peaks of variable width, superimposed on a noise floor that is predominantly white, but which may have spectral features originating from RIN and dark noise sources. This section outlines steps that can be followed to derive an appropriate estimate of the wind speed.

First, the noise floor is “whitened” so that each spectral bin contains the same mean noise level, achieved by dividing the power value in each bin of the spectrum by a previously-measured value for the same bin obtained with the shutter closed. A flat threshold is then applied at a pre-determined level above the mean noise; see Figure 23. A suitable and conservative choice for the threshold is 5 standard deviations ( $5\sigma$ ) above the mean noise level. In the absence of any wind signal (e.g. with the output of the lidar blocked) such a setting will give rise to negligible occurrences in which the noise alone exceeds threshold. It follows that any bin whose level exceeds the threshold is deemed to contain a valid contribution to the wind signal. For each 20 ms measurement, the wind spectrum is reconstructed by subtracting the mean noise contribution from the contents of each bin that exceeds threshold, and applying a small re-correction for any distortion resulting from the noise whitening. In order to proceed to the next stage, a single velocity value is derived from the resulting spectrum. A number of options are available, including peak and median values; a common solution is to calculate the mean (or centroid) value  $\langle V_{\text{LOS}} \rangle$ .

A series of these values of mean line-of-sight wind speed is generated as the ZephIR lidar performs a conical scan. Wind parameters are usually calculated from data obtained from three revolutions of the scanner. With a rotation time of  $\sim 1$  s, up to 150 line-of-sight values are available for the next stage, in which a least-squares fitting algorithm is applied. Data can also be generated for a 1 s, single scan rotation (based on a 50-point fit), as required by the user.

### Least-squares fitting routine

The data that are fed to the fitting routine consist of up to 150 pairs of values of  $\langle V_{\text{LOS}} \rangle$  and azimuth angle  $\phi$ . In conditions of uniform wind flow, this gives rise to a rectified cosine wave of the form:

$$\langle V_{\text{LOS}} \rangle = |a \cos(\phi - b) + c|. \quad (77)$$

The derivation of this function is straightforward and can be found in a number of publications, e.g. Banakh et al. (1993). The peaks of the function correspond to the azimuth angle aligned parallel or anti-parallel to the wind direction. The function passes through zero when the azimuth angle is perpendicular to wind bearing since there is no component of velocity along the line of sight. The data are also conveniently displayed on a polar plot (Figure 24), which provides information at a glance on the speed, direction and vertical wind component. A standard least-squares fitting routine provides the best

estimates of the values of the three floating parameters ( $a$ ,  $b$  and  $c$ ).

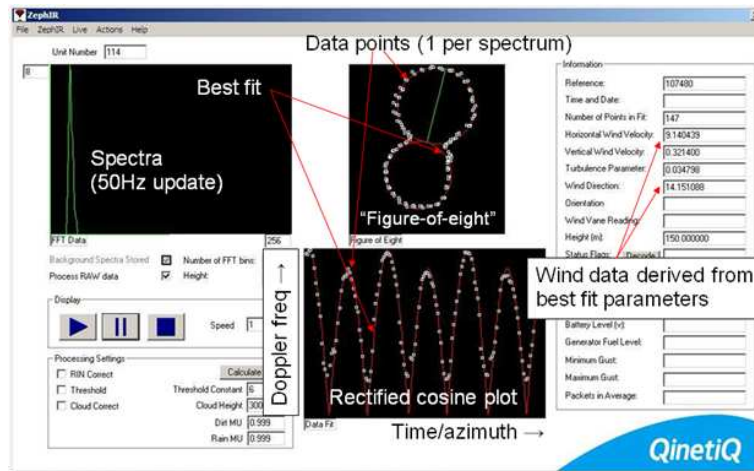


Figure 24: Wind lidar output screen, illustrating many of the features of a wind profile measurement. This example has been obtained at a height 150 m above ground level, one of several heights being probed in sequence. The lower trace shows 147 individual line-of-sight wind speed values, obtained over a total period of 3 s, plotted as white squares against azimuth scan angle. The same data, along with the least-squares fit in red, are displayed above this in polar coordinates on the figure-of-eight plot showing the wind bearing to lie slightly to the East of North. The wind parameters, derived from the fit, appear in the table on the right; the horizontal wind speed at this height is determined to be  $9.1 \text{ m s}^{-1}$ . The plot on the left shows just one of the spectra from which each point on the other 2 graphs is derived

The high level of redundancy in the fitting process is advantageous and can be used to identify non-uniform flow. The root mean square deviation of the points from the optimum solution gives an indication of the quality of fit, and this can be related to the value of turbulent kinetic energy (TKE; see Wagner et al. (2009)). More work is needed to establish a full understanding of the turbulence information available from lidar signals (Banakh et al., 1999). Note that information on turbulence is also available from the spectral widths of the individual line-of-sight wind speed measurements, but this is not currently used to evaluate turbulence parameters. Owing to data storage constraints, spectral information is commonly discarded after the velocity estimation process.

### Parameter extraction

The wind parameters for each 3 s measurement period are extracted from the best fit as follows ( $\theta \approx 30^\circ$ ):

$$\begin{aligned} \text{Horizontal speed } V_H &= a / \sin \theta, \\ \text{Vertical speed } w &= -c / \cos \theta, \\ \text{Bearing } B &= b, \text{ or } b \pm 180^\circ. \end{aligned} \tag{78}$$

Where there is an ambiguity in the sign of the Doppler shift, there are two equally valid best-fit solutions corresponding to values of  $b$  separated by  $180^\circ$ . The correct choice is usually easily made by choosing the solution that lies closest to a conventional measurement from a met station situated close to ground. Conventionally, a wind profiling lidar incorporates such a station that performs these (and other) measurements and feeds the results to the analysis software.

The 3 s (or alternatively 1 s) wind parameter values are stored internally for subsequent analysis; they can also undergo further processing for extraction of average values.

## Data averaging

It is a common requirement to calculate 10 min averaged wind data for compatibility with industry standards. This is most easily achieved by calculation of the arithmetic mean (“scalar average”) of the individual values of  $V_H$ ,  $w$  and  $B$  that have been obtained during the required period. A vector average is also possible in which the resultant of the individual measurements is calculated over each 10 min period. In practice the results from the two methods differ negligibly in reasonably stable conditions. In accordance with industry standards, ZephIR computes a scalar average for  $V_H$  and  $w$ , and a vector average for  $B$ .

When a CW lidar is operating as a wind profiler it is necessary to measure each height in series. Hence, at any given height the wind is not monitored continuously. Instead, an individual measurement (taking 1 to 3 s to obtain) is followed by a period of order 7–20 s during which the lidar is focused at other heights. Since this sampling is carried out randomly with respect to any behaviour of the wind, this duty cycle of order 15% has negligible impact on the validity of the resulting 10 min averaged values. Also the typically large scan area ensures the beam samples a much higher fraction of the overall turbulent fluctuations.

## 3.5 Uncertainty analysis

### Rain/snow/cloud, solid objects

In general the Doppler shift measured by coherent laser radar is very accurate. This is apparent from Eq. (72) as long as the laser wavelength remains stable and the signal processing has been correctly performed - both good assumptions in practice. The values of  $\langle V_{LOS} \rangle$  that are derived from the centroids of the spectra can be measured to considerably better than a bin width. A greater source of error arises from uncertainty about what provides the scattering from which the Doppler shift is derived. The scattering is assumed to originate from atmospheric particles moving at the same speed as the wind and positioned close to the focus of the lidar beam (section 3.3). An obvious example where this breaks down is when the beam intersects a solid object (e.g. a bird) that is moving at a different speed from the wind giving a measurement which could be in error. However, in such a case the value of  $\langle V_{LOS} \rangle$  so derived will stand out as clearly anomalous on the polar plot (Figure 23). The presence of such points will be diluted by approximately 150 correct values of  $\langle V_{LOS} \rangle$  obtained from uncontaminated parts of the atmosphere, and their inclusion should not introduce any bias. A further safeguard against these erroneous points is provided by a simple “outlier removal” algorithm. This identifies points that lie anomalously far from the best fit solution to Eq. (77) and eliminates them. The least-squares routine is then rerun on this slightly reduced set of  $\langle V_{LOS} \rangle$ , data pairs.

The presence of precipitation within the probe volume leads to a different source of uncertainty. The downward motion of rain and snow inevitably leads to some error in the vertical component of wind speed. However, the presence of rain and snow is normally easily identified from the measurement process (for example by detecting activation of a rain sensor), and the resulting values of vertical wind eliminated from the data.

### Cloud effects

CW laser wind profilers focus the beam in order to measure wind speed at a given height. This technique has the advantage of uniformly high sensitivity independent of focus measurement height, and of very small probe lengths at lower heights where detailed investigation of shear is important. However, the signals do require correct processing when the beam impacts a cloud base at higher altitude since the contribution to the Doppler signal from cloud provides an additional contribution to that from the aerosols

at the desired height.

A general approach to mitigating this problem needs first to identify the presence of a cloud return and then remove its contribution from the Doppler spectra. Cloud returns have a number of characteristics that allow them to be distinguished from aerosol returns:

- Velocity usually higher
- Spectral width usually narrower
- Power in Doppler peak has clear dependence on lidar focus; the power is maximised when the lidar beam is focused close to the height of the cloud base
- Doppler spectrum is independent of focus range

The latter two characteristics are highly dependable and form the basis for identification and elimination of spurious cloud returns. The general strategy for removal of cloud signals is outlined in the following steps (and illustrated in Figure 25):

1. Routinely run the lidar at an additional greater height (e.g. 800 m - essentially a collimated beam output) immediately before or after the maximum height of interest, say 150 m for the sake of argument.
2. For each azimuth angle around scan at 150 m, identify the 800 m (“cloud”) spectrum obtained at the closest value of azimuth angle.
3. Apply test conditions to the 150 m spectra to determine whether any cloud signal is present in the spectral data; apply cloud removal algorithm.
4. Run standard thresholding and centroiding routines on resulting “clean” spectra and fit to the rectified cosine wave (Eq. (77)) as usual to obtain wind parameters.

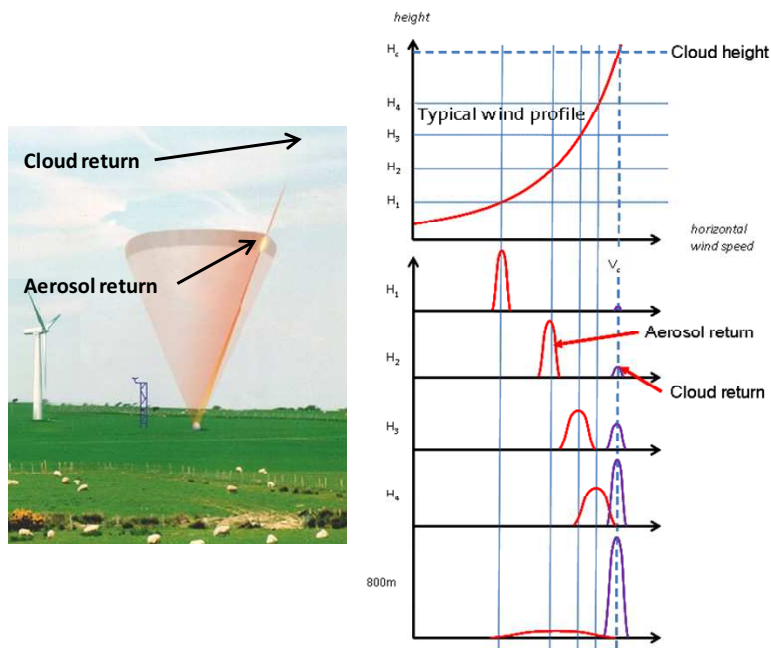


Figure 25: Cloud removal. The left plot shows the lidar conical scan focused at a typical height above ground level. The Lorentzian sensitivity curve is also shown; a spurious return is generated when the far wing of this curve intersects a strongly scattering low cloud layer. The right plot shows the aerosol (red) and cloud (purple) returns as the lidar is focused at various heights - the level of cloud contamination increases with focus height. The cloud signal is easily identified from the 800 m focus, and these data are then used to eliminate the cloud return at the measurement heights



A cloud removal algorithm based on this approach is implemented in ZephIR; this has been extensively tested in a number of locations, and its effectiveness demonstrated by correlation analysis against calibrated tall masts. During the 800 m (“wind profile”) scan, background measurements are taken to quantify the specific cloud return and any cloud effect is then removed from the processed data.

In general, lidars of various types of design will all have difficulty measuring in very low cloud and fog scenarios where the light emitted from the lidar is unable to reach all the heights of interest due to absorption in the atmosphere. While this atmospheric condition mostly occurs during low wind speed periods, it is important that these periods be identified. In the majority of cases they are removed by filtering methods.

Recent trials of a ZephIR unit at Risø DTU’s test site at Høvsøre (Courtney and Gottschall, 2010) took place in long periods of low cloud and hence provide a demonstration of the performance in challenging cloud conditions. The data set summarised in Table 4 below was taken during a period of 4 weeks in October and November 2009. Cloud height was measured using a ceilometer; 25% of data was obtained with the cloud base below 300 m, and 43% obtained with the cloud base below 600 m. The results of the trial (Table 4) indicate a good agreement between lidar and mast at all heights from 40 up to 116 m. Filtering has been applied to remove sectors prone to the influence of turbine wakes, and speeds below  $4 \text{ m s}^{-1}$ .

*Table 4:* Results of correlation analysis (10 min averaged horizontal wind speed) of a ZephIR trial at Høvsøre in late 2009. A gradient  $m$  (forced through the origin) and correlation coefficient  $R^2$  both of value 1.00 would imply perfect agreement between lidar and mast-mounted cup anemometer. It should be noted that the slopes very close to 1.0 are slightly fortuitous, since the cup anemometer measurements have uncertainties at least of order  $\pm 1\%$ , due to calibration and mounting/shadowing effects

Height AGL [m]	Slope $m$	$R^2$
116	0.991	0.981
100	0.997	0.978
80	0.999	0.981
60	0.997	0.987
40	0.999	0.985

### System positioning accuracy

Correct alignment ensures the risks are low, but errors in aligning the lidar during set-up will have an impact on the measurement of wind bearing (if the lidar is rotated from its correct orientation) and vertical wind speed (if the lidar is tilted, so that the axis of its conical scan is not precisely vertical). For a small tilt angle  $\delta$ , the error in vertical wind speed  $w$  will vary from  $\pm V_H \sin \delta$  (if the tilt is towards or away from the direction of the wind) to zero (if the tilt is perpendicular to the wind). Any bias on  $V_H$  is negligible to first order.

### Probe volume effects and operation at greater heights

As discussed in section 3.2, the lidar samples the motion of air from a finite volume, centred on the beam waist at the focus. Clearly there is minimal risk of bias while all the air within the probe volume moves at the same speed; however, there is usually some degree of shear across the sample region. For a linear shear this leads to spectral broadening of the returns, but no overall bias. A strong non-linear shear profile across the probe volume is required to induce any bias of significance; in practice such conditions

will be rare, certainly for measurement heights around hub height and below where the probe length is relatively small.

Most lidar comparisons have taken place beside masts of heights around 100 m or less. However, in early 2009 a study took place in Iowa, USA against a 200 m mast in flat terrain. The results showed high correlation (Table 5, taken from Barker (2009)) even at the greater heights examined (150 and 200 m), which approach the expected maximum operating range for focused CW lidar.

*Table 5:* Results of a comparative trial of a ZephIR lidar against a very tall mast, equipped with two types of cups at each height. The data indicate that the extended probe length at greater heights did not result in excessive bias or errors. [1]: Forced through the origin; [2]: Only hourly averages containing 6 valid 10 min measurements compared

Height AGL [m]	NRG IceFree3				NRG MAX#40C			
	Ten min average		Hourly average <sup>[2]</sup>		Ten min average		Hourly average <sup>[2]</sup>	
	R <sup>2</sup>	Slope <sup>[1]</sup>	R <sup>2</sup>	Slope <sup>[1]</sup>	R <sup>2</sup>	Slope <sup>[1]</sup>	R <sup>2</sup>	Slope <sup>[1]</sup>
193	0.984	0.987	0.987	0.987	0.982	0.993	0.988	0.992
157	0.982	1.006	0.988	1.005	0.984	1.000	0.989	1.000

### Flow uniformity and complex terrain

In complex terrain, the flow undergoes stable and unstable non-uniformities, and the figure-of-eight plot (Figure 24) can distort systematically for a given wind direction, reflecting the speeding up and slowing down in certain regions of the scan. The ZephIR lidar provides some information about the flow non-uniformity, with up to 50 points being interrogated around the scan disk. Because only line-of-sight wind components are measured, a single ground-based lidar unit inevitably provides an incomplete picture of the 3D vector flow, regardless of the scan pattern employed. The full vector at a given point can therefore only be measured by the provision of three (or more) lidar units positioned on the ground at an appropriate separation distance (comparable to the measurement height for best accuracy), such as the Windscanner system under development by Risø DTU (Mikkelsen, 2008).

In the presence of non-uniformity in flow (section 3.2), a lidar measurement can indicate a wind speed different to that from a point measurement by a mast-mounted cup anemometer. Work is ongoing to combine lidar data with the output from flow-modelling software, using both linear models (Bingöl et al., 2008, 2009; Bingöl, 2010) and computational fluid dynamics, CFD (Harris et al., 2010). This pragmatic approach generates measurements equivalent to a “point-in-space” sensor by using the results of flow modelling to adjust the lidar wind speed. This topic will be dealt with in detail in Chapter 7, examining possible improvement of lidar resource assessment capability in complex terrain.

### Dependence on backscatter level

Under conditions of high backscatter, the spectrum provides an accurate measure of the distribution of line-of-sight velocities within the probe volume, weighted according to Eq. (68). As the backscattering strength drops (usually associated with increased air clarity) this has a similar effect to raising the detection threshold, and will lead to elimination from the spectrum of weaker components of velocity. The impact of the system noise floor on the detailed spectral shape will also be increased. The centroid values  $\langle V_{LOS} \rangle$

will be unbiased and independent of threshold level when the spectrum is symmetrical. However, for a skewed (asymmetric) spectrum the precise value of  $\langle V_{LOS} \rangle$  will be sensitive to the threshold. Hence a small difference in measured wind speed is possible between two measurements under conditions that are identical in every way apart from the level of backscatter. However, there is no evidence from comparisons so far to suggest that this leads in practice to a significant discrepancy.

A further possibility to be considered is the effect of saturation (by very strong scattering returns from thick cloud) of the lidar detector, electronics or signal processing. In the event that the input signal exceeds these limits, the spectrum will become distorted, possibly featuring higher harmonic components of the true Doppler frequencies. In practice, the range of inputs to the ADC can be tailored to accommodate the highest levels of backscatter that will reasonably be encountered, eliminating the risk of bias.

### Beam obscuration and attenuation

Lidar can operate successfully even when part of its scan is obscured. This confers great flexibility so that the system can easily be located adjacent to masts, buildings or in forests. Stationary objects pose no major problem other than the loss of wind measurements from the relevant obscured sector of the scan.

In the above cases, the fit to Eq. (77) will no longer contain data over the full  $360^\circ$  range of  $\phi$ . Laboratory experiments on moving belt targets have indicated that accurate measurements are obtained even when over half of the scan is obscured. Catastrophic errors in the least-squares fitting process become possible as the obscuration increases yet further; such conditions are identified and a null result returned.

### Wind direction

The two best-fit solutions ZephIR obtains to Eq. (77) give values of wind direction that are  $180^\circ$  apart. Selection between the two options is made with reference to the measurement of wind direction from a ground-based anemometer. This needs to be in disagreement by over  $90^\circ$  with the direction at the chosen height for the incorrect choice to be made. While such a directional shear (veer) is conceivable in highly complex terrain and at very low wind speed, it is much less likely in the reasonably uniform conditions of interest for wind energy applications. In the event of the wrong choice being made, leading to a wind direction that is in error by  $180^\circ$ , the value of vertical component of the wind  $w$  will have the wrong sign. In other words, an updraught will be wrongly identified as a down draught (of the same absolute speed) and vice versa.

## 3.6 Calibration, validation and traceability

Currently, the clearest demonstration of validity is provided by direct side-by-side comparisons between the lidar system and a fully instrumented IEC-compliant meteorological mast of suitable height. Rigorous comparisons must be carried out with great care to avoid a number of problems associated with cup anemometers (Kristensen, 1999). These are well known and include the following:

- Shadowing of the cup anemometer by the mast from certain directions
- Cup overspeeding in turbulence and sensitivity to any vertical wind component
- Cup icing
- Valid cup anemometer calibration
- Topographic effects leading to non-uniform flow across the area occupied by mast and lidar scan (including turbine wakes)

A lidar/mast comparison is commonly used to provide a validation of lidar performance, and examples of such checks were provided by the results in Tables 4 and 5. The lidar can then be used as a traceable reference for comparison with other units.

Lidar systems are normally calibrated in the laboratory before shipping. Routine checks on the calibration of units on their return to base provide confidence of long-term stability. As an example, the calibration process undertaken for a ZephIR lidar is outlined below. This consists of three stages:

1. Velocity and direction check against a calibrated moving belt. The process provides a direct check of laser wavelength and scanner cone angle, each of which affects the velocity calibration (via Eqs. (71) and (77) respectively).
2. A focus range check is carried out with a moving target located at precise distances from the lidar. The closed loop positioning system ensures no drifts over time. An example of the output data from a focus calibration test was plotted in Figure 22 (section 3.4).
3. Finally, each unit undergoes an outdoor test to measure wind speed at several heights side-by-side against a reference unit. The reference unit has been checked against a tall mast to provide traceability. Figure 26 shows an example correlation plot of 10min average horizontal wind speed, obtained over a period of 7 days.

Each of the three tests above gives information on the sensitivity of the unit; for deployments in “clean” air, it is important to ensure this aspect of performance is fully optimised and has not deteriorated, or there is a risk of reduced data availability.

It is important that no adjustments are performed during validation trials, or afterwards for as long as the lidar remains a traceable reference unit. The certification process outlined above has been defined in collaboration with industry experts including Garrad Hassan and provides the traceability that is a key element of formal energy prediction reports used by the financial community.

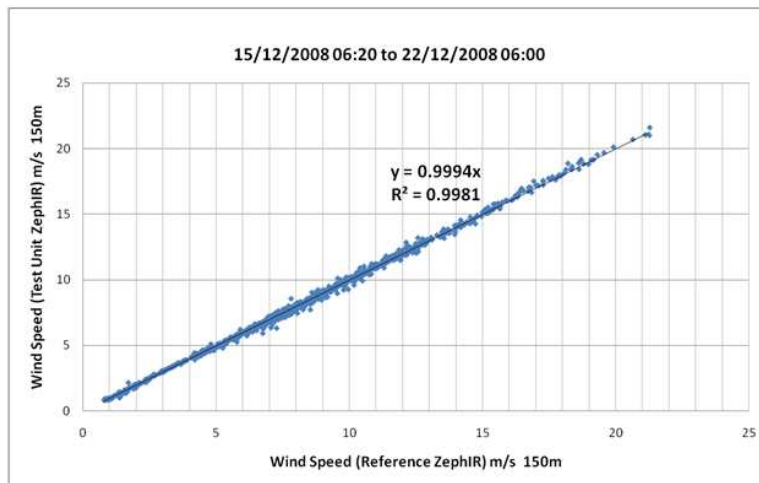


Figure 26: A new ZephIR system is compared to the reference system showing strong correlation and a gradient close to unity. This comparison has been carried out at 150 m height

Lidar offers a potential advantage for accurate shear profiling (both for speed and direction) in that the same instrument is used to make the measurements at all heights. By contrast, a mast relies on consistent calibration of the full set of cups and vanes; any differences in calibration of the individual instruments will lead to uncertainty and error in the shear assessment. There is currently a need for agreement on a unified method to allow meaningful comparison between the performances of different remote sensing systems.

### 3.7 Summary, state of the art, and future developments

Coherent monostatic CW lidar is a method capable of rapid wind speed measurement at relatively short ranges (all the way from 10 to 200 m) and hence is well suited to several requirements in the field of wind energy. Examination of the measurement process reveals that the basic acquisition of line-of-sight Doppler spectra is a well-established method with little scope for gross errors and miscalibration. The subsequent steps required to convert these spectra into a profile of wind speed are more complex, however, and their validity relies on a number of well-established assumptions. Much work has been performed to test the validity of assumptions outlined in section 3.3, and to understand the uncertainties and other issues discussed in section 3.5.

Complex terrain remains a topic of great interest as it becomes increasingly necessary to explore less ideal locations as potential wind farm sites. In such sites the horizontal wind speed deduced by conically-scanned lidar can be subject to differences in comparison to that measured by co-located cup anemometers when the flow is non-uniform across the lidar measurement disk. A method has recently been developed in which the impact of inhomogeneous flow at complex flow sites is examined using computational fluid dynamics (CFD) modelling to predict the bias that will be experienced by a lidar in comparison to a conventional met mast equipped with cup anemometers. Similar percentage changes in wind speed as measured by a mast are shown to occur if the mast were to be moved by  $\pm 50$  m from its original location. This suggests a methodology for resource assessment in complex terrain in which lidar is used in combination with CFD modelling in order to (i) adjust the lidar data for the impact of non-uniform flow and (ii) investigate the wind variations across the site that are a major source of uncertainty for current techniques.

Lidar offers some potential advantages in turbine power curve measurement. The measurement over an extended volume may give a more representative estimate of the wind energy content of the air interacting with the blades, and the ability to re-position the lidar quickly is clearly advantageous. A study reported by Wagner et al. (2008) has shown that exploiting the lidar wind profile data can reduce the scatter of points in a measured power curve. In another recent study (Cayla, 2010) a ZephIR lidar gave an almost identical power curve to an IEC-instrumented power performance mast. The scatter of the points in the power curve obtained using the ZephIR data at hub height was somewhat lower than that for the mast. This result needs further investigation and possibly is a consequence of the more effective sampling of the wind around the scan disk. It follows, interestingly, that remote sensing equipment that agrees perfectly with the mast would therefore have provided higher scatter in the power curve than ZephIR!

The extraction of turbulence data relevant to the wind industry from lidar signals is an area that will benefit from further research and verification through field comparisons. Turbulence can manifest itself as gusts, eddies, and fluctuations in wind speed. It is important in wind energy applications to characterise the levels of turbulence encountered at a specific site location. A commonly-used basic measure of turbulence is turbulence intensity (TI). ZephIR calculates the turbulence intensity that a conventional cup would have obtained at the same measurement height by analysing the variation in individual wind speed values during a 10 min averaging period. This value of TI is automatically logged in the output data. The calculation takes into account the difference between point measurements obtained from a cup anemometer, and spatially-averaged lidar data where a volume is interrogated. ZephIR's measurements of turbulence have been investigated in a number of independent studies against calibrated met masts in flat, offshore and complex terrain, and at different heights above ground (Wagner et al., 2009).

Resource assessment in maritime locations is becoming increasingly relevant as offshore wind farms assume greater importance. The cost of installing an offshore tall mast is very high, so remote sensing may prove particularly advantageous in such locations. ZephIR lidars have been involved in successful trials on several offshore platforms in the North Sea

(e.g. Peña et al. (2009)), the Baltic, and around the lakes and coasts of North America. A floating lidar platform offers an exciting future concept; an early attempt to develop a ZephIR system on a buoy (SeaZephIR) took place in 2004/5. After a redesign, the system took to the water off S Norway in 2009. A world-first demonstration trial took place over a period of several weeks in late 2009, involving one ZephIR unit stationed on land, with the floating SeaZephIR unit positioned 800 m out to sea. The wind speeds measured by the two ZephIR units showed excellent correlation, with differences in mean wind of  $\sim 1\%$  or less at all heights over a 3 week test period (see Table 6, from Wiggins (2009)). In this trial there was no attempt to compensate for the platform motion; it may be necessary in very severe conditions to use measurements of the 6 degrees of freedom (3 rotational and 3 translational) that can in principle distort the lidar measurement. The low impact of the motion observed in trials so far may be a consequence of the high stability of the buoy combined with the very fast 50 Hz measurement rate for the ZephIR lidar, which allows a snapshot of the wind around a  $360^\circ$  disk to be obtained in 1 s. Further development of SeaZephIR is ongoing.

*Table 6:* Correlation analysis from the first SeaZephIR trial in 2009: the table shows  $m$  and  $R^2$  for plots of 10 min wind speed for SeaZephIR on a floating platform versus those measured by a second ZephIR unit positioned 800 m away on land

Height AGL [m]	Slope $m$	$R^2$
120	0.993	0.972
90	0.998	0.970
60	1.004	0.968
30	0.990	0.954
10	0.984	0.953

Forward-looking turbine mounted lidar, either on the nacelle or in the hub, is another exciting potential future application for advance warning of changes in wind speed. Incorporation of such data into the turbine control system offers possibilities for load reduction and increased energy yield. At the time of writing, it remains to be seen whether lidar will prove sufficiently beneficial to justify the effort of installation; any such system will have to satisfy stringent reliability and cost requirements. Interest in the concept has increased significantly since the world-first proof-of-principle demonstration of turbine-mounted lidar in 2003 (Harris et al., 2006, 2007), with several groups currently working towards evaluating the concept. Recent developments include incorporation of a conical-scanning ZephIR lidar in the spinner of a large turbine (Mikkelsen et al., 2010) giving an unobscured view of the approaching wind.

## Acknowledgements

I am grateful to colleagues too numerous to mention (at QinetiQ, Natural Power, Risø DTU and elsewhere), for their valuable assistance in lidar research, development and testing over many years. I am indebted to Dr J Michael Vaughan for first introducing me to the field of wind lidar, and to Ian Locker and Dave Smith for convincing me that it has an important role to play in the wind energy industry.

## Notation

$a$	floating parameter for the fit of the line-of-sight velocity
$A$	beam radius at the output lens
ADC	analogue-to-digital converter
$b$	floating parameter for the fit of the line-of-sight velocity
$B$	wind bearing
$c$	speed of light
	floating parameter for the fit of the line-of-sight velocity
CFD	computational fluid dynamics
CLR	coherent laser radar
CNR	carrier-to-noise ratio
CW	continuous wave
DFT	digital Fourier transform
$D(\nu)$	power spectral density from dark noise
$E_{LO}$	LO field
$E_s$	stable signal field
FFT	fast Fourier transform
FPGA	field-programmable gate array
$h$	Planck constant
$i$	fluctuating detector power output
IR	infrared
LO	local oscillator
$m$	slope of the linear regression
$P_s$	time-average optical signal power
$P_T$	transmitted laser power
$R$	distance of the beam focus from the lidar output lens
	correlation coefficient
RIN	laser relative intensive noise
$D(\nu)$	power spectral density from RIN
SNR	signal-to-noise ratio
$t$	time variable
TI	turbulence intensity
TKE	turbulent kinetic energy
$u$	wind speed component in the $x$ -direction
$v$	wind speed component in the $y$ -direction
VAD	velocity-azimuth-display
$V_H$	horizontal wind speed
$V_{LOS}$	line-of-sight wind speed
$w$	wind speed component in the $z$ -direction
$x$	horizontal position in longitudinal direction
$y$	horizontal position in transverse direction
$z$	position perpendicular to the horizontal plane
$\beta$	atmospheric backscatter coefficient
$\Gamma$	half-width of the lidar's peak sensitivity
$\delta$	lidar's tilt angle
$\delta\nu$	Doppler shift in frequency
$\Delta$	target distance from the focus position along the beam direction
$\eta$	lidar efficiency
$\theta$	lidar's cone half-angle
$\lambda$	laser wavelength
$\nu$	laser frequency
$\phi$	lidar's azimuth angle
$\sigma$	standard deviation
$\omega_{LO}$	local oscillator frequency
$\omega_s$	stable signal frequency
$\langle X \rangle$	ensemble average of a variable $X$

## References

- Banakh V. A., Smalikho I. N., Köpp F., and Werner C. (1993) Representativeness of wind measurements with a CW Doppler lidar in the atmospheric boundary layer. *Appl. Opt.* **34**:2055–2067
- Banakh V. A., Smalikho I. N., Köpp F., and Werner C. (1999) Measurements of turbulent energy dis-

- sipitation rate with a CW Doppler lidar in the atmospheric boundary layer. *J. Atmos. Oceanic Tech.* **16**:1044–1061
- Barker W. (2009) Analysis of ZephIR data from Mason City, Iowa. Natural Power internal report
- Bingöl F., Mann J., and Foussekis D. (2008) Lidar error estimation with WAsP engineering. *IOP Conf. Series: Earth and Environ. Sci.* **1**:012058
- Bingöl F., Mann J., and Foussekis D. (2009) Conically scanning lidar error in complex terrain. *Meteorol. Z.* **18**:189–195
- Bingöl F. (2010) Complex terrain and wind lidars. Risø-PhD-52(EN), Roskilde
- Bleaney B. I. and Bleaney B. (1976) Electricity and magnetism, Oxford University Press, Section 23.4
- Cayla M. (2010) Comparison of ZephIR measurements against cup anemometry and power curve measurements. Natural Power internal report
- Chanin M. L., Gariner A., Hauchecorne A., and Portneuve J. (1989) A Doppler lidar for measuring winds in the middle atmosphere. *Geophys. Res. Lett.* **16**:1273–1276
- Clifford S. F. and Wandzura S. (1981) Monostatic heterodyne lidar performance: the effect of the turbulent atmosphere. *Appl. Opt.* **20**:514–516
- Courtney M. and Gottschall J. (2010) ZephIR 145 validation test. Risø report for Natural Power
- Hardesty R. M. and Weber B. F. (1987) Lidar measurement of turbulence encountered by horizontal-axis wind turbines. *J. Atmos. Oceanic Tech.* **67**:191–203
- Harris M., Pearson G. N., Hill C. A., and Vaughan J. M. (1994) Higher moments of scattered light fields by heterodyne analysis. *Appl. Opt.* **33**:7226–7230
- Harris M., Constant G., and C Ward (2001) Continuous-wave bistatic laser Doppler wind sensor. *Appl. Opt.* **40**:1501–1506
- Harris M., Pearson G. N., Ridley K. D., Karlsson C. J., Olsson F. A., and Letalick D. (2001) Single-particle laser Doppler anemometry at 1.55  $\mu\text{m}$ . *Appl. Opt.* **40**:969–973
- Harris M., Hand M., and Wright A. (2006) Lidar for turbine control. Tech. Report NREL/TP-500-39154
- Harris M., Bryce D. J., Coffey A. S., Smith D. A., Birkemeyer J., and Knopf U. (2007) Advance measurements of gusts by laser anemometry. *J. Wind Eng. Ind. Aerodyn.* **95**:1637–1647
- Harris M., Locker I., Douglas N., Girault R., Abiven C., and Brady O. (2010) Validated adjustment of remote sensing bias in complex terrain using CFD. *European Wind Energy Conf.*, Warsaw
- Jelalian A. V. (1992) Laser radar systems, Artech House, Boston
- Karlsson C. J., Olsson F. A., Letalick D., and Harris M. (2000) All-fiber multifunction CW 1.55 micron coherent laser radar for range, speed, vibration and wind measurements. *Appl. Opt.* **39**:3716–3726
- Kindler D., Oldroyd A., MacAskill A., and Finch D. (2006) An 8 month test campaign of the QinetiQ ZephIR system: preliminary results. *ISARS 13th Conf. Wiss. Ber. FZKA 7222*: 165–167 Garmish-Partenkirchen
- Kristensen L. (1999) The perennial cup anemometer. *Wind Energy* **2**:59–75
- Lading L., Hanson S., and Skov Jensen A. (1984) Diffraction-limited lidars: the impact of refractive turbulence. *Appl. Opt.* **23**:2492–2497
- Loudon R. (2000) The quantum theory of light, Oxford University Press, 3rd edition
- Mikkelsen T., Mann J., Courtney M., and Sjöholm M. (2008) Windscanner: 3-D wind and turbulence measurements from three steerable doppler lidars. *IOP Conf. Series: Earth and Environ. Sci.* **1**:012018 (9 pp)
- Mikkelsen T., Hansen K., Angelou N., Sjöholm M., Harris M., Hadley P., Scullion R., Ellis G., and Vives G. (2010) Lidar wind speed measurements from a rotating spinner. *European Wind Energy Conf.*, Warsaw
- Pearson G. N., Roberts P. J., Eacock J. R., and Harris M (2002) Analysis of the performance of a coherent pulsed fiber lidar for aerosol backscatter applications. *Appl. Opt.* **41**:6442–6450
- Peña A., Hasager C. B., Gryning S.-E., Courtney M., Antoniou I., Mikkelsen T. (2009) Offshore wind profiling using light detection and ranging measurements. *Wind Energy* **12**:105–124



- Smith D. A., Harris M., Coffey A. S., Mikkelsen T., Jørgensen H. E., and Mann J. (2006) Wind lidar evaluation at the Danish wind test site in Høvsøre. *Wind Energy* **9**:87–93
- Sonnenschein C. M. and Horrigan F. A. (1971) Signal-to-noise relationships for coaxial systems that heterodyne backscatter from the atmosphere. *Appl. Opt.* **10**:1600–1604
- Siegman A. E. (1986) *Lasers*, University Science Books, Mill Valley
- Vaughan J. M. and Forrester P. A. (1989) Laser Doppler velocimetry applied to the measurement of local and global wind. *Wind Eng.* **13**:1–15
- Wagner R., Mikkelsen T., and Courtney M. (2009) Investigation of turbulence measurements with a continuous-wave conically scanning lidar. Risø-R-1682(EN), Roskilde
- Wagner R., Jørgensen H. E., Paulsen U. S., Larsen T. J., Antoniou I., and Thesbjerg L. (2008) Remote sensing used for power curves. *IOP Conf. Series: Earth and Environ. Sci.* **1**:012059
- Wiggins J. (2009) Unpublished internal report. Natural Power
- Zak J. A. (2003) Atmospheric boundary layer sensors for application in a wake vortex advisory system. NASA/CR-2003-212175

# 4 Pulsed lidars

**Jean-Pierre Cariou**  
*Leosphere, Orsay, FR*

---

This section complements the description of the measurement process for a Doppler lidar for wind speed and direction determination, by focusing more on the pulsed lidar technology, and particularly on the WINDCUBE<sup>TM</sup> Doppler pulsed lidar, one of the most accurate remote sensing devices available at the present time in the wind industry.

## 4.1 Introduction

There is a pressing need for good wind-speed measurements at greater heights and at more site locations to assess the availability of the resource in terms of power production and to identify any frequently occurring atmospheric structural characteristics that may impact the operational reliability and lifetime of wind turbines and their components. To measure the wind field up to the height of new generation wind turbines and at any location of interest, remote sensors are needed to complement masts.

Different technologies are in use in this field, among them pulsed lidars (Light Detection And Ranging). The underlying principle of pulsed lidar measurement of wind and aerosols is the use of optical heterodyne (coherent) detection, in which laser pulses are transmitted into the atmosphere and scattered off of naturally-occurring small dust particles (aerosols) entrained in the ambient flow field (Frehlich et al., 1994; Huffaker and Hardestry, 1996; Soreide et al., 1997; Frehlich et al., 1998). Even though the measurement principle is well known and similar to pulsed radars, pulsed lidars have only been used in wind energy site assessment only since 2008. Their recent introduction is mainly due to laser revolution coming from fiber telecommunication development in the late 1990s.

In this section, we describe the architecture of pulsed lidars, based on the WINDCUBE<sup>TM</sup> lidar developed by LEOSPHERE and ONERA, the French Aerospace Lab. We define the different modules of a pulsed lidar, their specific functions and the individual level of uncertainties they might bring to the lidar wind speed retrieval. We also show the differences between pulsed and continuous wave (CW) lidars, used as well for wind sensing. We eventually give the lidar equation in pulsed mode, giving the relationship between parameters, and we focus on range and speed accuracy and resolution.



Figure 27: Leosphere Windcube7, first version (left) and V2 (right).

## 4.2 End-to-end description of pulsed lidar measurement process

### Architecture of pulsed lidars

Figure 28 illustrates the general set up of a pulsed lidar. The following paragraphs provide more details of the key hardware components and explain the requirements and trade-offs on solutions for the main parts of the lidar

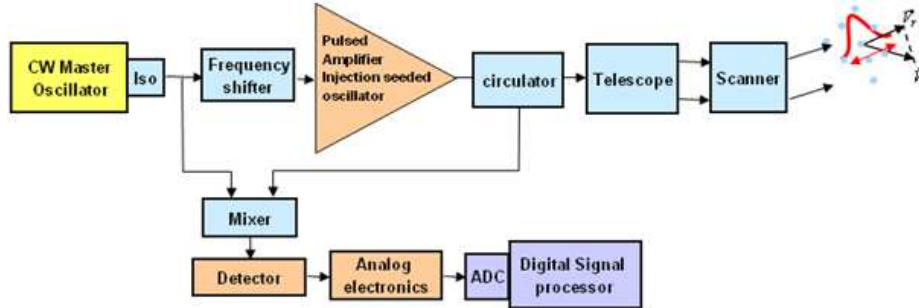


Figure 28: Pulsed lidar set up.

**Laser source** A pulsed lidar needs a continuous wave laser, called master oscillator (MO) to generate the local oscillator (LO) beam and a pulsed laser to generate the powerful transmitted pulse. The frequency offset between the two sources need to be stable with time to allow an unbiased measurement of the Doppler shift.

The master oscillator provides the laser wavelength, the laser linewidth, the laser intensity noise and the state of polarization. Each of these parameters has to be well known and stable to guarantee the lidar performance. The required CW power is at least some milliwatts.

The pulsed laser delivers cyclic pulses of high energy. The pulse duration is some hundreds of nanoseconds, that determines the length of the pulse in the atmosphere and so the spatial resolution.

Table 7: Spatial resolution versus pulse duration

Pulse duration [ns]	Pulse length [m]	Minimum spatial resolution [m]
200	60	30
400	120	60
800	240	120

The pulse repetition frequency (PRF) is as high as possible, but cannot exceed a maximum value  $\text{PRF}_{\max}$ . To avoid ambiguity between return signals, the time between pulses ( $1/\text{PRF}$ ) must be longer than the round trip time of flight of the pulse to the greatest height to be measured  $Z_{\max}$ ,  $\text{PRF}_{\max} = c/(2Z_{\max})$ , where  $c$  is the speed of light.

Two technologies are used for the pulsed laser. In the first one, called MOPA (master oscillator power amplifier), pulses are emitted from the MO by use of an optical pulse modulator. Resulting low power pulses are amplified into a single pass high bandwidth optical amplifier to generate high power pulses, having the same duration, frequency and polarization state as the incoming pulses. In the second scheme, the MO is used as a seeder in a Q-Switched pulsed laser. Cavity frequencies have to be matched to allow the seed frequency to be amplified. Pulse duration and PRF depend on the cavity parameters. First solution allows higher PRF but lower energy/pulse than the second one. Both deliver an equivalent average power.

Table 8: PRF<sub>max</sub> versus lidar range

PRF [KHz]	Maximum range [m]
10	15000
20	7500
50	3000

Laser wavelength is an important parameter. Following the recent improvement of solid state lasers in late 90s, the near Infrared spectrum (1.4–2.2 μm) is widely used for operational wind lidars. Efficient technology, good Doppler sensitivity, fiber architecture, eye safety and good atmospheric transmission are the main reasons (Cariou et al., 2006).

**Circulator** Figure 29 describes the circulator and the different elements which compose it. The function of the circulator is to transmit the laser pulse from the laser (1) to the telescope (2) and to direct the backscattered light from the telescope (2) to the receiver (3). Power handling, transmission efficiency and isolation between (1) and (3) ports are critical parameters. In coherent pulsed lidars, most circulators use polarization to perform this function. Polarization is rotated in the telescope thanks to a quarter wave plate. The transmitted polarization is circular.

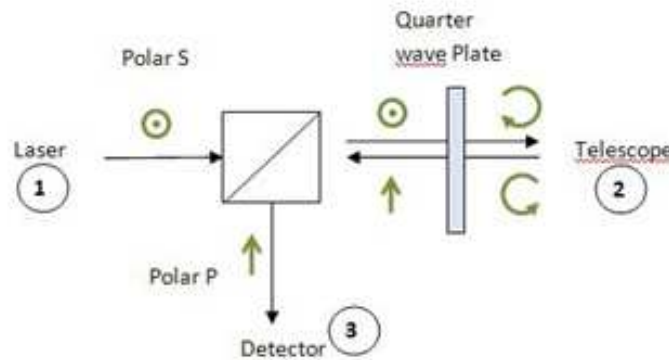


Figure 29: Circulator.

**Telescope** The telescope magnifies the laser beam in order to reduce its divergence in the far field, and focuses the beam at any distance. The larger the beam, the smaller the divergence and the better the signal-to-noise ratio (SNR) at long range. Since the lidar SNR is inversely proportional to the beam area, beam diameter must be minimized over the global measurement range to ensure maximum efficiency.

The telescope can use reflective or refractive optics, perfectly corrected from geometrical aberrations. In order to lose less than 3 dB on the detection efficiency, wavefront distortion on the global roundtrip optical path has to be less than λ/4 RMS, including components and atmospheric distortion.

Atmospheric turbulence as well creates wave distortion that degrades heterodyne efficiency. To keep this distortion negligible, the telescope aperture has to be smaller than the coherence diameter of the beam expressed by:

$$d_o = 2.4e10^{-8} \lambda^{6/5} Z^{-3/5} C_n^{-6/5}. \quad (79)$$

Considering maximum values of index structure constant ( $C_n^2 = 10^{-13} \text{ m}^{-2/3}$ ) and propagation over about  $Z = 1 \text{ km}$ , this limits the size of the telescope to about 10 cm at

ground level.

**Scanner** Coherent lidar measure the radial component of the wind, i.e. the projection of the wind vector on the line of sight (LOS). To provide two or three components of the vector, the beam has to be directed in two or three independent different directions (more details in Section 2.6). The scanner can move the entire telescope, for example Mitsubishi (Ando et al., 2008), or only the beam. Some manufacturers prefer skipping the scanner and duplicate the telescope to suppress all moving parts from the lidar (for example Catch The Wind or Leosphere WindcubeV2).

To perform the vertical wind profile, beams are directed upwards along a cone around the zenithal direction. For that, a single rotating prism or dual flat mirrors are used (see Figure 30).

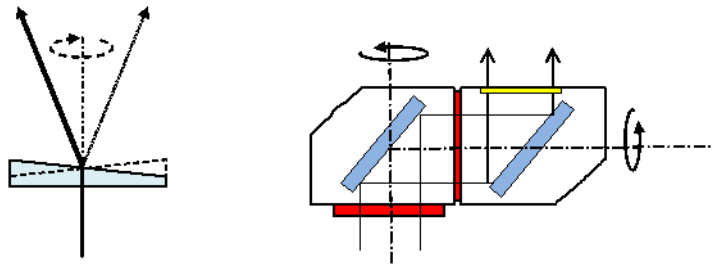


Figure 30: Prism scanner and dual flat mirror scanner.

To measure the wind speed in any direction, and display 2D or 3D wind maps, a more flexible scanner is needed. Double flat mirror scanners are mostly used (CTI, Halophotonics, Leosphere), while double prism scanners, like those in Risø DTUs Windscanners (Mikkelsen, 2008), offer a more original and compact solution. A global hemispherical field of view can be obtained with both solutions.

### Differences between pulsed vs. continuous wave lidars

In CW lidars, light is continuously transmitted to the atmosphere. Assuming atmospheric parameters do not vary, the backscattered signal average power is constant, coming from all distances at the same time. The distance weighting function is defined by the beam aperture and the focus distance (see chapter on CW lidars from Mike Harris). Spectral bandwidth is limited by atmospheric turbulence if laser line width is narrow. The size of the range gate (contributing to the signal) increases as the square of the distance. The range gate can be small and well defined at short distance but is always too large when the range exceeds few hundreds of meters. Table 9 summarizes the main differences between CW and pulsed lidars:

In pulsed lidars, short pulses are transmitted to the atmosphere, illuminating at each instant only a limited part of the line of sight. Therefore, backscattered signal arriving onto the detector at a time only comes from a given range of distance. The time delay between the pulse start and the measurement time informs on the distance of the analyzed zone. The range gate length is always the same, at short and long range.

Pulsed LIDARs, as their name implies, emit regularly spaced emissions of highly collimated light energy for a specified period of time (pulse length). Precision timing circuits then isolate the returned signals to a period of time that corresponds to a specified segment of radial distance along the beam called a range gate. The backscattered signals contained within each gate are then processed to derive the radial velocities along the path of the LIDAR beam.

Table 9: Main differences between CW and pulsed lidars

	CW lidar	Pulsed lidar
Velocity accuracy	limited by coherence time of the atmosphere	limited by the pulse duration
Range gate	determined by focus, increases as $R^2$	constant, around $c\tau/2$
Number of range gates	less than 10, sequentially addressed	more than 100, simultaneously addressed
Sensitivity to targets out of focus	high	no
Maximum range	few hundreds of meters	some kilometers
Laser source	1000 mW laser	10 mW MO + 200 mW power amplifier
Linear polarization	not necessary	mandatory

### Signal processing

After the pulse has left by the laser, the detector starts to collect the backscattered signal from the successive range gates. It first crosses the telescope optics and provides a zero Doppler signal, used as a marker for the zero distance. Even if the stray light is small thanks to optimized coatings ( $10^{-6}$  order), this signal is always larger than the light backscattered by the atmosphere ( $10^{-12}$  order).

Each layer of atmosphere then backscatters light to the lidar. The power is proportional to the backscattering atmospheric coefficient  $\beta$  while the frequency shift is proportional to the radial velocity. For each pulse, the collected signal contains the total wind speed information on the LOS.

However, both the signal and the noise fluctuate from pulse to pulse and it is necessary to average signals to get a good estimation of the spectral content. Because of the short wavelength ( $10^4$  less than radars and sodars), signal phase changes quickly with particle motion, atmospheric turbulence and small laser spectral drifts. This is useless to average time series. To improve SNR on the Doppler spectrum, successive spectra corresponding to the same range gate are summed. SNR increases as the square root of the number of average pulses  $N$ . This computation is performed for all range gates.

To sum up, the successive steps for the signal processing are for every LOS (Figure 31):

- Break the time series into gates
- Compute the spectrum for each gate
- Average spectra for same range gate from different pulses
- Find frequency peak for each gate to find Doppler shift and convert to radial velocity
- Reconstruct wind vector for each gate with radial velocity on the different LOS.

### Coherent detection

Basic principles of coherent detection are the same than for CW lidars (see chapter on CW lidars from Mike Harris). The return signal mixes with local-oscillator creating the beat signal. The electronic signal on the detector contains the same amplitude, frequency and phase information as the optical signal, but is frequency downshifted to allow detection with conventional high speed detectors. So the Doppler shift, which is small in comparison to the optical frequency  $\nu$  can be measured in base band. To allow both negative and

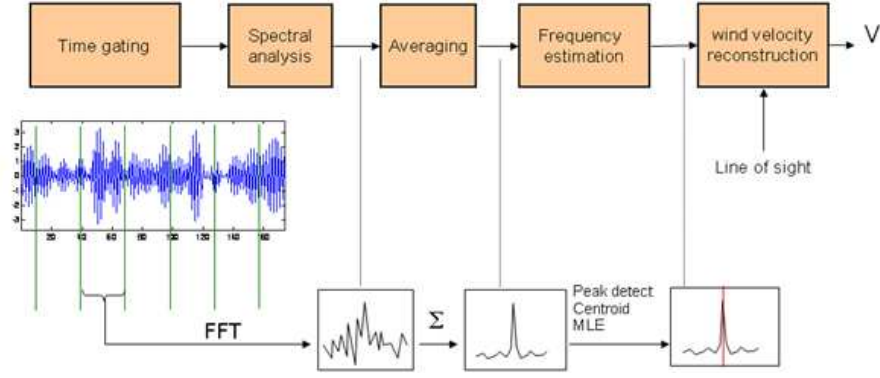


Figure 31: Radial wind velocity retrieval process.

positive shifts to be measured, an offset frequency  $F_i$  (intermediate frequency) is added on one arm of the interferometer.

$$F_{dop} = (\nu + F_i)_{LO} - (\nu + F_{dop})_{signal} = F_i + F_{dop}. \quad (80)$$

An important advantage of coherent detection is that it can be limited by signal photon noise, if some conditions are fulfilled. First condition is that the amplitude and phase match between signal beam and the LO beam must be perfect. The second condition is that temporal coherence is optimum, i.e the spectral width of the main oscillator must be narrower than the spectral width of the electronic signal. The third condition is that polarization state must be the same on the LO and the signal. System and component limitations lead however to a loss in heterodyne efficiency. Frehlich and Kavaya (1991) demonstrated that the heterodyne efficiency is limited to 40% by spatial coherence for a perfect Doppler lidar using a circular aperture and a Gaussian beam. A good actual operational lidar heterodyne efficiency is more than 20%.

### Lidar equation

The lidar equation gives the expected signal power returning from the atmosphere within the range gate to be analyzed. The signal power can then be compared to the noise power in order to determine the range of the lidar. The total optical power  $P_r(z)$  reflected back in the receiver telescope from the range gate at  $Z$  is:

$$P_r(Z) = P_{peak} T_{inst} T_{atm} \beta_\pi(Z) \frac{c\tau}{2} \Omega, \quad (81)$$

where  $P_{peak}$  is the transmitted pulse peak power,  $T_{inst}$  is the instrumental round trip transmission and  $T_{atm}$  is the atmospheric round trip transmission, expressed as:

$$T_{atm} = \exp\left(-2 \int_0^Z \alpha(x) dx\right). \quad (82)$$

$T_{atm} = \exp(-2\alpha Z)$  if the atmosphere is homogeneous and  $\beta_{pi}(Z)$  is the backscattering coefficient of the atmosphere at a distance  $Z$ ,  $\tau$  is the full-width-half-maximum (FWHM) pulsed duration and  $\Omega$  is the reception solid angle:

$$\Omega = \frac{\pi\sigma^2}{Z^2}, \quad (83)$$

where  $\sigma$  is the efficient telescope aperture radius and  $\alpha$  and  $\beta_\pi$  are roughly proportional since they both depend on aerosol concentration in the atmosphere.

However, because of the limited heterodyne efficiency, only a part of  $P_r(Z)$  is efficient for the coherent detection. The lost part of  $P_r(Z)$  comes from phase and polarization mismatches. An interesting way to estimate the detection antenna diagram is to propagate back in the atmosphere the LO, and to compute the overlap integral of the signal and LO

along the LOS. This defines the transverse and longitudinal efficiency of the lidar (BPLO theory (Siegman, 1966)). The efficient signal power incoming onto the detector is:

$$P_s(Z) = P_{peak} T_{inst} T_{atm} \beta_\pi(Z) \frac{c\tau}{2} \lambda I(Z), \quad (84)$$

where  $I(Z)$  is a Lorentzian function including  $\Omega$  and  $Z$  depending focus function:

$$I(Z) = \frac{\Delta Z}{(Z - Z_o)^2 + \Delta Z^2}, \quad (85)$$

with  $Z_o = F_t / (1 + (F_t/Z_r)^2)$ ,  $Z_r = \pi\sigma^2/\lambda$ ,  $\Delta Z = Z_o F_t / Z_r$  being  $Z_o$  the distance where  $I(Z)$  is maximum, i.e. maximum SNR,  $Z_r$  the Rayleigh distance,  $F_t$  the instrumental geometrical focus distance (wave curvature radius at telescope) and  $\Delta Z$  half of FWHM geometric depth of focus.

Figure 32 shows different plots of the Lorentzian function  $I(Z)$  for different values of the focus distance  $F_t$ . Short focus improves signal power at short range whereas long focus averages the power along the distance, leading to a more constant signal on the different range gates, but with a lower value.

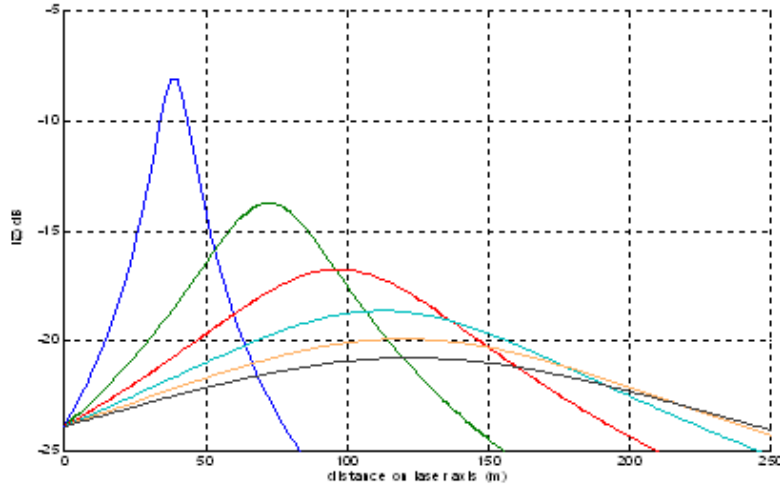


Figure 32: Variations of  $I(Z)$  with focus distance  $F_t = 40, 80, 120, 160, 200, 240$  m respectively.

The current power on the detector can then be derived using the same equations as in CW mode,

$$\langle i_{het}^2 \rangle = 2\eta_{het} S^2 P_{LO} P_s(Z), \quad (86)$$

where  $P_{LO}$  is the local oscillator power,  $\eta_{het}$  the heterodyne efficiency, which depends on phase, amplitude and polarization matching and  $S$  the detector sensitivity.

$$\eta_{het} = \frac{[\int \int_{Ad} E_s(x, y) E_{LO}^*(x, y) dx dy]^2}{\int \int_{Ad} E_s^2(x, y) dx dy \int \int_{Ad} E_{LO}^2(x, y) dx dy}, \quad (87)$$

$$\langle i_{het}^2 \rangle = \eta_{het} T_{inst} T_{atm} S^2 \beta_\pi(Z) P_{LO} P_{peak} \tau c I(Z). \quad (88)$$

The lidar equation shows that the signal power is proportional to pulse energy  $P_{peak}\tau$  and proportional to LO power. LO amplifies the signal allowing it to be detected over the detector noise.

### Spectral processing MLE

A maximum likelihood estimator (MLE) based on the likelihood of the Fourier transform of the signal is used as spectral processing. This estimator assumes an uncorrelated Fourier



transform in order to use data obtained from the accumulated spectrum. The estimator is slightly different from the likelihood of the spectrum traditionally used for spectral maximum likelihood estimators but still shows the same efficiency.

Signal spectrum is calculated using a temporal model such as the Feuilleté model (Cariou et al., 2006) and thus takes into account all the FFT algorithm disturbing effects such as the spectral leakage, which must be carefully characterized in the case of a pulsed atmospheric lidar.

### Wind vector reconstruction

Pulsed lidars provide radial wind components on different lines of sight at different altitudes. In an ideal case, and to mimic local sensors such as cup or sonic anemometers, beams intersect at the point of interest within a small volume. This is the goal of the Windscanner project with three lidars. In an operational situation, only one lidar is available. To reconstruct the 3D components of the wind vector, some assumptions are then necessary.

- Horizontal homogeneity: the three components of the wind are the same for the different points of the disc at a given altitude. The numerous measurement campaigns have proven that this assumption is valid on flat terrains and offshore, but not perfect on complex terrains (hills, mountains, forest borders)
- Temporal variations are slower than the inter-beam distance divided by the horizontal wind speed. This time increases with altitude and matches the conical geometry.
- Wind slowly varies within a range gate. Wind dispersion lowers the SNR and provides a bias if the shear is non linear.

The scanning configuration can be either velocity azimuth display (VAD) or Doppler beam swinging (DBS). VAD uses information from a continuous scan in a part or total cone angle and is mostly used in CW lidars. DBS is used in pulsed lidars to average more information on the LOS. Since VAD is described in the “Remote Sensing QinetiQ Lidar Measurement Report”, we focus here on DBS reconstruction.

First is important to define an orthogonal frame. The orthogonal frame of the WIND-CUBE is described in Figure 33:

Suppose the lidar probes the atmosphere with three beams in the three directions North, East, and Zenith. Then the three measured LOS velocities  $Vr_i$  are described as following ( $\theta$  being the angle between Zenith and North and East, the so-called cone-angle):

$$Vr_N = u \sin \theta + w \cos \theta, \quad (89)$$

$$Vr_E = v \sin \theta + w \cos \theta, \quad (90)$$

$$Vr_Z = w. \quad (91)$$

So the  $u$ ,  $v$  and  $w$  wind speed components can be retrieved as,

$$u = \frac{Vr_N - Vr_Z \cos \theta}{\sin \theta} \quad (92)$$

$$v = \frac{Vr_E - Vr_Z \cos \theta}{\sin \theta} \quad (93)$$

$$w = Vr_Z. \quad (94)$$

Supposing the lidar probes the atmosphere at four different locations, the LOS being East, West, North, South, the system of wind equations will be,

$$u = \frac{Vr_N - Vr_S}{2 \sin \theta} \quad (95)$$

$$v = \frac{Vr_E - Vr_W}{2 \sin \theta} \quad (96)$$

$$w = \frac{Vr_N + Vr_S + Vr_E + Vr_W}{4 \cos \theta}. \quad (97)$$

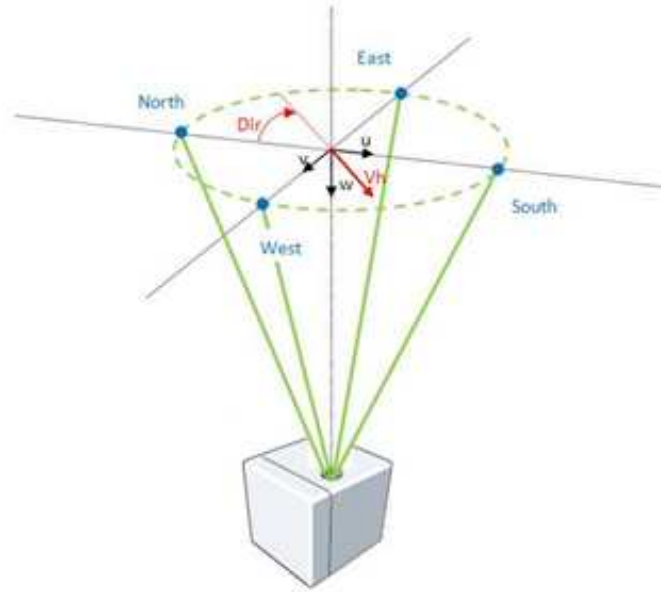


Figure 33: Orthogonal frame of the WINDCUBE for retrieving the wind speed components

Horizontal wind speed  $V_h$  and wind direction  $Dir$  are then retrieved as following:

$$V_h = \sqrt{u^2 + v^2} \quad (98)$$

$$Dir = \text{mod}(360 + \text{atan2}(v, u), 360). \quad (99)$$

If the North beam of the lidar is offset from the geographical North with an angle  $\alpha$ , the wind direction is:

$$Dir = \text{mod}(360 + \alpha + \text{atan2}(v, u), 360). \quad (100)$$

With three beams, the solution is unique. The vertical component  $w$  is perfectly determined if the one of the three axis is accurately vertical. No check of assumptions mentioned above is possible. With four beams, the additional equation allows wind homogeneity to be checked and skip undesired values.

Cone-angle  $\theta$  is a trade-off between lidar velocity resolution and atmosphere homogeneity. The smaller is  $\theta$ , the better is the wind homogeneity but worse is the projection of the wind vector on every beam. Boquet et al. (2010a) demonstrated that best  $\theta$  values are between  $15^\circ$  and  $30^\circ$ . Even in complex terrains, in general wind non homogeneity condition, no better estimation is obtained when reducing the cone angle (Boquet et al., 2009).

### Fiber lidars

Before early 2000s, LIDAR systems were based on solid-state laser technologies that do not meet operational requirements for remote site wind assessment due to high power consumption, size, weight, reliability, and life cycle cost. It was therefore the purpose of Leosphere, thanks to a partnership with French Aerospace Lab ONERA to introduce a unique fiber laser technology geared for the wind industry requirements, enabling efficient realization of compact wind Doppler lidar systems.

Fiber lidars use fiber amplifiers and coherent detection and fiber architecture based on mainstream telecommunication components. Fiber amplifiers use codoped Erbium Ytterbium silica fibers to amplify with a large bandwidth low power pulses cut out of a CW laser at  $1.5 \mu\text{m}$  (MOPA configuration). The electrical to optical efficiency of  $1.5 \mu\text{m}$  fiber laser sources is of the order of 10%, thus allowing low electrical consumption.

This wavelength is also the most favorable for eye-safe lidar designs: the eye-safety laser energy limitation being high, the laser power can be increased with little constraints on the lidar operation or design. One advantage of the IR fiber technology is its reliability. It is now well established that a fiber architecture is easy to adjust and mechanically reliable in a vibrating environment. The other advantages of fiber architectures are their compactness and flexibility in terms of installation. The lidar can be split up into sub-systems spatially far apart and linked together using fiber optics. The new technologies of large-mode-area (LMA) fibers enable high peak power generation without nonlinear effects, while maintaining a good spatial mode and polarization state. The average power exceeds several watts and high PRF compensates efficiently the relative low pulse energy. Moreover, the MOPA architecture flexibility in terms of pulse duration allows fulfilling a large panel of requirements, either with high spatial resolution or long range.

### 4.3 Lidar performances

#### Noise

In coherent detection, noise sources come principally from 3 origins:

$$\langle i_{SN}^2 \rangle = 2eS P_{LO}B \quad \text{LO shot noise} \quad (101)$$

$$\langle i_{NEP}^2 \rangle = 2eS NEP B \quad \text{Detector noise} \quad (102)$$

$$\langle i_{RIN}^2 \rangle = (S P_{LO})^2 10^{RIN/10} B \quad \text{RIN noise,} \quad (103)$$

where  $NEP$  is the noise equivalent power density,  $B$  is the detection bandwidth and,

$$\langle i_n^2 \rangle = \langle i_{SN}^2 \rangle + \langle i_{NEP}^2 \rangle + \langle i_{RIN}^2 \rangle. \quad (104)$$

For optimum detection, LO shot noise must be the main noise contributor. When other sources are negligible, CNR (Carrier to Noise Ratio), describing the signal to noise ratio on the carrier frequency is,

$$\text{CNR} = \frac{\langle i_{het}^2 \rangle}{\langle i_n^2 \rangle} = \eta_{het} T_{inst} T_{atm} \frac{S}{2eB} \beta_{\pi}(Z) P_{peak} \tau_c I(Z). \quad (105)$$

#### Best Focus

Focus distance can be adjusted in order to optimize CNR over the measurement range. Figure 34 shows the simulated CNR variation versus focus distance, expressed as the wave radius of curvature at the instrument exit (beam radius being 11 mm@1/e<sup>2</sup> at the lens).

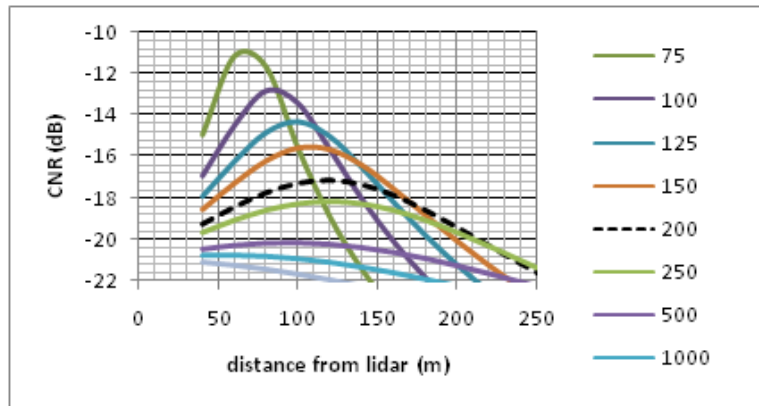


Figure 34: Variation of CNR vs distance (Altitude/cos( $\theta$ -dev)) for different beam radius of curvature

Best focus corresponds to maximizing the data availability at all altitudes, from  $H = 40$  m ( $Z = 46$  m) to  $H = 200$  m ( $Z = 230$  m). Practically, it corresponds to balancing and maximizing the CNR for  $H = 40$  m and  $H = 200$  m. For the Windcube WLS7,  $F_{opt}=120$  m ( $H_{opt}=104$  m), corresponding to a beam curvature of 200 m at lens (black dot line).

For a beam radius of curvature of 200 m, the beam diameter slowly varies along the propagation in the range of interest. Beam radius ( $1/e^2$ ) is  $\sigma = 11$  mm at lens, 9 mm at 46 m, 7 mm at 120 m and 10 mm at 230 m, giving a maximum of 2 dB difference along the total range. (CNR is proportional to  $1/\sigma^2$ ).

Maximum focus distance corresponds to half of the Rayleigh distance  $Z_r$ :

$$Z_{max} = \frac{Z_r}{2} = \frac{\pi\sigma^2}{2\lambda}, \quad (106)$$

where  $Z_{max} = 123$  m for the WINDCUBE7 v2 parameters. This configuration minimizes the beam diameter variation from  $Z = 0$  to  $Z = Z_r$ .

Lindelöw (2007) demonstrated a velocity error coming from the unbalanced velocity weighting function due to a variation of CNR within the range gate. In the case of the WINDCUBE7 v2, the difference of CNR is always less than 0.5 dB/range gate, leading to a maximum bias in the velocity of around  $0.06 \text{ m s}^{-1}$  under a vertical linear wind shear of  $0.02 \text{ m s}^{-1}/\text{m}$ .

### Distance range and resolution

Because of the footprint of the laser pulse on the line of sight, range resolution is limited. Moreover, during the measurement time  $\tau_m$ , the pulse has moved further, enlarging the range resolution. Figure 35 describes the pulse space and time propagation and the portion of atmosphere illuminated during a time window analysis of length  $\tau_m$ .

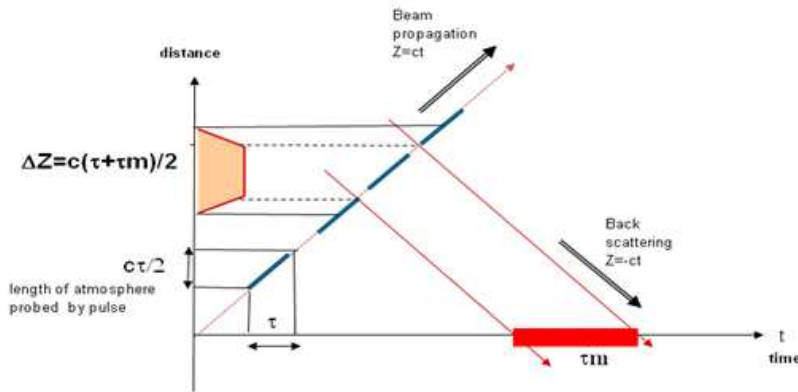


Figure 35: Pulse propagation and width of range gate represented on a time-distance plot

Velocity measurement at one point  $V_d(Z)$  depends on the velocity  $V_r(R)$  at close points and on the range weighting function  $RWF(R)$ ,

$$V_d(Z) = \int_{-\infty}^{\infty} RWF(R)V_r(R)dR. \quad (107)$$

For a pulsed lidar, Banakh and Smalikho (1994) gave an analytical equation for RWF, when the pulse is Gaussian (FWHM =  $\tau$ ) and range gate is flat (width  $\tau_m$ ), as the convolution between the pulse power profile and the range gate profile:

$$RWF(Z) = \frac{1}{\tau_m c} \left[ \text{erf} \left( \frac{4\sqrt{\ln 2}}{c\tau} (Z - Z_o) + \frac{\sqrt{\ln 2}}{\tau} \right) - \text{erf} \left( \frac{4\sqrt{\ln 2}}{c\tau} (Z - Z_o) - \frac{\sqrt{\ln 2}}{\tau} \right) \right]. \quad (108)$$

Range resolution is defined as the FWHM of the function  $RWF$  which is roughly:

$$\Delta z_1 = \frac{c\tau_m}{2\text{erf} \left( \sqrt{\ln 2}\tau_m/\tau \right)}. \quad (109)$$

Eq. (109) is adapted for collimated system but does not give accurate results for focused lidars, i.e. focusing the laser beam leads to better resolution near the focusing point. Moreover, this method is only valid for a Gaussian pulse and a flat measurement window.

In order to make this calculation more general, Lindelöw (2007) proposed multiplying the focusing efficiency by the convolution of the pulse and the range gate profile:

$$RWF(Z) = \eta_{foc}(Z) (Pulse FFT_{window})(Z), \quad (110)$$

where  $\eta_{foc}(Z)$  is the focusing efficiency,

$$\eta_{foc}(Z) = \left( 1 + Z_r^2 \left[ \frac{1}{Z} - \frac{1}{Z_{foc}} \right] \right)^{-1}. \quad (111)$$

These methods can be applied to the current WINDCUBE7 v2 pulse shape and range gate profile. The “impulse response” FWHM is calculated to be 27 m. The altitude resolution is therefore around 23.8 m (LOS zenithal deviation angle is 28°). Lindelöw’s RWF is 26.3 m, i.e.  $\sim 23.2$  m altitude resolution.

### Velocity range and resolution

**Velocity range ambiguity** Radial velocity is proportional to Doppler frequency shift. Velocity range is then determined by frequency range. The intermediate frequency  $F_i$  used in most pulsed lidars allows the measurement of both positive and negative shifts. Maximum downshift is limited by the value of  $F_i$ , since no negative frequency can be measured. Maximum upshift is limited by the Nyquist frequency, half of the sampling frequency  $F_s$ . Figure 36 describes the spectrum and velocity ranges.

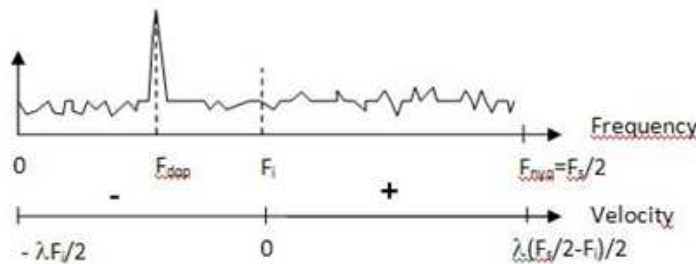


Figure 36: Lidar spectrum and velocity range

Because of spectral extent of the signal and low frequency noise, this range is in fact a bit smaller. For example, with  $\lambda = 1.55 \mu\text{m}$ ,  $F_i = 68 \text{ MHz}$  and  $F_s = 250 \text{ MHz}$ , the practical horizontal velocity range is  $[-50 \text{ m s}^{-1}, +50 \text{ m s}^{-1}]$ . A passband filter cancels outband Doppler shifts to avoid Doppler ambiguities.

**Velocity resolution** Velocity precision depends on both atmospheric parameters and lidar parameters. Both are broadening the Doppler spectrum and hence limit the frequency estimation. Atmospheric parameters are wind gradient within the range gate and turbulence. Lidar parameters are pulse duration CNR and number  $N$  of average spectra. The smaller the pulse duration, the smaller the range gate and the velocity dispersion but larger the frequency spectrum.

Eq. (112) gives the minimum velocity resolution as a function of relative parameters. It is called Cramer Rao lower bound (CRLB),

$$\sigma v_{crlb} = \frac{\sqrt{2}\lambda}{2\tau} \frac{\sqrt{1 + \text{CNR}}}{\sqrt{N\text{CNR}}}. \quad (112)$$

Eq. (112) assumes an infinite correlation time of the signal. In an actual lidar,  $\sigma v$  is limited by the finite correlation time  $\tau_c$ , the smallest value between the pulse duration

and the correlation time of the atmosphere,

$$\sigma v_{sat} = \frac{\lambda}{2\sqrt{N}4\pi\tau_c}. \quad (113)$$

The global velocity resolution is then:

$$\sigma v = \sqrt{\sigma v_{crlb}^2 + \sigma v_{sat}^2}. \quad (114)$$

Figure 37 illustrates the variation of  $\sigma v$  with CNR for  $N = 100$  and  $N = 10000$ .

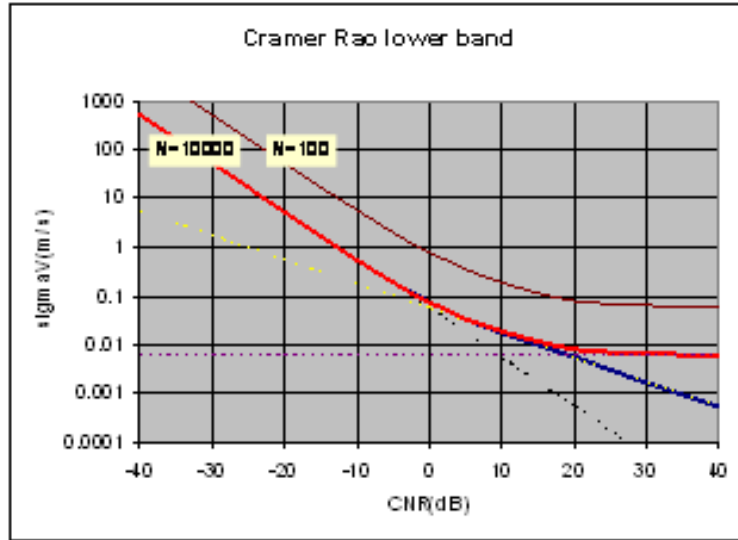


Figure 37: Cramer Rao boundary for 100 averaged spectra (dark red) and 10000 averaged spectra (light red). CNR is measured in narrow band ( $B = 1/\tau_m$ )

For low CNR values,  $\sigma v$  decreases as  $1/\text{CNR}$ . Doubling the pulse energy divides by 2 the velocity resolution. For high CNR values,  $\sigma v$  is constant. Spectral broadening comes from speckle fluctuations in the signal. The only way to reduce  $\sigma v$  is to increase  $N$ . For intermediate CNR,  $\sigma v$  varies as  $1/\sqrt{\text{CNR}}$ . It is therefore equivalent to increase pulse energy or number of pulses. In this region,  $\sigma v$  depends only on the average laser power. Using a low energy, high pulse repetition rate (PRF) laser is then equivalent to using a high energy, low PRF laser, assuming the average power is constant. This is one for the reasons of the recent raise of high PRF fiber lasers for pulsed Doppler lidars.

**Range ambiguity** The rate at which pulses are transmitted, the PRF limits the range over which heights can be unambiguously determined. To avoid ambiguity between return signals, the inter pulse period (IPP=1/PRF) must be longer than the round trip time of flight of the pulse to the greatest height. For example, to measure without ambiguity up to 5 km, the PRF needs to be less than 30 KHz,

$$\text{PRF}_{\max} = \frac{c}{2Z_{\max}}. \quad (115)$$

### Time-bandwidth tradeoffs

Spatial resolution is proportional to pulse duration. The shorter the pulse, the smaller the resolution. Velocity resolution is proportional to spectrum width and is smaller when the spectrum is narrow. Because the spectrum width is inversely proportional to the pulse duration, range resolution and velocity resolution are also inversely proportional.

## Existing systems and actual performances

In 2010, only a few pulsed lidars are available. Table 10 summarizes the characteristics of commercial ones, which can be used in the wind industry, meteorology or airport safety.

Table 10: Comparison of commercially available pulsed lidars

System	Wave length [ $\mu\text{m}$ ]	Range/ accuracy [m]/[ $\text{m s}^{-1}$ ]	Data update	Sample volume length [m]	pulse duration/ energy [ns]/[ $\mu\text{J}$ ]	PRF [kHz]	Beam config.
Leosphere	1.5	40–200/0.1	1 s/10 alt	20	200/10	20	Four beams
WindCube7							
LMCT	2	500–5000/1	0.1 s	60	400/2000	500000	LOS
Windtracer							mapping
Mitsubishi	1.5	100–1500/NA	1 s	90	600/6.5	1	Scanning head
Halophotonics	1.5	30–2000/0.25	0.1–30 s	20–60	150/10	20	LOS
Gallion							mapping
CatchTheWind	1.5	NA/NA	NA	NA	NA/NA	NA	three
Vindicator							telescopes

## Validation of measurements

Since the instrumental sources of uncertainty are now well identified and the range of deviation they might incur in the wind speed measurement are well estimated, it is necessary to compare the measurement of a new lidar unit against a tall mast equipped with traditional anemometry or against a well-known and validated lidar in a double phase verification/validation.

Validation is the process of ensuring that a WINDCUBE measures wind speed characteristics in conformity with what a reference instrument would give. Today, validation is done against well-known traditional anemometry, like a mast equipped with calibrated cup anemometers. This instrument comparison introduces additional uncertainties, not related to the inner performances of each individual instrument but related to the differences in the measurement process between the two instruments. These differences in the measurement process might incur differences in measured values, which will be site and time specific. Even if these are small, it is important to closely define the range of variation that might occur on the validation site.

With more than 140 field deployments worldwide for the past 4 years, the Windcube has been extensively tested in different conditions and under a diversity of climates. Several authors have reported very good measurement accuracy with reference to calibrated cup anemometers in good operating conditions (Oldroyd et al., 2009; Faghani et al., 2009; Jaynes, 2009).

## 4.4 Conclusions and perspectives

This chapter summarizes the principles of operation, the performances and critical parameters of Doppler pulsed wind lidars, such as the WINDCUBE lidar from LEOSPHERE. It takes into account the different steps of the velocity measurement process. This detailed process analysis provides the backbone for a pulsed lidar development, optimization and issues related to serial production.

More generally, pulsed and CW lidars have shown great reliability and accuracy in

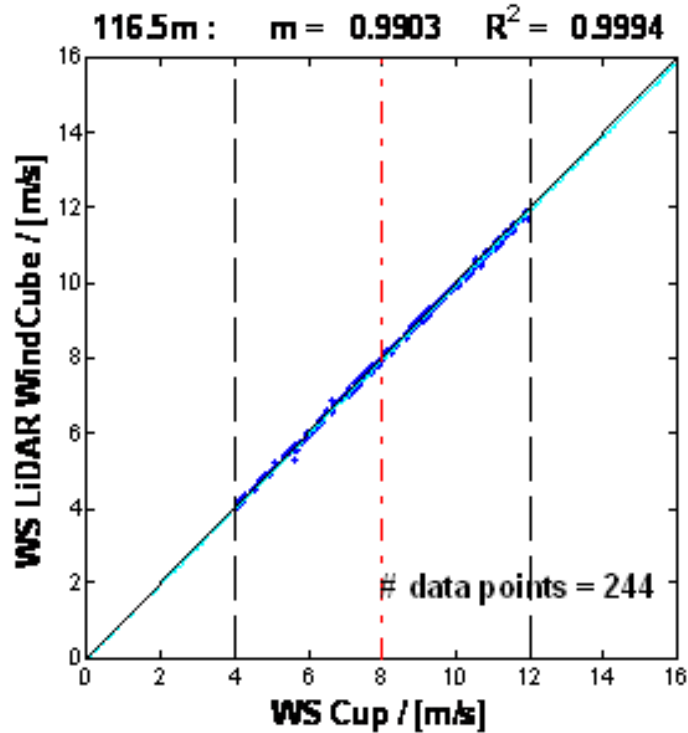


Figure 38: Comparison of Windcube 10-min averages with calibrated mast at Risø Høvsøre

the measurement of wind characteristics such as horizontal and vertical wind speed and wind direction at various heights on flat terrains and offshore (Courtney et al., 2009; Westerhellweg et al., 2010). The high data recovery rate up to above blade top ensures a high quality analysis of the wind conditions available on the project site, leading to an optimized layout design and the choice of the suitable turbines.

Regarding future improvements, the measurement of additional wind parameters like turbulence intensities, kinetic fluxes or inflow-angles is under investigation at the present time and should be available in the near future.

One of the remaining challenges is also reaching high accuracy in complex terrains where flow distortion occurs and impairs the lidar wind components retrieval from measured radial velocities. Since lidar radial velocities are still very accurate even on complex and rough terrains, a methodology using CFD modeling has been recently developed to avoid taking the flow homogeneity assumption (Boquet et al., 2009; Bingöl et al., 2009; Boquet et al., 2010a). Even though new, this methodology has already shown good results on sites of various complexities. The measurement of additional wind parameters like turbulence intensities, kinetic fluxes or inflow angles is under investigation at the present time and should be available in the near future.

To sum up, lidar anemometry has already proven its great utility in the development of wind farm projects, as an instrument allowing considerable financial gains through a better understanding of the wind conditions at a site and therefore reducing the capital risk of the investors (Boquet et al., 2010b), but also for operational power curves measurements (Gottshall et al., 2010; Albers et al., 2010). With the general trend to develop larger wind turbines and wider wind farms, the lidar technology is elected to be more and more widely used.



## Notation

$B$	detector bandwidth
$c$	speed of light
$C_n$	index structure constant
CNR	carrier-to-noise ratio
CRLB	Cramer Rao lower bound
CW	continuous wave
$d_o$	coherence diameter of the beam
DBS	Doppler beam swinging
$FFT$	fast Fourier transform
$F_i$	intermediate frequency
$F_s$	sampling frequency
$F_t$	instrumental geometrical focus distance (wave curvature radius at telescope)
FWHM	full width half maximum
$\langle i_{NEP}^2 \rangle$	detector noise
$\langle i_{RIN}^2 \rangle$	rin noise
$\langle i_{SN}^2 \rangle$	shot noise
$I(Z)$	Lorentzian function
IPP	inter pulse period
LMA	large mode area
LOS	line of sight
LO	local oscillator
MLE	maximum likelihood estimator
MO	master oscillator
MOPA	master oscillator power amplifier
$NEP$	noise equivalent power density
$P_{LO}$	local oscillator power
$P_{peak}$	transmitted pulse peak power
$P_r$	total optical power
PRF	pulse repetition frequency
$PRF_{max}$	maximum pulse repetition frequency
$N$	number of average pulses
$R$	focus distance
$RWF(Z)$	range weighting function
$S$	detector sensitivity
SNR	signal to noise ratio
$T_{atm}$	atmospheric round trip transmission
$T_{inst}$	instrumental round trip transmission
$u$	north-south wind speed component
$v$	east-west wind speed component
VAD	velocity azimuth display
$V_d(Z)$	velocity measurement at one point
$V_{r_i}$	LOS velocities, $i = N$ North, $i = E$ East, $i = S$ South, $i = W$ West and $i = Z$ Zenith
$w$	vertical wind speed component
$Z$	height
$Z_{max}$	maximum height to be measured
$Z_o$	distance where $I(Z)$ is maximum, i.e. signal to noise is maximum
$Z_r$	Rayleigh distance
$\beta$	backscattering atmospheric coefficient
$\Delta Z$	half of FWHM geometric depth of focus
$\eta_{foc}$	focusing efficiency
$\eta_{het}$	heterodyne efficiency
$\theta$	lidar cone angle
$\lambda$	laser wavelength
$\nu$	optical frequency
$\sigma$	efficient telescope aperture radius
$\sigma_v$	global velocity resolution
$\sigma_{v_{crlb}}$	Cramer Rao lower bound of velocity resolution
$\sigma_{v_{sat}}$	smallest value of the velocity resolution
$\tau$	pulse duration
$\tau_c$	finite correlation time
$\tau_m$	measurement time

## References

- Albers A., Janssen A. W. and Mander J. (2010) Hot to gain acceptance for lidar measurements. *DEWEK*
- Ando T., Kameyama S. and Hirano Y. (2008) All-fiber coherent Doppler lidar technologies at Mitsubishi Electric Corporation. *IOP Conf. Series: Earth and Environ. Science* **1**:012011
- Banakh V. and Smalikho I. (1994) Estimation of the turbulence energy dissipation rate from the pulsed Doppler lidar data. *J. Atmos. Oceanic Technol.* **10**
- Bingöl F., Mann J. and Foussekis D. (2009) Conically scanning lidar error in complex terrain. *Meteorol. Z.* **18**:1–7
- Boquet M., Parmentier R. and Cariou J. P. (2009) Analysis and optimization of pulsed Doppler lidar in complex terrain. *EWEC*, Marseille
- Boquet M., Parmentier R. and Cariou J. P. (2010) Correction of pulsed wind lidars bias in complex terrain. *ISARS*
- Boquet M., Callard P., Neve N. and Osler E. G. (2010) Return on investment of a lidar remote sensing device. *DEWI Magazin* **37**:56–61
- Cariou J.-P., Augere B. and Valla M. (2006) Laser source requirements for coherent lidars based on fiber technology. *Comptes Rendus Physique* **7**:213–223
- Courtney M., Wagner R. and Lindelöw P. (2009) Commercial lidar profilers for wind energy. A comparative guide. *EWEC*, Marseille
- Faghani D. et al. (2009) Remote sensing: practical use for wind power project. *AWEA Wind Resource & Project Energy Assessment Workshop*, Portland
- Frehlich R. G. and Kavaya M. J. (1991) Coherent laser radar performance for general atmospheric refractive turbulence. *Appl. Opt.* **30**
- Frehlich R. G., Hannon S. M., Henderson S. W. (1993) Performance of a 2-coherent Doppler lidar for wind measurements. *J. Atmos. Oceanic Technol.* **11**:1517–
- Frehlich R. G., Hannon S. M. and Henderson S. W. (1998) Coherent Doppler lidar measurements of wind field statistics. *Bound.-Layer Meteorol.* **86**:233–256
- Gottshall J., Courtney M. S., Lindelöw P. and Albers A. (2010) Classification of lidar profilers: How to introduce lidars to power performance testing. *EWEC*, Brussels
- Huffaker R. M. and Hardestry R. M. (1996) Remote sensing of Atmospheric wind velocities using solid state and CO<sub>2</sub> coherent laser systems. *Proc. IEEE* **84**
- Jaynes D. (2009) Lidar validation and recommendations for wind resource assessments. *Wind Power Conf.*, Chicago
- Lindelöw P. (2007) Effective sample volume fiber based coherent lidars for remote sensing of wind. PhD thesis from Ørsted-DTU, Lyngby
- Mikkelsen T. (2008) WindScanner: a facility for wind and turbulence measurements around large wind turbines. In *Nordic Conf. on: Global Challenges-Regional Opportunities: How can research infrastructure and Science support Nordic competitiveness?*, Stockholm
- Oldroyd A. et al. (2009) Testing and calibration of various lidar remote sensing devices for a 2 year offshore measurement campaign. *EWEC*, Marseille
- Siegman A. E. (1966) The antenna properties of optical heterodyne receivers. *Appl. Optics* **5**:1588–1594
- Soreide D., Boque R. K., Seidel J. and Ehernberger L. J. (1997) The use of a lidar forward looking turbulence sensor for mixed-compression inlet unstart avoidance and gross weight reduction on a high speed civil transport Nasa Technical memorandum
- Westerhellweg A., Beeken A., Canadillas B., Neumann T. (2010) One year of lidar measurements at Fino1-platform: comparison and verification to met-mast data. *DEWEK*

# 5 What can remote sensing contribute to power curve measurements?

Rozenn Wagner

*Wind Energy Division, Risø DTU, Roskilde, Denmark*

---

## 5.1 Introduction

Power performance measurement is central to the wind industry since it forms the basis for the power production warranty of the wind turbine. The power curve measurement has to be realised according to the IEC 61400-12-1 standard. The power curve is obtained with 10-min mean power output from the turbine plotted against simultaneous 10-min average wind speeds. The standard requires the wind speed to be measured by a cup anemometer mounted on top of a mast having the same height as the turbine hub and located at a distance equivalent to 2.5 rotor diameters from the turbine.

Such a plot usually shows a significant spread of values and not a uniquely defined function. The origin of the scatter can mainly be grouped into three categories: the wind turbine components characteristics, sensor error and the wind characteristics. Within the last group, the current standard only requires the wind speed at hub height and the air density measurement. However, other wind characteristics can influence the power production like the variation of the wind speed with height (i.e. wind speed shear). The influence of wind speed shear on the power performance was shown in several studies: some based on aerodynamic simulations (Antoniou, 2009; Wagner et al., 2009) others based on measurements (Elliot and Cadogan, 1990; Sumner and Masson, 2006).

A major issue is to experimentally evaluate the wind speed shear. The wind speed profile is usually assumed to follow one of the standard models such as the logarithmic or power law profiles. However, these models are valid for some particular meteorological conditions, and therefore, cannot represent all the profiles experienced by a wind turbine. Measurements are then a better option but are also challenging. Indeed characterising the wind speed profile in front of the rotor of a multi-MW wind turbine requires measurements of wind speed at several heights, including some above hub height, i.e. typically above 100 m. Remote sensing instruments such as lidar or sodar then appear as a very attractive solution.

This chapter starts with a description of the influence of the wind speed shear on the power performance of a multi-MW turbine. The challenge of describing the wind speed profile is then discussed followed by a description of an experiment using a lidar for its characterisation. This is followed by the introduction of the definition of an equivalent wind speed taking the wind shear into account resulting in an improvement of the power performance measurement. Finally, some recommendations about remote sensing instruments are given to successfully apply this method.

## 5.2 Power performance and wind shear

### Shear and aerodynamics

In order to see the effect of the wind speed shear on a wind turbine, aerodynamic simulations were carried out for two inflow cases:

1. constant wind speed profile (same wind speed everywhere) with  $8 \text{ m s}^{-1}$
2. power law profile with  $8 \text{ m s}^{-1}$  at hub height and a shear exponent of 0.5

The power law profile is defined as:

$$u = u_{hub} \left( \frac{z}{z_{hub}} \right)^\alpha, \quad (116)$$

where  $u$  is the wind speed at height  $z$ ,  $z_{hub}$  the hub height,  $u_{hub}$  the wind speed at that height and  $\alpha$  the shear exponent. Both profiles are shown in Figure 39.

The model used was HAWC2Aero. The modeled turbine was a Siemens 3.6 MW with a rotor diameter of 107 m and a hub height of 80 m. The wind speed is assumed horizontally homogeneous (i.e. the wind speed is the same everywhere on each horizontal plane). In order to emphasize the effect of wind speed shear, the simulations were carried out with laminar inflow, the tower shadow was turned off and the tilt angle of the rotor was set to  $0^\circ$ .

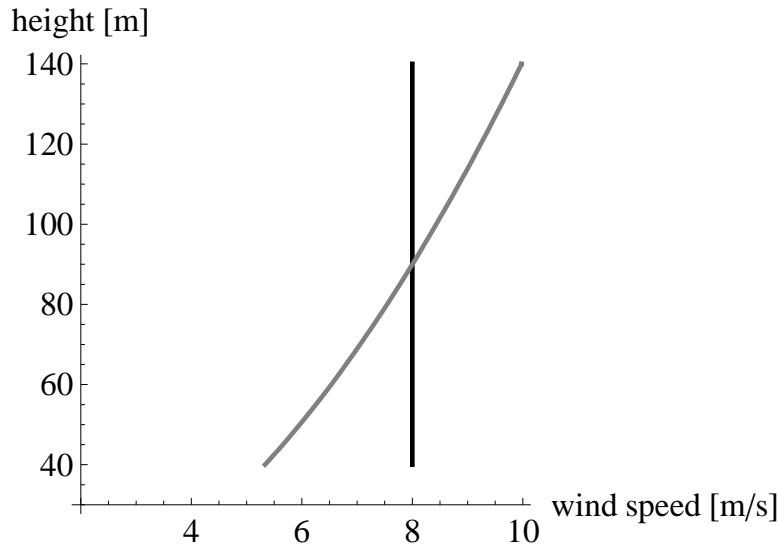


Figure 39: Wind profiles used as input for the wind speed shear aerodynamic investigation. Black curve: no shear; grey curve: power law profile with shear exponent of 0.5. Both profiles have the same wind speed at hub height

Figure 40 shows the free wind speed (i.e. the absolute wind speed in absence of a turbine) seen by a point at a radius of 30 m from the rotor centre, rotating at the same speed as the rotor as a function of time for the 2 inflow cases. Whereas in a uniform flow the blade is subjected to a constant wind speed, in a sheared flow, the point is exposed to large variations of wind speed even though the inflow is laminar. The variation of the wind speed seen by this rotating point in time is only due to the fact that it is rotating within a non uniform flow (wind speed varying with height).

Figure 41 shows the variations of the free wind speed seen by the same rotating point as function of the azimuth position ( $0^\circ =$  downwards). The point experiences the hub height wind speed (same as uniform inflow) when it is horizontal ( $\pm 90^\circ$ ), lower wind speed when it is downward ( $0^\circ$ ) and higher wind speed when it is upward ( $180^\circ$ ).

A rotating blade does not experience the free wind speed because of the induction from the drag of the rotor. In reality, a rotating blade is directly subjected to the relative wind speed (i.e. the speed of the wind passing over the airfoil relative to the rotating blade) and the angle of attack  $\phi$  (i.e. the angle between the blade chord line and the relative wind speed) with the effects of the induced speed included. The variations of these two parameters as function of  $\theta$  are shown in Figure 42. As these two parameters directly depend on the free wind speed, they vary with the azimuth angle in a sheared inflow, whereas they remain constant in a uniform inflow.

The relative speed and the angle of attack are derived from the rotor speed and the induced velocity. Therefore, they depend on the way that the induction is modeled and

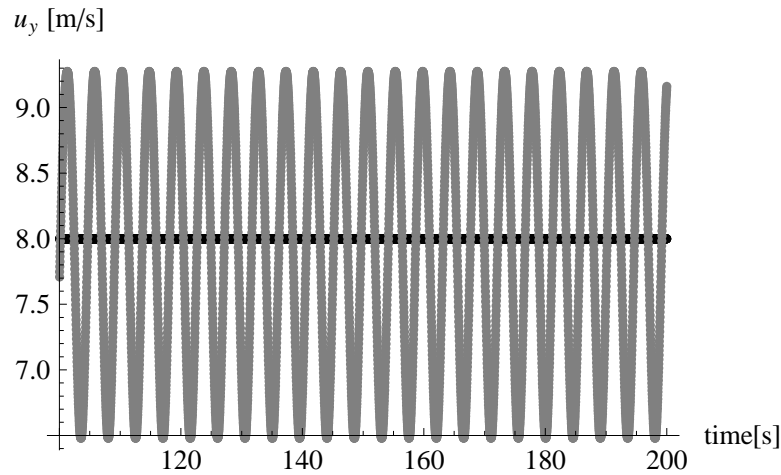


Figure 40: Time series of free wind speed seen from a rotating point, positioned at a radius of 30 m, rotating at rotor rotational speed (no induced velocity). Black curve: no shear; grey curve: power law profile with shear exponent of 0.5

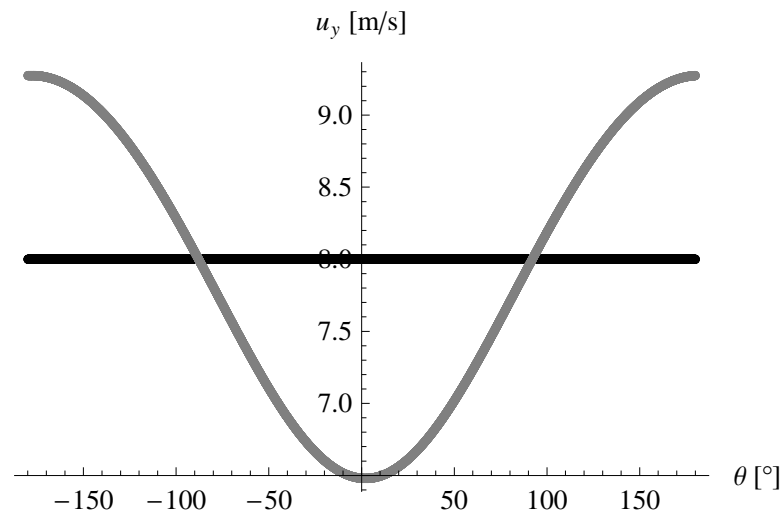


Figure 41: Free wind speed seen from a rotating point, positioned at a radius of 30 m, rotating at rotor rotational speed, as function of the azimuth angle  $\theta$ . Black curve: no shear; grey curve: power law profile with shear exponent of 0.5

it is difficult to evaluate their variations due to a non uniform flow in a simple way. However, some basic considerations (ignoring the induction) can give a basic insight to the variation of the relative speed and the angle of attack as the blade rotates. In case of uniform inflow, the free wind speed is the same at any point of the swept rotor area. Therefore, the angle of attack and the relative speed are the same at any azimuthal position (see Figure 43).

In case of sheared inflow, the free wind speed depends on the position of the blade. When the blade is horizontal, the free wind speed is the speed at hub height and the speed triangle is the same as in Figure 43. Below hub height, the wind speed is lower than the hub height speed, see Figure 44 (left). Consequently  $w$  and  $\phi$  are lower than those at hub height. Above hub height, the wind speed is higher than the hub height wind speed. Consequently  $w$  and  $\phi$  are higher than those at hub height, see Figure 44 (right). The variations in  $\phi$  and  $w$  cause a variation of the local lift and drag as the blade rotates, which finally results in the variation of the local tangential force contributing to the wind turbine power (see Figure 45). For a given  $\phi$ , local lift  $dF_L$  and local drag  $dF_D$ ,

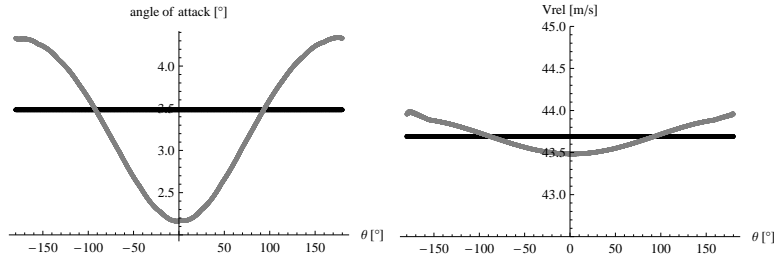


Figure 42:  $\phi$  (left) and  $w$  (including induction) (right) as a function of  $\theta$ , seen from a point at radius  $r = 30$  m on a rotating blade. Black curve: no shear; grey curve: power law profile with shear exponent of 0.5

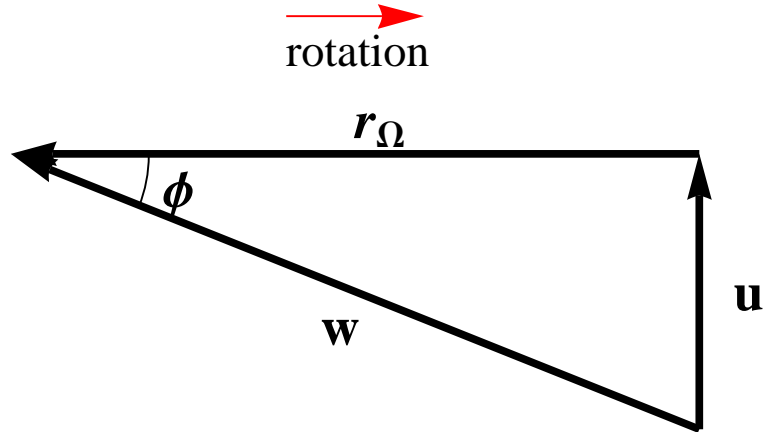


Figure 43: Speed triangle for a blade element at radius  $r$ .  $r_\Omega$  is the blade speed and  $w$  corresponds to the sum of the pitch angle, the twist angle and  $\phi$ . As the twist angle is constant for a given position on the blade and the pitch angle is  $0^\circ$  for wind speeds below rated speed,  $\phi$  represents the variation of the angle of attack

the local tangential force  $dF_T$  is given by (Manwell et al., 2002):

$$dF_T = dF_L \sin \phi - dF_D \cos \phi. \quad (117)$$

As the wind speed increases with height (e.g. in the case of the power law profile), the amplitude of the variations of the free wind speed seen by a rotating point increases with the radius (not shown here). The local tangential force consequently varies with the radius too. As the torque results from the integral of the tangential force over the whole rotor, it thus depends on the wind speed profile.

### Consequences on the power production

A series of cases were simulated with theoretical wind speed shear defined from the power law in Eq. (116), with  $-0.1 < \alpha < 0.5$  and  $5 \text{ m s}^{-1} < u_{hub} < 10 \text{ m s}^{-1}$ . The relative variations in power (defined as the percentage difference between the power outputs obtained with a shear inflow and an uniform inflow) are shown in Figure 46. According to the simulations results, the power output obtained with shear inflow is generally smaller than the power output obtained with an uniform inflow. Moreover, it decreases as the shear exponent increases except at  $5 \text{ m s}^{-1}$  where the power output reaches a minimum for  $\alpha = 0.2$  and increases for larger shear exponents, even exceeding the power output from uniform inflow with  $\alpha = 0.5$ .

The first difference between a sheared and an uniform inflow is the kinetic energy flux.

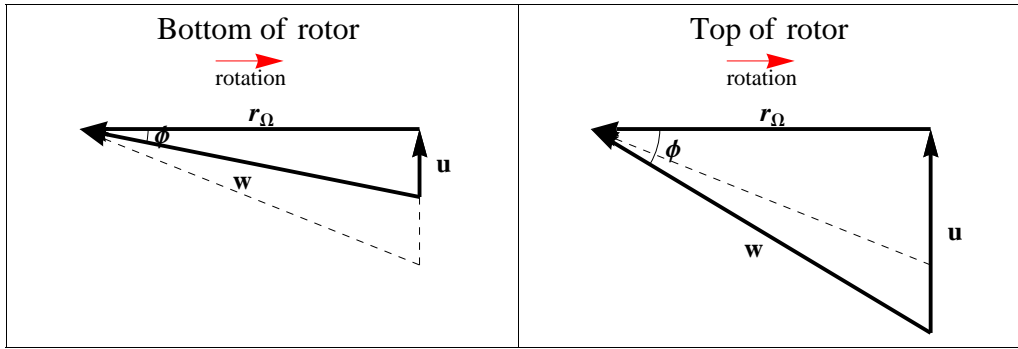


Figure 44: Speed triangles at the top and bottom of the rotor showing the effect of wind speed shear. The speed triangle at hub height is shown with dashed arrows

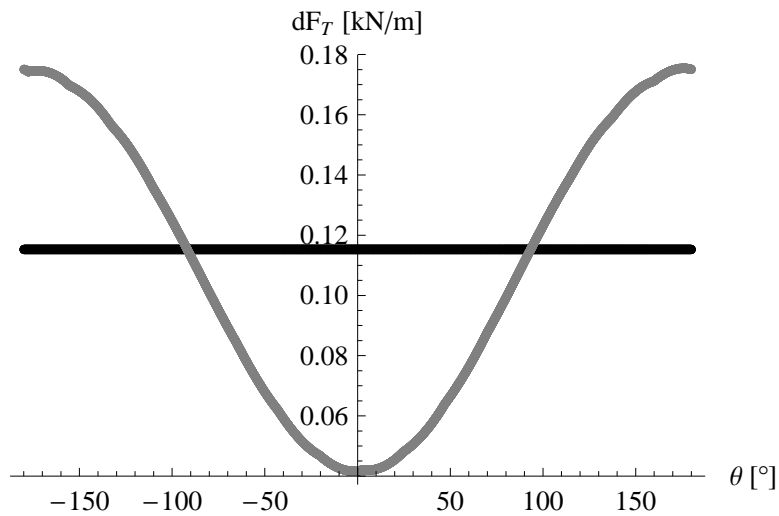


Figure 45: Local tangential force seen from a point  $r = 30$  m on a rotating blade as function of  $\theta$ . Black curve: no shear; Gray curve: power law profile with shear exponent of 0.5

In case of horizontally homogeneous inflow, the kinetic energy flux can be expressed by:

$$KE_{\text{profile}} = \int_{H-R}^{H+R} 0.5\rho u^3 c(z - (z_{\text{hub}} - R)) dz, \quad (118)$$

where  $\rho$  is the air density,  $R$  the rotor radius and  $c$  is the chord (of the circle defined by the rotor swept area) as function of  $z$  which varies between the bottom and the top of the rotor:

$$c = 2\sqrt{2Rz - z^2}. \quad (119)$$

In order to compare to the power output variations, Figure 46 also shows the difference between the kinetic energy flux for a power law profile and a constant profile, normalised with the power obtained with a constant profile  $KE_{\text{profile}} - KE_{\text{hub}}/KE_{\text{hub}}$  (see gray dashed line)<sup>5</sup>. Figure 46 shows two other interesting results:

1. The kinetic energy flux varies with shear exponent.
2. The power output of the turbine does not follow the same trend as the kinetic energy flux.

<sup>5</sup>The kinetic energy flux is not an output of HAWC2Aero, it has been here estimated and for power law profiles, the normalized difference does not depend on the wind speed

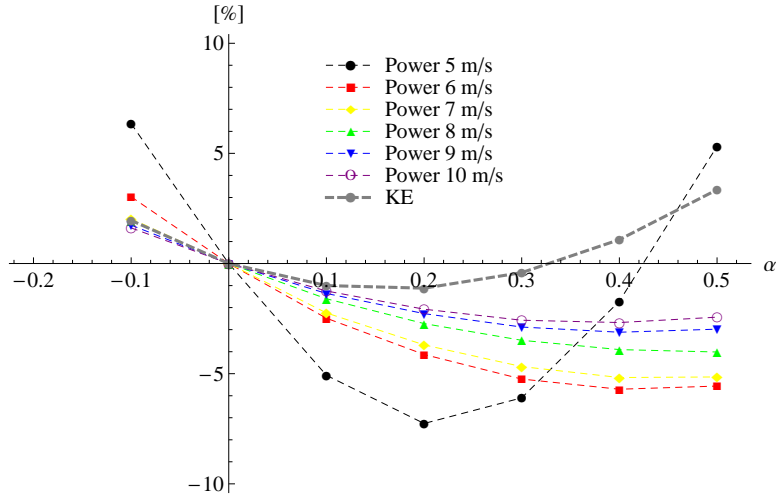


Figure 46: Normalised difference in power output and kinetic energy flux between shear and uniform case as function of the shear exponent, for various wind speed at hub height

Despite the high uncertainty in the modeled power output for a sheared inflow, the results highlight that the influence of the shear on the power performance of a turbine can be seen as the combination of two effects:

- The variation in kinetic energy flux (power input).
- The ability of the turbine to extract the energy from the wind, which depends on the details of the design and the control strategy of the turbine.

These results clearly indicate that wind speed profiles encountered by the turbine during a power performance measurement should be known and taken into account.

### 5.3 Wind speed profiles

Within the power performance evaluation context, the wind speed shear is often described by  $\alpha$  obtained from the assumption of a power law profile (Eq. (116)). This procedure was applied to profiles measured by a high meteorological mast located at the test site for large wind turbines, at Høvsøre, on the west coast of Denmark with  $z_{hub} = 80$  m and  $z = 40$  m to determine  $\alpha$ . For some cases, this model fits the measured profile very well, but it cannot represent all kinds of profiles observed at Høvsøre. Figure 47 shows two examples of measured profiles and their corresponding modelled profiles.

The distribution of the error made by such an approximation is shown in Figure 48. We define the error as the difference between the wind speed at 116.5 m (top of the mast) estimated by the power law model and the speed measured by the cup anemometer. Over a year of measurements, for a large wind sector  $60^\circ$ – $300^\circ$  degrees (with predominant wind from west), 7% of the profiles show a wind speed error at 116.5 m larger than 10%. We should keep in mind that all the anemometers are mounted on a boom except the top anemometer, and this can induce an error in the profile extrapolation to the top (116.5 m).

As shown by the simulations presented in section 5.2, such an error in the wind speed profile can significantly affect the power curve. The shear exponent from wind speed measurements at two heights is not acceptable for this application. Therefore it is important to measure the wind speeds at several heights below and above hub height. For this purpose remote sensing instruments such as lidar and sodar are highly relevant since in many cases they can measure up to 200 m with the required degree of accuracy.

An experimental campaign using a lidar to measure the wind speed profile in front of a multi-MW turbine showed the importance of measuring the complete profile for power



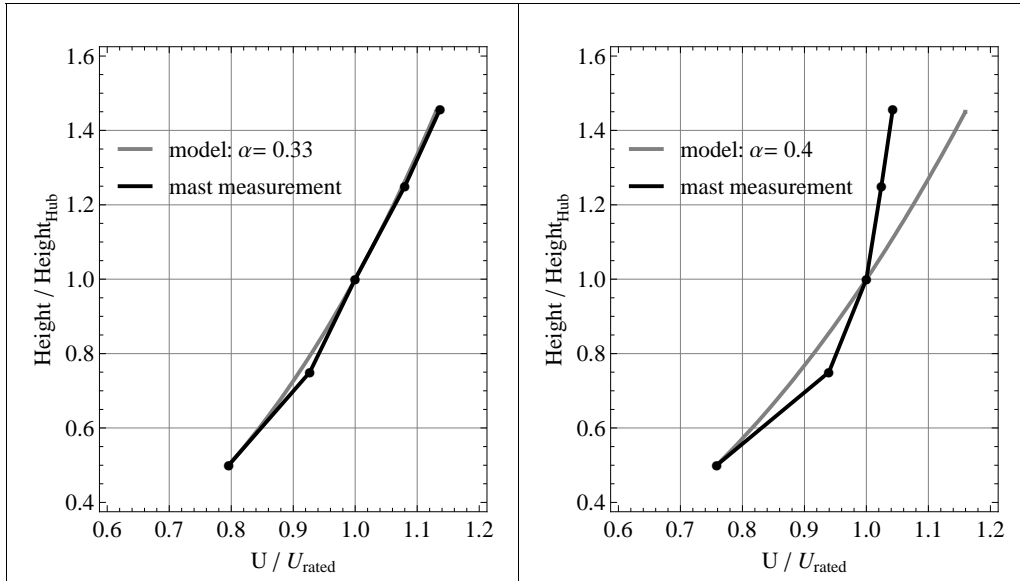


Figure 47: Two examples of profiles and their fit to the power law model (using the wind speed values at 40 and 80 m). The model fits very well the measured profile on the left, but it does not work for the profile on the right

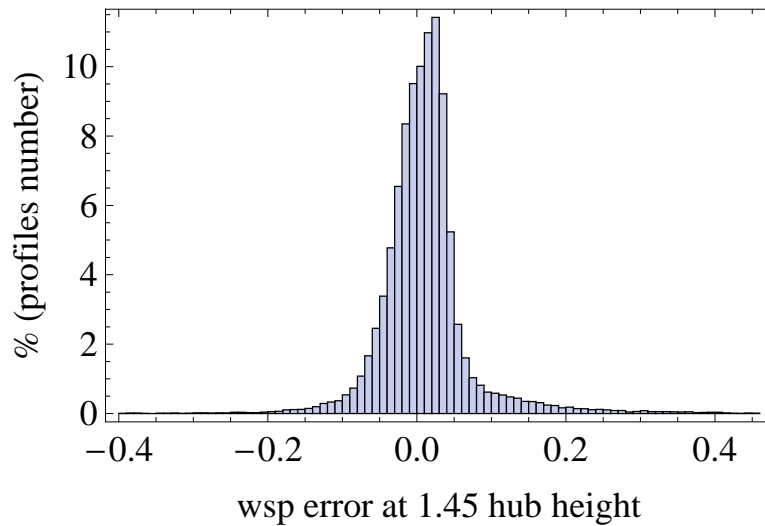


Figure 48: Distribution of the error made on the wind speed at 116.5 m height when assuming a power law profile with a shear exponent estimated with the wind speeds at 40 and 80 m

performance. In our experiment, the lidar measured the wind speed at 9 uniformly distributed heights covering 90% of the vertical rotor diameter. Each wind speed profile measured by the lidar was fitted to a power law profile in order to find the most representative shear exponent for this profile ( $\alpha_{fit}$ ). The fit is forced through the point of coordinate  $(u_{hub}, z_{hub})$ :

$$u_{fit}(z) = u_{hub} \left( \frac{z}{z_{hub}} \right)^{\alpha_{fit}}. \quad (120)$$

In order to separate the profiles for which the power law assumption was acceptable, we evaluated the goodness of fit with the residual sum of squares RSS, defined as:

$$RSS = \sum_i (u_{fit}(z_i) - u_i)^2, \quad (121)$$

where  $u_{fit}$  is the fit function defined in Eq. (120) and  $u_i$  the wind speed measured by the lidar at height  $z_i$  ( $i = 1$  to 9). Figure 49 shows two examples of measured profiles with their shear exponents and RSSs.

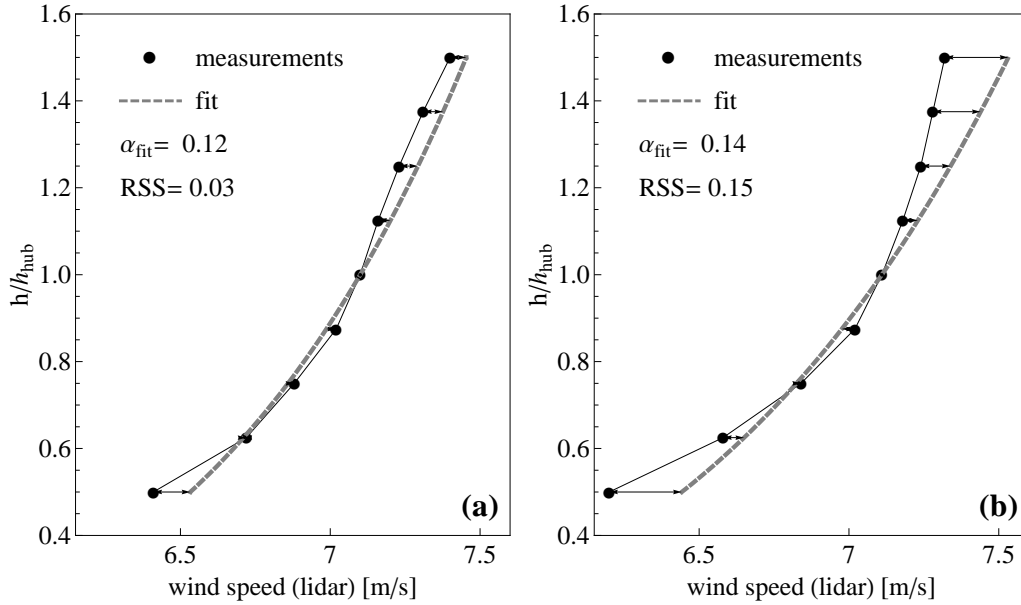


Figure 49: Example of measured wind profiles and their fit to a power law profile. (a)  $RSS \leq 0.1$ , (b)  $RSS > 0.1$

The profiles were then divided into two groups according to the RSS:

- Group 1:  $RSS \leq 0.1$  – the profiles from this group have a shape close to a power law profile and are referred to as the power law profiles.
- Group 2:  $RSS > 0.1$  – the profiles from this group have a shape that cannot be well represented by a power law profile and are referred to as the non power law profiles.

According to this classification, profile (a) in Figure 49 would be in group 1 and profile (b) in group 2. The value of 0.1 was chosen here as threshold for the RSS, because it gave two groups of data showing two trends (shown below) while being statistically comparable (as they count similar numbers of data: 511 in group 1 and 396 in group 2). It is recognized that this threshold is somewhat arbitrary and should subsequently be “fine-tuned” using a large number of datasets.

## 5.4 Equivalent wind speed

### Standard power curve for the two groups of wind profiles

Figure 50 shows the standard scatter plot of the power (a) and the  $C_p$  (b) as function of the wind speed at hub height.  $C_p$  is defined as in the current IEC standard 61400-12-1:

$$C_p = \frac{P}{0.5\rho u_{hub}^3 A}, \quad (122)$$

where  $P$  is the electrical power output of the turbine and  $A$  is the rotor swept area. The two colours represent the two groups of wind profiles: points obtained with the group 1 profiles ( $RSS \leq 0.1$ ) are displayed in black and those obtained with group 2 profiles ( $RSS > 0.1$ ) are displayed in red.

Figures 50(a) and (b) show two trends (one for each group) leading to two mean power curves and  $C_p$  curves (obtained after binning the data into  $0.5 \text{ m s}^{-1}$  wind speed bins

and averaging as required by the IEC 61400-12-1 standard) (Figures 50(c) and (d)). The power output of the turbine for a given wind speed (at hub height) is smaller for data from group 2 (non power-law profiles) than for data from group 1 and the data from group 2 generally give a lower  $C_p$ .

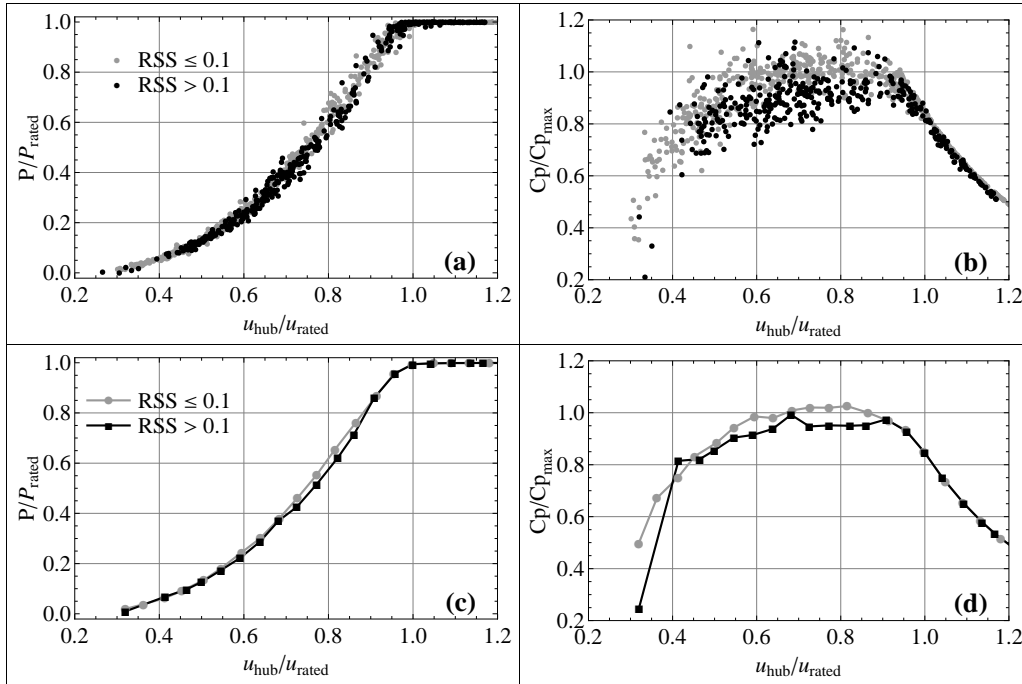


Figure 50: (a) Scatter plot of power curves, (b) Scatter plot of  $C_p$  curves, (c) Averaged power curves, (d) Averaged  $C_p$  curves. These plots are obtained by using the wind speed at hub height only and  $C_p$  calculated as in the IEC standards

What might appear here, for the non-power law profiles, as an underperformance of the wind turbine is an overestimation of the kinetic energy flux of the wind. Indeed, the  $C_p$  definition given by Eq. (122) implicitly assumes that the wind speed is constant over the entire rotor swept area:

$$u(z) = u_{hub} \quad KE_{hub} = 0.5\rho u_{hub}^3 A, \quad (123)$$

or, in other words, the wind speed shear is ignored.

### A better approximation of the kinetic energy flux

However, as mentioned earlier, the real kinetic energy flux is obtained with Eq. (116). The kinetic energy flux for each profile measured by the lidar can be approximated by:

$$KE_{profile} = \sum_i 0.5\rho_i u_i^3 A_i, \quad (124)$$

where  $u_i$  is the wind speed measured at the  $i$ th height in the profile and corrected for the air density and  $A_i$  is the area of the corresponding segment of the rotor swept area (see Figure 51).

The ratio  $KE_{profile}/KE_{hub}$  is displayed in Figure 45. The profiles from group 1 (black points) follow rather well the analytical results showing a moderate error due to the constant wind profile assumption.

The non power-law profiles (group 2), on the other hand, do not follow the analytical curve and show a much larger difference between the two ways of evaluating the kinetic energy flux. The approximation of a constant wind speed over the whole rotor swept area

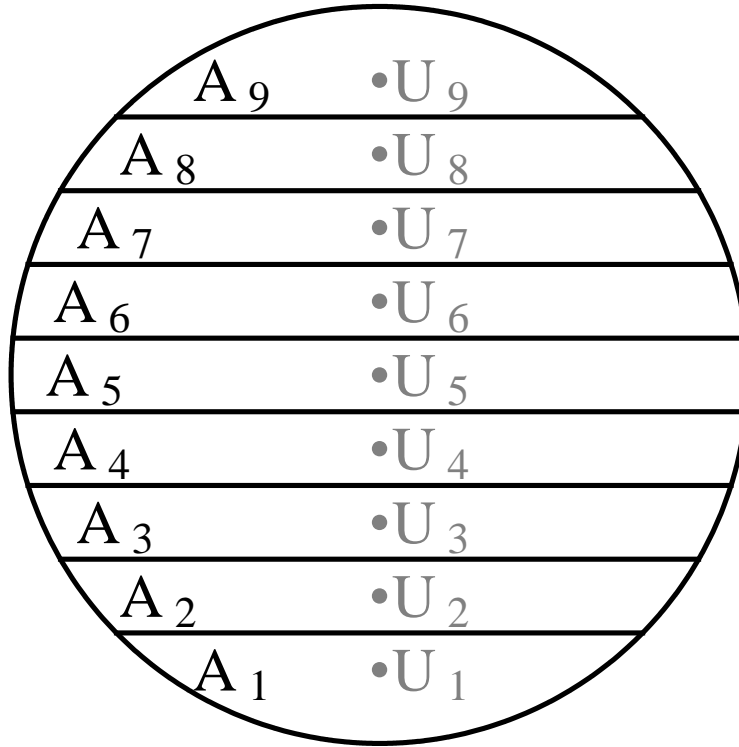


Figure 51: Rotor swept area divided into 9 segments corresponding to the 9 heights where lidar observations are performed. Each wind speed is assumed to be constant in each segment

overestimates the kinetic energy flux for most of the data of group 2 and underestimates it for a few of them.

Two wind speed profiles can have the same wind speed at hub height but different kinetic energy. In a standard power curve, such profiles would have the same abscissa (hub height wind speed), whereas they would almost certainly result in different power outputs. This is partially why the two groups of wind profiles give two different power curves. The kinetic energy flux overestimation has even more impact on  $C_p$ , explaining the lower  $C_p$  for the group 2 wind profiles compared to that for group 1.

Another contribution to the differences between the power curves in figure 50 can be the influence of the wind speed shear on the power output. Indeed, two wind profiles resulting in the same kinetic energy may give different turbine power output, because for some wind speed shear conditions (e.g a power law profile with a large shear exponent), the turbine is not able to extract as much energy as in other shear conditions (e.g. a constant profile).

### Equivalent wind speed definition

Intuitively, the power output of the turbine should be more closely related to the kinetic energy flux derived from the whole profile than that derived from the wind speed at hub height. We should then consider the power output of the turbine as a function of the kinetic energy flux. In order to do so, an equivalent wind speed is suggested:

$$u_{eq} = \left( \sum_i u_i^3 \frac{A_i}{A} \right)^{1/3} . \quad (125)$$

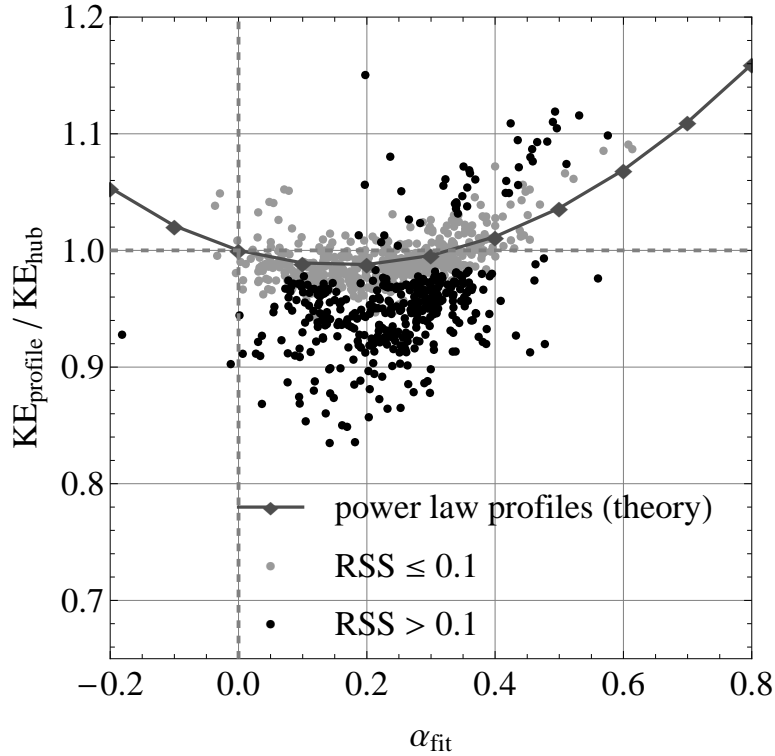


Figure 52: Ratio between the kinetic energy flux obtained with the wind speed profiles ( $KE_{\text{profile}}$  for the theoretical and measured profiles) and the kinetic energy assuming a constant wind speed with height equal to the hub height wind speed ( $KE_{\text{hub}}$ )

Then  $C_p$  becomes:

$$\begin{aligned}
 C_p &= \frac{P}{0.5\rho_0 u_{eq}^3 A} = \frac{P}{0.5\rho_0 \left( \sum_i \left( \left[ \frac{\rho_i}{\rho_0} \right]^{1/3} u_i \right)^3 \frac{A_i}{A} \right) A} \\
 &= \frac{P}{\sum_i 0.5\rho_i u_i^3 A_i} = \frac{P}{KE_{\text{profile}}}.
 \end{aligned} \tag{126}$$

Figure 53 shows plots comparable to the plots in Figure 50: in Figure 53, the power and  $C_p$  are plotted as a function of the equivalent wind speed defined in Eq. (125) (instead of the wind speed at hub height in Figure 43) and  $C_p$  is calculated according to Eq. (126) (instead of Eq. (122) in Figure 50). In Figure 53, profiles from both groups follow the same trend. The mean power and  $C_p$  curves obtained with each group of points overlap each other. This shows that the difference in power curves between the two groups shown in Figure 53 was mainly due to the error in kinetic energy flux.

### Choice of instrument

The question now is: can any remote sensing instrument be used to measure a power curve and reduce the scatter with the equivalent wind speed method? Figures 54(a) and (b) show the comparison of the simultaneous 10-min mean wind speed measured by a remote sensing instrument (sodar and lidar respectively), and a cup anemometer at the same height. The lidar and the sodar were placed next to each other but with a lateral distance of 100 m from a mast equipped with a top-mounted cup anemometer used for the comparisons. Both datasets include the same 10-min periods. It can be clearly seen that the sodar data are noisier than the lidar data. There was no indication of any major problem with the sodar during this experiment. The difference in measurements

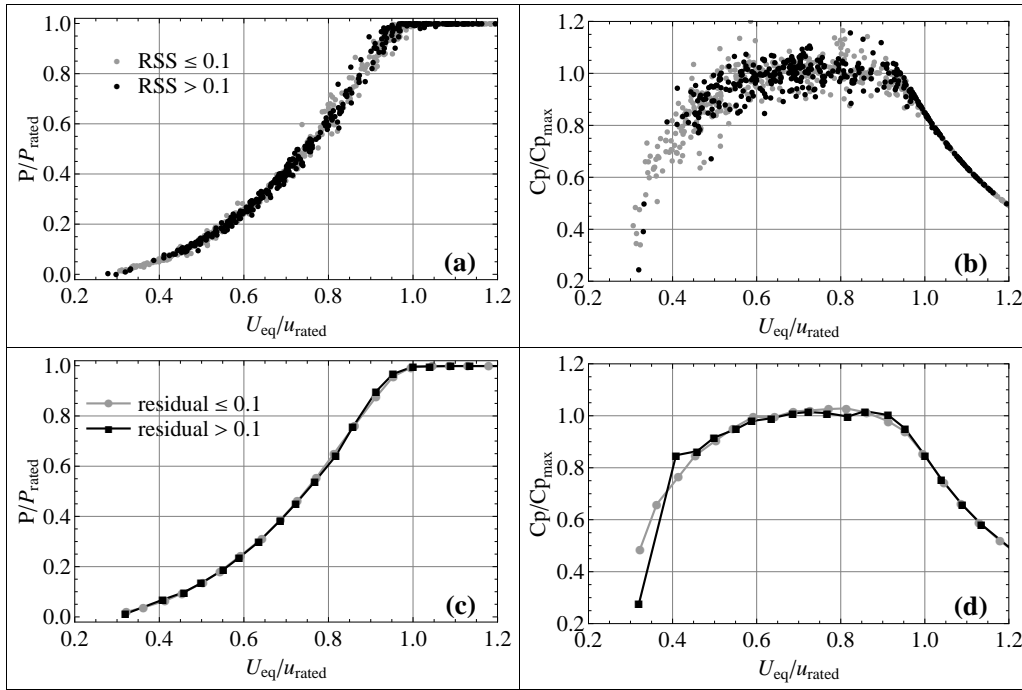


Figure 53: (a) Scatter plot of power curves, (b) Scatter plot of  $C : p$  curves, (c) Averaged power curves, (d) Averaged  $C_p$  curves. These plots are obtained using the equivalent wind speed Eq. (125) and a  $C_p$  definition taking the wind shear into account

from the two instruments can be explained by the difference in the way they operate. Because sodar measurements are based on sound properties, they are sensitive to noise from the surroundings and obstacles (which is not the case for light beams). Moreover, the sampling frequency of a sodar is much smaller than that of a lidar. A sodar measures one wind speed every 10 min, whereas a lidar can measure the wind speed 30 to 100 times during that time.

The power curve obtained with such noisy measurements (at hub height) presents a much larger scatter than the power curve obtained with the cup anemometer (Figure 54(c)), whereas the scatter in power curve obtained with better remote sensing measurements is similar to that obtained with the cup anemometer (Figure 54(d)). If the remote sensing instrument increases the scatter in power curve compared to a cup anemometer, it is very unlikely that the observation of wind speed profiles from that same instrument can help to reduce the scatter. Thus, an instrument presenting noisy measurements is not suitable for power curve measurement and cannot be used to calculate an equivalent wind speed in order to reduce the scatter. This restricts very much the possibility of using sodar because of the inherent noise in the measurements. However, the point here is not to disqualify sodars, but to make the difference between an instrument which is suitable and one which is not suitable for the application of the equivalent wind speed method.

Figure 55 shows a lidar cup comparison for two lidar systems (same brand, same test location). Even though the gain factor and the coefficient of determination ( $R^2$ ) is good for both instruments, a clear difference appears when we look at the lidar error (i.e. difference between wind speed measured by the lidar and the cup). Lidars are very attractive because of their capacity to measure wind speed and direction profiles with the convenience of a ground based measurement device. However, this is still a new and rather immature technology and it is strongly recommended to verify each instrument against a tall mast (equipped with good wind speed sensors at several heights) in flat terrain. A remote sensing classification and a verification procedure are currently being defined within the standard committee.

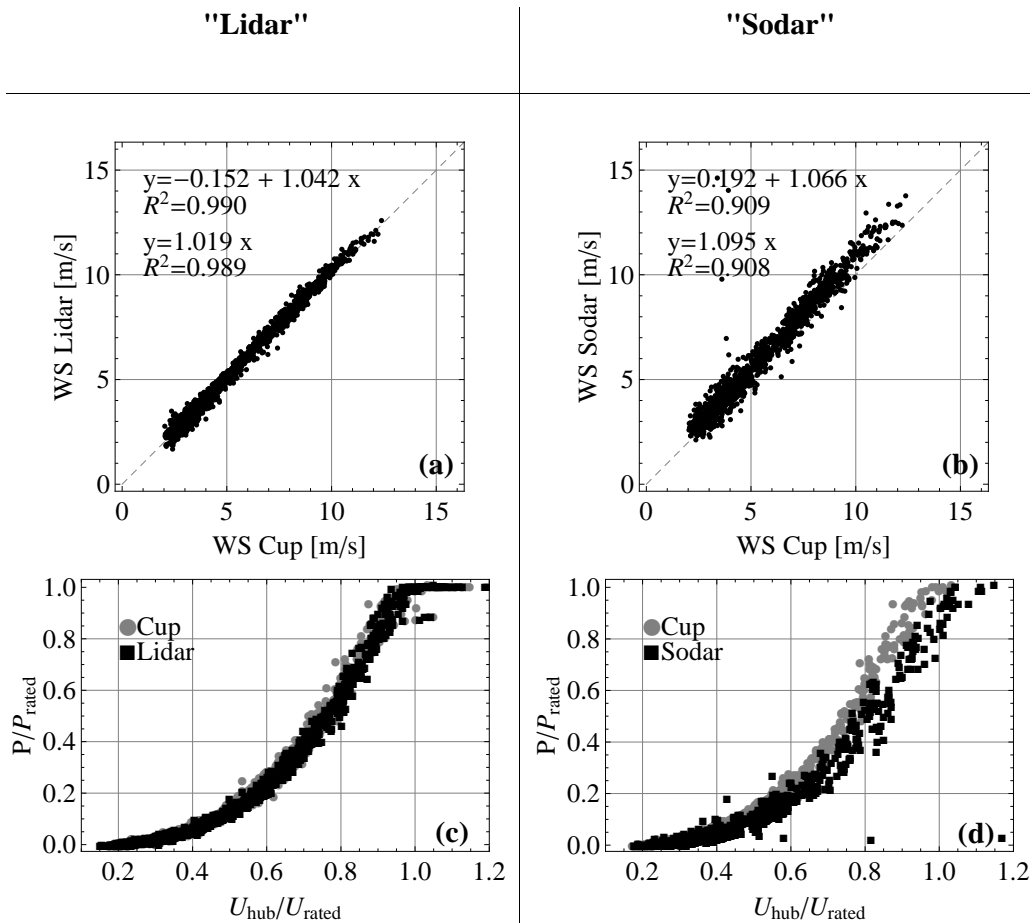


Figure 54: (a) Linear regression of 10-min mean wind speed measured by a lidar and a cup anemometer; (b) Linear regression of 10-min mean wind speed measured by a sodar and the same cup anemometer as in (a) for the same 10-min periods; (c) power curve obtained with wind speed measurement at hub height with a cup and a lidar; (d) power curve obtained with wind speed measurement at hub height with a sodar and the same cup anemometer as in (c) for the same 10-min periods

## 5.5 Summary

As wind speed shear influences the power performance of multi-MW turbines, it is necessary to characterize the wind speed profile in front of the turbine rotor. Remote sensing instruments are of great interest, since they can measure the wind speed profile over the whole rotor range. Such measurements avoid the use of assumptions about the shape of the wind speed profile. A more accurate kinetic energy flux can then be calculated resulting in a better evaluation of the power performance of the turbine. The use of an equivalent wind speed taking the wind speed shear into account reduces the scatter in the power curve and the uncertainty in power performance measurement. In that sense, the use of remote sensing measurements can improve the power performance measurements. However, this can only be achieved with a good instrument. Finally, the remote sensing instrument should not show more scatter in the power curve than that of a cup at a given height. This requires a verification of the instrument prior to the power performance measurement.

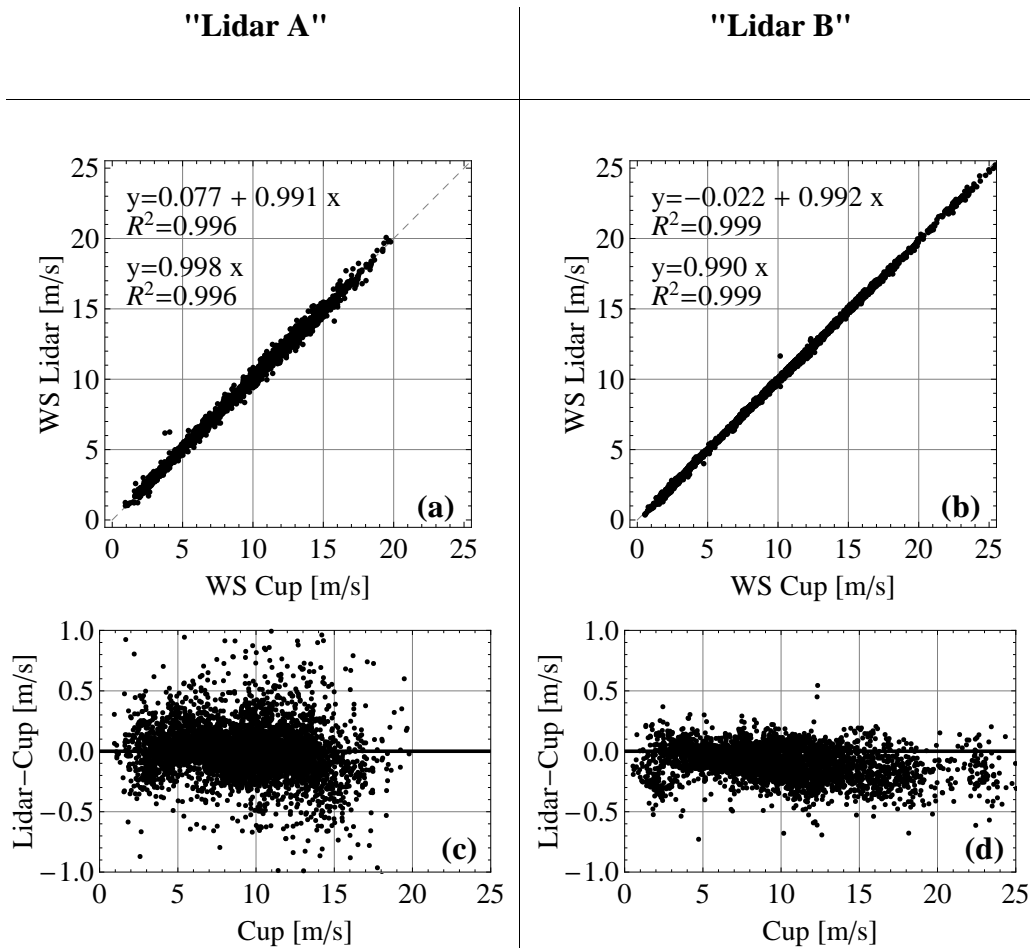


Figure 55: (a and b) Linear regression of 10-min mean wind speeds measured by a lidar and a cup anemometer from two lidar systems; (c and d) lidar error for each system

## Notation

$A$	rotor swept area
$A_i$	area of the $i$ th element
$c$	chord defined by the rotor swept area
$C_p$	power coefficient
$dF_D$	local drag force
$dF_L$	local lift force
$dF_T$	local tangential force
$KE_{hub}$	kinetic energy flux of a constant wind profile
$KE_{profile}$	kinetic energy flux of the wind profile
$P$	electrical power output of the turbine
$r$	radial position
$r\Omega$	blade speed
$R$	coefficient of determination
$R$	rotor radius
RSS	residual sum of squares
$u$	wind speed
$u_{eq}$	equivalent wind speed
$u_{fit}$	fit wind speed function to the power profile
$u_{hub}$	hub height wind speed
$u_i$	wind speed at height $z_i$
$w$	relative wind speed
$z$	height above the ground
$z_{hub}$	hub height
$z_i$	lidar height
$\alpha$	shear exponent of the power law



$\alpha_{fit}$	shear exponent fit
$\theta$	azimuth angle
$\rho$	air density
$\phi$	angle of attack

## References

- Antoniou I. (2009) Wind shear and uncertainties in power curve measurement and wind resources. *WindPower*
- Elliot D. L. and Cadogan J. B. (1990) Effects of wind shear and turbulence on wind turbine power curve. *Proc. of the European Community Wind Energy Conf.*, Madrid
- IEC (2005) IEC 61400-12-1 Wind turbines - Power performance measurements of electricity producing wind turbines. Int. Electrotechnical Commission
- Manwell J. F., McGowan J. G., and Rogers A. L. (2002) Wind energy explained: Theory, design and application, John Wiley & Sons Ltd, 577 pp
- Sumner J. and Masson C. (2006) Influence of atmospheric stability on wind turbine power performance curves. *J. Solar Energy Eng.* **128**:531–538
- Wagner R., Antoniou I., Pedersen S. M., Courtney M., and Jørgensen H. E. (2009) The influence of the wind speed profile on wind turbine performance measurements. *Wind Energy* **12**:348–362

# 6 Lidars and wind profiles

Alfredo Peña

*Wind Energy Division, Risø DTU, Roskilde, Denmark*

---

## 6.1 Introduction

Wind lidars have been able to observe wind profiles since the beginning of their commercialization in 2005.<sup>6</sup> The ZephIR continuous wave (cw) lidar, nowadays manufactured by Natural Power, entered the wind energy community to compete with the traditional instrumentation, such as cup anemometers and wind vanes, offering in advantage the measurement of wind speed and direction profiles up to 200 m above ground level (AGL), avoiding the flow distortion effects that the traditional instruments suffer when they are mounted on structures. The performance of the ZephIR, when compared with cup anemometers at several heights up to about 100 m, showed high agreement from first studies over land (Smith et al., 2006) and over the sea (Kindler et al., 2007).<sup>7</sup>

Later, observations from cup anemometers were combined with ZephIR measurements at the Nysted (Antoniou et al., 2006) and at the Horns Rev (Peña et al., 2009) offshore wind farms to reproduce wind profiles up to about 160 m above mean sea level (AMSL). Although the results from the campaign at Horns Rev showed good agreement with the wind profile theory, limitations on the measurement range were found due to the contamination of the lidar's Doppler spectra by clouds, which gave the opportunity to Natural Power to improve the cloud correction algorithms of the ZephIR.

Since we are interested in wind profile retrieval within 30–200 m where large wind turbines operate, cloud contamination is a serious concern. In fact, when this issue was first addressed, the role of the aerosol profile on the lidar's probe volume (for any kind of lidar) became more important, specially since the expertise on this subject is rather limited. Mist and fog have also been realized as serious hazards for cws lidars (Courtney M., 2009, personal communication), which for wind profile analysis results in high wind shears close to the ground,<sup>8</sup> i.e. that—for example, neutral wind profiles might be interpreted as stable.

Nowadays, the Windcube and Galion pulsed lidars, from the companies LeoSphere and Sgurr Energy, respectively, are also in the market. Both lidars offer instantaneous wind profile observation up to about 2000 m, but the instruments' range actually depends on the atmospheric conditions, namely on the amount of aerosols in the atmosphere, which is proportional to the signal-to-noise ratio (SNR).

As with the ZephIR, a number of campaigns combining observations from cup and sonic anemometers at high meteorological masts and from pulsed lidars have started. Peña et al. (2010b) described the neutral wind profile and Peña et al. (2010a) the diabatic wind profile, both for homogenous and flat terrain up to 300 m AGL, both using the Windcube to extend wind speed observations from traditional meteorological instrumentation at the National Test Station for Large Wind Turbines (NTWT) at Høvsøre, Denmark.

Other meteorological campaigns are envisioned for the description of the wind profile up to 500 m (Gryning S.-E., 2009, personal communication), which will not only help for increasing the accuracy in wind power calculations, but also for the improvement of the parameterizations used in boundary-layer meteorology.

---

<sup>6</sup>By wind profile, it is meant the horizontal wind speed profile

<sup>7</sup>High agreement refers to 1 : 1 comparisons of wind velocity observations with correlation coefficients close to 1

<sup>8</sup>By wind shear, it is meant the vertical wind shear

## 6.2 Wind profile theory

Mixing-length theory, firstly introduced by Prandtl (1932) for the description of atmospheric flow, is here chosen for the analysis of the wind profile. The local wind shear  $\partial U/\partial z$ , where  $U$  is the mean horizontal wind speed and  $z$  the height above the ground, is parameterized as

$$\frac{\partial U}{\partial z} = \frac{u_*}{l} \quad (127)$$

where  $u_*$  is the local friction velocity and  $l$  is the local mixing length.

### Surface layer

In the surface layer, which covers the first 5–10% of the atmospheric boundary layer (ABL), the mixing length  $l_{SL}$  is given as

$$l_{SL} = \kappa z \phi_m \quad (128)$$

where  $\kappa$  is the von Kármán constant ( $\approx 0.4$ ) and  $\phi_m$  the dimensionless wind shear from Monin-Obukhov similarity theory (MOST) (Monin and Obukhov, 1954), which is defined as

$$\phi_m = \frac{\kappa z}{u_{*o}} \frac{\partial U}{\partial z} \quad (129)$$

where  $u_{*o}$  is the surface-layer friction velocity ( $u_*$  is rather constant in the surface layer). Several experiments have suggested expressions for the behaviour of  $\phi_m$  with stability, which have resulted in the so-called flux-profile relationships. For unstable and stable conditions, respectively, these are given as

$$\phi_m = (1 - az/L)^p \quad \text{and} \quad (130)$$

$$\phi_m = 1 + bz/L \quad (131)$$

where  $a$ ,  $b$ , and  $p$  are empirical constants (Businger et al. 1971; Högström 1988) and  $L$  is the Obukhov length estimated as

$$L = -\frac{u_{*o}^3 T_o}{\kappa g w' \Theta_{v'o}} \quad (132)$$

where  $T_o$  is the mean surface-layer temperature,  $g$  is the gravitational acceleration, and  $w' \Theta_{v'o}$  is the surface-layer kinematic virtual heat flux. Assuming  $u_* = u_{*o}$  and  $l = l_{SL}$  in Eq. (127), and combining it with Eqs. (128) and (129), the integration with height of Eq. (127) gives the surface-layer wind profile,

$$\frac{U}{u_{*o}} = \frac{1}{\kappa} \left[ \ln \left( \frac{z}{z_o} \right) - \psi_m \right] \quad (133)$$

where  $z_o$  is the surface roughness length and  $\psi_m$  is the diabatic correction of the wind profile, which is derived from the integration with the dimensionless stability parameter  $z/L$  of  $\phi_m$  in Eqs. (130) and (131) (Stull, 1988). For neutral conditions, which are favorable for wind energy due to high wind speed characteristics,  $\phi_m = 1$  and  $\psi_m = 0$ , thus resulting in the well-known logarithmic wind profile.

Figure 56 illustrates the average dimensionless wind profiles observed for different stability conditions over flat and homogenous terrain at Høvsøre, Denmark. Each average wind profile is computed by classifying the individual 10-min wind profiles into stability classes, based on the Obukhov length as performed in Gryning et al. (2007) and Peña et al. (2010a). As shown in the figure, Eq. (133) fits well the observations in the surface layer and the observations start to depart from the surface-layer wind profile at about 100 m for near-neutral conditions and 60 m for very stable conditions. The roughness length is estimated fitting Eq. (133) to the first observational height only.

With such dimensionless x-axis, the wind profile is a function of roughness length and stability only. In the surface layer and over flat and homogenous land, Eq. (133)

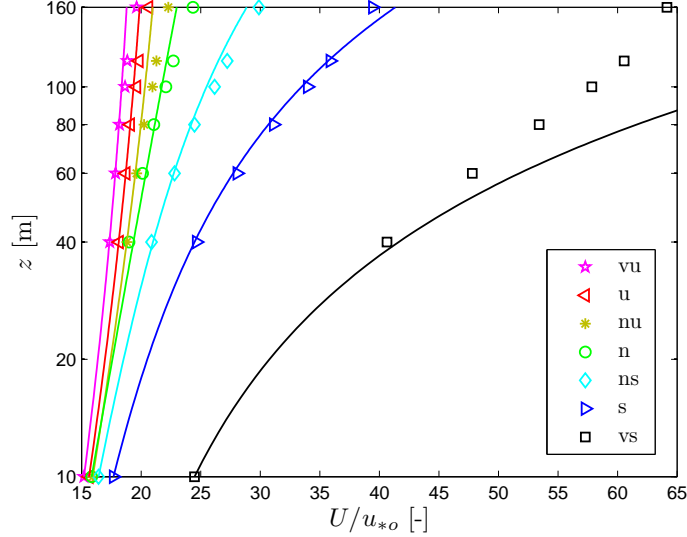


Figure 56: Wind profiles observed for different stability classes at Høvsøre, Denmark. The markers indicate the observations and the solid lines the predictions using Eq. (133). Legend: vu (very unstable), u (unstable), nu (near unstable), n (neutral), ns (near stable), s (stable), and vs (very stable).

generally fits well the average observations and the wind profile can easily be studied using such dimensionless fashion, because  $z_o$  does not vary significantly. The standard error for the observations in Fig. 56 increases with height, indicating that other external parameters, such as the boundary-layer height  $z_i$ , start to play a more important role for the description of the wind profile. However, even for the observations at 160 m, the highest standard error is 0.35, i.e. the individual wind profiles concentrate close to the average.

### Marine surface layer

Over water, the roughness length is not constant and depends, among others, on wind stress, waves, and fetch. The scaling  $U/u_{*o}$  is appropriate for the surface-layer wind profile for constant  $z_o$  values. Using the simple parameterization of Charnock (1955),

$$z_o = \alpha_c \frac{u_{*o}^2}{g} \quad (134)$$

where  $\alpha_c$  is the Charnock's parameter ( $\approx 0.012$ ), it is straightforward to realize that the scaling  $U/u_{*o}$  produces wind profiles that do not converge onto a straight line. Peña and Gryning (2008) analyzed this issue and suggested the following scaling for the marine wind profile,

$$\frac{U}{u_{*o}} + \frac{1}{\kappa} \ln \left[ 1 + 2 \frac{\Delta u_{*o}}{\overline{u_{*o}}} + \left( \frac{\Delta u_{*o}}{\overline{u_{*o}}} \right)^2 \right] = \frac{1}{\kappa} \left[ \ln \left( \frac{z}{z_o} \right) - \psi_m \right] \quad (135)$$

where  $\Delta u_{*o} = u_{*o} - \overline{u_{*o}}$ , i.e.  $\Delta u_{*o}$  is a *fluctuating* surface-layer friction velocity equal to the difference between the observation  $u_{*o}$  and the ensemble average  $\overline{u_{*o}}$ .  $\overline{z_o}$  is a mean roughness length parameterized as Eq. (134), but replacing  $u_{*o}$  with the ensemble average  $\overline{u_{*o}}$ . Eq. (135) differs from Eq. (133), because it adds a dimensionless wind speed, the left term in square brackets in Eq. (135), which allows the wind profiles to converge onto a straight line for the same stability class. It also uses a mean roughness length, which allows for an empirical estimation of the Charnock's parameter.

## Boundary layer

The surface-layer wind profile was previously derived from the assumption that the length scale grows infinitively with height. At about 100 m AGL and neutral conditions—for example, this assumption is not longer valid. The IEC (2005) standard suggests to use surface-layer scaling for the length scale up to 60 m AGL and to assume a constant length scale upwards.

There has been a number of suggestions for the behaviour with height of the mixing length in the ABL, which departure from Eq. (128). Blackadar (1962) and Panofsky (1973) limited the growth of the length scale and proposed neutral mixing-length models, which were used to numerically compute the ABL wind profile. Lettau (1962) proposed a similar model to that of Blackadar (1962), but in which the length scale starts to decrease slowly beyond the surface layer. Gryning et al. (2007) proposed a mixing-length model, which assumes that the top of the boundary layer acts as the ground, and therefore, the length scale has a zero value at the top of the ABL. Based on the length-scale behaviour observed from turbulence measurements far beyond the surface layer, as shown in Caughey and Palmer (1979), and the close relation between the length scale of the wind profile and that derived from turbulence measurements as observed in Peña et al. (2010b), the idea of a decreasing mixing-length with height is rather reasonable.

Simple analytical models for the ABL wind profile can be derived, using such *limiting* mixing-length models and a model for the local friction velocity, by integrating with height Eq. (127). This was performed by Gryning et al. (2007) and Peña et al. (2010a) for the diabatic flow over flat land and homogeneous terrain, Peña et al. (2008) for diabatic flow over the sea, and Peña et al. (2010b) for neutral flow over flat and homogeneous land. The main results of the comparison of these models and wind speed observations at great heights at Høvsøre and at the Horns Rev wind farm are presented in the following section.

## 6.3 Comparison with observations at great heights

### Marine observations

Marine wind speed observations from combined cup anemometer and ZephIR measurements up to 161 m AMSL, within a sector where the upstream flow is free and homogeneous at the Horns Rev wind farm, were compared to wind profile models in Peña et al. (2008) showing good agreement. The neutral and unstable wind profile models are identical to those traditionally used for the surface layer, Eq. (133), although the physics involved in their derivation are different. For the stable wind profile, a correction is applied to the stability parameter to take into account the boundary-layer height,  $z_i$ :

$$\frac{U}{u_{*o}} = \frac{1}{\kappa} \left[ \ln \left( \frac{z}{z_o} \right) - \psi_m \left( 1 - \frac{z}{2z_i} \right) \right]. \quad (136)$$

Figure 57 illustrates the results using the scaling proposed in Peña and Gryning (2008), which can be used for wind profile comparison whenever the wind speed can be scaled with the friction velocity.

The stable boundary-layer height was estimated in Peña et al. (2008) by use of the Rossby and Montgomery (1935) formula,

$$z_i = C \frac{u_{*o}}{|f_c|} \quad (137)$$

where  $C$  is a proportionality parameter ( $\approx 0.15$ ) and  $f_c$  is the Coriolis parameter. Eq. (137) is valid for neutral conditions only, thus, the buoyancy contribution was accounted for in stable conditions by decreasing the value of  $C$ .

### Neutral observations over flat land

Near-neutral wind speed observations from combined cup anemometer and Windcube measurements up to 300 m AGL, within an homogenous upwind sector at Høvsøre, were

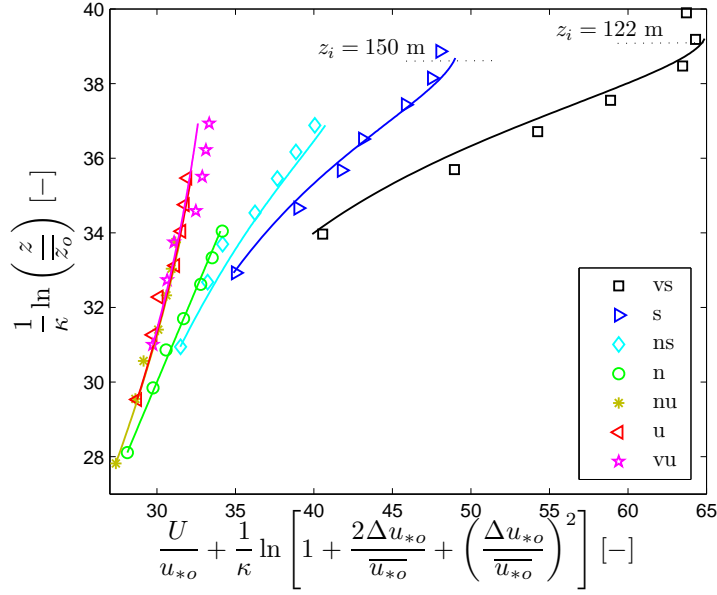


Figure 57: Wind profiles for different stability classes from combined lidar/cup anemometer observations at the Horns Rev wind farm in Denmark. The markers indicate the observations and the solid lines the predictions using Eq. (133) for unstable and neutral conditions and Eq. (136) for stable conditions. The boundary-layer height  $z_i$  is also indicated. Legend as in Fig. (56).

compared in Peña et al. (2010b) to a set of neutral wind profile models:

$$U = \frac{u_{*o}}{\kappa} \ln\left(\frac{z}{z_o}\right), \quad (138)$$

$$U = \frac{u_{*o}}{\kappa} \left[ \ln\left(\frac{z}{z_o}\right) + \frac{1}{d} \left(\frac{\kappa z}{\eta}\right)^d - \left(\frac{1}{1+d}\right) \frac{z}{z_i} \left(\frac{\kappa z}{\eta}\right)^d - \frac{z}{z_i} \right], \quad (139)$$

$$U = \frac{u_{*o}}{\kappa} \left[ \ln\left(\frac{\sinh(\kappa z/\eta)}{\sinh(\kappa z_o/\eta)}\right) - \frac{z}{z_i} \frac{\kappa z}{2\eta} \right], \quad (140)$$

$$U = \frac{u_{*o}}{\kappa} \left[ \ln\left(\frac{z}{z_o}\right) + \frac{z}{l_{MBL}} - \frac{z}{z_i} \left(\frac{z}{2l_{MBL}}\right) \right], \quad (141)$$

which correspond to the logarithmic wind profile, a simple analytical solution for the wind profile from the mixing-length model of Blackadar (1962) ( $d = 1$ ) and Lettau (1962) ( $d = 5/4$ ), another simple solution using the mixing-length model of Panofsky (1973), and the wind profile model of Gryning et al. (2007), respectively.  $d$  is a parameter that controls the growth of the length scale,  $\eta$  is the limiting value for the length scale in the upper atmosphere, and  $l_{MBL}$  is a middle boundary-layer length scale.

$\eta$  has traditionally been parameterized as,

$$\eta = D \frac{u_{*o}}{|f_c|} \quad (142)$$

where Blackadar (1965) suggested  $D = 63 \times 10^{-4}$  and from the analysis of Lettau (1962) and assuming  $Ro = 5.13 \times 10^5$ , where  $Ro$  is the surface Rossby number,  $D = 96 \times 10^{-4}$ . In this fashion, when combining Eq. (143) with Eqs. (138)–(141), the ratio  $u_{*o}/|f_c|$  in can be replaced by  $z_i/C$  from Eq. (137).  $l_{MBL}$  was parameterized by Gryning et al. (2007) as

$$l_{MBL} = \frac{u_{*o}/|f_c|}{-2 \ln\left(\frac{u_{*o}}{|f_c|z_o}\right) + 55}. \quad (143)$$

The results of the comparison are illustrated in Figure 58. The models, which limit the growth of the length scale, have a better agreement with the wind speed observations be-

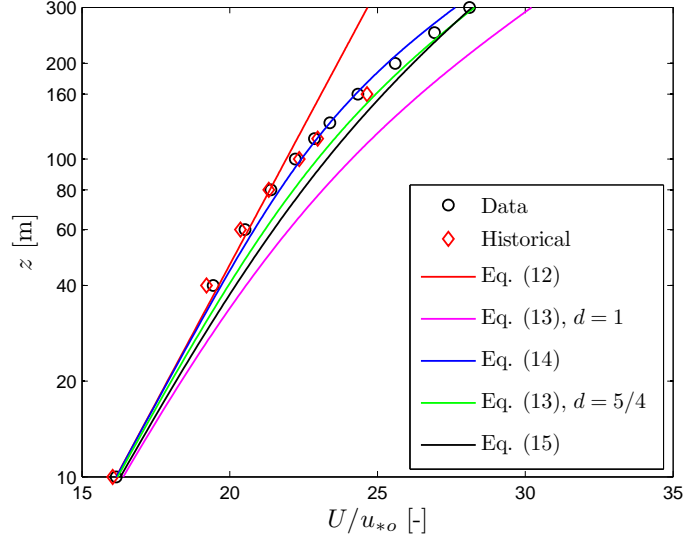


Figure 58: Neutral wind profile observed at Høvsøre, Denmark. The markers indicate combined lidar/cup anemometer observations (Data) and the mean wind profile from about 3 years of cup anemometer observations (Historical). The solid lines indicate the predictions using  $C = 0.15$ ,  $D = 73 \times 10^{-4}$ ,  $58 \times 10^{-4}$ , and  $100 \times 10^{-4}$  for Eq. (139) with  $d = 1$ , Eq. (140), and Eq. (139) with  $d = 5/4$ , respectively.

yond the surface layer ( $\approx 80$  m). The logarithmic wind profile fits well the measurements within the surface layer only.

### Diabatic observations over flat land

Wind speed observations from combined cup anemometer and Windcube measurements up to 300 m AGL, within an homogenous upwind sector and for different stability conditions at Høvsøre, were compared in Peña et al. (2010a) to a set of diabatic wind profile models. These models were derived by extending the surface-layer length scale of the mixing-length models of Blackadar (1962), Lettau (1962), and Gryning et al. (2007) to account for atmospheric stability using MOST. For example, using the extended mixing-length models of Blackadar (1962) and Lettau (1962), the wind profile is given as,

$$U = \frac{u_{*o}}{\kappa} \left[ \ln \left( \frac{z}{z_o} \right) - \psi_m + \frac{1}{d} \left( \frac{\kappa z}{\eta} \right)^d - \left( \frac{1}{1+d} \right) \frac{z}{z_i} \left( \frac{\kappa z}{\eta} \right)^d - \frac{z}{z_i} \right], \quad (144)$$

$$U = \frac{u_{*o}}{\kappa} \left[ \ln \left( \frac{z}{z_o} \right) + b \frac{z}{L} \left( 1 - \frac{z}{2z_i} \right) + \frac{1}{d} \left( \frac{\kappa z}{\eta} \right)^d - \left( \frac{1}{1+d} \right) \frac{z}{z_i} \left( \frac{\kappa z}{\eta} \right)^d - \frac{z}{z_i} \right] \quad (145)$$

for unstable and stable conditions, respectively.

$\eta$  was parameterized in Peña et al. (2010a) using Rossby-number similarity as,

$$\eta = \frac{\kappa z_i}{[d(1+d)]^{1/d}} \left[ \left( \left[ \ln \left( \frac{u_{*o}}{f_c z_o} \right) - A \right]^2 + B^2 \right)^{1/2} + 1 - \ln \left( \frac{z_i}{z_o} \right) \right]^{-1/d} \quad (146)$$

where  $A$  and  $B$  are the integration constants for a given stability from the resistant laws. A similar parameterization is found in Gryning et al. (2007) for  $l_{MBL}$ .  $z_i$  was estimated from Eq. (137) for neutral and stable conditions, and from observations of the aerosol backscatter coefficient from a Vaisala CL31 ceilometer for unstable conditions. Figure 59 (top frame) illustrates the behaviour of the aerosol backscatter coefficient,  $\beta$ , during a day where most of the unstable profiles were measured. It is observed that during

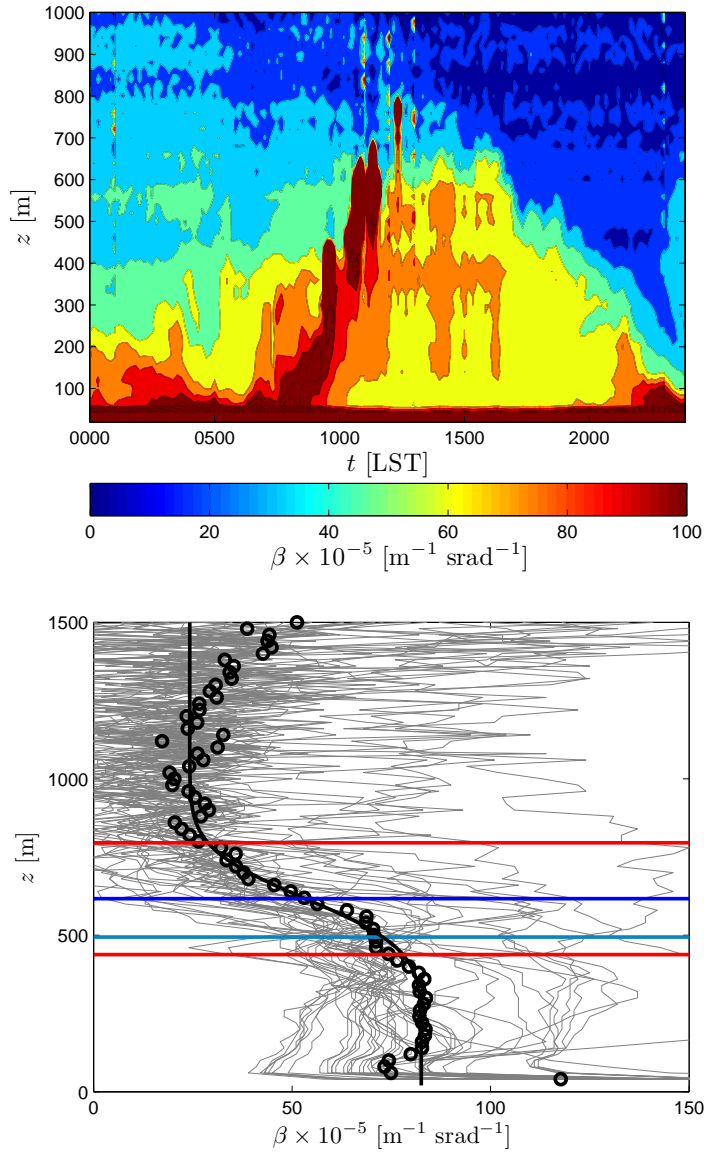


Figure 59: Top frame: Ceilometer observations of the aerosol backscatter coefficient  $\beta$  during a convective day at Høvsøre, Denmark. Bottom frame: Aerosol backscatter profile from ceilometer measurements at Høvsøre for neutral conditions. The gray lines show the aerosol profiles, the markers the average aerosol profile, the black line the fit function from Steyn et al. (1999), and the horizontal lines the estimation of  $z_i$  from the fit function (blue), the entrainment zone depth (red lines), and the estimation of  $z_i$  from Eq. (137) (cyan).

daylight time (1000–1800 LST), the aerosols reached 600–700 m marking the height of the unstable boundary layer. In Peña et al. (2010a), aerosol backscatter profiles observed simultaneously with the wind profiles for each stability class are used to estimate the boundary-layer height. The results for the neutral stability class are illustrated in Figure 59 (bottom frame).  $z_i$  is estimated using the modified error function suggested by Steyn et al. (1999) and a good agreement was found when compared to the estimation from Eq. (137) for neutral conditions.

Once  $\eta$  and  $z_i$  are estimated, the wind speed observations can be compared to the models. Figure 60 illustrates the comparison of the models in Eqs. (144) and (145) with  $d = 5/4$ , the surface-layer wind profile, Eq. (133), and the wind speed observations for the number of stability classes also used in Figures 56 and 57. As with the neutral obser-



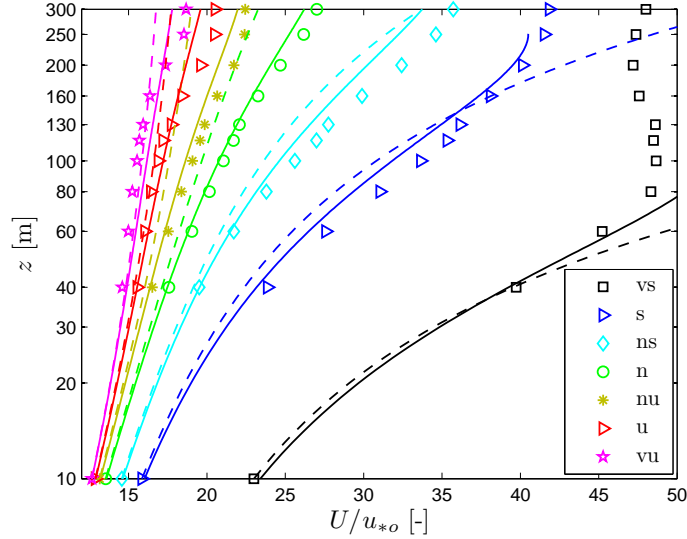


Figure 60: Wind profiles observed for different stability classes at Høvsøre, Denmark. The markers indicate the combined lidar/cup anemometer observations, the solid lines the predictions using Eqs. (144) and (145) with  $d = 5/4$ , and the dashed lines the predictions from Eq. (133). Legend as in Fig. 56.

variations, surface-layer scaling fits well the observations within the surface layer only. The wind profile model, which limits the value of the length scale, corrects for the departures of the observations beyond the surface layer. Similar results were obtained in Peña et al. (2010a) using Eqs. (144) and (145) with  $d = 1$  and the wind profile models in Gryning et al. (2007).

## 6.4 Summary

- The use of ground-based remote sensing instruments has been useful for the study and description of the wind profile in and beyond the surface layer and for the improvement of the models that are traditionally used in wind power and boundary-layer meteorology.
- Over flat land and homogenous terrain and over the sea, the surface-layer wind profile fits well the observations for a wide range of atmospheric stability conditions within the surface layer only. For the analysis of wind profiles over water, however, a new scaling should be added in order to account for the variable roughness length.
- Wind speed observations from combined lidar/cup anemometer measurements up to 160 m AMSL at the Horns Rev offshore wind farm are well predicted by wind profile models that limit the value of the length scale, as suggested by Gryning et al. (2007), where the boundary-layer height becomes an important parameter, particularly for stable conditions.
- Near-neutral wind speed observations from combined lidar/cup anemometer measurements up to 300 m AGL at Høvsøre, Denmark, departure from the logarithmic wind profile beyond the surface layer. Simple analytical models, which limit the value of the length scale, predict such departure and fit well the observations.
- Wind profile models, extended for diabatic conditions, are compared to wind speed observations from combined lidar/cup anemometer measurements up to 300 m AGL at Høvsøre, Denmark, for a number of stability conditions. The models, which also limit the growth of the length scale, agree better with the observations compared

to the surface-layer wind profile, which under- and over-predicts the wind speed beyond the surface layer. The models also depend on the boundary-layer height, which is estimated under neutral and stable conditions using surface-layer turbulence measurements and under unstable conditions using ceilometer observations of the aerosol backscatter profile.

## Notation

$a$	parameter for the convective dimensionless wind shear
$A$	integration constant for a given stability from the resistant laws
ABL	atmospheric boundary layer
AGL	above ground level
AMSL	above mean sea level
$b$	parameter for the stable dimensionless wind shear
$B$	integration constant for a given stability from the resistant laws
cw	continuous wave
$C$	proportionality constant for the boundary-layer height
$d$	parameter for the control of the length scale
$D$	proportionality parameter for the limiting length scale
$f_c$	Coriolis parameter
$g$	gravitational acceleration
$l$	local mixing length
$l_{MBL}$	middle boundary-layer length scale
$l_{SL}$	surface-layer mixing length
$L$	Obukhov length
LST	local standard time
MOST	Monin-Obukhov similarity theory
NTWT	National Test Station for Large Wind Turbines
$p$	parameter for the convective dimensionless wind shear
Ro	surface Rossby number
SNR	signal-to-noise ratio
$T_o$	mean surface-layer temperature
$u_*$	local friction velocity
$u_{*o}$	surface-layer friction velocity
$\overline{u_{*o}}$	average surface-layer friction velocity
$U$	horizontal mean wind speed
$w'\Theta_v'/o$	surface-layer kinematic virtual heat flux
$z$	height above the ground or above mean sea level
$z_i$	boundary-layer height
$z_o$	surface roughness length
$\overline{z_o}$	mean surface roughness length
$\alpha_c$	Charnock's parameter
$\beta$	aerosol backscatter coefficient
$\Delta u_{*o}$	fluctuating surface-layer friction velocity
$\eta$	limiting value for the length scale
$\kappa$	von Kármán constant
$\phi_m$	dimensionless wind shear
$\psi_m$	adiabatic correction of the wind profile
$\partial$	partial derivative

## References

- Antoniou I., Jørgensen H. E., Mikkelsen T., Frandsen S., Barthelmie R., Perstrup C., and Hurtig M. (2006) Offshore wind profile measurements from remote sensing instruments. *Proc. of the European Wind Energy Conf.*, Athens
- Blackadar A. K. (1962) The vertical distribution of wind and turbulent exchange in a neutral atmosphere. *J. Geophys. Res.* **67**:3095–3102
- Blackadar A. K. (1965) A Single-layer theory of the vertical distribution of wind in a baroclinic neutral atmospheric boundary layer. In: Flux of heat and momentum in the planetary boundary layer of the atmosphere. AFCRL-65-531, The Pennsylvania State University, 1–22

- Businger J. A., Wyngaard J. C., Izumi Y., and Bradley E. F. (1971) Flux-profile relationships in the atmospheric surface layer. *J. Atmos. Sci.* **28**:181–189
- Caughy S. J. and Palmer S. G. (1979) Some aspects of turbulence structure through the depth of the convective boundary layer. *Quart. J. Roy. Meteor. Soc.* **105**:811–827
- Charnock H. (1955) Wind stress over a water surface. *Quart. J. Roy. Meteorol. Soc.* **81**:639–640
- Gryning S.-E., Batchvarova E., Brümmner B., Jørgensen H., and Larsen S. (2007) On the extension of the wind profile over homogeneous terrain beyond the surface layer. *Bound.-Layer Meteorol.* **124**:251–268
- Högström U. (1988) Non-dimensional wind and temperature profiles in the atmospheric surface layer: a re-evaluation. *Bound.-Layer Meteorol.* **42**:55–78
- IEC (2005) IEC 61400-12-1 Wind turbines - Design requirements. Int. Electrotechnical Commission
- Kindler D., Oldroyd A., MacAskill A., and Finch D. (2007) An eight month test campaign of the QinetiQ ZephIR system: Preliminary results. *Meteorol. Z.* **16**:479–489
- Lettau H. H. (1962) Theoretical wind spirals in the boundary layer of a barotropic atmosphere. *Beitr. Phys. Atmos.* **35**:195–212
- Monin A. S. and Obukhov A. M. (1954) Osnovnye zakonomernosti turbulentnogo peremeshivaniya v prizemnom sloe atmosfery (Basic laws of turbulent mixing in the atmosphere near the ground). *Trudy Geofiz. Inst. AN SSSR* **24**(151):163–187
- Panofsky H. A. (1973) Tower Micrometeorology. Haugen D. A. (Ed.) Workshop on Micrometeorology. American Meteorology Society, 151–176
- Peña A. and Gryning S.-E. (2008) Charnock’s roughness length model and non-dimensional wind profiles over the sea. *Bound.-Layer Meteorol.* **128**:191–203
- Peña A., Gryning S.-E., and Hasager C. B. (2008) Measurements and modelling of the wind speed profile in the marine atmospheric boundary layer. *Bound.-Layer Meteorol.* **129**:479–495
- Peña A., Gryning S.-E., and Hasager C. B. (2010a) Comparing mixing-length models of the diabatic wind profile over homogeneous terrain. *Theor. Appl. Climatol.* **100**:325–335
- Peña A., Gryning S.-E., Mann J., and Hasager C. B. (2010b) Length scales of the neutral wind profile over homogeneous terrain. *J. Appl. Meteorol. Climatol.* DOI 10.1175/2009JAMC2148.1
- Peña A., Hasager C. B., Gryning S.-E., Courtney M., Antoniou I., Mikkelsen T. (2009) Offshore wind profiling using light detection and ranging measurements. *Wind Energy* **12**:105–124
- Prandtl L. (1932) Meteorologische Anwendung der Strömungslehre (Meteorological application of fluid mechanics). *Beitr. Phys. Atmos* **19**:188–202
- Rosby C. G. and Montgomery R. B. (1935) The layers of frictional influence in wind and ocean currents. *Pap. Phys. Oceanogr. Meteorol.* **3**(3):101 pp
- Smith D. A., Harris M., Coffey A. S., Mikkelsen T., Jørgensen H. E., Mann J., and Danielian R. (2006) Wind lidar evaluation at the Danish wind test site in Høvsøre. *Wind Energy* **9**:87–93
- Steyn D. G., Baldi M., and Hoff R. M. (1999) The detection of mixed layer depth and entrainment zone thickness from lidar backscatter profiles. *J. Atmos. Ocean. Technol.* **16**:953–959
- Stull R. B. (1988) An introduction to boundary layer meteorology, Kluwer Academic Publishers, 666 pp

# 7 Complex terrain and lidars

Ferhat Bingöl

*Wind Energy Division, Risø DTU, Roskilde, Denmark*

---

## 7.1 Introduction

The term “complex terrain” can be simply defined as any site where the wind is under effect of the terrain. This general definition includes landscapes with either vegetation or sudden elevation changes. In recent years, the interest of the European wind energy industry for such sites has increased. Formerly, they were considered as suboptimal for investments. This is not a coincidence and there are many reasons for such interest; most importantly the following two. Firstly, most of the suitable flat terrains have already been used. One example to this case is Northern Europe where the installed capacity is reaching its limit on flat terrain and the investors became more interested in complex sites. Secondly, the market is also growing in regions where wind resources are not fully utilized, like Mediterranean countries, where the land surface is dominated by rough terrain in the form of hills, mountains and forests (Figure 61).

In both cases, the terrain poses a challenge for flow modelling because the assumptions of classical boundary-layer theory are violated which has a great impact on the site assessment. If one has to identify the wind conditions in complex terrain, knowledge beyond the classical site assessment methods would be needed. Hence, procedures are needed for the verification of the power curve for wind turbines erected in complex terrain because the power curve variation is 6 – 8%, higher compared to that measured over flat terrain (Pedersen et al., 2002). Therefore, current site assessment techniques are not *generally* reliable in such conditions, which may lead to reduced turbine/wind park lifetime and loss of investment.

In addition to land cover and elevation complexity challenges in the terrain, the wind industry faces another equally important challenge related to the size of the wind turbines. In the last decade, the turbine hub heights have doubled, reaching a minimum of 100 m with 100 m of rotor diameter. The top and bottom edges of the blade of such turbines are typically at 150 and 50 m above ground level (a.g.l.), respectively.

This multitude of factors has created the need for a new generation of measurement devices with certain capabilities. The instruments;

1. should be able to measure up to 200 m to cover the whole rotor swept area,
2. must be able to perform in profile measurement standards (e.g. IEC (2005)),
3. and be easy to install/operate in complex terrains.

The above requirements cannot easily be fulfilled with conventional meteorological masts; installation of a meteorological mast and its maintenance, is a big logistical problem. Furthermore minor adjustments on the position of the meteorological mast entails almost the same amount of work as installing it. A category of instruments which can meet these goals is the wind energy Light Detection and Ranging instruments; mostly known as wind lidars or just lidars in wind energy. In this chapter, we will discuss on using the lidars in complex terrain.

## 7.2 Lidars

The lidars have become a part of wind energy meteorology after 1997 (Mayor et al., 1997). The capabilities of the instrument were well-known but the necessary investment

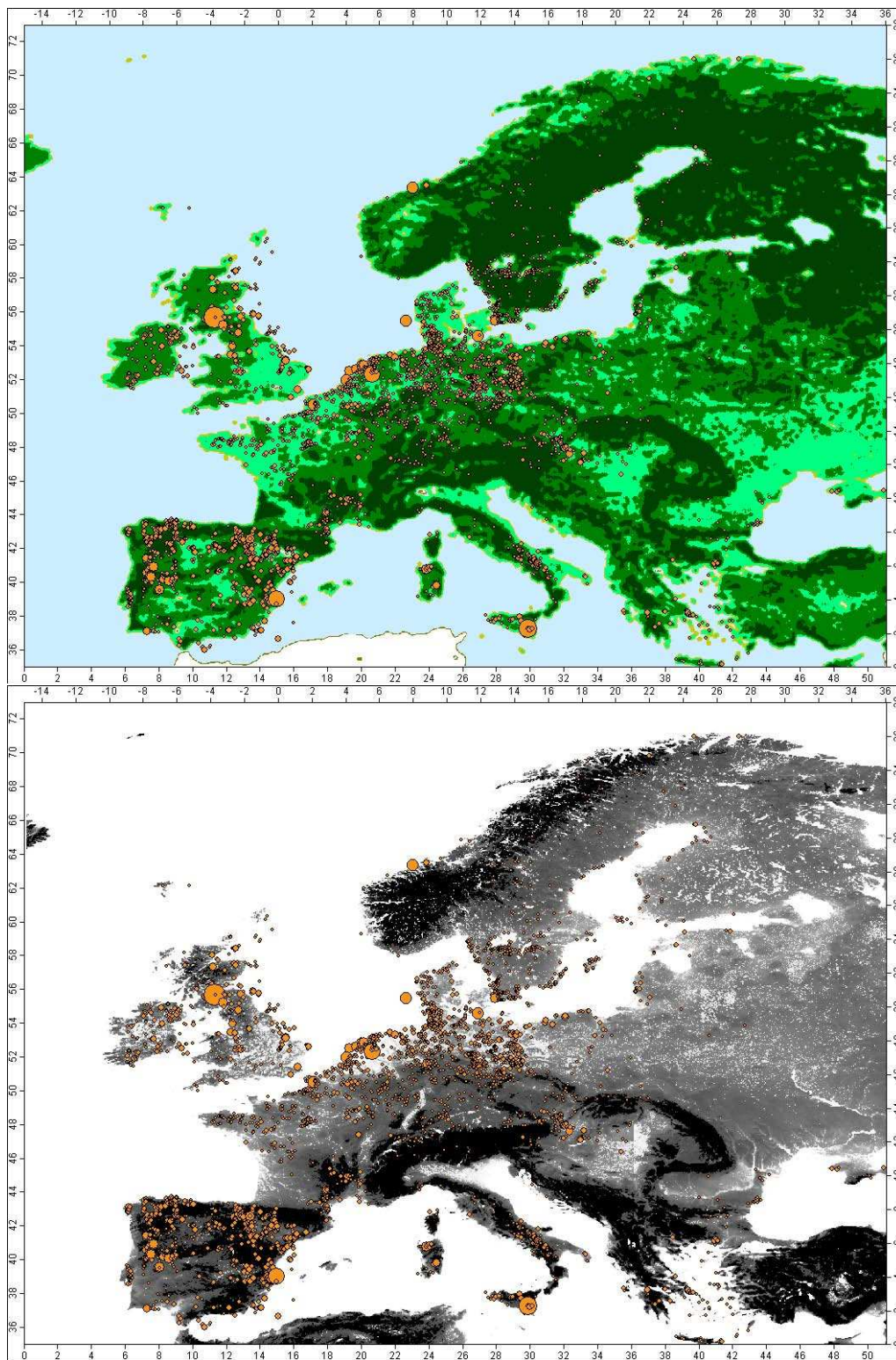


*Figure 61:* Spatial distribution of land use (top) and terrain slope map (bottom) in Europe derived from an EEA study (JRC, 2006) and grid size map of Hastings et al. (1999), respectively (Bingöl, 2009). Dark green areas are forest; green areas are sparse forest or shrub/herbaceous cover. Light green areas are crop land. The black areas are the regions where the slope is higher than 20°. Wind park locations with capacity between 3 and 322 MW are denoted by orange disks. The diameter of the disk is proportional to the installed capacity (TheWindPower.net, 2009)

was too high for many applications and the operating heights were not relevant to wind energy related studies. Therefore, the usage of them is recent and it has started after the “wind energy lidars” are developed (Jørgensen et al., 2004).

The main drawback of the wind lidars in complex terrain is that the horizontal wind measured from the instruments are based on the assumption that the data are collected on flat homogeneous terrain where the flow is homogeneous. Hence an adaptation to complex terrain is needed. Lidars have been previously adapted to various needs and used out of their designed envelope (Bingöl, 2005; Mikkelsen et al., 2008; Trujillo et al., 2009; Bingöl et al., 2009b). Such adaptations are of interest to wind turbine producers, wind park developers and the boundary layer meteorology community, as well as the lidar producers.

## ZephIR

The British company QinetiQ designed a cost effective lidar model, ZephIR, in 2002. Risø DTU bought the first *prototype* (Figure 62-right) in 2004 and the *commercial* version (Figure 62-left) in 2005.

The prototype and the commercial models differ from each other mainly in physical appearance and in minor signal processing capabilities. The prototype is a combination of two parts; an optical head and the laser source/sensor. The parts are separated by means of an optical cable, while in the commercial model the two part have to be assembled directly together with a third containing a battery. For both versions, comparisons with several tall, meteorological masts have already proven the instrument to be accurate over flat homogeneous terrain (Antoniou et al., 2004; Smith et al., 2006) and offshore (Peña et al., 2009). In complex terrain, the interpretation of the lidar data is still under development and Bingöl et al. (2009b) addresses this issue.

The instrument is a scanning tool that focuses the laser beam at different heights between 10 and 180 m and essentially assesses the radial velocity along the beam direction at the point of focus. The laser beam is deflected an angle  $\phi \approx 30^\circ$  from the vertical by making use of a prism, which rotates one full revolution every second. The along beam or radial velocity component of the wind is thus measured on a circle as indicated in Figure 63-(left). The ZephIR is a continuous wave lidar, therefore it can only measure at the focus height. For each focus height, the prism rotates three times before the instrument changes focus to the next height. At each full revolution, 49 radial velocities are recorded and a total of 147 measurements in three seconds are used to derive the wind speed. It is possible to change the focus distance in 1 s. The number of prism rotations, the signal processing speed and the recursive focus height change can be adjusted freely for the prototype model (Bingöl, 2005; Bingöl et al., 2010).

In conical scanning mode, the measured radial wind speed,  $v_r$ , combined with the scan azimuth angles,  $\theta$ , are fitted to the function (Harris et al., 2006, 2007):

$$v_r(\theta) = |A \cos(\Theta - \theta) + B| \quad (147)$$

where

$$U = \frac{A}{\sin \phi} \quad w = \frac{B}{\cos \phi} \quad . \quad (148)$$

The instrument can only measure the absolute value of the velocity. Therefore, the wind direction,  $\Theta$ , is directly taken from the fit with a ambiguity of  $180^\circ$  which can be identified with the wind direction readings from the instrument’s built-in mast. If the built-in vane is not present, as in prototype, a wind direction measurement is needed. The instrument records the 3 s statistics as well as the 10 min averages and one can use the raw data, which can be also recorded on demand, to calculate longer period averages or turbulence parameters. In this study, 30 min radial wind speeds are used, if the raw data are present, otherwise 10 min averages are preferred.

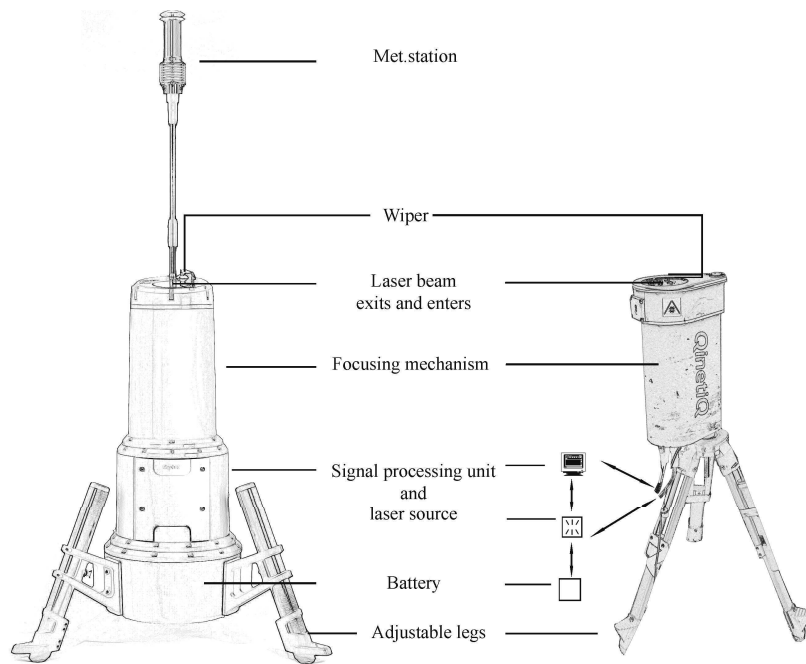


Figure 62: The ZephIR models which are used in the study. (Left) The commercial model which is 1.7 m tall and 0.5 m width. The instrument weights 100 kg. (Right) The prototype which is 1.5 m tall with adjustable legs. Including the signal processing unit, laser source/sensor and battery which are separated from the head by means of an optical cable, it weights 120 kg.

It is possible to remove the prism from a lidar and turn it into a “straight shooter” scanner where it measures the wind speed in the direction it is pointed. This working mode is referred as *staring mode* in this study. In staring mode, the beam direction is fixed and the instrument focuses at different distances and measures the component of the wind vector (Figure 63-right). The wind direction cannot be measured. Therefore, the beam direction must be known and the measured data must be used combined with a wind direction measurement instrument.

The staring mode approach was applied for the first time by Harris et al. (2006) with the aim of investigating possibilities for controlling the wind turbine based on upstream wind measurements with the prototype model of the ZephIR lidar. Subsequently, the prototype is used in other experiments in this context, like by mounting on a wind turbine to measure the wake behind (Bingöl et al., 2010; Trujillo et al., 2009), for synchronized multi-lidar field measurements (Mikkelsen et al., 2008) and horizontal wind profile measurements (Bingöl et al., 2009a).

## Windcube

The second wind energy lidar that came into the market is the Windcube, developed by the French company LeoSphere. The Windcube lidar is also a vertical profile measurement device and used in more recent studies (e.g. Peña et al. (2010)). Evaluation reports, mostly for the measurements over flat terrain, are also available recently (Albers and Janssen, 2008).

Contrary to the ZephIR, Windcube is a pulse lidar, which measures the wind speed and direction at measurement points  $90^\circ$  apart from each other on the conical scan circle for all chosen heights simultaneously. Each sector is scanned for 1 s and every 6 s (2 extra seconds are used to move the wedge), the values are used to derive wind speed and

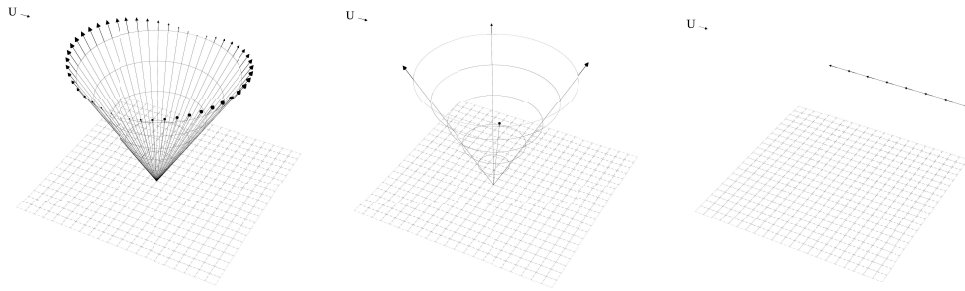


*Figure 63:* Lidar working modes. The arrows denote the laser beam direction and the measured wind components. (Top) The original conical scanning mode of ZephIR. At upwind and downwind directions the absolute value of the along beam velocity component has the maximum value. When the wind is perpendicular to the beam direction the wind component on the radial vector has a minimum value. (Middle) Conical Scanning Mode of the Windcube lidar. The data is recorded only in four equally separated sectors on the conical circle. (Bottom) Illustration of the Staring Mode. The beam direction is fixed and the instrument focuses at different distances and measures the component of the wind vector indicated by the arrows. In this mode, the lidar data is used combined with separate wind direction measurements

direction profiles; calculated via (Lindelöw, 2007);

$$u = \sqrt{u_1^2 + u_2^2} \quad (149)$$

where  $u_1$  and  $u_2$  are the horizontal plane wind speed components, derived as

$$u_1 = v_r(0) - v_r(\pi), \quad u_2 = v_r(\frac{\pi}{2}) - v_r(\frac{3\pi}{2}) \quad (150)$$

and

$$w = \frac{v_r(0) + v_r(\pi)}{2 \cos \phi} = \frac{v_r(\frac{\pi}{2}) + v_r(\frac{3\pi}{2})}{2 \cos \phi}, \quad \Theta = \arctan(u_1, u_2) \quad (151)$$

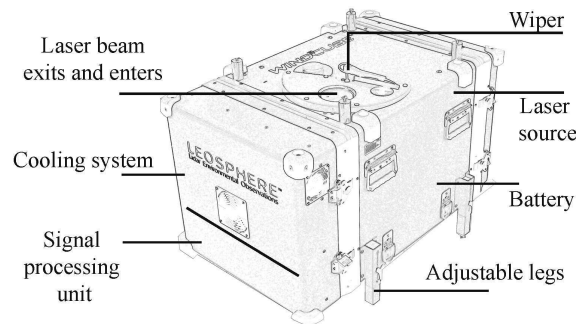


*Figure 64:* Leosphere Windcube; the laser source is located right on top of the unit and generates the beam in the direction to the the prism located under the beam exit lens where it is tilted to upwards. The dimensions are  $0.7 \text{ m} \times 0.4 \text{ m} \times 0.4 \text{ m}$  and the instrument weights  $\approx 55 \text{ kg}$ .

The Windcube is equally mobile to ZephIR with the added advantage that the wedge opening angle,  $\phi$ , can be adjusted between  $15^\circ$  and  $30^\circ$ . This option is introduced as a “bypass” for complex terrain problems such as inhomogeneous flow. This hypothesis is discussed in the section 7.3. Windcube is also being used in staring mode in recent studies (e.g. Mikkelsen et al. (2008)) but there is no published journal article available on the topic that the author is aware of.



## Other lidars

The other lidar instruments like Gallion, by Sgurr Energy, has the classical design of the conical scan as well as the possibility of making any possible pattern between  $0^\circ$  and  $0^\circ$  in pan, between  $0^\circ$  and  $0^\circ$  in tilt. The instrument is new and is not used in any of the experiments related to this chapter. When this chapter is written Gallion was still under tests at Risø Høvsøre Test Site. An early technical report was published (Gottschall et al., 2009).

## 7.3 Challenges and Known Issues

### The conical scanning error in complex terrain

The success of the lidar conical scan operation is limited to flat terrain. In complex terrain, the flow is no longer homogeneous and that can give a large bias on the horizontal wind speed estimated from the lidar up to 10% in horizontal wind speed measurements (Bingöl et al., 2008a). The basic problem also applies to any other conically scanning lidar and sodars as well (Bradley, 2008). Some of the lidar producers present the smaller half opening angle (Leosphere, 2009) or custom scan regimes (SgurrEnergy, 2009) as one of the possible solutions to overcome the problem caused by the inhomogeneous flow.

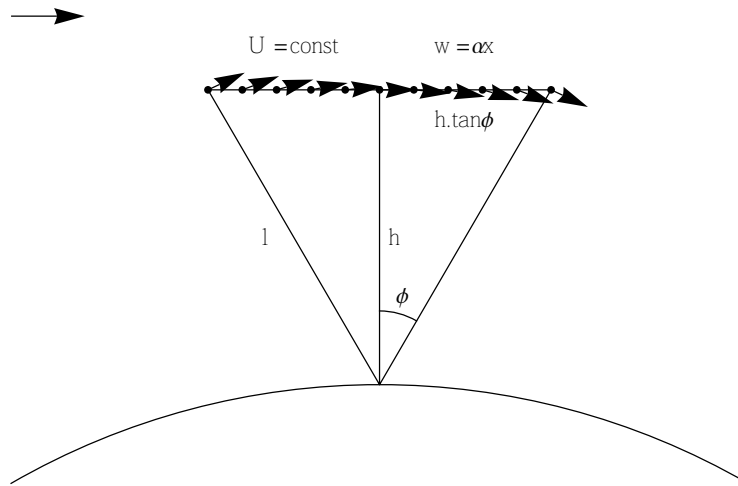


Figure 65: Simplified lidar scanning geometry in a linearly changing mean flow. The lidar is shooting upstream and downstream with a half opening angle  $\phi$ .

The error can be illustrated as in Figure 65 where the horizontal wind speed  $U$  is taken constant, but the vertical wind speed  $w$  is assumed to change linearly with the downwind position; parametrised with a factor of  $\alpha$ . This is similar to the case over a hill. The upstream has positive and the downstream has negative tilt relative to the top of the hill. The projected wind speed on the upwind and downwind beams are

$$v_{up} = -(U + h\alpha) \sin \phi \quad v_{down} = (U + h\alpha) \sin \phi \quad . \quad (152)$$

Assuming horizontal inhomogeneity, the horizontal velocity can be calculated as

$$U_{lidar} = \frac{v_{down} - v_{up}}{2 \sin \phi} = U + h\alpha, \quad (153)$$

which shows, in the case of a negative  $\alpha$  that the horizontal wind is *underestimated* (Bingöl et al., 2008a). A simplified three dimensional analysis of the error is derived by Bingöl et al. (2008b), where the the mean wind field  $\mathbf{U} = (u, v, w)$  is assumed to vary

linearly. In such case, the wind vector estimations become:

$$w_{\text{lidar}} = u + h \frac{\partial w}{\partial x} \quad (154)$$

$$v_{\text{lidar}} = v + h \frac{\partial w}{\partial y} \quad (155)$$

$$w_{\text{lidar}} = w - \frac{l}{2} \tan^2 \phi \frac{\partial w}{\partial z} \quad (156)$$

where  $l$  is the focus distance  $h/\cos\phi$ . Eq. 156 shows that the error due to inhomogeneity of the mean flow vanishes for the vertical component as the half opening angle  $\phi$  goes to zero. The errors on the horizontal components are independent of  $\phi$ .

### Predicting the error by means of a flow model

Conical scanning mode of the lidar can be simulated in flow models. An automated script for commercial software WAsP Engineering has been written by the author for the ZephIR and Windcube lidars and has been published (Bingöl and Mann, 2009). The method can be simplified as below and can be adapted to different scanning regimes such as different  $\phi$ .

A unit vector in the direction of the laser beam can be written as,

$$\mathbf{n} = (\cos\theta \sin\phi, \sin\theta \sin\phi, \cos\phi) \quad (157)$$

where  $\phi$  is half opening angle and  $\theta$  is the geographical angle in which the beam is pointing. As it is previously stated, assuming the flow field to be roughly homogeneous over the averaging circle with a mean  $\mathbf{U} = (u, v, w)$ . The radial velocity in the direction of the laser beam, the radial wind speed  $v_r$ , calculated at  $\theta$  azimuth of the prism is the projection of  $\mathbf{U}$  onto  $\mathbf{n}$ :

$$v_r(\theta) = \mathbf{n}(\theta) \cdot \mathbf{U}(\mathbf{n}(\theta)l - (0, 0, z')), \quad (158)$$

where  $z'$  is absolute position of the instrument a.g.l. if it is placed on an artificial elevation (e.g. tower).

For ZephIR lidar, after calculating 60 points on the conical circle, all three velocity components can be obtained through a linear fit to trigonometric series

$$a + b \cos\theta + c \sin\theta, \quad (159)$$

as;

$$u = \frac{b}{\sin\phi} \quad v = \frac{c}{\sin\phi} \quad w = \frac{a}{\cos\phi} \quad \Theta = \arctan \frac{v}{u} . \quad (160)$$

For Windcube, radial wind speed  $v_r$  from calculated at four measurement points are used in Eq. (149)–(151) directly to derive wind speed components and direction.

### Does smaller cone angle make better measurements?

The standard cone angle,  $\phi$ , for most of the lidars is  $30^\circ$  but reducing the cone angle to  $15^\circ$  is introduced as a “bypass” for complex terrain problems such as inhomogeneous flow. In section 7.3, we have seen that, theoretically, the error is not dependent on the cone angle. A validation of this theory has been made with a field measurement campaign (Bingöl, 2009) and experimental results are discussed further in section 7.4 of this chapter.

### Extracting momentum flux

Momentum flux measurements are important in order to understand the atmospheric flow over the terrain. It is possible to extract the momentum flux from lidars in conical scanning mode. The methods listed in this section describes a general idea of extracting

momentum fluxes from lidar, which would not only be helpful in flat terrain but would be very significant parameter in complex terrain. Although this basic information is given here, the readers are encourage to make further reading about the standard bias of lidars for these methods from the reference Mann et al. (2010). In refereed article it has been shown that the error of calculating the momentum flux with the method below can be between 15% to 60% for ZephIR lidar and around 20% for Windcube lidar at the heights of interest of wind energy developers. Furthermore the paper, includes a section explaining how to avoid this possible error in flat terrain. The method is not tested in complex terrain and readers should be aware of this phenomenon.

**From ZephIR lidar** The variance of the radial velocity for ZephIR lidar can be calculated as (Eberhard et al., 1989):

$$\begin{aligned}
\sigma^2(v_r(\theta)) &= \left\langle [\mathbf{n}(\theta) \cdot \mathbf{u}'(\mathbf{n}(\theta)l)]^2 \right\rangle \\
&= \sigma_u^2 \sin^2 \phi \cos^2 \theta + \sigma_v^2 \sin^2 \phi \sin^2 \theta + \sigma_w^2 \cos^2 \phi + \\
&\quad 2 \langle u'v' \rangle \sin^2 \phi \cos \theta \sin \theta + \\
&\quad 2 \langle u'w' \rangle \cos \phi \sin \phi \cos \theta + \\
&\quad 2 \langle v'w' \rangle \cos \phi \sin \phi \sin \theta
\end{aligned} \tag{161}$$

For the upwind ( $\theta = 180^\circ$ ), and the downwind ( $\theta = 0^\circ$ ) the variances can be extracted as,

$$\begin{aligned}
\sigma_{\text{up}}^2 \equiv \sigma^2(v_{\text{up}}) &= \sigma_u^2 \sin^2 \phi + \sigma_w^2 \cos^2 \phi \\
&\quad - 2 \langle u'w' \rangle \sin \phi \cos \phi
\end{aligned} \tag{162}$$

$$\begin{aligned}
\sigma_{\text{down}}^2 \equiv \sigma^2(v_{\text{down}}) &= \sigma_u^2 \sin^2 \phi + \sigma_w^2 \cos^2 \phi \\
&\quad + 2 \langle u'w' \rangle \sin \phi \cos \phi .
\end{aligned} \tag{163}$$

The momentum flux is the difference between Eq. (162) and (163):

$$\langle u'w' \rangle = \frac{\sigma_{\text{down}}^2 - \sigma_{\text{up}}^2}{4 \sin \phi \cos \phi} . \tag{164}$$

**From Windcube lidar** Following the same logic, for Windcube we can derive from four azimuthal positions separated  $\pi/2$  around the circle formed by the conical scanning. Therefore, the momentum flux can be defined as;

$$\begin{pmatrix} \Delta_0 \\ \Delta_{\pi/2} \end{pmatrix} = \begin{pmatrix} \sigma^2(v_r(\theta)) - \sigma^2(v_r(\theta + \pi)) \\ \sigma^2(v_r(\theta + \pi/2)) - \sigma^2(v_r(\theta + 3\pi/2)) \end{pmatrix}, \tag{165}$$

i.e. the differences in variances in two perpendicular directions. We can then use Eq. (161) to get

$$\begin{pmatrix} \Delta_0 \\ \Delta_{\pi/2} \end{pmatrix} = 2 \sin 2\phi \begin{pmatrix} \cos \theta & \sin \theta \\ -\sin \theta & \cos \theta \end{pmatrix} \begin{pmatrix} \langle u'w' \rangle \\ \langle v'w' \rangle \end{pmatrix}. \tag{166}$$

So knowing the half opening angle  $\phi$  and the angle of the first beam direction relative to the mean wind direction,  $\theta$ , we can calculate the vertical flux of horizontal momentum in the mean wind direction and perpendicular to that:

$$\begin{pmatrix} \langle u'w' \rangle \\ \langle v'w' \rangle \end{pmatrix} = \frac{1}{2 \sin 2\phi} \begin{pmatrix} \cos \theta & -\sin \theta \\ \sin \theta & \cos \theta \end{pmatrix} \begin{pmatrix} \Delta_0 \\ \Delta_{\pi/2} \end{pmatrix}. \tag{167}$$

## 7.4 Experimental studies

Conically scanning lidars assume the flow to be homogeneous in order to deduce the horizontal wind speed as it has been described in section 7.3. However, in moderately

complex or complex terrain this assumption is not valid implying a risk that the lidar will derive an erroneous wind speed. The magnitude of this error was measured by collocating a meteorological mast and a lidar at two Greek sites, one hilly and one mountainous. In order to predict the error for various wind directions the flows at both sites were simulated with the linearised flow model LINCOM as described in section 7.3. The measurement data were compared with the model predictions with good results for the hilly site.

In both experiments lidar data are collected by the standard QinetiQ software and synchronized with mast data by the CRES WindRose software. Instruments are calibrated according to the requirements of IEC61400-12-1:2005/Annex F and MEASNET guidelines at CRES Laboratory for Wind Turbine Testing.

### **Hilly site; Lavrio**

The Lavrio site is located 38 km SE of the center of Athens close to the coast of the Aegean Sea. The experiment took place between 2008-Dec-01 and 2008-Jan-15. The highest point is 200 m ASL and main wind direction is  $0^\circ$ . The 100 m triangular lattice reference meteorological mast is equipped with cup anemometers and vanes at five heights (10, 32, 54, 76, and 100 m). Cups are to the east and vanes are to the west. There are also ultrasonic 3D Gill anemometers at three heights (34, 78, and 98 m) which are not used in this study due to problems with icing but this does not influence the used cup anemometers and vanes. Additionally, the temperature profile is measured using differential thermometers, as well as, the atmospheric pressure and the solar radiation. Dedicated instrumentation is used for signal protection, filtering and conditioning. The lidar is located nearly 12 m north of the mast. The measurement heights are 32 and 78 m.

At Lavrio, most of the winds are northerly which means it is blowing from lidar to the mast. The scatter plots (Figure 66-top) show generally 5 to 7% errors in wind speed measurements. For the WASP Engineering model we have used  $3\text{ km} \times 3\text{ km}$  map with 4 m resolution simulating the wind direction from  $0^\circ$  to  $360^\circ$  with  $6^\circ$  bins. We have used all the data from the mast at each height and averaged them according to the wind direction in  $10^\circ$  bins.

The comparison between the model and the measurements is shown in Figure 66 (lower two plots) and shows good correlation in some sectors. The mast is voluminous, thus the selected data must be far from boom direction which is  $113^\circ$ . These sectors are marked with light grey areas in the plots for  $\pm 30^\circ$ . The ideal ratio line of one is also shown and it represents the cases where there is no difference between the lidar and the mast measurements. The black line is the model and the points are the measurement results.

Especially for northerly directions the model predicts the lidar error well for both heights, while for the southerly directions the prediction is not so good. We believe this can be a result of the limitation of WASP Engineering. In southerly directions very close to the site there are steep slopes. In this sector and height, the flow model has difficulties predicting the tilt angles as compared to sonic measurements for periods with no icing problems.

### **Mountainous site; Panahaiko**

The Panahaiko site is located 165 km northwest of Athens, at Vounogiorgis mountain south east of the village Sella, 14 km south of the Patras Sea. The experiment ran from 2007-Sep-19 to 2007-Oct-11. The terrain in the vicinity of the site is very complex. Highest point is 2000 m in the region where the experiment surrounding is between 1700 and 1750 m ASL. The prevailing wind directions are ENE and SW. The triangular lattice reference meteorological mast has six cup anemometers (10, 20, 30, 40, and 54 m) and two vanes (40 and 54 m). Additionally, there are also air temperature and relative humidity measurements at 54 m. The boom cross-section is  $40\text{ mm} \times 40\text{ mm}$ . All wind sensors are mounted at a height of 75 cm above the boom and at a distance of 225 cm from the outer

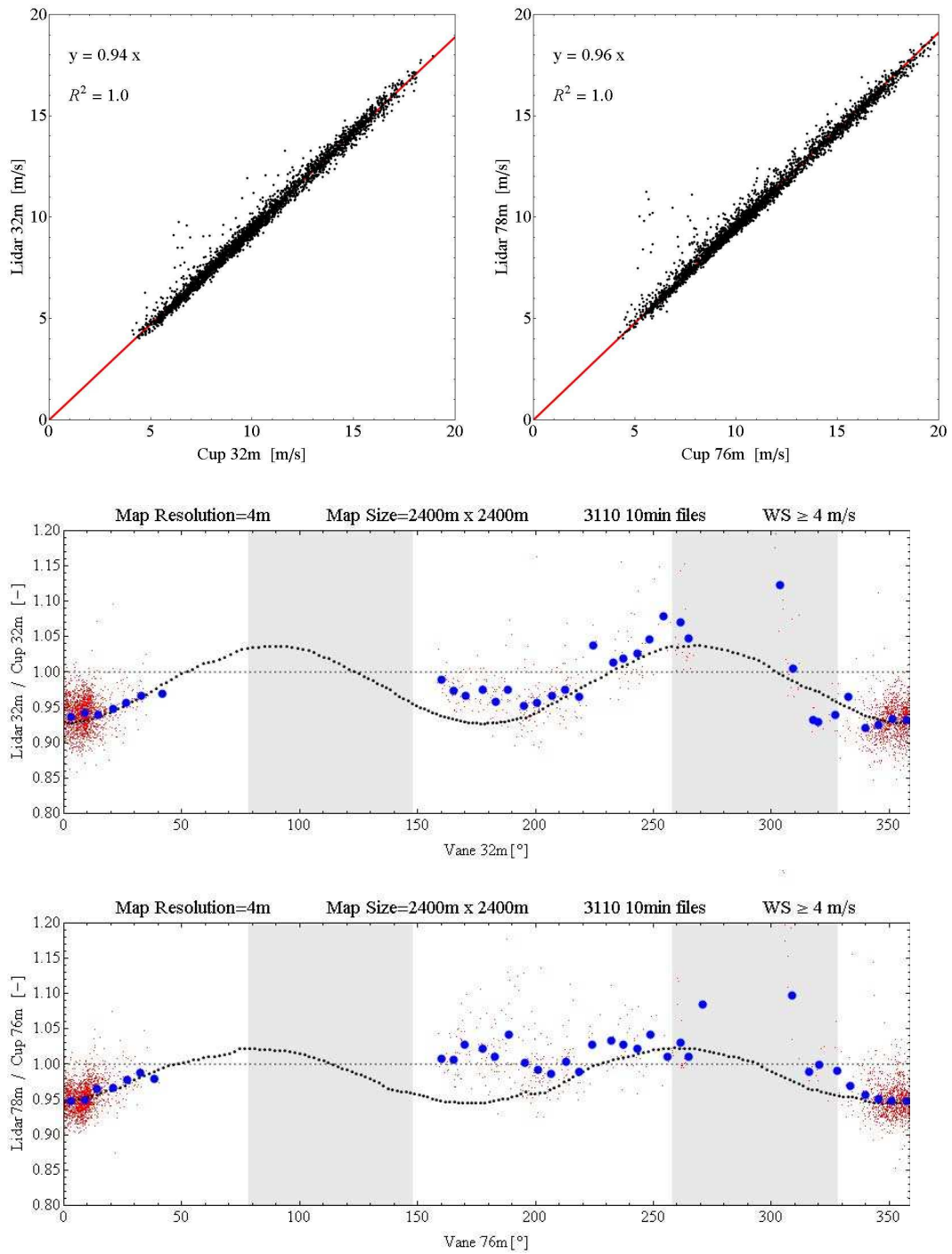


Figure 66: Lavrio: The scatter plots show generally 4% to 6% errors in wind speed measurements (top). Lower two plots are the comparison between the model and the measurement data for two different heights. Small red dots are the error ratio for each 10 min measurement, big blue dots are the averaged  $6^\circ$  bins according to the wind direction and medium black dots are the model results. The mast shadow is marked with grey rectangles. The ideal ratio line of one, dashed blue, is also shown and it represents the cases where there is no difference between the lidar and the mast measurements. Especially for northerly directions the model predicts the lidar error well for both heights, while for the southerly directions the prediction is not so good.

mast leg. The lidar is located nearly 20 m WSW of the mast. The lidar measurement heights are 30 m and 55 m.

The second site, Panahaiko, is much more complex than Lavrio, so there are many sectors which could be problematic for WAsP Engineering to model. The scatter plots in Figure 67 (top) show data for all directions. The mast at Panahaiko is smaller than at Lavrio so the sector with flow distortion is smaller ( $\pm 25^\circ$ ) shown in grey in the figure. The boom direction is  $210^\circ$ .

The comparison between the modelled error and the measurements as a function of direction is shown in Figure 67 (lower two plots). It is not a perfect prediction, but the model gives the right order of magnitude for this complex site.

The outliers mainly seen for the larger heights in Figures 66 and 67 are probably due to cloud return as discussed in Courtney et al. (2008).

### Validation of cone angle hypothesis

The hypothesis that reducing the cone angle will not change the systematic error on the horizontal wind measured by the lidar (section 7.3) was tested with measurements on a non-forested hilly site in Greece. The experiment was made by CRES and statistical data were shared with the author<sup>9</sup>.

One ZephIR and two Windcube lidar units were located next to a tall meteorological mast at Greece Renewable Energy Laboratories test site at Lavrio (Figure 68) which is described in section 7.4. The experiment took place between 2008-Sep-17 and 2009-Jan-17. The measurement location was on a hill with a gentle slope of approximately  $10^\circ$  in the main wind direction sector to both sites. Further away the northerly sector is a flat terrain, southerly sector includes more hill after approximately 150 m (Figure 69).

The 100 m triangular lattice reference meteorological mast was equipped with cup anemometers and vanes at three heights (54, 76 and 100 m). Cups are to the east and vanes are to the west. The lidars were located between 12 and 20 m north of the mast. One of the Windcube units and the ZephIR lidar were in operation with a  $\phi = 30^\circ$  prism while the other Windcube operated with  $\phi = 15^\circ$ . The ZephIR unit measured at 54, 78, 100 and 120 m. Both Windcube units measured at 40, 54, 78, 100, 120, 140 and 160 m.

The data from northerly sector,  $0 \pm 15^\circ$  were selected for comparison. All available data, 1163 of 10 min runs, were used. Initially, the horizontal wind speed, wind direction and standard deviation of the horizontal wind speed were compared with the sonic anemometers at same heights; 54, 78 and 100 m (Figures 70, 71 and 72). The results agreed with a previous experiment at the same site for the same wind sector (Bingöl et al., 2008a). The horizontal wind speed measurements from the lidars were in good correlation but wind direction and the standard deviation of the horizontal wind speed deteriorate for the  $15^\circ$  Windcube.

Subsequently, horizontal wind speed and flow inclination angles were compared between the  $30^\circ$  prism instruments and the  $15^\circ$  Windcube for available common heights (Figures 73 and 74). The results showed that the horizontal wind speed measurements were not effected by the cone angle. However, the flow inclination angles showed less scatter with the lower cone angle as it was expected.

As a conclusion, it can be stated that the lower half opening angle,  $\phi = 15^\circ$  do not help in complex terrain on improving the horizontal wind speed measurements. For any other statistical term the  $\phi = 15^\circ$  has an even higher bias in measurements. Therefore, the hypothesis described at the beginning of this section agrees with the measurements and the  $30^\circ$  prism is advised by the author instead of  $15^\circ$  prism at such sites.

---

<sup>9</sup>Courtesy of Dimitri Foussekis, The Centre for Renewable Energy Sources (CRES) GREECE

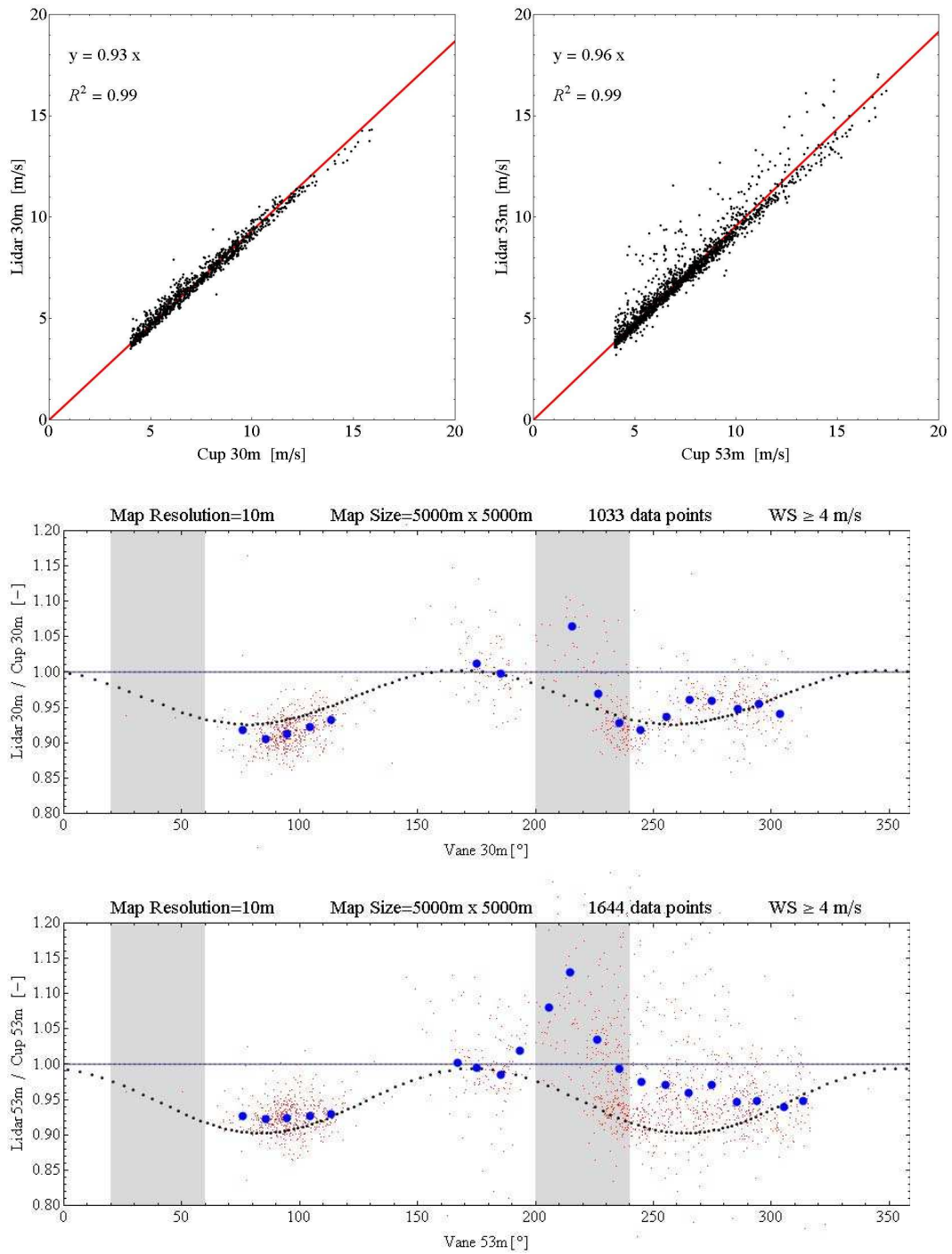


Figure 67: Panahaiko: The scatter plots show generally 4% to 7% errors in wind speed measurements (top). Lower two plots are the comparison between the model and the measurement data for two different heights. Small red dots are the error ratio for each 10 min measurement, big blue dots are the averaged  $10^\circ$  bins according to the wind direction and medium black dots are the model results. The mast shadow is marked with grey rectangles. The ideal ratio line of one, dashed blue, is also shown and it represents the cases where there is no difference between the lidar and the mast measurements. It is not a perfect prediction, but the model gives the right order of magnitude for this complex site.



Figure 68: The experimental set-up at Lavrio, Greece for the comparison of the lidars in different working modes.

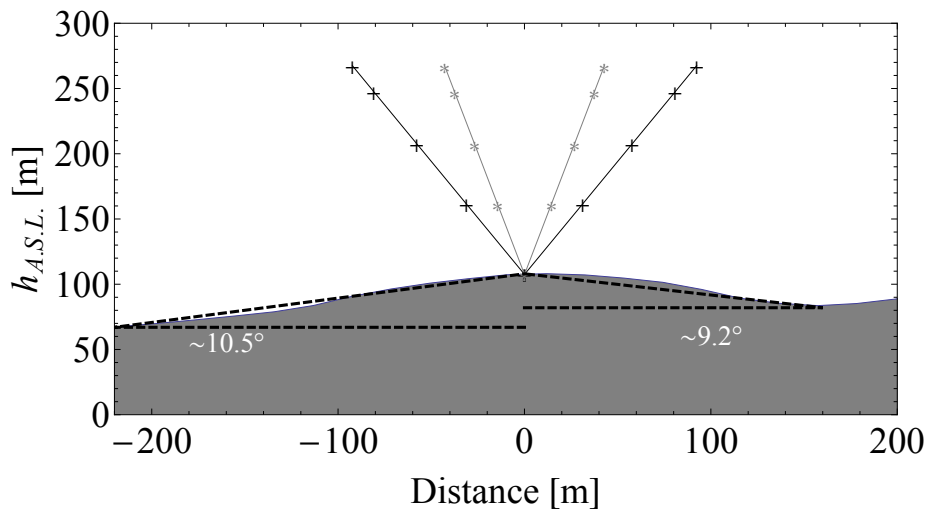


Figure 69: The hill transect at Lavrio. Left is northerly direction which is the dominant wind direction.

## 7.5 Conclusions

Lidars, used over flat homogeneous terrain, show errors in the mean wind speed of only a few percent. We have shown that in complex terrain of the type commonly used for wind turbine parks, errors in the horizontal wind speed as measured by a conically scanning lidar can be of the order of 10%. This is due to the lack of horizontal homogeneity of the flow, which is assumed in the interpretation of the lidar data. The findings are based on two experiments involving collocated lidars and meteorological masts in complex terrain, together with flow calculations over the same terrains. For that calculation we use WAsP Engineering, and we find that the calculations match the experiment except for some sectors where the terrain is particularly steep. This is not surprising, since the WAsP Engineering is built on a linearized flow model, which is only valid for limited terrain



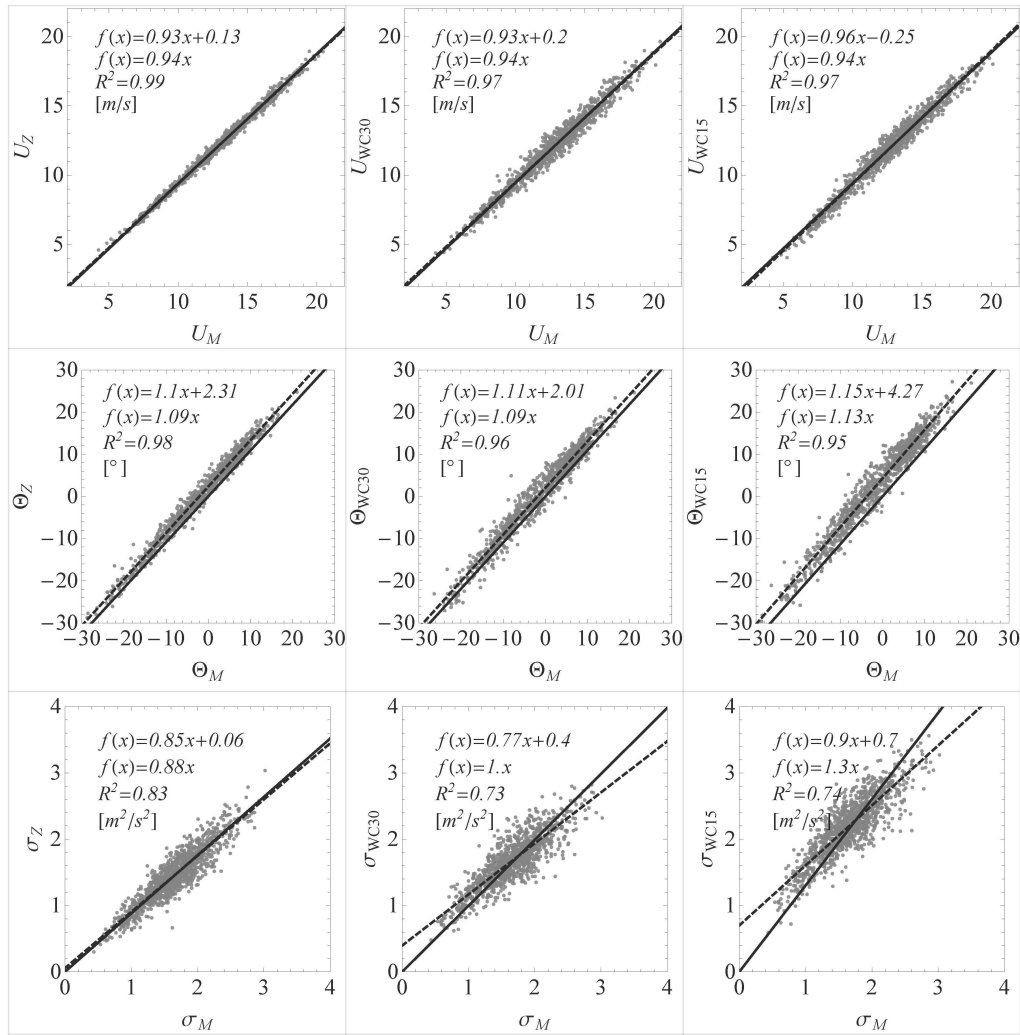


Figure 70: Lidars vs Sonics at 54 m. Top row is the horizontal wind speed, middle row is the wind direction and bottom row is the standard deviation of the horizontal wind speed.

slopes. The model is not for highly complex terrain that can incorporate the stability effect in any reliable way. Furthermore most of the wind speeds analyzed, from both sites, are quite high so it is not unreasonable to assume neutral stratification. That is why there is concluding thoughts about stability. To make more reliable predictions of the error in very steep terrain, other more advanced flow models ((Castro et al., 2003)) must be used.

The hypothesis that the lidar conical scan error due to inhomogeneity of the mean flow is independent of the half opening angle  $\phi$  on the horizontal components has been supported with experimental results from moderately-complex terrain site measurements. The synchronized measurements from the lidars with different half opening angles and meteorological mast instruments reported no positive effect of smaller half opening angle in horizontal wind speed measurements, contrary to what was being suggested by some of the producers and academics. The measurements agreed with the described hypothesis and it can be concluded that smaller half opening angles can only be helpful in sites with the presence of dense canopy or obstacles, in order to measure the desired height easily.

As a general conclusion of this study, lidars can be used in complex terrain with support of flow models which should include well defined flow separation predictions. It is

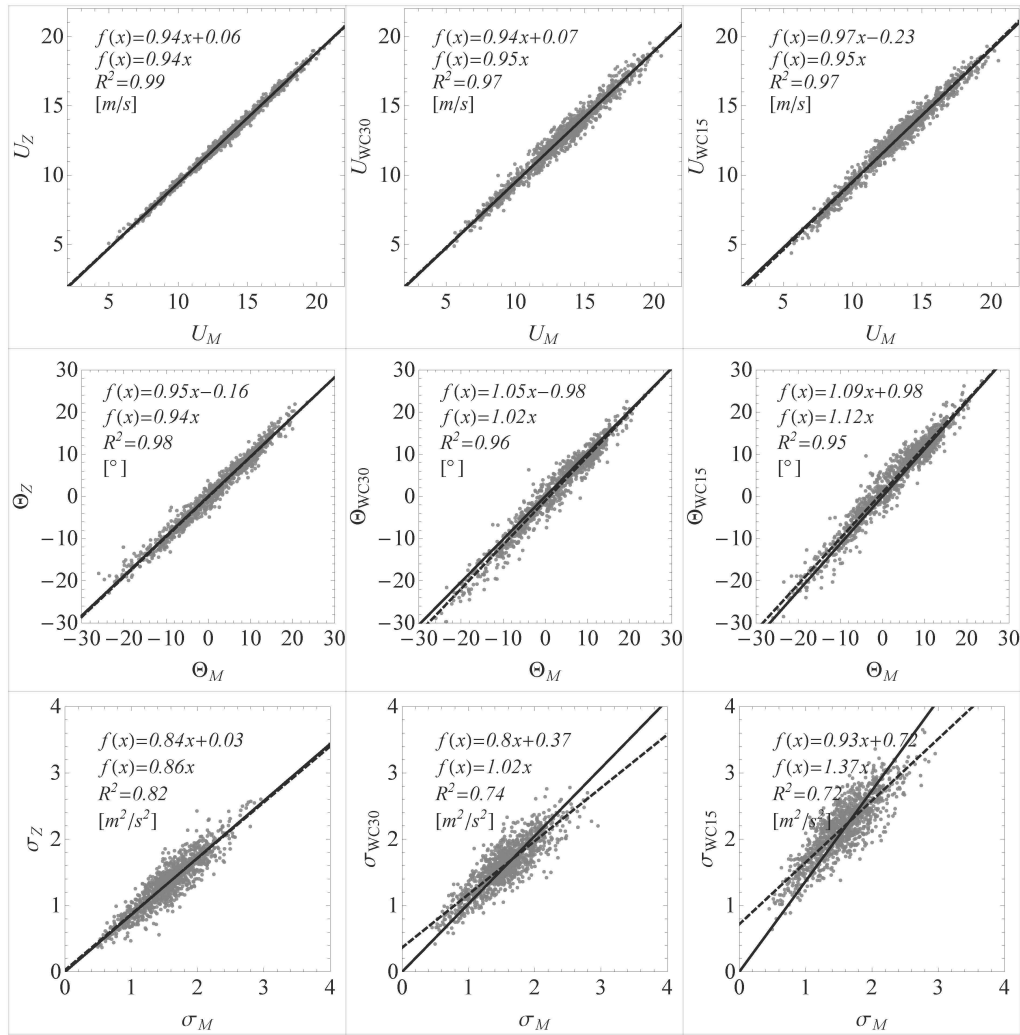


Figure 71: Lidars vs Sonics at 78 m. Top row is the horizontal wind speed, middle row is the wind direction and bottom row is the standard deviation of the horizontal wind speed.

important to note that modelling must be accompanied by flow analysis before and after the measurements. Prior to the measurements, models should be used to detect possible suitable locations for lidar placement. This can be done with linearised or advanced CFD models because any of these can perform a simple assessment based on rough calculations of error values. Thus, the majority of sub-optimal locations can be eliminated. Subsequently, any attempt to correct the lidar data must be performed with an advanced flow model, preferably a CFD model that has already been tested in complex terrain with measurements. It is advised that the described modelling steps for lidar data correction should be included in wind turbine and site assessment and implemented in well established international standards (e.g. IEC 61400 series) after further studies.

The author also would like to bring to attention certain shortcomings of the current commercial versions of the lidar instruments. Some of the experiments, which are conducted in this study or cited in the manuscript, would not have been possible without full software and hardware access to the instruments. The re-formulation of signal processing methods and the physical manipulation of instrument parts were essential to achieve the necessary scanning speed and to create custom scan regimes. This underlines the importance of instrument flexibility for a wide range of uses (e.g. in complex terrain).

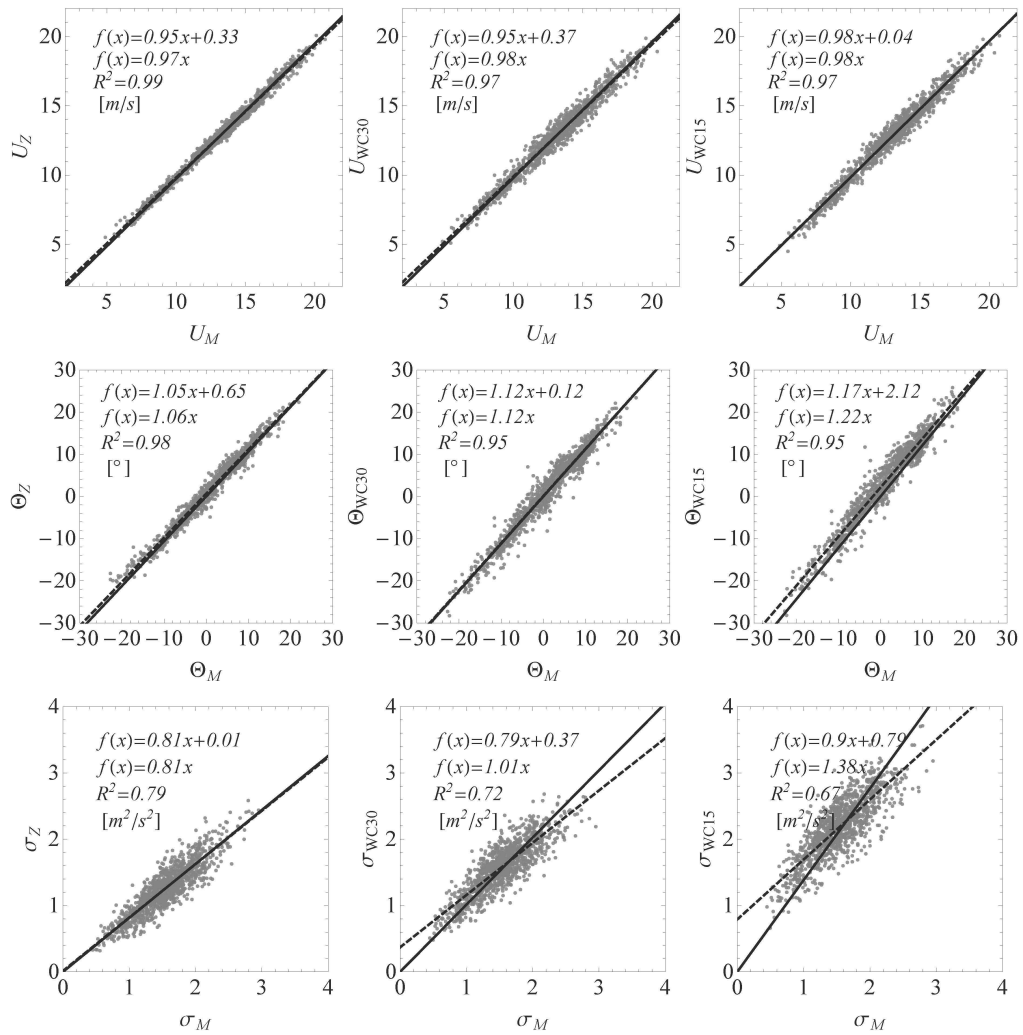


Figure 72: Lidars vs Sonics at 100 m. Top row is the horizontal wind speed, middle row is the wind direction and bottom row is the standard deviation of the horizontal wind speed.

Unfortunately, most of the producers of currently available commercial models are gradually stepping back from such an approach in an effort to create stable, robust instruments. In order to achieve faster development in lidar technology in complex terrain, the author believes that these instruments must be accessible in a software as well as a hardware level, and suggests a more detailed documented developer interface mode.

Concluding, current standards of the instruments are adequate to perform wind measurements over most of the terrain types and it is believed that it is possible for lidars to replace conventional meteorological mast in the future if the data interpretation is improved, particularly.

## Notation

- a.g.l. above ground level
- $h$  focusing height
- $l$  focus distance
- $\mathbf{n}$  unit vector in the direction of the laser beam
- $u$  longitudinal wind speed component
- $u_i$  wind speed component in the  $i$  direction

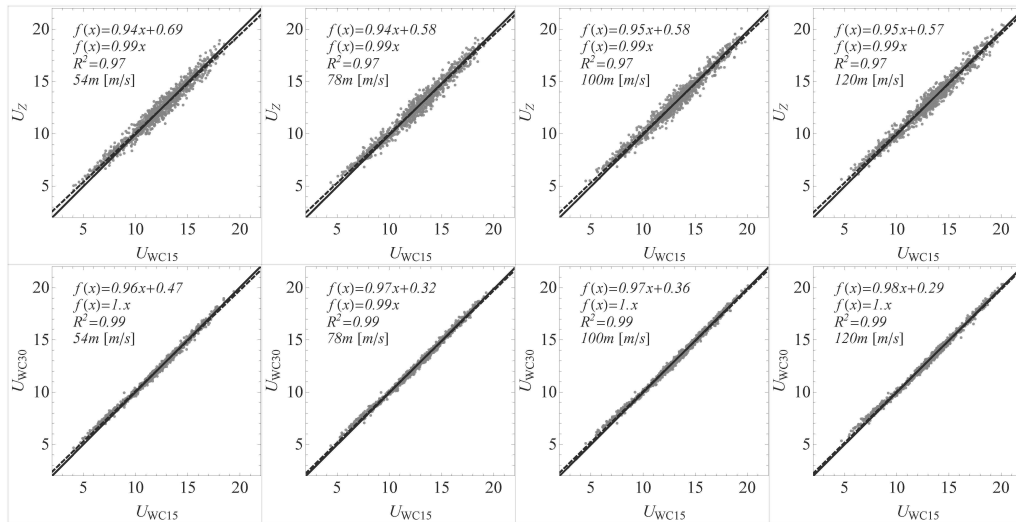


Figure 73: Horizontal wind speed correlation between the 30° prism instruments vs. 15° Windcube for available heights; 54, 78, 100 and 120 m. The ZephIR is at the top

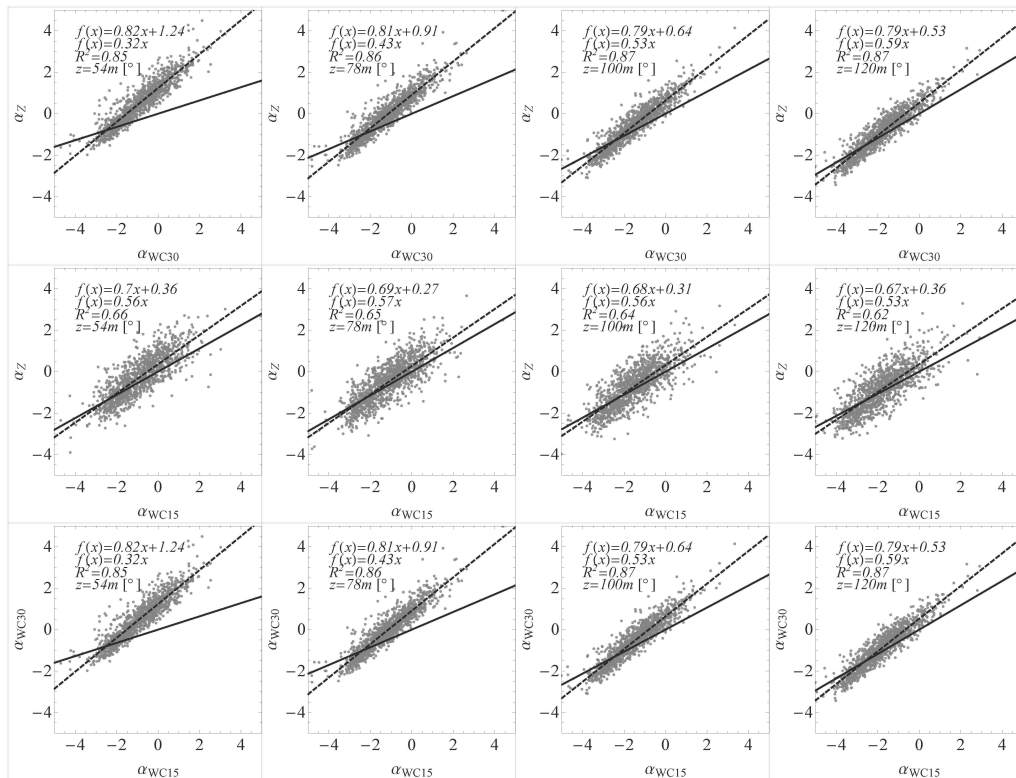


Figure 74: Flow inclination angles correlation between the 30° prism instruments vs 15° Windcube for available heights

- $U$  horizontal wind speed
- $\mathbf{U}$  mean wind field
- $v$  transversal wind speed component
- $v_{down}$  projected wind speed in the downstream beam
- $v_{up}$  projected wind speed in the upstream beam
- $v_r$  radial wind speed
- $w$  vertical wind speed
- $X'$  fluctuation part of a variable  $X$  from the mean

$z'$	absolute position of the instrument a.g.l
$\alpha$	linear factor for parametrization of the vertical wind speed
$\theta$	scan azimuth lidar angle
$\Theta$	wind direction
$\sigma_X^2$	variance of a variable $X$
$\phi$	deflection lidar angle from the vertical or wedge angle
$\langle X \rangle$	time average of a variable $X$

## References

- Albers A. and Janssen A. (2008) Windcube evaluation report. Technical report, Deutsche WindGuard Consulting GmbH
- Antoniou I., Jørgensen H. E., Mikkelsen T., Petersen T. F., Warmbier G, and Smith D. (2004) Comparison of wind speed and power curve measurements using a cup anemometer, a lidar and a sodar. *Proc. of the European Wind Energy Conf.*, London
- Bingöl F. (2005) Adapting Laser Doppler Anemometer into Wind Energy. Master's thesis, Technical University of Denmark, Lyngby
- Bingöl F. (2009) *Complex Terrain and Wind Lidars*. PhD thesis, Risø DTU, Roskilde
- Bingöl F. and Mann J. (2009) Lidar performance estimation script for WASP Engineering. Technical report, Risø DTU, Roskilde
- Bingöl F., Mann J., and Foussekis D. (2008) Lidar error estimation with wasp engineering. *IOP Conf. Series: Earth and Environ. Sci.*, 012058 (9pp)
- Bingöl F., Mann J., and Foussekis D. (2008) Modeling conically scanning lidar error in complex terrain with WASP Engineering. Risø-R-1664(EN), Risø DTU, Roskilde
- Bingöl F., Mann J., Dellwik E., Sogachev A., and Rathmann O. (2009) Flow over limited size forest; measurements and modelling. *Wind Energy*, under review.
- Bingöl F., Mann J., and Foussekis D. (2009) Conically scanning lidar error in complex terrain. *Meteorologische Z.*, **18**:189–195
- Bingöl F., Mann J., and Larsen G.-C. (2010) Lidar measurements of wake dynamics Part I: One Dimensional Scanning. *Wind Energy* **13**:51–61
- Bradley S. (2008) Wind speed errors for lidars and sodars in complex terrain. *IOP Conf. Series: Earth and Environ. Sci.* 012061 (7pp)
- Castro F., Palma J., and Lopes A. (2003) Simulation of the askervein flow. part 1: Reynolds averaged Navier-Stokes equations (k-epsilon turbulence model). *Bound.-Layer Meteorol.* **107**:501–530
- Courtney M., Wagner R., and Lindelöw P. (2008) Testing and comparison of lidars for profile and turbulence measurements in wind energy. *IOP Conf. Series: Earth and Environ. Sci.* 012021 (14pp)
- Eberhard W. L., Cupp R. E., and Healy K. R. (1989) Doppler lidar measurement of profiles of turbulence and momentum flux. *J. Atmos. Oceanic Tech.* **6**:809–819
- Gottschall J., Lindelöw P., and Courtney M. (2009) Executive summary of key test results for SgurrEnergy galion. Independent test results, Risø DTU, Roskilde
- Harris M., Hand M., and Wright A. (2006) Lidar for turbine control. Technical Report NREL/TP-500-39154, NREL
- Harris M., Bryce D. J., Coffey A. S., Smith D. A., Birkemeyer J., and Knopf U. (2007) Advance measurement of gusts by laser anemometry. *J. Wind Eng. Ind. Aerodyn.* **95**:1637–1647
- Hastings D. A., Dunbar P. K., Elphinstone G. M., Bootz M., Murakami H., Maruyama H., Masaharu H., Holland P., Payne J., Bryant N. A., Logan T. L., Muller J. P., Schreier G., and MacDonald J. S. (1999) The global land one-kilometer base elevation (globe) digital elevation model, version 1.0. Digital data base on the www and cd-roms, National Oceanic and Atmospheric Administration, National Geophysical Data Center, Boulder
- IEC (2005) 61400-12-1: Power performance measurements of electricity producing wind turbines. Technical report, International Electrotechnical Commission
- JRC (2006) Global land cover 2000 - Europe. Technical report, European Environmental Agency

- Jørgensen H., Mikkelsen T., Mann J., Bryce D., Coffey A. S., Harris M., and Smith D. A. (2004) Site wind field determination using a CW Doppler lidar - comparison with cup anemometers at Risø. *Proc. EWEA Special Topic Conference: The Science of Making Torque from Wind* 261–266. Delft University, Delft
- Leosphere (2009) Windcube information booklet
- Lindelöw P. (2007) Uncertainties in wind assessment with lidar. Risø technical report, Risø-I-1234(EN), Risø DTU, Roskilde
- Mann J., Peña A., Bingöl F., Wagner R., and Courtney M. S. (2010) Lidar scanning of momentum flux in and above the surface layer. *J. Atmos. Oceanic Tech.*, in press
- Mayor S. D., Lenschow D. H., Schwiesow R. L., Mann J., Frush C. L., and Simon M. K. (1997) Validation of NCAR 10.6- $\mu\text{m}$   $\text{CO}_2$  Doppler lidar radial velocity measurements and comparison with a 915-MHz profiler. *J. Atmos. Oceanic Tech.*, **14**:1110–1126
- Mikkelsen T., Mann J., Courtney M., and Sjöholm M. Windscanner: 3-D wind and turbulence measurements from three steerable doppler lidars (2008) *IOP Conf. Series: Earth and Environ. Sci.* 012018 (9pp)
- Pedersen T. F., Gjerding S., Ingham P., Enevoldsen P., Hansen J. K., and Jørgensen H. K. (2002) Wind turbine power performance verification in complex terrain and wind farms. Technical report, Risø-R-1330(EN), Risø DTU, Roskilde
- Peña A., Gryning S.-E., and Hasager C. B. (2010a) Comparing mixing-length models of the diabatic wind profile over homogeneous terrain. *Theor. Appl. Climatol.* **100**:325–335
- Peña A., Hasager C. B., Gryning S.-E., Courtney M., Antoniou I., Mikkelsen T. (2009) Offshore wind profiling using light detection and ranging measurements. *Wind Energy* **12**:105–124
- SgurrEnergy (2009) Galion
- Smith D. A., Harris M., Coffey A. S., Mikkelsen T., Jørgensen H. E., Mann J., and Danielian R. (2006) Wind lidar evaluation at the Danish wind test site in Høvsøre. *Wind Energy* **9**:87–93
- TheWindPower.net (2009) Windparks in Europe. Database, TheWindPower
- Trujillo J. J., Bingöl F., Larsen G. C., Mann J., and Kühn M. Lidar measurements of wake dynamics, Part II : Two dimensional scanning. *Wind Energy*, In press

# 8 Nacelle wind lidar

**Andreas Rettenmeier, Jan Anger, Oliver Bischoff,  
Martin Hofsäß and David Schlipf**

*Endowed Chair of Wind Energy, Institute of Aircraft Design,  
Universität Stuttgart, Stuttgart, Germany*

---

## 8.1 Summary

The use of a nacelle-based LIDAR system allows measuring turbine inflow and wake in a very high spatial and temporal resolution. The new measurement techniques to be developed have direct applications on- and offshore for the verification of wake models, predictive control strategies and new methods for power curve determination and load estimation.

An adaptive scanning device was developed for the standard pulsed LiDAR system Windcube. This additional system has been conceived with a certain flexibility to allow different trajectories and to scan horizontally the flow field in front and behind of turbines covering the whole rotor disc. The design and construction of the device was supported by a software tool for wind turbine LiDAR simulation (Schlipf et al., 2009). Based on the results of the simulation of different trajectories, requirements to the hardware and software adaptation could be defined.

## 8.2 Introduction

Installation of the LIDAR system on the nacelle of a turbine is advantageous because in this way the LIDAR yaws with the turbine and the laser beam is always orientated along the up- or downwind wind direction, depending on the application.

If the LiDAR system “is looking” upwind one can measure the incoming wind for e.g. predictive turbine control, load estimation or power curve determination. If the LiDAR is looking downwind it is possible to measure the turbine’s wake wind and thus making the validation of wake models possible. The wind speed component of the line-of-sight vector is much higher when operating horizontally from a nacelle than from the ground.

The development of different nacelle-based LiDAR systems are on the one hand commercial products (e.g. Catch the Wind, Leosphere Upwind) with two/three beam directions which mainly focus to support the yaw control of the turbine. On the other hands different research LiDAR were developed for nacelle applications. For this reason one of the first CW-LiDARs from QinetiQ was used for the first investigations regarding turbine control (Harris et al., 2006) and wake (Trujillo et al., 2008). Another CW- LiDAR was mounted in the rotating spinner of a wind turbine (Mikkelsen et al., 2010). The LiDAR system presented here is based on the pulsed LiDAR device “Windcube” of Leosphere (Rettenmeier et al., 2010).

## 8.3 The units of the LiDAR system

The SWE LiDAR system consists of two components. The first component is the commercial “Windcube WLS-7” from Leosphere. The second part of the used system is a scanner specifically created for nacelle-based LiDAR measurements.

## Windcube

The “Windcube WLS 7” was developed to measure wind speed and wind direction from the ground in order to replace the conventional met masts for wind potential analyses in some areas and to support the certification process regarding power curve and load measurements in the future. The working principle of the pulsed LiDAR system is described by Cariou and Boquet (2010).

In order to use the standard Windcube for a nacelle-based measurement campaign several adaptations had to be made. The internal deflection mirror with  $45^\circ$  was removed and the optical axis from the Windcube to the scanner had to be ensured. The software had to be adapted insubstantially:

- The Windcube has to be synchronized with the controller unit of the scanner so that the movement of the mirror and the measuring of the laser is synchronized.
- The ten arbitrary heights from the ground-based system have been reduced to five arbitrary focus distances in front of the LiDAR system for the nacelle-based version. With a fixed focus length the scanning figure is described on a cubic surface (Figure 75(left)). It is possible to vary the focus length at each measurement point so that the focus plane is vertical which means a “slicing” of the wind field (Figure 75(right)).
- The maximum number of measurement points of a scanning pattern is limited to 49.
- The scanning modes are either “Start-Stop” or “Bang-Bang”. At the Start-Stop mode the mirror stops at the measurement point, the measurements involve shooting and averaging the spectras to the line-of-sight wind speed. Afterwards the mirror moves to the next measurement point. The employment of this mode allows to average a higher number of shots which are taken into account to calculate the line-of-sight velocity. The result is a good signal to noise ratio (SNR) and a higher maximum measurement range. In the ”Bang-Bang” mode the mirror always moves, but decelerates shortly before reaching the measurement point and accelerates after passing the measurement point. In this mode the number of shots to be averaged has to be lowered. This means that the carrier to noise ration (CNR) is worse compared to the “Start-Stop” mode, but the movement is much faster and therefore the temporal resolution is better.

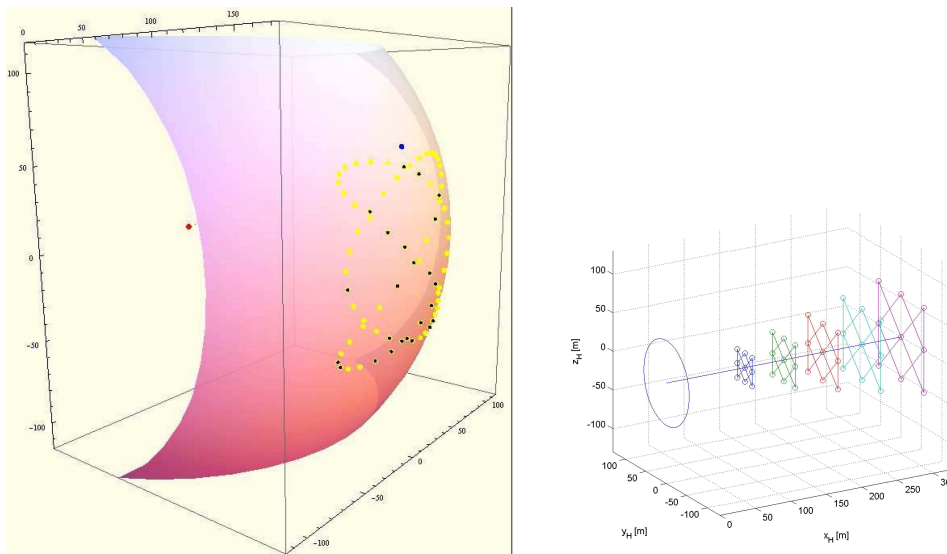


Figure 75: Measuring on a cubic shape with a fixed focus length (left) and using variable focus length to “cut” the wind field vertically (right).



## Scanner

A scanner device with two degrees of freedom has been developed for the nacelle measurement campaigns in order to be able to position the laser beam of a standard Windcube LiDAR system in any direction. The requirements for the development of the scanner system were:

- Angle of projection:  $53.2^\circ$ . In a distance of 1D the measurement area should cover the whole swept rotor disc.
- Flexible trajectories. Depending on the different applications, various scan patterns should be possible.
- High speed and acceleration. To get a good temporal and spatial resolution, it is necessary that the measurements are fast and have a high repeatable accuracy.

The scanner system developed is based on a single mirror which is moved by a mechanical system with two independent rotation stages (see Figure 76(left)). The mirror has a mechanical angle range of  $\pm 15^\circ$  in the pan and tilt direction (horizontal and vertical). The motors are controlled by an external unit which is synchronized with the Windcube. The two mentioned rotation stages and the supporting structure with the transmission rods form the scanning system which was mounted in a modular way in order to simplify attachment to the standard Windcube (see Figure 76(right)). The scanner was integrated in a second housing so that an adaptation to the original Windcube was easy and water tightness as well as structural stability could be assured. Thus, the orientation of the laser beam and the alignment of the optical axis could be guaranteed.

The mirror which deflects the beam in the original Windcube system is removed so that the laser beam goes through both casings and is deviated by the 2-DOF mirror (see Figure 77(left)).

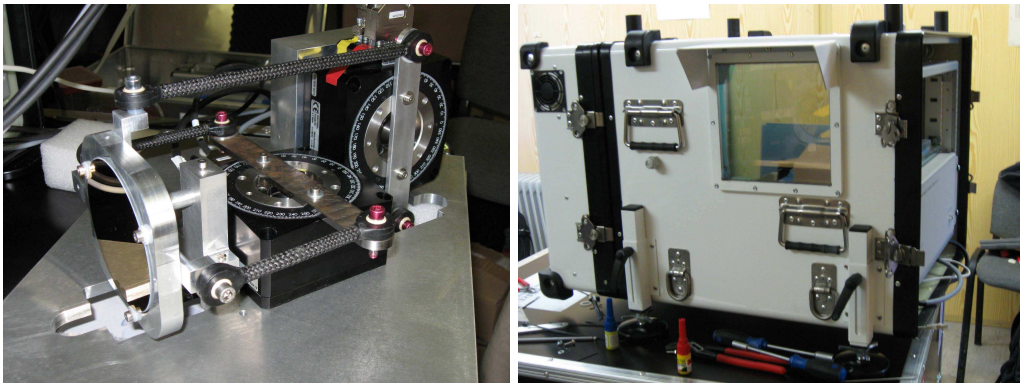


Figure 76: Scanner assembly (left) and integration to a second housing (right).

## 8.4 Scan pattern

Measuring the wind field from the nacelle of a turbine makes it possible to gather wind field information (wind speed, wind direction) in a high temporal and spatial resolution. To scan a wind field in any vertical and horizontal direction, the laser beam runs along a predetermined path and executes the measurement at predefined points. For designing a scan pattern the wind turbine simulator WITLIS was developed (Schlipf et al., 2009). This software supports the development of trajectories considering the motor speed and acceleration. WITLIS scans a synthetic wind field generated with Vindsim and interpolates the measurements to a defined grid. Then the calculated wind field is compared with the synthetic one. Some investigations were carried out in accordance with the planned

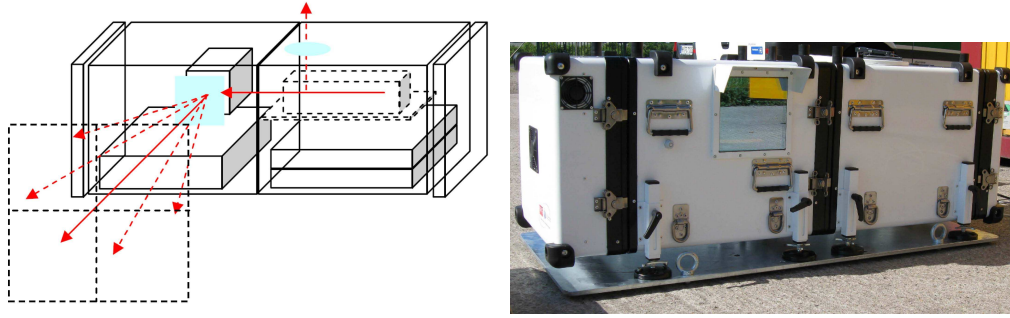


Figure 77: Way of the laser beam and the optical axis (left) and the assembled system modules (right).

application of inflow and wake measurements taking into account the maximum measurement points per focus plane. The software WITLIS is also used to post-process the measured data.

As a result of the consideration to scan as many points as possible in the shortest possible time inside a square, the trajectories based on Lissajous-figures show the best ratio of temporal and spatial resolution. A Lissajous figure can be created by superposing two harmonious waves that can be driven from the two independent rotation stages used. In mathematics, a Lissajous curve (Lissajous figure or Bowditch curve) is the graph of a system of parametric equations which describe complex harmonic motion. (Eqs. (168) and (169)):

$$x = A \sin(at + \delta), \quad (168)$$

$$y = B \sin(bt + \delta). \quad (169)$$

This family of curves was investigated by Nathaniel Bowditch in 1815, and later in more detail by Jules Antoine Lissajous in 1857. The appearance of the figure is highly sensitive to the ratio  $a/b$ . For a ratio of 1, the figure is an ellipse, with special cases including circles ( $A = B$ ,  $\delta = \pi/2$  radians) and lines ( $\delta = 0$ ). Another simple Lissajous figure is the parabola ( $a/b = 2$ ,  $\delta = \pi/2$ ). Other ratios produce more complicated curves, which are closed only if  $a/b$  is rational. The visual form of these curves is often suggestive of a three-dimensional knot, and indeed many kinds of knots, including those known as Lissajous knots, project to the plane as Lissajous figures. [[http://en.wikipedia.org/wiki/Lissajous\\_curve](http://en.wikipedia.org/wiki/Lissajous_curve)]

One of the basic trajectories used in different measurement campaigns was a Lissajous figure with a ratio of 3:4. If a LiDAR scans the figure in such a way, it becomes more difficult to evaluate and recalculate a wind field from the measured points. Therefore, specific measurement points have to be defined, and the figure was adapted to  $7 \times 7$  measurement grid points. The time needed to scan the 49 measurement points was 8.4 s. which led to a good temporal and spatial resolution. Based on the pulsed LiDAR technology, each trajectory point is measured at 5 focus planes simultaneously which even allows an interpolation between the different focus planes.

To ensure that the scan pattern works with a high accuracy a visible red laser was used and the scan pattern was photographed with a long exposure time (Figure 80(left)). As a second step, the use of an infrared camera and an IR-sensitive card makes even the real eye-safe beam visible.

## 8.5 CNR

CNR is deemed to be as an indication of the quality of the measurement. It describes the ratio of sent photons  $C$  to the number of reflected photons  $N$  using the unit dB (see chapter 4),

$$\text{CNR} = \frac{C}{N}, \quad (170)$$

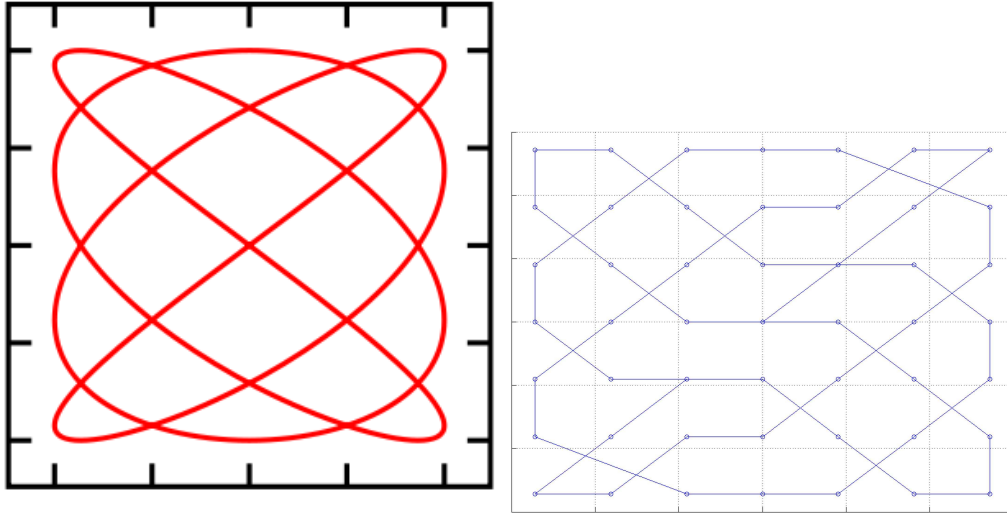


Figure 78: Lissajous figure with a frequency ratio of 3:4 (left) and adapted to  $7 \times 7$  measurement grid (right).

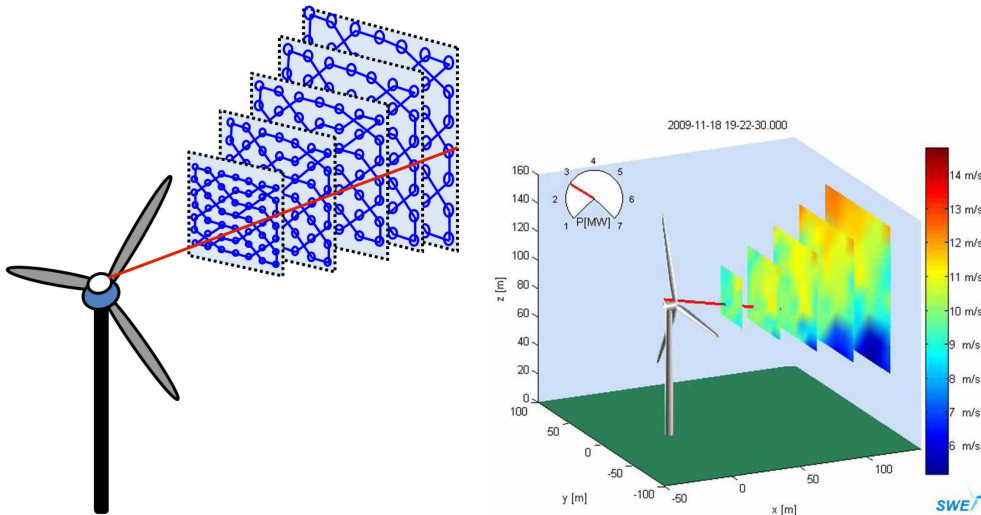


Figure 79: Sketch of simultaneous measurements at different distances (left) and real measured data with an interpolation within one focus plane (right).

$$\text{CNR}(\text{dB}) = 10 \log_{10} \frac{C}{N}. \quad (171)$$

The CNR value of every point measurement can be used to obtain information about the quality of the line-of-sight velocity. Measurements with a bad CNR value ( $< -17$  dB) have to be ignored. There are several reasons for poor CNR values, from a dirty window/prism to the quantity and kind of the aerosols in the air. During -and directly after- a heavy rain the air is very clean and contains too few aerosols to reflect the laser beam. Here the ratio between carriers to noise is quite bad. In offshore conditions the value of CNR is often higher due to the salty air.

If we examine nacelle-based measurements, the impact on the rotor blades causes a bad CNR signal when the system is installed behind the rotor. About 30% of the data has to be removed due to rotor impact. Synchronizing the scan pattern with the rotor position or scanning the pattern in the opposite direction of the rotor direction will reduce the ignored data sets. If any faults in the LiDAR system occur, there is a need to know that issue especially when the output data and information is linked to the control of the

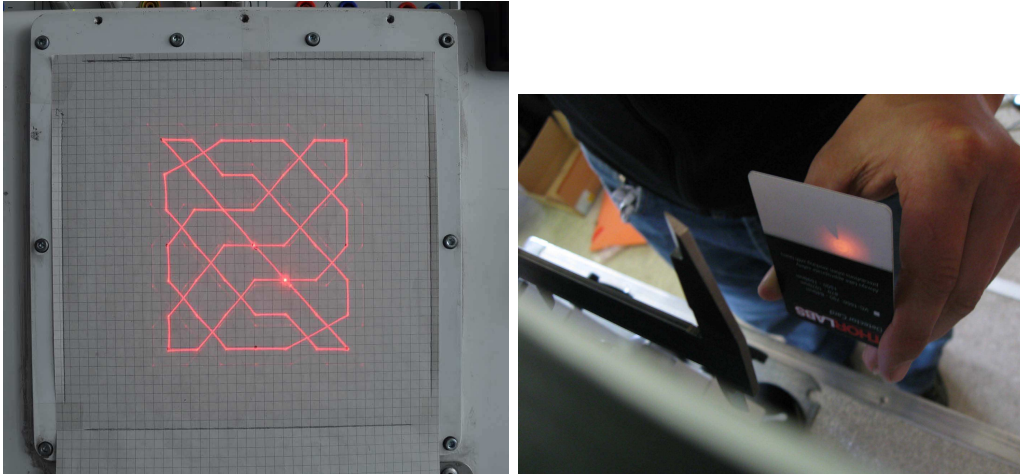


Figure 80: Photo of Liss2Grid trajectory taken with long exposure time (left). Use of an IR-sensitive card for the invisible laser beam (right).

turbine.

## 8.6 Wind field reconstruction

To reconstruct the wind speed and the wind field some assumptions have to be made. This is due to the fact that one can measure only the line-of-sight velocity along the laser beam. Based on the supposition that the wind field is parallel to the ground, the following drawings show how the wind speed vector is mapped by the line-of-sight vector. The absolute values of the line-of-sight velocity  $v_{LOS}$  at points  $P_i$  for every focus area  $m$  and the angles of the vertical and horizontal beam deflection are needed to recalculate the wind field. By means of these angles the coordinates of the measured points (for every five focus planes) can be calculated.

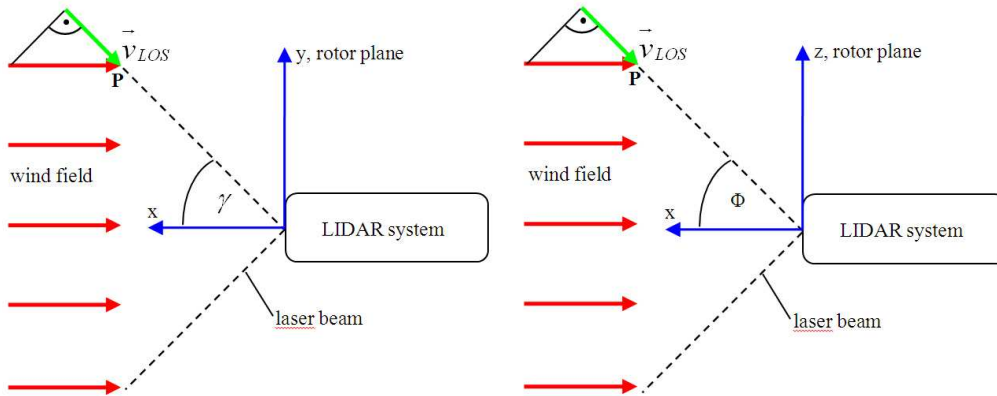


Figure 81: Schematic drawing of the LiDAR coordinate system from top and lateral views (left, right).

For a Cartesian coordinate system, where the LiDAR system is the origin of the coordinate system, the coordinates of a measured point  $P_i$  are  $x_p, y_p, z_p$ . Using these coordinates

the normal vector  $\mathbf{n}_{LOS} = [x_n, y_n, z_n]^T$  of the laser beam can be defined as

$$x_n = \frac{x_p}{\sqrt{x_p^2 + y_p^2 + z_p^2}}, \quad (172)$$

$$y_n = \frac{y_p}{\sqrt{x_p^2 + y_p^2 + z_p^2}}, \quad (173)$$

$$z_n = \frac{z_p}{\sqrt{x_p^2 + y_p^2 + z_p^2}}. \quad (174)$$

Therefore  $|v_{LOS, fpm, Pi}|$  at focus plane  $m$  and point  $i$  yields to,

$$|v_{LOS, fpm, Pi}| = u_p \cdot x_n + v_p \cdot y_n + w_p \cdot z_n, \quad (175)$$

where the wind speed coordinates at point  $P_i$ ,  $u_p$ ,  $v_p$ ,  $w_p$ , are unknown. Assuming that a plane parallel wind field prevails, the wind speed vector can be simplified by setting the wind speed coordinate in horizontal direction  $v_p$  and the wind speed coordinate in vertical direction  $w_p$  to zero.

$$v_p = 0, \quad (176)$$

$$w_p = 0. \quad (177)$$

The normal wind direction vector  $\mathbf{n}_{winddir}$  for a plane parallel wind field (that always inflows right-angled to the rotor area) without vertical wind component can be described as followed:

$$\mathbf{n}_{winddir} = \begin{bmatrix} 1 \\ 0 \\ 0 \end{bmatrix}.$$

The angle  $\cos \varphi$  between  $\mathbf{n}_{winddir}$  and  $\mathbf{n}_{los}$  can be calculated,

$$\cos \varphi = \frac{\mathbf{n}_{los} \cdot \mathbf{n}_{winddir}}{|\mathbf{n}_{winddir}| |\mathbf{n}_{los}|}. \quad (178)$$

The wind speed component  $u$  in  $x$ -direction, is the projection of  $v_{los}$  in the direction of  $\mathbf{n}_{winddir}$ . It can be calculated with the angle between the vectors.

$$u_{los} = \frac{v_{los}}{\cos \varphi} \quad (179)$$

Assuming a plane parallel wind field and no vertical wind speed component enables a reconstruction of the wind field. But what's about horizontal and vertical shear, yaw error, turbulence? Here some measurements and basic investigations still take place to understand those issues.

## 8.7 “Visited” test sites of the SWE Scanner

### Onshore test site Bremerhaven

The prototype of the AREVA Wind M5000 wind turbine was erected in December 2004 in Bremerhaven, close to the North Sea. In cooperation with DEWI (German Wind Energy Institute) and AREVA Wind, former Multibrid Entwicklungsgesellschaft mbH (MEG), the Endowed Chair of Wind Energy at Stuttgart University (SWE) started a thorough measurement program in spring 2005. In 2007 the national funded project “Development of LiDAR measurement techniques for the German offshore test site” started with the objective to develop reliable and standardized remote sensing techniques for various new applications in the wind energy community and to support in a later step other RAVE projects at the German offshore test site “alpha ventus”. Except for a FINO1 campaign, all LiDAR measurements from ground and from nacelle were carried out in Bremerhaven.

The M5000 is a 5 MW wind turbine designed for offshore purposes. With a hub height of 102 m and a rotor diameter of 116 m the M5000 is currently one of the largest wind

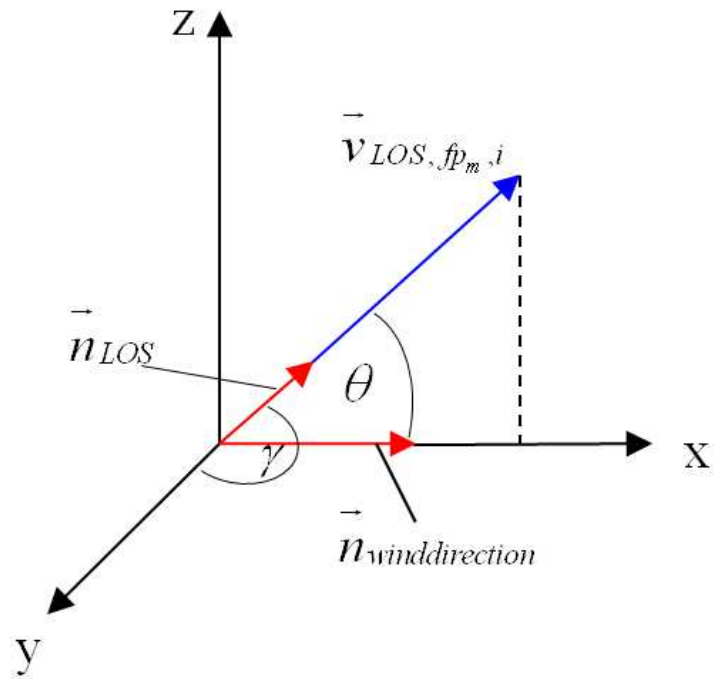


Figure 82: Schematics of the normalized vectors and  $v_{los}$ .

turbines. The cut-in wind speed is  $4 \text{ m s}^{-1}$ , the rated wind speed is  $12 \text{ m s}^{-1}$  and the cut-out wind speed  $25 \text{ m s}^{-1}$ . The M5000 is a pitch-controlled, variable speed wind turbine with a permanent magnet generator.



Figure 83: Onshore test site with AREVA M5000 and SWE met mast (102 m) (left) Installation of the LiDAR system on the nacelle of the turbine (approx. 105 m AGL) (right).

### Onshore test site Risø-DTU

The measurement campaigns at this test site mainly focus on fundamental investigations concerning the minimum number of trajectory points for equivalent wind speed, turbulence measurements, horizontal/vertical wind shear and mean wind speed accuracy compared to a cup anemometer on a met mast. The test site of Risø-DTU is located close to the research center in Risø (Denmark). The SWE-LiDAR system was first installed on ground, tilted up with  $25^\circ$  and pointed towards the met mast. In a second campaign, the LiDAR system was installed on a platform of a Nordtank wind turbine in about 38 m height. From this platform, the LiDAR system shot almost horizontally to a met mast where the laser pointed to three sonic anemometers at different heights.



*Figure 84:* Test site at Risø-DTU with the Nordtank and Tellus wind turbines and several met masts (left). Tilted SWE LiDAR system pointing to a met mast (right).

### Offshore test site “alpha ventus”

The offshore test site “alpha ventus” is located 45 km north of the island of Borkum next to the research platform FINO 1. It comprises twelve offshore wind turbines with a total capacity of 60 MW. Six AREVA Wind M5000 turbines were installed in summer 2009, six REpower 5M turbines followed in 2010. The German Federal Environment Ministry supports alpha ventus with a major research funding. The RAVE initiative is accompanying the construction and operation of the test site to attain a broad basis of experience and expertise for future offshore wind parks. Several research projects are currently carried out. Within the RAVE-OWEA research project two scanning LiDAR systems, one installed on the nacelle of the AREVA Wind M5000 the other one on

REpower 5M, measure the inflow and the wake of the turbines under offshore conditions.



Figure 85: LiDAR system (scanner unit and Windcube) on the top of a Repower 5M measuring the inflow.

## 8.8 Measurement campaigns and some results

Different measurement campaigns regarding different applications such as the verification of Taylor's frozen turbulence hypothesis, validation of wake models, predictive control, load estimation and power curve determination are still on-going or have been terminated. If we look at the power curve determination and load measurements, the wind field information has to be summed up to an equivalent wind speed and turbulence intensity (Klausmann, 2010; Bischoff et al., 2010).

### Equivalent wind speed

The advantage of measuring from the nacelle of a turbine is that the whole swept rotor area is covered and that horizontal and vertical wind shear can be taken into account. According to the standard, fewer sectors have to be excluded because there is no met mast in the wake of the turbine or of other obstacles. Thus measurement campaigns can be carried out in a shorter time.

To determine a power curve, the mean values as well as the standard deviation of the electric power and the average wind speed over 10 min are necessary. The main goal is to get a power curve including all wind field information, as well as to get a smaller standard deviation. A second goal consists in the definition of relevant trajectory points. Both methods presented here are based on the trajectory Liss2Gridopt. With  $7 \times 7$  measuring points a variety of different methods is feasible.

**Arithmetic average of all points** The first method is a simple arithmetic average over all mean wind speeds of measurement points during a 10 min period of time.

$$u_{mean} = \frac{1}{N} \sum_{i=1}^N v_i, \quad (180)$$

where  $N$  is the number of layers and  $v_i$  the average wind speed of trajectory layer  $i$ . The used trajectory for this example, Liss2Gridopt, has seven layers.

The curve is relatively similar to the power curve measured with a met mast and a cup anemometer according to the IEC standard. One can see that the bars of the standard deviation are significantly smaller. That means that the uncertainties in the measurements are lower and the accuracy is higher. In another approach, five single points were picked out of the 49 measurement points (Big-Cross). Even when reducing the measurement



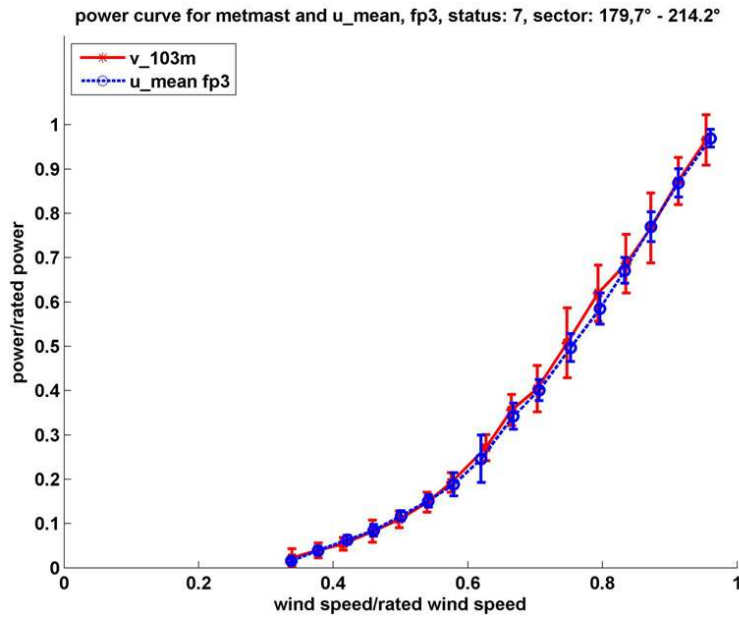


Figure 86: Power curve met mast and  $u_{mean}$  method.

points the standard deviation is still very small.

$$u_{bigcross} = \frac{1}{5} \sum_{i=1}^5 u_i. \quad (181)$$

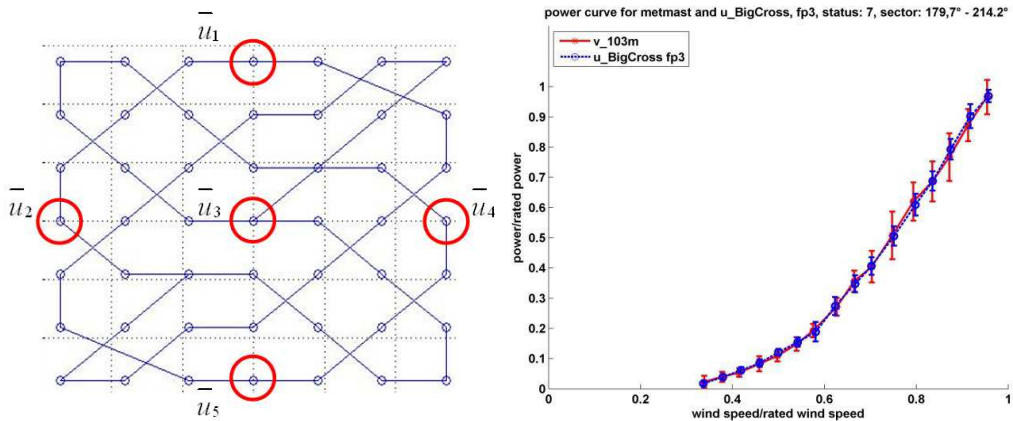


Figure 87: Five points out of 49 for the Big cross method (left) and calculated power curve (right).

## 8.9 Outlook & Conclusions

The use of a LiDAR system from the nacelle offers various applications in wake wind field analysis, wind turbine control, power curve determination and load estimation. The whole swept rotor area can be taken into account, but assumptions have to be made. Nacelle-based measurement methods show a great potential on- and offshore and even in complex terrain. But there are still some investigations that have to be done concerning turbulence, vertical and horizontal shear, comparison criteria and equivalent wind speed.

## Acknowledgements

The main content of the work presented here is based on results of the RAVE-LiDAR project, funded under contract No. 0327642 by the German Federal Ministry for the Environment, Nature Conservation and Nuclear Safety (BMU).

## Notation

$C$	number of sent photons
CNR	carrier to noise ratio
DEWI	German wind energy institute
$i$	index of layers of points
$m$	beam focus plane
$\mathbf{n}_{los}$	line of sight normal vector
$\mathbf{n}_{windir}$	normal wind direction vector
$N$	number of reflected photons and number of layers
$P_i$	beam focus area points
SNR	signal to noise ration
SWE	Endowed Chair of Wind Energy
$u_{bigcross}$	5-point average wind speed
$u_{los}$	wind speed component in $x$ -direction
$u_{mean}$	10-min mean wind speed
$u_p$	longitudinal wind speed at point $P$
$v_i$	average wind speed of trajectory layer $i$
$v_{los}$	line-of-sight velocity
$v_p$	transversal wind speed at point $P$
WITLIS	wind turbine simulator
$w_p$	vertical wind speed at point $P$
$x_n$	longitudinal coordinate of normal vector $\mathbf{n}_{los}$
$x_p$	longitudinal coordinate of point $P$
$y_n$	transversal coordinate of normal vector $\mathbf{n}_{los}$
$y_p$	transversal coordinate of point $P$
$z_n$	vertical coordinate of normal vector $\mathbf{n}_{los}$
$z_p$	vertical coordinate of point $P$
$\varphi$	angle between $\mathbf{n}_{los}$ and $\mathbf{n}_{windir}$

## References

- Bischoff O., Hofsaß M., Rettenmeier A., Schlipf D. and Siegmeier B. (2010) Statistical load estimation using a nacelle-based lidar system. *DEWEK*, Bremen
- Canadillas B., Schlipf D., Neumann T. and Kuehnel D. (2011) Validation of Taylor's hypothesis under offshore conditions. *EGU*, Vienna
- Cariou J.-P. and Boquet M. (2010) Leosphere pulsed lidar principles. Contribution to EU-project UpWind WP6
- Harris M., Hand M. and Wright A. (2006) Lidar for turbine control. Tech Report NREL/TP-500-39154
- Klausmann P. (2010) Calculation of power curves based on interpolated line-of-sight velocities of nacelle-based lidar-measurements. Study thesis, SWE
- Mikkelsen T., Hansen K., Angelou N., Sjöholm M., Harris M., Hadley P., Scullion R., Ellis G. and Vives G. (2010) Lidar wind speed measurements from a rotating spinner. *EWEC*, Warsaw
- Rettenmeier A., Bischoff O., Hofsaß M., Schlipf D. and Trujillo J. J. (2010) Wind field analysis using a nacelle-based lidar system. *EWEC*, Marseille
- Schlipf D., Trujillo J. J., Basterra V. and Kühn M. (2009) Development of a wind turbine lidar simulator. *EWEC*, Marseille
- Schlipf D., Trabucchi D., Bischoff O., Hofsaß M., Mann J., Mikkelsen T., Rettenmeier A., Trujillo J. J. and Kühn M. (2010) Testing for frozen turbulence hypothesis for wind turbine applications with a scanning lidar system. *ISARS*, Paris
- Trujillo J. J., Bingöl F., Larsen G., Mann J. and Kühn M (2008) Lidar measurement and modelling of wind turbine far-wake dynamics *DEWEK*, Bremen

- Trujillo J. J. (2009) Measurements of a multi-MW turbine near-wake using lidar from the nacelle. *Euro-mech Colloquium*, Madrid
- Trujillo J. J., Trabucchi D., Bischoff O. Hofsaß M, Mann J., Mikkelsen T., Rettenmeier A., Schlipf D. and Kühn M. (2010) Testing for frozen turbulence hypothesis for wind turbine applications with a staring lidar. *EGU*, Vienna
- Trujillo J. J., Kühn M, Bischoff O. Hofsaß M, Rettenmeier A. and Schlipf D. (2010) Meandering model with near wake lidar measurements. *DEWEK*, Bremen

# 9 Lidars and wind turbine control

David Schlipf, Oliver Bischoff, Martin Hofsäß,  
Andreas Rettenmeier, Juan José Trujillo, and Martin Kühn  
*Endowed Chair of Wind Energy, Institute of Aircraft Design,  
Universität Stuttgart, Stuttgart, Germany*

---

## 9.1 Introduction

Reducing mechanical loads caused by atmospheric turbulence and energy optimization in the presence of varying wind are the key issue for wind turbine control. In terms of control theory changes in the inflowing wind field as gusts, varying shears and directional changes represent unknown disturbances. However, conventional feedback controllers can compensate such excitations only with a delay since the disturbance has to be detected by its effects to the turbine. This usually results in undesired loads and energy losses of wind turbines.

From the control theory point of view disturbance rejection can be improved by a feed-forward control if the disturbance is known. Not fully covered by theory, but used in practice is the further advantage of knowing the disturbance in the future, e.g. in chassis suspension or in daily life when vision is used to circumnavigate obstacles with a bicycle.

In a similar way wind field measurements with remote sensing technologies such as lidar might pave the way for predictive wind turbine control strategies aiming to increase energy yield and reduce excessive loads on turbine components. Remote sensing offers wind speed tracking at various points in space and time in advance of reaching the turbine and before hitting sensors at the blades or nacelle. This provides the control and safety system with sufficient reaction and processing time.

In Figure 88 the different steps for predictive wind turbine control are shown. The objective of the first step is to obtain wind fields in different distances in front of the turbine, e.g. by use of lidar. In the next step, turbulence theory, e.g. the “Taylor’s frozen turbulence theorem”, is considered when modelling the wind on its way towards the turbine. In the last step, the predicted future wind fields are used to improve wind turbine control by model predictive control strategies.

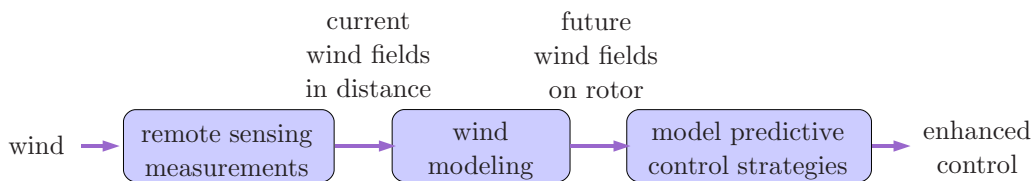


Figure 88: Steps in model predictive wind turbine control assisted by remote sensing

## 9.2 Measuring wind fields with lidar

Wind fields can be considered as time variant vector fields: one vector  $\mathbf{a}$  in each point in space  $\mathbf{p}$ . Therefore the objective of wind fields assessment is to reconstruct wind fields in discrete space and time points as much as possible.

Commercial lidar systems have the disadvantage that they are not flexible due to measurement in conical domain and normally they are ground based and don't measure in main wind direction. Thus nacelle based lidar systems with scanner or beam splitter are better suited, but still some issues have to be considered:

- Which points have to be scanned to get best information for control purpose?
- How does the probe volume effect the measurements?
- How can 3D vectors be reconstructed from line-of-sight measurements to obtain information for control? (see section 9.2)

To investigate these effects, a lidar simulator is presented in section 9.2.

### The “Cyclops” dilemma

As a Cyclops cannot see three-dimensionally with only one eye, it isn’t possible to measure a 3D wind vector with only one lidar system. Three lidar systems focusing in the same point with linearly independent laser beams are needed. With one nacelle mounted lidar system, the two missing systems can be substituted by different assumptions, e.g.:

1. no vertical and no horizontal wind component, or
2. no vertical component and homogenous flow on each height

In Figure 89 the effect of both assumption possibilities is shown. In this case the 3D vectors in  $p_1$  and  $p_2$  (measured in the same height) should be reconstructed from the line-of-sight wind speeds  $v_{los1}$  and  $v_{los2}$ . The first assumption yield  $a_{11}$  and  $a_{21}$  representing a horizontal shear. With the second assumption the resulting vectors  $a_{21}$  and  $a_{22}$  are equal representing a cross-flow, as homogenous flow on each height was assumed.

The dilemma consist, if the lidar measurement should be used for yaw and pitch control at the same time: If the first assumption is used to calculate the inhomogeneous inflow, perfect alignment is assumed. If the second assumption is used to obtain the misalignment, homogeneous flow is assumed.

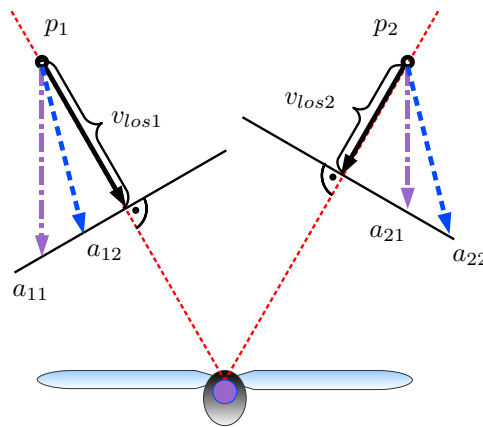


Figure 89: Different possibilities of 3D wind vector reconstruction

### WITLIS (WInd Turbine Lidar Simulator)

To understand better the above mentioned effects and to plan measurement campaigns it is helpful to simulate lidar measurements. The main objective of the simulation tool is to reproduce the operation of a nacelle-mounted lidar system. Thus the tool facilitates the evaluation of scanning patterns to find the best hardware and software solution for applications like control, power curve assessment and wake measurements. Wind turbine control strategies based on lidar can be tested with aeroelastic wind turbine simulation tools in a realistic setup. A modular setup provides software parts that can be used to process measurement data in the same way as simulated data (see Figure 90).

Figure 91 depicts the wind field reconstruction of a simulated measurement: On the left side a generic wind field from TurbSim (Jonkman, 2009) is shown superposed with a wake for better illustration. On the right side the interpolated wind field with WITLIS can be seen. The dots represent a real trajectory as can be done by the adapted Windcube lidar and perfect alignment is assumed. It can be seen that main characteristics can be measured.

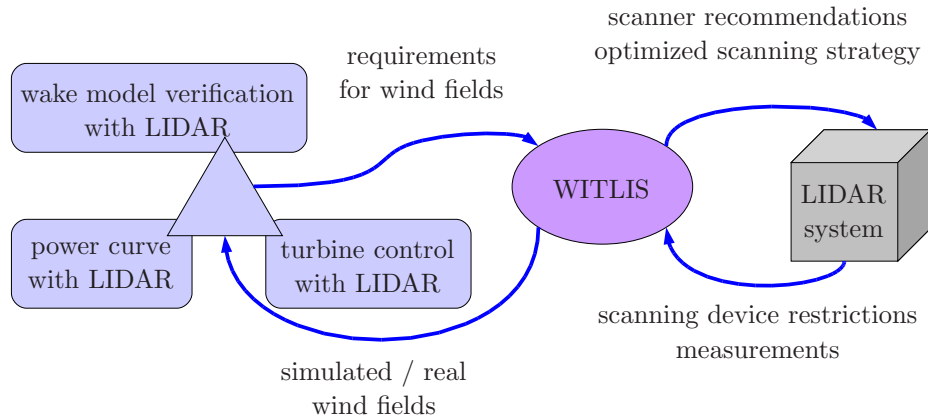


Figure 90: Interactions between the applications, the simulator and the lidar system

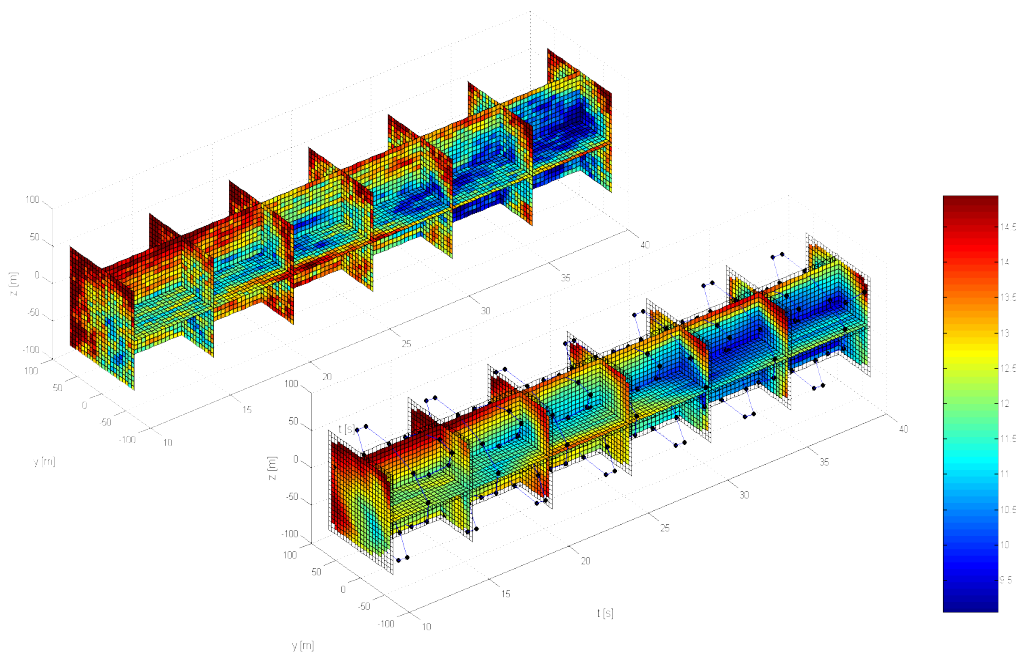


Figure 91: Simulation of realistic lidar measurements in a turbine wake: Original downflow wind component (left) and scanned (right) downflow wind component

### 9.3 Prediction of wind fields

The inflow wind field for control purpose shouldn't be measured in the rotor plane because of several reasons:

- Because of stability and performance reasons the undisturbed wind field should be measured. But wind in rotor plane is affected by the turbine itself.

- It is difficult to perform measurements in the rotor plane, e.g. with pitot tubes or lidar on the blades.
- Measuring in front of the turbine provides the control system more time to react. The easiest way to model the wind on its way towards the turbine is to use “Taylor’s frozen turbulence theorem”. It assumes that wind characteristics remain the same while being transported through space with the mean wind speed.

## 9.4 Improving control

The new information of upwind wind speeds obtained by lidar measurements can be used for improving the turbines control systems. Thereby we distinguish between four different control activities: Yaw control, speed control, collective pitch control and individual pitch control. Possible benefit and potential is listed respectively in table 11.

*Table 11:* Possible application and benefit of lidar based control. Here is assumed that measurements are at least as beneficial as (e)stimation.

	benefit	potential	reference
yaw	more energy	up to 12%	Cath the Wind (2009)
speed	more energy	up to 10%(e)	Boukhezzar and Siguerdidjane (2005)
collective pitch	less loads	up to 20%	Schlipf and Kühn (2008)
individual pitch	less loads	up to 30%(e)	Selvam et al. (2009)

In this paper we will focus on advanced collective pitch control only.

### Predictive Disturbance Compensation (PDC)

Fluctuating wind speed causes the speed of rotation to vary, which affects the loads to the turbine. The objective of pitch control in full operating load range is therefore to maintain a constant rotational speed of the rotor. The wind speed data provided by a lidar can be used to compensate wind speed fluctuations. The block diagram in figure 92 illustrates the control schema.

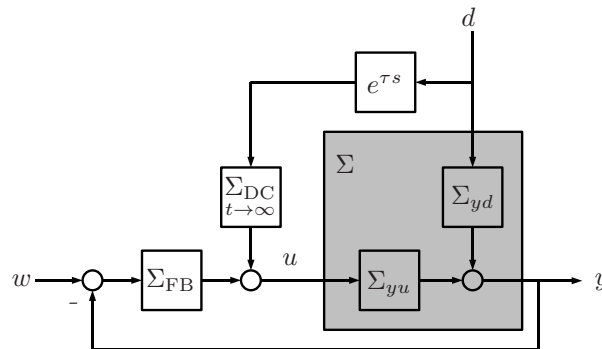


*Figure 92:* Control loop with predictive disturbance compensation.

The output  $y$  (in this case the rotor speed  $\Omega$ ) is influenced by two signals: pitch angle  $\beta$  which is identically equal to the control input  $u$  and the effective wind speed  $v_{\text{eff}}$  which is a disturbance  $d$  in terms of control theory. Subsequently the wind turbine system  $\Sigma$  can theoretically be divided into two subsystems,  $\Sigma_{yu}$  and  $\Sigma_{yd}$ . If  $d$  is now forwarded by a transfer function  $\Sigma_{DC}$  to the control input  $u$ , a compensation of the disturbance can be reached. In this case the feedback controller  $\Sigma_{FB}$  is responsible for reference signal tracking and  $\Sigma_{DC}$  for disturbance rejection.

$\Sigma_{\text{DC}} = -\Sigma_{yu}^{-1}\Sigma_{yd}$  would give a perfect compensation, but in practice the inversion of the nonlinear dynamic turbine model  $\Sigma_{yu}$  cannot be calculated. Therefore a static compensation is proposed

$$\Sigma_{\text{DC}} = u_{\text{ss}}(d_{\text{ss}})_{t \rightarrow \infty}$$

which is the static value  $u_{\text{ss}}$  of the system input subject to the static disturbance  $d_{\text{ss}}$ . The feedback controller  $\Sigma_{\text{FB}}$  then will react during the dynamic transitions.

The time interval of the transition is influenced by the difference in the dynamic orders of  $\Sigma_{yd}$  and  $\Sigma_{yu}$ . In the case of pitch control  $\Sigma_{yu}$  has a higher dynamic order, because pitch angles have a delayed impact on the rotor speed compared to the wind disturbance. Therefore a prediction time  $\tau$  shifts the disturbance signal in time in the way that the pitch moves earlier. Due to the lidar measurement in front of the rotor plane this prediction is possible.

Stability of the control loop is influenced neither by the added static feed-forward control nor by time shift, because none of the newly implemented blocks is part of the closed control loop and no new poles were introduced.

## Simulation

For evaluation of the proposed controller a Simulink implementation of the generic aero-elastic NREL offshore 5-MW baseline wind turbine model (Jonkman et al., 2009) was used (see Table 12).

Table 12: Specification of the generic NREL wind turbine model.

Rotor	upwind, 3 blades
Rated power output	$P_{\text{rated}} = 5 \text{ MW} @ \Omega_{\text{rated}} = 12.1 \text{ rpm}$
Dimensions	$D = 126 \text{ m}, h = 90 \text{ m}$
Controller	collective pitch with gain scheduling
Pitch actuator	2 <sup>nd</sup> order
Filter	$\Omega, \beta, v_w : 1^{\text{st}} \text{ order}$

For the PDC implementation the shift time  $\tau$  is chosen to

$$\tau = T_{63, \text{ filter wind}} + T_{63, \text{ pitch actuator}} = 1 \text{ s}$$

where  $T_{63}$  denotes the rise time to 63 % of the filters and actuators final value respectively.

The static pitch over wind speed denoted  $\beta_{\text{ss}}(v_{w, \text{ss}})$  is given in Jonkman et al. (2009) and shown in Figure 93.

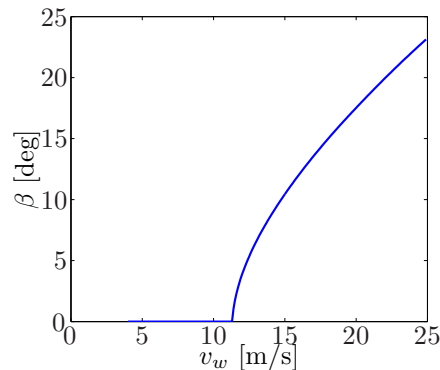


Figure 93: Static pitch over wind speed of the NREL turbine model.

The wind is modeled using the stochastic, full-field, turbulent-wind simulator TurbSim (Jonkman, 2009). The measuring of the full-field wind is simulated using WITLIS, see



section 9.2. In order to use the wind data for collective pitch control, it is necessary to reduce it to one effective wind speed  $v_{\text{eff}}$ . Therefore a weighting function (Figure 94) has been developed Schlipf and Kühn (2008). It takes account of the impact of the wind on the aerodynamic torque with respect to the radius using Prandtl root and tip losses.

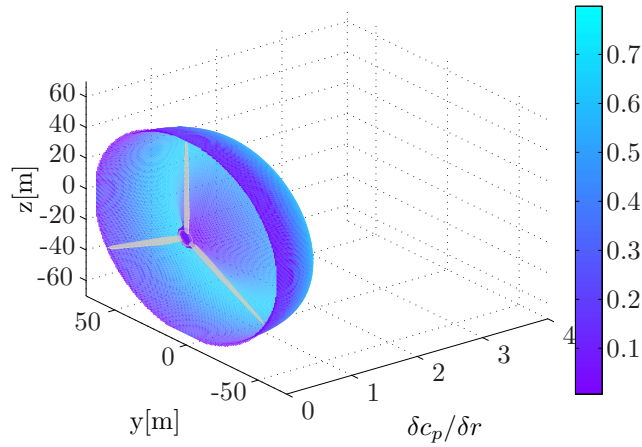


Figure 94: Weighting function for the calculation of the effective wind speed.

## Results

The following simulation results show the impact of the proportional-integral (PI) controller and the PDC on rotor speed and bending moment respectively. In frequency domain for PDC a better disturbance rejection in the frequency range up to 0.3 Hz can be observed (figure 95), in which according to the Kaimal spectrum the wind contains most of its energy.

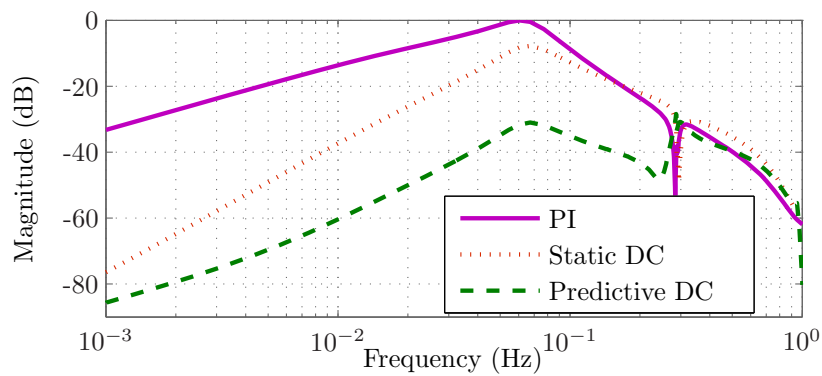


Figure 95: Frequency domain: disturbance rejection of different control strategies.

## Extreme Operating Gust (EOG)

Figure 96 shows the results in time domain of simulations of an EOG according to IEC (2005) applied on the NREL wind turbine model. Here, no turbulence occurs and perfect measurement is assumed.

PDC control technique leads to a significantly reduced rotor overspeed. Consequently the fore-aft bending moment  $M_{yT}$  at the tower base is decreased by PDC as well, compare table 13.

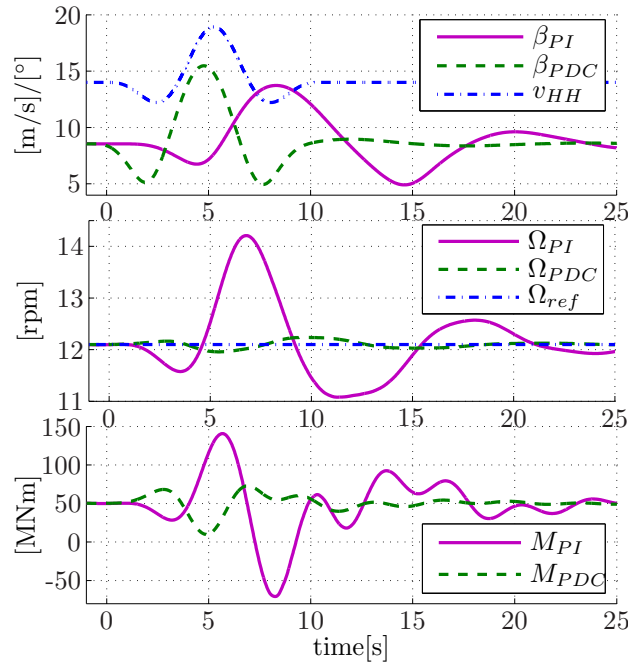


Figure 96: Comparison of conventional and PDC control strategy (EOG). The subscript *ref* denotes reference

Table 13: Standard deviation of signals from figure 96

	PI	PDC	PDC/PI
$\sigma(\Omega) / [\text{rpm}]$	0.74	0.08	9%
$\sigma(M_{yT}) / [\text{MNm}]$	38.2	11.0	29%

### Turbulent Wind Field

Figure 97 and table 14 show the results for simulations with realistic turbulent wind fields with a spatial resolution of 9 m and a time resolution of 0.05 s. It is based on a Kaimal spectrum with a mean wind speed at hub height of  $v_H = 18 \text{ m s}^{-1}$  and turbulence intensity of  $TI = 16 \%$ . Again, perfect measurement is assumed.

Table 14: Standard deviation of signals from figure 97

	PI	PDC	PDC/PI
$\sigma(\Omega) / [\text{rpm}]$	0.42	0.09	21%
$\sigma(M_{yT}) / [\text{MNm}]$	12.8	8.72	68%
$\sigma(\beta) / [\text{deg/s}]$	0.60	0.47	78%

PDC reduces rotor speed variation and loads at the tower base despite lower pitch dynamics occur. Simulations also show reduced loads at the blades.

### Measurement simulation using WITLIS

In a third simulation the influence of a non-perfect measurement, simulated by WITLIS (see section 9.2) was investigated. From table 15 it can be seen that there is still a remarkable improvement using PDC.

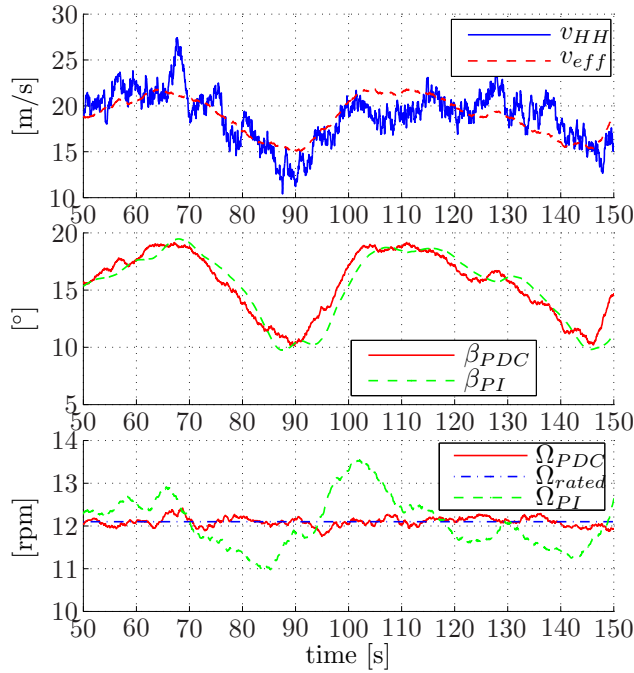


Figure 97: Comparison of conventional and PDC control strategy (turbulent wind field).  $v_{HH}$  is the hub height wind speed

Table 15: Standard deviation of signals from simulation including WITLIS.

	PI	PDC	PDC/PI
$\sigma(\Omega) / [\text{rpm}]$	0.48	0.17	35%
$\sigma(M_{yT}) / [\text{MNm}]$	15.1	11.8	87%
$\sigma(\beta) / [\text{deg/s}]$	0.79	0.65	83%

## Robustness

A weaker performance of the PDC than the conventional PI controller is possible, if there are errors which are not included in the simulation, e.g.

- inaccurate measurements of the wind speed
- wrong calculation of the effective wind speed
- incorrect static pitch curve
- errors in the model used
- invalidity of Taylor's frozen turbulence theorem
- wrong estimate of the shift time  $\tau$

Simulations with a varying parameter  $\tau$  (figure 98) result in a wide range, where the performance results of the PDC remain superior to the PI control.

## Conclusions PDC

The proposed predictive disturbance compensation was presented as a new and powerful control strategy for wind turbine control in full load range. PDC has a guaranteed stability and implementation needs static pitch over wind speed information and one prediction time parameter only.

The performed simulations indicate a significant decrease in rotor speed variation and tower and blade loads without higher pitch actuator activity.

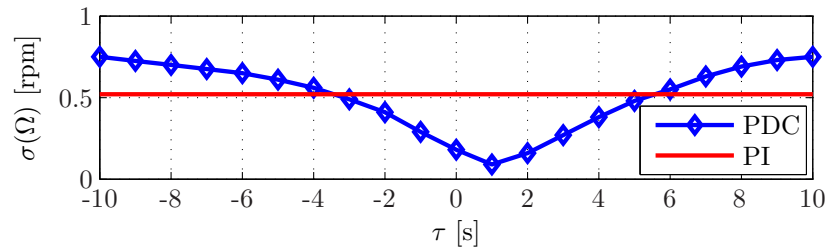


Figure 98: Standard deviation of  $\Omega$  subject to different prediction time shifts  $\tau$  for PDC and PI control

Further research concerns the other control objectives of table 11 as yaw control, speed control and individual pitch control by use of lidar measurements.

## Notation

$a$	horizontal shear of the flow
$\mathbf{a}$	wind vector
$d$	disturbance
$D$	rotor diameter
EOG	extreme operating gust
$h$	hub height
$M_{yT}$	tower fore-aft bending moment
$\mathbf{p}$	vector point in space
$P_{\text{rated}}$	rated power output
PDC	predictive disturbance compensation
PI	proportional-integral (controller)
$T_X$	X% rising time
$TI$	turbulence intensity
$u$	control input
$v_{\text{eff}}$	effective wind speed
$v_{\text{HH}}$	hub height wind speed
$v_{\text{los}}$	line-of-sight wind speed
WITLIS	wind turbine lidar simulator
$x_{SS}$	steady state of variable $x$
$y$	system output
$\beta$	pitch angle
$\sigma_X$	standard deviation of a variable $X$
$\Sigma$	a model system or a subsystem, e.g. a wind turbine
$\Sigma_{\text{FB}}$	feedback controller
$\Sigma_{\text{DC}}$	disturbance compensation
$\tau$	prediction time of a signal
$\Omega_{\text{rated}}$	rated rotor speed

## References

- Boukhezzar B. and Siguerdidjane H. (2005) Nonlinear control of variable speed wind turbines without wind speed measurement. *Proc. of the 44th IEEE Conf. on Decision and Control and the European Control Conf.*, Seville
- Catch the Wind (2009) Boosting power production. Catch the Wind, Inc. 1:15 pp
- IEC (2005) IEC 61400-12-1 Wind turbines - Design requirements. Int. Electrotechnical Commission
- Jonkman B. J. (2009) TurbSim User's Guide. Technical Report NREL/TP-500-46198, **1.5**, 85 pp
- Jonkman B. J., Butterfield S., Musial W., and Scott G. (2009) Definition of a 5-MW reference wind turbine for offshore system development. Technical Report NREL/TP-500-38060, **1**, 75 pp
- Schlipf D. and Kühn M. (2008) Prospects of a collective pitch control by means of predictive disturbance compensation assisted by wind speed measurements. *DEWEC* **1**:4 pp
- Selvam K., Kane S., van Wingerden J. W., van Engelen T., and Verhaegen M. (2009) Feedback-feedforward individual pitch control for wind turbine load reduction. *Int. J. Robust Nonlinear Control* **19**:72–91

# 10 Turbulence measurements by wind lidars

**Ameya Sathe**

*Wind Energy Division, Risø DTU, Roskilde, Denmark*

---

## 10.1 Introduction

It is now well established that wind lidars (henceforth referred to as lidars) measure the 10-min mean wind speed with acceptable accuracy. Several measurement campaigns have been carried out in this regard, where cup anemometers are used as reference instruments (Smith et al., 2006; Kindler et al., 2007; Peña et al., 2009). Turbulence measurements using lidars is still a subject of research, and an acceptable method is yet to be established. At first it is important to understand which turbulence measurements we refer to in this chapter. They are the second-order moments of wind speeds. It is then interesting to know why turbulence measurements are useful for wind energy. Amongst a whole range of applications, we can list a few, such as,

- Load calculations of wind turbines - The driving loads causing fatigue of wind turbines is atmospheric turbulence. Currently, the three dimensional spectral tensor model of Mann (1994) is used to quantify turbulence. Expressions of turbulence spectra from Kaimal et al. (1972) are also used in load calculations. These theoretical and empirical models are obtained for neutral and homogeneous conditions. Wind turbines operate under all terrain types and atmospheric conditions. Hence, the best input of turbulence for load calculations is by directly measuring it at the site where wind turbines will operate.
- Power curve measurements - The power curve of a wind turbine is sensitive to turbulence intensity, especially in the region around the rated wind speed. Turbulence measurements will enable accurate power curve measurements that are vital for a wind farm developer.
- Validation of wind profile models - In recent years with the increase in the size of the wind turbines, wind profile models that extend in the entire boundary layer are developed (Gryning et al., 2007; Peña et al., 2010a). These models are based on the assumption that momentum flux changes linearly with height. If we are able to measure turbulence at several heights, we can verify these assumptions. Alternatively, empirical relations of the variation of momentum flux with height can also be derived.

The next interesting question is what is the current standard for the measurement of turbulence in wind energy. The answer is the sonic anemometer. They are compact instruments that can measure all three components of wind velocity in relatively small sample volume that for all practical purposes can be considered a point. They need to be mounted on a meteorological mast (met-mast), such that the flow distortion due to the mast itself is kept to a minimum. Despite this there are disadvantages of using sonic anemometers in turbulence measurements, the most important being that tall met-masts are very expensive, and offshore, the costs increase significantly. We thus have to look for alternatives. Remote sensing methods such as sodars and lidars are viable alternatives, but they are still a subject of research for turbulence measurements. In this chapter we restrict the discussion to turbulence measurements using lidars only.

Although lidars have been introduced in wind energy recently, for meteorology they have been investigated previously to measure turbulence using different scanning tech-

niques. A common technique is by conical scanning and using the velocity azimuth display (VAD) technique of processing the data. One of the first remote sensing (Doppler radar) turbulence studies using a full 360° scan in a horizontal plane was carried out by Browning and Wexler (1968), where the limitations of horizontal homogeneity and vertical wind shear are explained in detail. Wilson (1970) modified the technique from Browning and Wexler (1968) and performed turbulence measurements over snow. Kropfli (1986) extended the technique to accommodate turbulence scales of motion larger than those described in Wilson (1970) and showed that these techniques could be used to make reasonable estimates of turbulent kinetic energy and momentum flux by modelling the random errors in the measurements.

Eberhard et al. (1989) studied turbulence using Doppler lidar and modelled the random errors using a partial Fourier decomposition method, which gave better estimates of the errors than Wilson (1970) and Kropfli (1986). Gal-Chen et al. (1992) presented a technique to analyse lidar data for turbulence measurements using the scans at two levels, and produced estimates of fluxes in the mixed layer, and spectra of the horizontal velocity at the surface. Banakh et al. (1995) presented an analysis of estimating the random errors in the measurement of the mean wind speed by lidars using the theory of isotropic turbulence. Banta et al. (2002) studied the turbulence characteristics under the conditions of low-level jets, using the vertical-slice scans of radial velocities. Smalikho et al. (2005) presented a method to use lidar data for the estimation of turbulent energy dissipation rate to study wake vortices of an aircraft. A comprehensive review is given in Engelbart et al. (2007) that covers different remote sensing techniques for turbulence measurements including lidars. A review of the use of lidars for wind energy applications is also presented in Emeis et al. (2007). Pichugina et al. (2008) demonstrated the sensitivity of the streamwise velocity variance to the spatial and temporal averaging, also by using the technique of vertical-slice scans of radial velocities. Recently, studies have been carried out to model the spatial averaging effects (Sjöholm et al., 2009) and compare the 3D turbulence measurements using three staring lidars (Mann et al., 2009). Wagner et al. (2009) modelled the systematic errors by approximating the conical scan and the scan time as a length scale, providing first estimates of the variances of the longitudinal component of wind velocity. Mann et al. (2010) estimated the momentum fluxes using lidars and modelled the unfiltered turbulence from the CW lidar, where the model compares reasonably well with the measurements.

The main objective of this chapter is to understand if lidars can measure turbulence. Wind speeds are measured using the conical scanning and VAD technique is used to process the data. Much of the text is taken from Sathe et al. (2011). A theoretical model is developed to estimate the systematic errors in the second-order moments of wind speeds in the atmospheric surface layer measured by lidars. The systematic errors are those that arise due to the averaging effect in the sample or pulse volume and the relatively large circle in which Doppler lidars scan to obtain 2-component horizontal wind profiles. Two types of lidars are considered, a continuous wave (CW) ZephIR lidar developed by QinetiQ (Natural Power) and a pulsed WindCube lidar developed by Leosphere. The verification is carried out by comparing the variances measured by the ZephIR and WindCube with that of the sonic anemometers placed at different heights on a meteorological mast. Section 10.2 describes the theory, where the systematic errors in the second-order moments are modelled for the ZephIR and WindCube. Section 10.3 describes the results along with some inferences. Section 10.4 gives a discussion on the systematic errors, and section 10.5 provides a conclusion. Finally, section 10.6 provides future perspectives.

## 10.2 Theory

The approach is similar to Wyngaard (1968), Citriniti and George (1997), where turbulence measured by the hot-wire anemometer probe was modelled. The general working principle of lidars (in particular CW lidar) is explained in detail in chapter 3, but to

familiarize the reader with the notations a brief explanation is also given here. Fig. 99

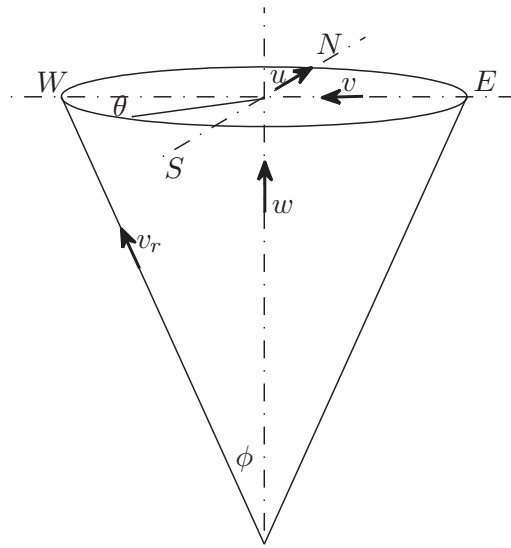


Figure 99: Schematic of the velocity azimuth display scanning

shows the lidar emitting the laser beam at different azimuth angles  $\theta$ . The azimuth angles increase from  $0^\circ$ – $360^\circ$  in the clockwise direction as for the geographical convention. The line-of-sight velocity (also called radial velocity  $v_r$ ) is measured by the lidar at each azimuth angle. The half-opening angle  $\phi$  ( $= 90^\circ - \text{elevation angle}$ ) is kept constant throughout the scan. The CW and pulsed lidars work on the principle of backscattering of the emitted radiation, and subsequent detection of the Doppler shift in the frequency of the received radiation. The Doppler shift in the frequency is related to  $v_r$  by,

$$\delta f = 2 \frac{v_r}{\lambda}, \quad (182)$$

where  $f$  and  $\lambda$  are the frequency and wavelength of the emitted radiation. Mathematically,  $v_r$  is given as the dot product of the unit directional vector and the velocity field at the point of focus for a CW lidar, and the center of the range gate (Lindelöw, 2007) for the pulsed lidar,

$$v_r(\theta) = \mathbf{n}(\theta) \cdot \mathbf{v}(d_f \mathbf{n}(\theta)), \quad (183)$$

where  $d_f$  is the focus distance for the CW lidar or the distance to the center of the range gate for the pulsed lidar at which the wind speeds are measured,  $\mathbf{v} = (u, v, w)$  is the instantaneous velocity field evaluated at the focus point or the center of the range gate  $d_f \mathbf{n}(\theta)$ , and  $\mathbf{n}(\theta)$  is the unit directional vector given as,

$$\mathbf{n}(\theta) = (\cos \theta \sin \phi, \sin \theta \sin \phi, \cos \phi). \quad (184)$$

In practice it is impossible to obtain the backscattered radiation precisely from only the focus point, and there is always backscattered radiation of different intensities from different regions in space along the line-of-sight. Hence, it is necessary to assign appropriate weights to the backscattered intensity such that the weight corresponding to the focus point or the center of the range gate is the highest. Mathematically, the weighted average radial velocity can be written as,

$$\tilde{v}_r(\theta) = \int_{-\infty}^{\infty} \varphi(s) \mathbf{n}(\theta) \cdot \mathbf{v}(s \mathbf{n}(\theta) + d_f \mathbf{n}(\theta)) ds, \quad (185)$$

where  $\varphi(s)$  is any weighting function, integrating to one, and  $s$  is the distance along the beam from the focus or the center of the range gate. For simplicity we assume that  $s = 0$  corresponds to the focus distance or center of the range gate.

Following are the main assumptions of the model:

1. The terrain is homogeneous
2. The flow field is frozen during the scan
3. Eq. (185) with an appropriately chosen  $\varphi(s)$  models the averaging well
4. The spatial structure of the turbulent flow is described well by the spectral tensor model of Mann (1994)

### Systematic turbulence errors for the ZephIR lidar

The ZephIR transmits the laser beam through a constantly rotating prism, giving the required half-opening angle of nominally  $30^\circ$ . Each of up to five heights are scanned for one or three seconds, corresponding to one or three complete rotations of the prism. The beam is then re-focused to the next height in the sequence and the scanning procedure is repeated. Up to five different heights can be selected, the sequence (with five heights and three second scans) taking up to 18 seconds to complete. Thus the lidar spends less than 20% of the time required to make a wind profile on any one of the five heights. A typical scan at each height consists of 50 measurements of  $v_r$  on the azimuth circle. If we assume the coordinate system such that  $u$  is aligned to the mean wind direction,  $v$  is perpendicular to the mean wind direction,  $w$  is the vertical component, and the mean wind comes from the North then  $\tilde{v}_r(\theta)$  can be expressed as,

$$\tilde{v}_r(\theta) = A + B \cos \theta + C \sin \theta, \quad (186)$$

where the coefficients  $A = w_{qq} \cos \phi$ ,  $B = u_{qq} \sin \phi$  and  $C = v_{qq} \sin \phi$  and the sign ambiguity in  $\tilde{v}_r(\theta)$  is neglected (see Mann et al. (2010)). We use the subscript  $qq$  to denote the velocity components measured by ZephIR, since they are not the true velocity components  $u$ ,  $v$  and  $w$ . The assumption that the mean wind comes from the North is only made for simplicity. For a lidar measuring at many points on the azimuth circle the choice of the mean wind direction does not matter since averaging over the entire circle is carried out. The values of the coefficients  $A$ ,  $B$  and  $C$  are found using least squares method by fitting Eq. (186) to the measured values of  $\tilde{v}_r(\theta)$  at all scanned azimuth angles. The coefficients can be written as Fourier integrals,

$$A = \frac{1}{2\pi} \int_0^{2\pi} \tilde{v}_r(\theta) d\theta, \quad (187)$$

$$B = \frac{1}{\pi} \int_0^{2\pi} \tilde{v}_r(\theta) \cos \theta d\theta, \quad (188)$$

$$C = \frac{1}{\pi} \int_0^{2\pi} \tilde{v}_r(\theta) \sin \theta d\theta. \quad (189)$$

We proceed by deriving expressions for the  $w_{qq}$  variance. The expressions for the (co-) variances of the remaining components of wind velocity can be derived in a similar manner.

The variance of  $A$  is defined as  $\sigma_A^2 = \langle A'^2 \rangle$ , where  $\langle \rangle$  denotes ensemble averaging of a variable and  $'$  denotes fluctuations. From the above definition of  $A$  we can write,

$$\sigma_A^2 = \langle w_{qq}^{\prime 2} \rangle \cos^2 \phi. \quad (190)$$

Using Eq. (187) we can also write,

$$\sigma_A^2 = \left\langle \left( \frac{1}{2\pi} \int_0^{2\pi} \tilde{v}_r'(\theta) d\theta \right)^2 \right\rangle. \quad (191)$$

Substituting  $\tilde{v}_r(\theta)$  from Eq. (185) into Eq. (191), converting the square of the integral



into a double integral, interchanging the order of integration and averaging we get,

$$\begin{aligned}\sigma_A^2 &= \frac{1}{4\pi^2} \int_0^{2\pi} \int_0^{2\pi} \int_{-\infty}^{\infty} \int_{-\infty}^{\infty} \langle v'_i(s_1 \mathbf{n}(\theta_1) + d_f \mathbf{n}(\theta_1)) v'_j(s_2 \mathbf{n}(\theta_2) + d_f \mathbf{n}(\theta_2)) \rangle \\ &\quad \varphi(s_1) \varphi(s_2) n_i(\theta_1) n_j(\theta_2) ds_1 ds_2 d\theta_1 d\theta_2, \\ &= \frac{1}{4\pi^2} \int_0^{2\pi} \int_0^{2\pi} \int_{-\infty}^{\infty} \int_{-\infty}^{\infty} R_{ij}(\mathbf{r}) \varphi(s_1) \varphi(s_2) n_i(\theta_1) n_j(\theta_2) ds_1 ds_2 d\theta_1 d\theta_2,\end{aligned}\quad (192)$$

where  $\langle v'_i(s_1 \mathbf{n}(\theta_1) + d_f \mathbf{n}(\theta_1)) v'_j(s_2 \mathbf{n}(\theta_2) + d_f \mathbf{n}(\theta_2)) \rangle = R_{ij}(\mathbf{r})$  is the covariance tensor separated by a distance  $\mathbf{r} = (s_1 \mathbf{n}(\theta_1) + d_f \mathbf{n}(\theta_1)) - (s_2 \mathbf{n}(\theta_2) + d_f \mathbf{n}(\theta_2))$  and is related to the three dimensional spectral velocity tensor  $\Phi_{ij}(\mathbf{k})$  by the inverse Fourier transform,

$$R_{ij}(\mathbf{r}) = \int \Phi_{ij}(\mathbf{k}) e^{i\mathbf{k}\cdot\mathbf{r}} d\mathbf{k},\quad (193)$$

where  $\int d\mathbf{k} \equiv \int_{-\infty}^{\infty} \int_{-\infty}^{\infty} \int_{-\infty}^{\infty} dk_1 dk_2 dk_3$ ,  $\mathbf{k} = (k_1, k_2, k_3)$  denotes the wave vector and the subscripts  $i, j$  take the values from 1 to 3. Inserting Eq. (193) into Eq. (192) we get,

$$\begin{aligned}\sigma_A^2 &= \int \Phi_{ij}(\mathbf{k}) \left( \int_{-\infty}^{\infty} \varphi(s_1) \left[ \frac{1}{2\pi} \int_0^{2\pi} n_i(\theta_1) e^{i(s_1+d_f)\mathbf{k}\cdot\mathbf{n}(\theta_1)} d\theta_1 \right] ds_1 \right) \\ &\quad \left( \int_{-\infty}^{\infty} \varphi(s_2) \left[ \frac{1}{2\pi} \int_0^{2\pi} n_j(\theta_2) e^{-i(s_2+d_f)\mathbf{k}\cdot\mathbf{n}(\theta_2)} d\theta_2 \right] ds_2 \right) d\mathbf{k}.\end{aligned}\quad (194)$$

Let  $\alpha_i(\mathbf{k}) = \left( \int_{-\infty}^{\infty} \varphi(s) \left[ \frac{1}{2\pi} \int_0^{2\pi} n_i(\theta) e^{i(s+d_f)\mathbf{k}\cdot\mathbf{n}(\theta)} d\theta \right] ds \right)$ , which physically represents the line-of-sight and conical averaging. Eq. (194) can then be written as (using Eq. 190),

$$\langle w_{qq}^{\prime 2} \rangle \cos^2 \phi = \int \Phi_{ij}(\mathbf{k}) \alpha_i(\mathbf{k}) \alpha_j^*(\mathbf{k}) d\mathbf{k},\quad (195)$$

where  $*$  denotes complex conjugation. Thus the integral reduces to evaluating  $\alpha_i(\mathbf{k})$ , since the analytical expressions for  $\Phi_{ij}(\mathbf{k})$  are given in Mann (1994). Eq. (195) can then be estimated numerically. For a CW lidar,  $\varphi(s)$  is well approximated by a Lorentzian function (Sonnenschein and Horrigan, 1971),

$$\varphi(s) = \frac{1}{\pi} \frac{l}{l^2 + s^2},\quad (196)$$

where  $l$  is the Rayleigh length ( $= \lambda d_f^2 / \pi r_b^2$ , where  $\lambda = 1.55 \mu\text{m}$  and  $r_b = 19.5 \text{ mm}$  is the beam radius). An attempt has been made to obtain analytical expressions for  $\alpha_i(\mathbf{k})$ . However, no general analytical solution exists for  $\alpha_i(\mathbf{k})$  and at most the integral can be reduced (by integrating over  $s$ ) to

$$\alpha_i(\mathbf{k}) = \frac{1}{2\pi} e^{id_f k_3 \cos \phi} \int_0^{2\pi} n_i(\theta + \theta_0) e^{id_f k_h \sin \phi \cos \theta} e^{-l|k_h \cos \theta \sin \phi + k_3 \cos \phi|} d\theta,\quad (197)$$

where  $k_h = \sqrt{k_1^2 + k_2^2}$  is the magnitude of the horizontal wave vector,  $\cos \theta_0 = k_1/k_h$ ,  $\sin \theta_0 = k_2/k_h$ , and  $n_i(\theta + \theta_0)$  is the component of the unit directional vector obtained from Eq. (184). Thus numerical integration has to be applied also for the evaluation of  $\alpha_i(\mathbf{k})$ .

A similar approach is taken for deriving  $u_{qq}$  and  $v_{qq}$  variances, where we obtain,

$$\langle u_{qq}^{\prime 2} \rangle \sin^2 \phi = \int \Phi_{ij}(\mathbf{k}) \beta_i(\mathbf{k}) \beta_j^*(\mathbf{k}) d\mathbf{k},\quad (198)$$

$$\langle v_{qq}^{\prime 2} \rangle \sin^2 \phi = \int \Phi_{ij}(\mathbf{k}) \gamma_i(\mathbf{k}) \gamma_j^*(\mathbf{k}) d\mathbf{k}.\quad (199)$$

The corresponding  $\beta$  and  $\gamma$  functions are,

$$\beta_i(\mathbf{k}) = \frac{1}{\pi} e^{id_f k_3 \cos \phi} \int_0^{2\pi} n_i(\theta + \theta_0) \cos(\theta + \theta_0) e^{id_f k_h \sin \phi \cos \theta} e^{-l|k_h \cos \theta \sin \phi + k_3 \cos \phi|} d\theta, \quad (200)$$

$$\gamma_i(\mathbf{k}) = \frac{1}{\pi} e^{id_f k_3 \cos \phi} \int_0^{2\pi} n_i(\theta + \theta_0) \sin(\theta + \theta_0) e^{id_f k_h \sin \phi \cos \theta} e^{-l|k_h \cos \theta \sin \phi + k_3 \cos \phi|} d\theta. \quad (201)$$

The derivation of the co-variances is merely a combination of the weighting functions  $\alpha_i(\mathbf{k})$ ,  $\beta_i(\mathbf{k})$ ,  $\gamma_i(\mathbf{k})$  and their complex conjugates used with  $\Phi_{ij}(\mathbf{k})$ .

### Modelling the low-pass filtering effect due to the three seconds scan

Since the ZephIR scans three circles in approximately three seconds, there will be a low-pass filter effect in turbulence measurements. We assume a length scale  $L_f = \langle u \rangle \times 3s$  such that it represents the three seconds averaging. We assume that the ZephIR scans a circle infinitely fast for three seconds. We model the corresponding filtering effect by a simple rectangular filter, such that,

$$f(x) = \begin{cases} \frac{1}{L_f} & \text{for } |x| < \frac{L_f}{2}; \\ 0 & \text{elsewhere,} \end{cases} \quad (202)$$

where  $x$  is the center of the scanning circle and  $f(x)$  is any function of  $x$ . The corresponding spectral transfer function is given as,

$$\hat{T}_f(k_1) = \text{sinc}^2\left(\frac{k_1 L_f}{2}\right), \quad (203)$$

where  $\text{sinc}(x) = \sin(x)/x$ . The variances of  $u_{qq}$ ,  $v_{qq}$  and  $w_{qq}$  are given as,

$$\langle u_{qq}'^2 \rangle \sin^2 \phi = \int \Phi_{ij}(\mathbf{k}) \beta_i(\mathbf{k}) \beta_j^*(\mathbf{k}) \hat{T}_f(k_1) d\mathbf{k}, \quad (204)$$

$$\langle v_{qq}'^2 \rangle \sin^2 \phi = \int \Phi_{ij}(\mathbf{k}) \gamma_i(\mathbf{k}) \gamma_j^*(\mathbf{k}) \hat{T}_f(k_1) d\mathbf{k}, \quad (205)$$

$$\langle w_{qq}'^2 \rangle \cos^2 \phi = \int \Phi_{ij}(\mathbf{k}) \alpha_i(\mathbf{k}) \alpha_j^*(\mathbf{k}) \hat{T}_f(k_1) d\mathbf{k}. \quad (206)$$

### Systematic turbulence errors for the WindCube lidar

The assumption made in section 10.2 that the mean wind direction comes from the North cannot be made for the WindCube, since it measures at four azimuth angles only (refer Fig. 99), e.g. North, East, South and West. In this case the coordinate system is such that  $u$  is aligned in the mean wind direction. Thus,

$$u_{wc} = u_{NS} \cos \Theta + u_{EW} \sin \Theta, \quad (207)$$

$$v_{wc} = u_{NS} \sin \Theta - u_{EW} \cos \Theta, \quad (208)$$

where  $u_{NS}$  and  $u_{EW}$  denote wind speeds in the North-South and East-West directions respectively,  $\Theta$  denotes the wind direction, and the subscript  $wc$  denotes the velocity components measured by the WindCube. From simple geometrical considerations (refer Fig. 99),

$$u_{NS} = \frac{\tilde{v}_{rN} - \tilde{v}_{rS}}{2 \sin \phi}, \quad (209)$$

$$u_{EW} = \frac{\tilde{v}_{rE} - \tilde{v}_{rW}}{2 \sin \phi}, \quad (210)$$

where  $\tilde{v}_{rN}$ ,  $\tilde{v}_{rS}$ ,  $\tilde{v}_{rE}$ ,  $\tilde{v}_{rW}$  are the weighted average radial velocities in the North, South, East and West directions respectively. For the  $w$  component,

$$w_{wc} = \frac{P(\tilde{v}_{rN} + \tilde{v}_{rS}) + Q(\tilde{v}_{rE} + \tilde{v}_{rW})}{2 \cos \phi}, \quad (211)$$

where  $P$  and  $Q$  are the weights associated with the wind direction such that  $P + Q = 1$ . Leosphere uses  $P = \cos^2 \Theta$  and  $Q = \sin^2 \Theta$ , and hence, we use the same in our calculations.

We proceed by deriving expressions for the  $u_{wc}$  variance. The expressions for the (co-) variances of the remaining components of wind velocity can be derived in a similar manner. Substituting Eqs. (209), (210) into Eq. (207) we get,

$$u_{wc} = \frac{1}{2 \sin \phi} [(\tilde{v}_{rN} - \tilde{v}_{rS}) \cos \Theta + (\tilde{v}_{rE} - \tilde{v}_{rW}) \sin \Theta]. \quad (212)$$

We define unit vectors in the four directions as,

$$\begin{aligned} \mathbf{n}_N &= \mathbf{n}(-\Theta), \\ \mathbf{n}_S &= \mathbf{n}(\pi - \Theta), \\ \mathbf{n}_E &= \mathbf{n}\left(\frac{\pi}{2} - \Theta\right), \\ \mathbf{n}_W &= \mathbf{n}\left(\frac{3\pi}{2} - \Theta\right), \end{aligned} \quad (213)$$

where  $\mathbf{n}_N$ ,  $\mathbf{n}_S$ ,  $\mathbf{n}_E$  and  $\mathbf{n}_W$  are the unit directional vectors in the North, South, East and West directions respectively. From Eq. (185), for the North direction,

$$\tilde{v}_{rN} = \int_{-\infty}^{\infty} \varphi(s) \mathbf{n}_N \cdot \mathbf{v}(s \mathbf{n}_N + d_f \mathbf{n}_N) ds. \quad (214)$$

To further simplify the notation we define the translation operator  $T_\delta$  acting on any scalar or vector field  $\xi(\mathbf{x})$ ,

$$T_\delta \xi(\mathbf{x}) = \xi(\mathbf{x} + \delta). \quad (215)$$

We also define a convolution operator  $C_{\mathbf{n}}$  acting on any scalar or vector field as,

$$C_{\mathbf{n}} \mathbf{v}(\mathbf{x}) = \int_{-\infty}^{\infty} \varphi(s) \mathbf{n} \cdot \mathbf{v}(\mathbf{x} + \mathbf{n}s) ds. \quad (216)$$

For the North direction, Eq. (214) can be written as,

$$\tilde{v}_{rN} = C_{\mathbf{n}_N} T_{d_f \mathbf{n}_N} \mathbf{v}. \quad (217)$$

We get similar expressions for South, East and West directions. Eq. (212) can then be written as,

$$u_{wc} = \frac{1}{2 \sin \phi} [(C_{\mathbf{n}_N} T_{d_f \mathbf{n}_N} - C_{\mathbf{n}_S} T_{d_f \mathbf{n}_S}) \cos \Theta + (C_{\mathbf{n}_E} T_{d_f \mathbf{n}_E} - C_{\mathbf{n}_W} T_{d_f \mathbf{n}_W}) \sin \Theta] \mathbf{v} \quad (218)$$

We also know that by definition,

$$\langle u'^2 \rangle = \int \langle \hat{u}(\mathbf{k}) \hat{u}^*(\mathbf{k}) \rangle d\mathbf{k}, \quad (219)$$

where  $\hat{\cdot}$  denotes Fourier transform and  $*$  denotes complex conjugation. In the Fourier space we have,

$$\widehat{T_\delta \mathbf{v}}(\mathbf{k}) = e^{i\mathbf{k} \cdot \delta} \hat{\mathbf{v}}(\mathbf{k}), \quad (220)$$

$$\widehat{C_{\mathbf{n}} \mathbf{v}}(\mathbf{k}) = \hat{\varphi}(\mathbf{n} \cdot \mathbf{k}) \mathbf{n} \cdot \hat{\mathbf{v}}(\mathbf{k}), \quad (221)$$

where  $\hat{\varphi}(k) = \text{sinc}^2(kl_p/2)$ , considering that the weighting function for a pulsed lidar is commonly defined as,

$$\varphi(s) = \begin{cases} \frac{l_p - |s|}{l_p^2} & \text{for } |s| < l_p; \\ 0 & \text{elsewhere,} \end{cases} \quad (222)$$

where  $l_p$  is the half length of the ideally rectangular light pulse leaving the lidar assuming the matching time windowing ( $= 2l_p/c$ , where  $c$  is the speed of light). Thus in Fourier space Eq. (218) can then be written as,

$$\begin{aligned}\hat{u}_{wc}(\mathbf{k}) &= \frac{1}{2\sin\phi} [(\mathbf{n}_N e^{id_f\mathbf{k}\cdot\mathbf{n}_N} \text{sinc}^2(\mathbf{k}\cdot\mathbf{n}_N l_p/2) - \mathbf{n}_S e^{id_f\mathbf{k}\cdot\mathbf{n}_S} \text{sinc}^2(\mathbf{k}\cdot\mathbf{n}_S l_p/2)) \cos\Theta \\ &\quad + (\mathbf{n}_E e^{id_f\mathbf{k}\cdot\mathbf{n}_E} \text{sinc}^2(\mathbf{k}\cdot\mathbf{n}_E l_p/2) - \mathbf{n}_W e^{id_f\mathbf{k}\cdot\mathbf{n}_W} \text{sinc}^2(\mathbf{k}\cdot\mathbf{n}_W l_p/2)) \sin\Theta] \cdot \hat{\mathbf{v}}(\mathbf{k}) \\ &\equiv \mathbf{b}(\mathbf{k}) \cdot \hat{\mathbf{v}}(\mathbf{k}),\end{aligned}\tag{223}$$

and the variance (from Eq. 219),

$$\langle u_{wc}'^2 \rangle = \int \Phi_{ij}(\mathbf{k}) b_i(\mathbf{k}) b_j^*(\mathbf{k}) d\mathbf{k},\tag{224}$$

where we have implicitly used the relation,  $\Phi_{ij}(\mathbf{k}) = \langle \hat{v}_i(\mathbf{k}) \hat{v}_j^*(\mathbf{k}) \rangle$ . The (co-) variances of other components can be estimated in a similar manner by first estimating the corresponding weighting functions  $c_i(\mathbf{k})$  and  $a_i(\mathbf{k})$  for  $v_{wc}$  and  $w_{wc}$  components respectively.

### Definition of the systematic error

For simplicity we define systematic error as the ratio of the lidar second-order moment to the true second-order moment. Thus a ratio equal to one would signify no systematic error, whereas deviations from unity signify systematic error. By definition, the true second-order moment of a velocity component is given as,

$$\langle v_i' v_j' \rangle = \int \Phi_{ij}(\mathbf{k}) d\mathbf{k}.\tag{225}$$

The theoretical systematic errors are calculated by taking the ratio of lidar second-order moments (Eqs. 195, 198, 199 and 223) to the true second-order moment (Eqn. 225). The numerical integration is carried out using an adaptive algorithm (Genz and Malik, 1980). For experimental comparison, the second-order moments measured by sonic anemometers are considered to be true second-order moments. Thus experimentally, the systematic errors are estimated by taking the ratio of the measured lidar second-order moments to sonic second-order moments.

## 10.3 Comparison of models with the measurements

The details of the measurement campaign are explained in Sathe et al. (2011). The estimation of  $\Phi_{ij}$  using the model from Mann (1994) requires three input parameters,  $\alpha\epsilon^{2/3}$ , which is a product of the spectral Kolmogorov constant  $\alpha$  (Monin and Yaglom, 1975) and the rate of viscous dissipation of specific turbulent kinetic energy  $\epsilon^{2/3}$ , a length scale  $L$  and an anisotropy parameter  $\Gamma$ . We use these input parameters obtained by fitting the sonic anemometer measurements under different atmospheric stability conditions, at several heights on the meteorological mast in the eastern sector (Peña et al., 2010b). The classification of atmospheric stability (table 16) is based on the Monin-Obukhov length ( $L_{MO}$ ) intervals (Gryning et al., 2007).  $L_{MO}$  is estimated using the eddy covariance method (Kaimal and Finnigan, 1994) from the high frequency (20 Hz) measurements at 20 m. Mathematically,  $L_{MO}$  is given as,

$$L_{MO} = -\frac{u_*^3 T}{\kappa g \overline{w'\theta'_v}},\tag{226}$$

where  $u_*$  is the friction velocity,  $\kappa = 0.4$  is the von Kármán constant,  $g$  is the acceleration due to gravity,  $T$  is the absolute temperature,  $\theta_v$  is the virtual potential temperature and  $\overline{w'\theta'_v}$  (covariance of  $w$  and  $\theta_v$ ) is the virtual kinematic heat flux.  $u_*$  is estimated as,

$$u_* = \sqrt[4]{\overline{u'w'^2} + \overline{v'w'^2}},\tag{227}$$

where  $\overline{u'w'}$  (covariance of  $u$  and  $w$ ) and  $\overline{v'w'}$  (covariance of  $v$  and  $w$ ) are the vertical fluxes of the horizontal momentum.

Table 16: Classification of atmospheric stability according to Monin-Obukhov length intervals

very stable (vs)	$10 \leq L_{MO} \leq 50$ m
stable (s)	$50 \leq L_{MO} \leq 200$ m
near-neutral stable (nns)	$200 \leq L_{MO} \leq 500$ m
neutral (n)	$ L_{MO}  \geq 500$ m
near-neutral unstable (nnu)	$-500 \leq L_{MO} \leq -200$ m
unstable (u)	$-200 \leq L_{MO} \leq -100$ m
very unstable (vu)	$-100 \leq L_{MO} \leq -50$ m

### Comparison with the ZephIR measurements

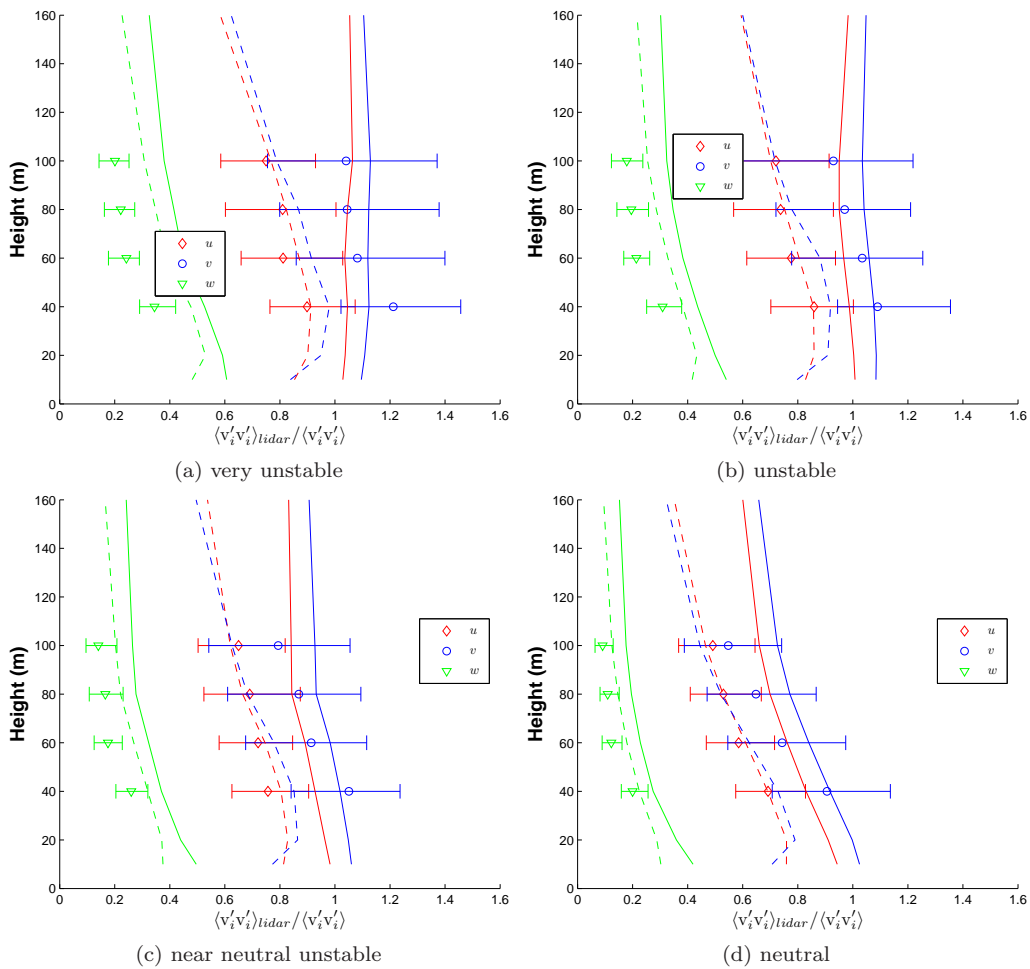


Figure 100: ZephIR systematic errors under different atmospheric stability conditions in the eastern sector. The markers indicate measurements. The solid lines are the theory without the low-pass filter, and the dashed lines are with the low-pass filter.

Figs. 100a–100g show the comparison of the modelled and measured systematic errors for  $u$ ,  $v$  and  $w$  variances over 10 minute periods. The theoretical points are shown with and without the low-pass filter. For the low-pass filter, the model is dependent on the mean wind speed and the plots are shown for  $\langle u \rangle = 9$  m/s at all heights, since this is the mean wind speed at Høvsøre. The measurements are represented as median (markers), first and third quartiles (error bars) respectively. We infer the following:

- The systematic errors vary considerably under different atmospheric stability con-

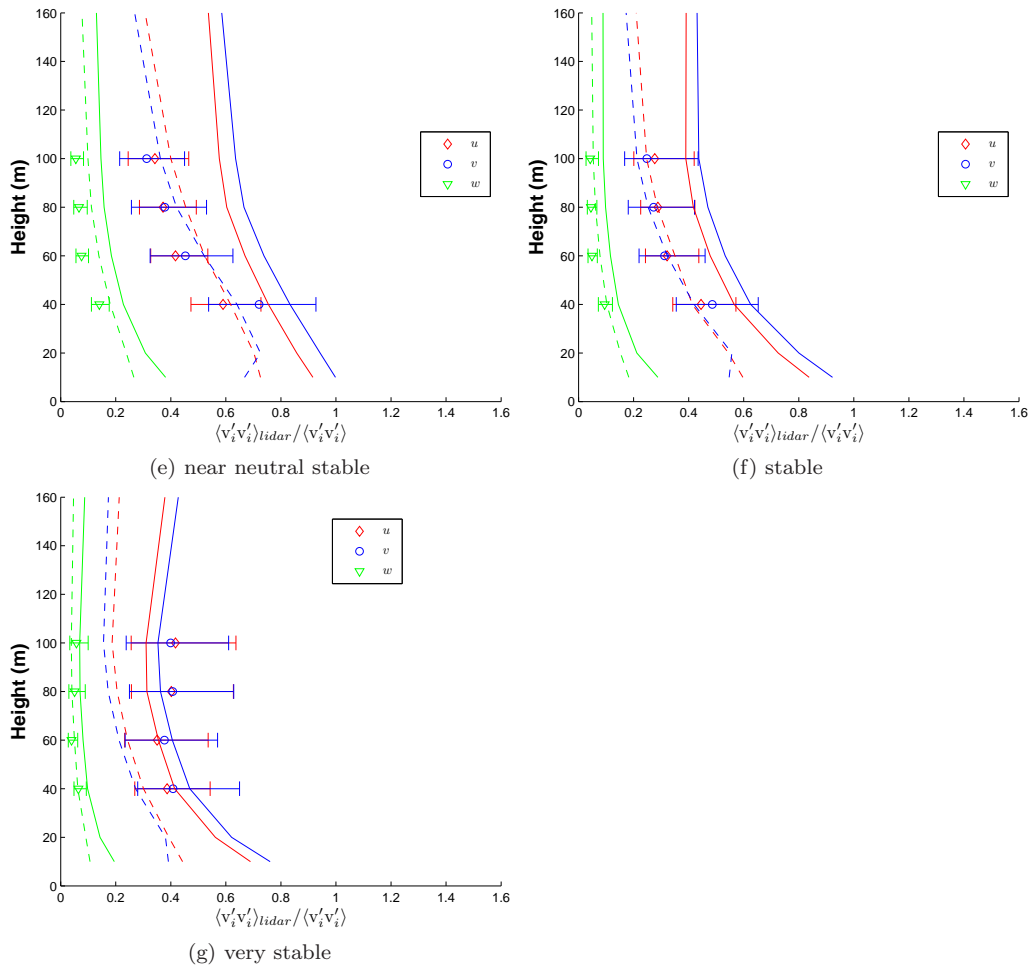


Figure 100: ZephIR systematic errors under different atmospheric stability conditions in the eastern sector. The markers indicate measurements. The solid lines are the theory without the low-pass filter, and the dashed lines are with the low-pass filter.

ditions – The variation is up to 50% for  $u$  and  $v$  variances, and up to 20% for  $w$  variance. This is due to a large variation in the length scales of different velocity components resulting in varying attenuation of the variances.

- The systematic errors increase with height under all atmospheric stability conditions – This is due to a quadratic increase in the sample volume with height (Lindelöw, 2007). The diameter of the scanning circle also increases with height.
- The systematic errors in  $w$  variance are much larger (approximately 3-5 times) than that of the  $u$  and  $v$  variances – This is due to the very small length scales of the  $w$  component as compared to those for  $u$  and  $v$ , resulting in the attenuation of the  $w$  variance of up to 90%. The  $u$  and  $v$  variances are attenuated up to 70%.
- There is a significant spread (first and third quartiles) in the systematic errors of  $u$  and  $v$  variances – These are the random errors and most likely occur due to the disjunct sampling (Lenschow et al., 1994) of the ZephIR. A thorough scientific investigation is needed to quantify random errors, but is not the focus of this paper.
- The trend of the systematic errors predicted by both models is in agreement with the observations at all heights.
- With the exception of very stable conditions, the model with the low-pass filter (Eqs. 204–206) is in better agreement with the measurements at all heights than without the low-pass filter.

In order to quantify the improvement in the model predictions using the low-pass filter, we compute the root mean square percent errors (RMSPE) between the measured and the modelled systematic errors for each stability condition. RMSPE is given as,

$$RMSPE = \sqrt{\frac{\sum \left( \frac{\left( \frac{\langle v'_i v'_i \rangle_{lidar}}{\langle v'_i v'_i \rangle} \right)_{measured} - \left( \frac{\langle v'_i v'_i \rangle_{lidar}}{\langle v'_i v'_i \rangle} \right)_{modelled} \times 100}{\left( \frac{\langle v'_i v'_i \rangle_{lidar}}{\langle v'_i v'_i \rangle} \right)_{measured}} \right)^2}{n}}, \quad (228)$$

where median values are used for the measurements.

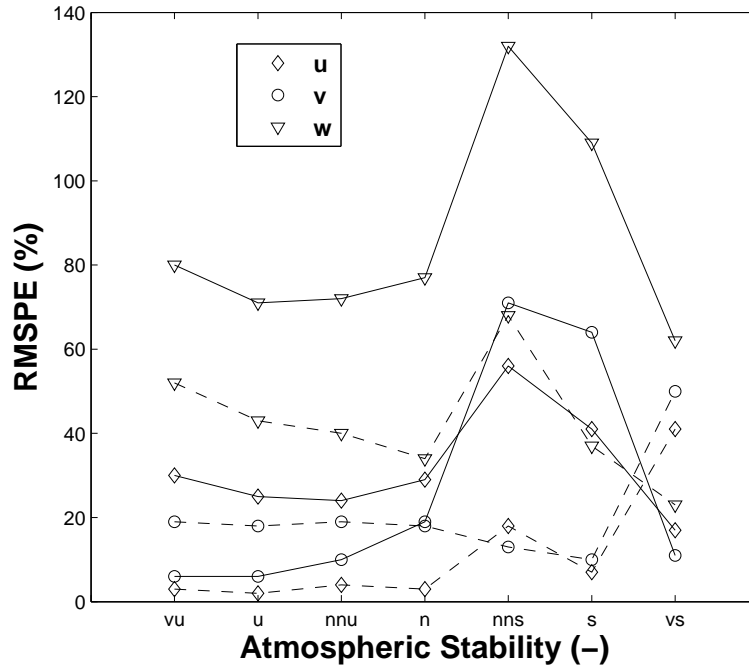


Figure 101: Root mean square percent error (RMSPE) in the prediction of the systematic errors for the ZephIR. The solid line shows the model without the low-pass filter and the dashed line shows the model with the low-pass filter. See table 16 for the meaning of the abbreviations on the x-axis.

Fig. 101 shows the comparison of the RMSPE in the prediction of the systematic errors with and without the low-pass filter for the ZephIR. A significant decrease in the RMSPE (of the order of 30%) of  $u$  and  $w$  variances is observed under all atmospheric stabilities (except for the very stable condition for  $u$  variance), when the low-pass filtering is used. For the  $v$  variance, there is a slight increase (up to 10%) in the RMSPE under unstable conditions, whereas for stable conditions a decrease of up to 40% is observed. Thus, in general, using the low-pass filter, the model predicts the systematic errors better than without using the low-pass filter. We also performed the calculations using the beam radius  $r_b = 24$  mm, and observed that the RMSPE for all three variance components changes only slightly ( $\pm 5\%$ ).

### Comparison with the WindCube measurements

Figs. 102a–102g show the comparison of the modelled and measured systematic errors (section 10.210.2) for  $u$ ,  $v$  and  $w$  variances over 10-min periods. We infer the following:

- The systematic errors vary considerably under different atmospheric stability conditions – The variation is up to 50% for  $u$  and  $v$  variances, and up to 20% for the  $w$  variance. The same is also observed for the ZephIR.

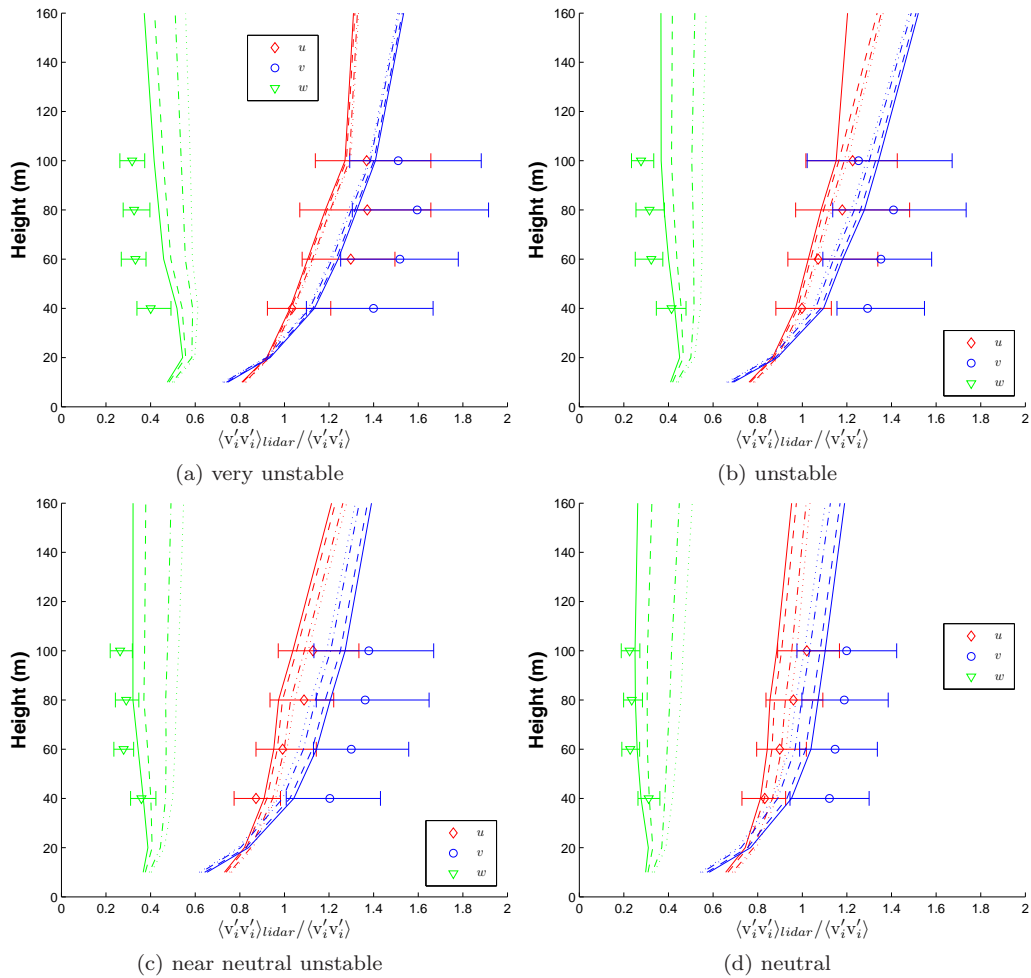


Figure 102: WindCube systematic errors under different atmospheric stability conditions in the eastern sector. The markers indicate measurements. The model variation with wind direction is plotted as dotted line for  $0^\circ$ , dash-dot line for  $15^\circ$ , dashed line for  $30^\circ$  and solid line for  $45^\circ$

- The systematic errors decrease with height for the  $u$  and  $v$  variances under all atmospheric stability conditions – For the WindCube, the probe length is constant (Lindelöw, 2007), and hence, at lower heights there is a combined averaging effect due to the probe length and the diameter of the scanning circle. Considering that at lower heights the length scales are smaller than at higher heights, it is likely that the variances are attenuated greater at lower heights than at higher heights. For  $w$  variance, the systematic error is approximately constant, and is most likely due to the small length scales.
- The systematic error in  $w$  variance is much larger (approximately 3-5 times) than that of the  $u$  and  $v$  variances. The same is also observed for the ZephIR.
- The spread in the systematic error (first and third quartiles) of the  $u$  and  $v$  variances is smaller than that of the ZephIR – This is most likely because the WindCube updates the velocity vector approximately every 6.5 seconds, whereas the ZephIR updates every 18 seconds.
- The systematic error varies significantly with the wind direction relative to the beam direction for  $w$  variance, and to a lesser degree for  $u$  and  $v$  variance under all stability conditions.



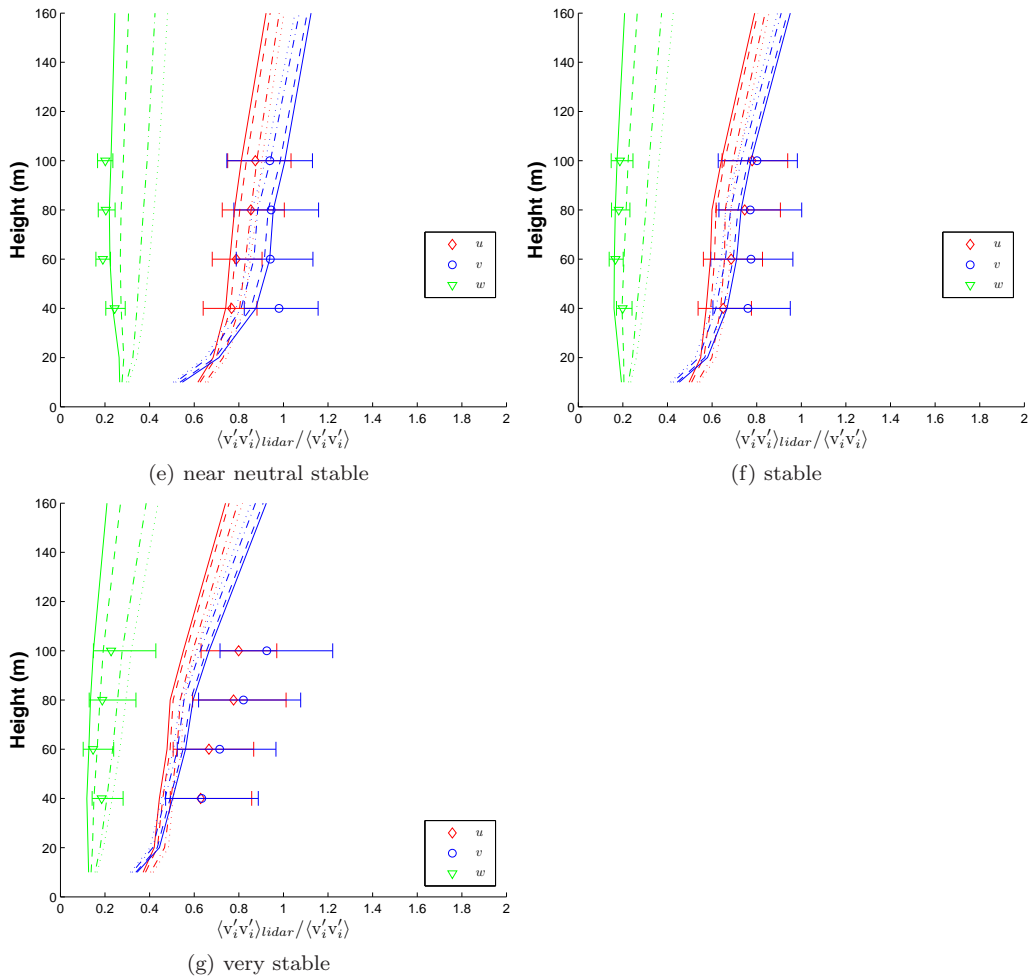


Figure 102: WindCube systematic errors under different atmospheric stability conditions in the eastern sector. The markers indicate measurements. The model variation with wind direction is plotted as dotted line for  $0^\circ$ , dash-dot line for  $15^\circ$ , dashed line for  $30^\circ$  and solid line for  $45^\circ$

Fig. 103 shows the comparison of the RMSPE in the prediction of the systematic errors for the WindCube and ZephIR (with the low-pass filter). It is observed that for  $u$  and  $v$  variances, with the exception of the near-neutral stable condition, the RMSPE in both lidars is approximately equal. There is a considerable variation in the RMSPE for the  $w$  variance. This is most likely because for the WindCube, the  $w$  variance is very sensitive to the wind direction due to its cosine and sine dependence. In general, for both lidars, except for the very stable condition, the model predicts the systematic errors for  $u$  variance reasonably well (RMSPE  $\approx 6\%$ ), followed by  $v$  variance (RMSPE  $\approx 12\%$ ). It is difficult to say whether the prediction for the  $w$  variance is less reliable or not (RMSPE of the order of 60%).

We do not model the filtering effect due to the scanning time ( $\approx 6.5$  seconds) of WindCube for two reasons:

1. Since the measurement is carried out at only four points, each lasting 0.5 seconds on the scanning circle, we cannot assume that the WindCube measures infinitely fast on the scanning circle (as we did for the ZephIR). The translations in each direction have to be convolved with the corresponding spectral transfer function, if the filtering is to be included.
2. The calculation becomes too cumbersome if the above procedure is followed.

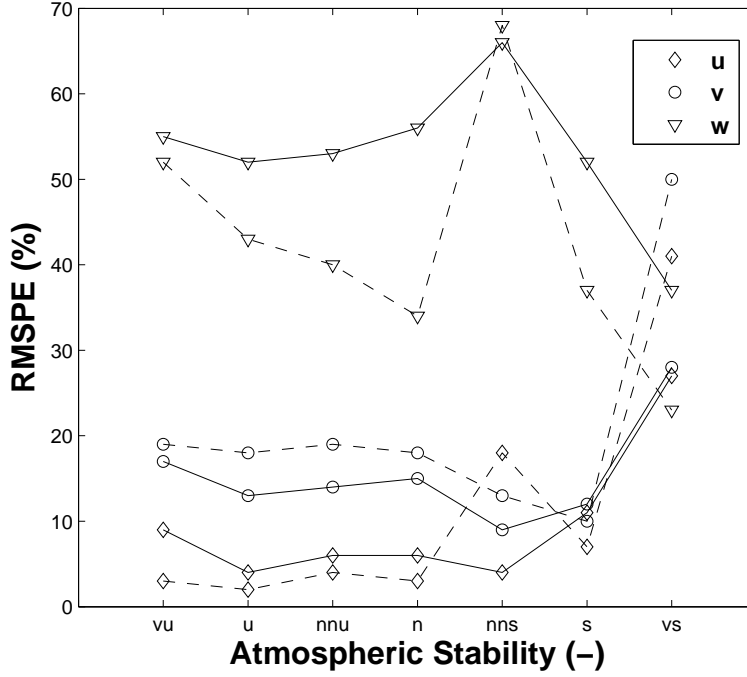


Figure 103: Comparison of the root mean square percent error (RMSPE) in the prediction of the systematic errors for the WindCube and ZephIR. The solid line is for the WindCube and the dashed line is for the ZephIR with the low-pass filter. See table 16 for the meaning of the abbreviations on the x-axis.

## 10.4 Discussion

Although the model is developed for specific lidars, the modelling framework would be the same for any other instrument. Additionally, we also model the low-pass filter for the three seconds scan in the ZephIR. We expected a large variation in the systematic errors under different atmospheric stability conditions, and hence, performed the analysis accordingly. Figs. 100 and 102 indeed justify our analysis.

In general, except for the very stable conditions, the model predicts the systematic errors quite well, where the RMSPE for the  $u$  and  $v$  variances are of the order of 4% and 15% respectively. For the ZephIR, when the low-pass filter is not used then the RMSPE is quite large (of the order of 30%) for the  $u$  variance. For the  $w$  variance, the high values of RMSPE (of the order of 60%) under all atmospheric stability conditions is observed. We think that two reasons could contribute to this:

1. The attenuation in the  $w$  variance is quite large (up to 90%), as compared to the  $u$  and  $v$  variances (up to 70%). Thus, a small difference in the model prediction and the measurements results in amplifying the RMSPE.
2. For the ZephIR, when the low-pass filter is used in the model, there is dependence on the mean wind speed. The model results (Fig. 100) are shown for  $\langle u \rangle = 9$  m/s only. Segregating the model and observations for different mean wind speeds will result in reducing the RMSPE.

For the WindCube, the model predicts a significant variation of the  $w$  variance with wind direction (Eq. 211). In order to estimate the influence of the weights  $P$  and  $Q$  on the prediction of systematic errors, we calculate  $\langle w_{wc}^2 \rangle$  from the equation for  $w$  that corresponds to Eq. (219) with two different ways of calculating  $w$ . The first is the formula use by Leosphere, e.g. Eq. (211) with  $P = \cos^2 \Theta$  and  $Q = \sin^2 \Theta$ , the second is  $P = Q = 1/2$ . The former is shown as a thin solid line in Fig. 104 and the latter as a thin dashed line. The spectral tensor parameters used are for neutral atmospheric stability

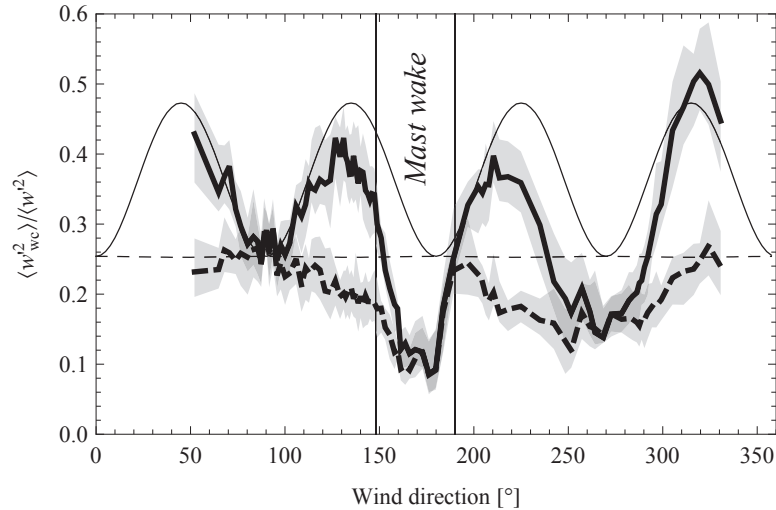


Figure 104: The ratio of the vertical velocity variance as measured by the WindCube and the actual variance measured and modeled at 100 m. The thin lines are the theoretical expectations using  $P = \cos^2 \Theta$  and  $Q = \sin^2 \Theta$  (solid line) and  $P = Q = 1/2$  (dashed line) in Eq. (211), respectively. The corresponding measurements are shown as broad curves with the first and third quartiles displayed as shades

from Peña et al. (2010b) at 100 m. The measurements of  $\langle w_{wc}'^2 \rangle / \langle w'^2 \rangle$ , shown as broad curves on Fig. 104, are from the same height, and both, measurements and theory show that  $\langle w_{wc}'^2 \rangle / \langle w'^2 \rangle$  using Leosphere's choice of  $P$  and  $Q$  can vary by a factor of two solely by changing the wind direction. If  $P = Q = 1/2$  is chosen the reduction of the vertical velocity variance does vary much less with wind direction, but the overall attenuation is stronger.

Since the model predicts the trend in the systematic errors in the  $w$  variance reasonably well (Figs. 100 and 102), qualitatively it could be said that the model also agrees well with the measurements for the  $w$  variance.

While comparing the performance of our model, the following should also be considered:

- The model is dependent on the three dimensional spectral velocity tensor (Mann, 1994), which is strictly valid for neutral conditions only. Thus, one has to be careful while comparing under different atmospheric stability conditions. In this study, we have reduced the uncertainty by using the the three input tensor parameters that are fitted to the measurements under different atmospheric stability conditions (Peña et al., 2010b).
- While using Eqs. (204)–(206), we have used the same mean wind speed at all heights. In reality, there is always wind shear, which also depends significantly on atmospheric stability (Motta and Barthelmie, 2005). However, the calculations will become too cumbersome, and hence, we made a crude approximation.
- The very stable conditions are generally difficult to analyze. There could be different reasons for the large deviation in the  $u$  and  $v$  variances, e.g.,
  - Uncertainty in the input tensor parameters
  - Lack of validity of the spectral tensor model (Mann, 1994) under different atmospheric stability conditions

Also, contrary to expectation, the measurements under very stable conditions (Figs. 100 and 102) show a decrease in the systematic errors for the  $u$  and  $v$  variances, as compared to the stable conditions.

There is also some room for reducing redundancy in the ZephIR measurements, which might reduce the spread of the systematic errors (quartile range). Instead of scanning

at several points on the circle, only four points are required. Reducing the measurement points would increase the dependence of the second-order moments on the wind direction (refer section 10.210.2). However, it would considerably reduce the time required for completing a VAD. There is also no need to scan the circle three times, e.g. in the present configuration, 50 points are scanned in approximately one second. Thus four points would take only 0.08 seconds. If it measures five heights sequentially, the next measurement would be after 0.4 seconds, giving a measurement frequency  $\geq 2$  Hz. Alternatively, at each of the four points the scans can also be performed rapidly at different heights sequentially before scanning the next point.

## 10.5 Conclusion

The systematic errors of the second-order moments measured by lidars using the conical scanning and VAD technique to process the data are quite large due to

1. the spatial separation of the data points along the line-of-sight and
2. the spatial separation of the data points in the conical section.

Also, from Eqs. (195, 198, 199 and 224) the general lidar equation for the second-order moments using the VAD data processing technique can be written as,

$$\langle v'_m v'_n \rangle_{lidar} = \int \Phi_{ij}(\mathbf{k}) X_i^m(\mathbf{k}) X_j^{*n}(\mathbf{k}) d\mathbf{k}; \quad (229)$$

$$X_i^m(\mathbf{k}) = \begin{cases} \beta_i(\mathbf{k}) \wedge b_i(\mathbf{k}), & m = 1 \\ \gamma_i(\mathbf{k}) \wedge c_i(\mathbf{k}), & m = 2 \\ \alpha_i(\mathbf{k}) \wedge a_i(\mathbf{k}), & m = 3 \end{cases}$$

The weighting functions  $\alpha_i(\mathbf{k})$ ,  $\beta_i(\mathbf{k})$ ,  $\gamma_i(\mathbf{k})$  are used for the ZephIR and  $a_i(\mathbf{k})$ ,  $b_i(\mathbf{k})$ ,  $c_i(\mathbf{k})$  are used for the WindCube. Thus, the measurement of the second-order moment by lidar involves interaction of all components of the spectral velocity tensor  $\Phi_{ij}(\mathbf{k})$  weighted by the corresponding weighting functions  $X_i^m(\mathbf{k})$  and  $Y_j^{*n}(\mathbf{k})$ . It is to be noted that Eqn. (229) is given in Einstein summation convention, and hence, in order to explicitly see the contribution of all components of  $\Phi_{ij}(\mathbf{k})$  on the measurement of the second-order moments by lidar, this equation must be expanded for all values of the subscripts  $i$  and  $j$ . In most cases, this results in the attenuation of the second-order moments, whereas in some cases this also results in amplification of the second-order moment, e.g. as observed for the WindCube in the unstable conditions (see Figs. 102a–102d).

## 10.6 Future Perspectives

It is clear that using the conical scanning and VAD technique to process the data turbulence cannot be measured precisely. However, it should not be misunderstood that lidars can never measure turbulence. It depends greatly on the measurement configuration. We are currently looking into alternative ways of analyzing the lidar data and different beam configurations that would render turbulence measurements more feasible. One idea is to use two different half opening angles as in Eberhard et al. (1989), who show that all terms in the Reynolds stress tensor can be obtained by using the single beam statistics, without resorting to beam covariances, which is done in this paper. That would require significant hardware modifications to the instruments treated here. Another idea is to supplement the analysis with information on the width of the Doppler spectra, as done for the momentum flux in Mann et al. (2010), in order to compensate for the effect of along-beam averaging.

## Notation

$\alpha$	spectral Kolmogorov constant
$\alpha_i$	ZephIR weighting function that represents the line-of-sight and conical averaging for the $w$ component
$\beta_i$	ZephIR weighting function that represents the line-of-sight and conical averaging for the $u$ component
$\mathbf{k}$	wave vector
$\mathbf{n}$	unit directional vector
$\mathbf{r}$	Separation distance
$\epsilon$	rate of viscous dissipation of specific turbulent kinetic energy
$\Gamma$	turbulence anisotropy parameter
$\gamma_i$	ZephIR weighting function that represents the line-of-sight and conical averaging for the $v$ component
$\hat{T}_f$	Spectral transfer function representing the three seconds averaging for the ZephIR
$\kappa$	von Kármán constant
$\lambda$	wavelength of the emitted radiation
$\langle v'_i v'_j \rangle$	true second-order moment
$v$	instantaneous velocity field
$\frac{u'v'}{w'\theta'_v}, \frac{v'w'}{w'\theta'_v}$	vertical fluxes of the horizontal momentum
$\frac{w'\theta'_v}{w'\theta'_v}$	virtual kinematic heat flux
$\phi$	half-opening angle
$\Phi_{ij}$	spectral velocity tensor
$\Theta$	Mean wind direction
$\theta$	azimuth angle
$\theta_v$	virtual potential temperature
$\tilde{u}_r$	weighted average radial velocity
$\varphi$	lidar weighting function along the line of sight
$a_i$	Windcube weighting function that represents the line-of-sight and conical averaging for the $w$ component
$b_i$	Windcube weighting function that represents the line-of-sight and conical averaging for the $u$ component
$c$	speed of light
$c_i$	Windcube weighting function that represents the line-of-sight and conical averaging for the $v$ component
$d_f$	focus distance/center of the range gate
$f$	frequency of the emitted radiation
$g$	acceleration due to gravity
$L$	Turbulence length scale
$l$	Rayleigh length
$L_f$	length scale that represents three seconds averaging in the ZephIR
$L_{MO}$	Monin-Obukhov length
$l_p$	half length of the ideally rectangular light pulse leaving the Windcube
$r_b$	beam radius
$R_{ij}$	Covariance tensor
$RMSPE$	root mean square percent errors
$s$	distance along the beam from the focus or center of the range gate
$T$	absolute temperature
$u$	Component of the velocity field in the mean wind direction
$u^*$	friction velocity
$u_{qq}$	Component of the velocity field in the mean wind direction measured by the ZephIR
$u_{WC}$	Component of the velocity field in the mean wind direction measured by the Windcube
$v$	Component of the velocity field perpendicular to the mean wind direction in a horizontal plane
$v_{qq}$	Component of the velocity field perpendicular to the mean wind direction in a horizontal plane measured by the ZephIR
$v_r$	radial velocity/line of sight velocity
$v_{WC}$	Component of the velocity field perpendicular to the mean wind direction in a horizontal plane measured by the Windcube
$w$	Component of the velocity field perpendicular to the mean wind direction in a vertical plane
$w_{qq}$	Component of the velocity field perpendicular to the mean wind direction in a vertical plane measured by the ZephIR
$w_{WC}$	Component of the velocity field perpendicular to the mean wind direction in a vertical plane measured by the Windcube

## References

- Banakh V. A., Smalikho I. N., Köpp F., and Werner C. (1995) Representativeness of wind measurements with a CW Doppler lidar in the atmospheric boundary layer. *Appl. Opt.*, **34**:2055–2067
- Banta R. M., Newsom R. J., Lundquist J. K., Pichugina Y. L., Coulter R. L., and Mahrt L. (2002) Nocturnal low-level jet characteristics over Kansas during CASES-99. *Bound.-Layer Meteorol.*, **105**:221–252

- Browning K. A. and Wexler R. (1968) The determination of kinematic properties of a wind field using a Doppler radar. *J. Appl. Meteorol.*, **7**:105–113
- Citriniti J. H. and George W. K. (1997) The reduction of spatial aliasing by long hot-wire anemometer probes. *Exp. Fluids*, **23**:217–224.
- Eberhard W. L., Cupp R. E., and Healy K. R. (1989) Doppler lidar measurements of profiles of turbulence and momentum flux. *J. Atmos. Oceanic Technol.*, **6**:809–819
- Emeis S., Harris M., and Banta R. M.. (2007) Boundary-layer anemometry by optical remote sensing for wind energy applications. *Meteorol. Z.*, **16**:337–347
- Engelbart D. A. M., Kallistratova M., and Kouznetsov R. (2007) Determination of the turbulent fluxes of heat and momentum in the ABL by ground-based remote-sensing techniques (a review). *Meteorol. Z.*, **16**:325–335
- Gal-Chen T., Xu M., and Eberhard W. L. (1992) Estimation of atmospheric boundary layer fluxes and other turbulence parameters from Doppler lidar data. *J. Geophys. Res.*, **97**:409–423
- Genz A. C. and Malik A. A. (1980) An adaptive algorithm for numerical integration over an n-dimensional rectangular region. *J. Comput. Appl. Math.*, **6**:295–302
- Gryning S.-E., Batchvarova E., Brümmner B., Jørgensen H., and Larsen S. (2007) On the extension of the wind profile over homogeneous terrain beyond the surface layer. *Bound.-Layer Meteorol.* **124**:251–268
- Kaimal J. C. and Finnigan J. J. (1994) *Atmospheric Boundary Layer Flows*, 255–257. Oxford University Press, New York
- Kaimal J. C., Wyngaard J. C., Izumi Y., and Coté O. R. (1972) Spectral characteristics of surface-layer turbulence. *Q. J. Royal Meteorol. Soc.*, **98**:563–589
- Kindler D., Oldroyd A., MacAskill A., and Finch D. (2007) An eight month test campaign of the QinetiQ ZephIR system: Preliminary results. *Meteorol. Z.* **16**:479–489
- Kropfli R. A.. (1986) Single Doppler radar measurement of turbulence profiles in the convective boundary layer. *J. Atmos. Oceanic Technol.*, **3**:305–314
- Lenschow D. H., Mann J., and Kristensen L. (1994) How long is long enough when measuring fluxes and other turbulence statistics? *J. Atmos. Oceanic Technol.*, **11**:661–673
- Lindelöw P. (2007) *Fibre Based Coherent Lidars for Remote Wind Sensing*. PhD thesis, Technical University Denmark
- Mann J. (1994) The spatial structure of neutral atmospheric surface-layer turbulence. *J. Fluid Mech.*, **273**: 141–168
- Mann J., Cariou J., Courtney M., Parmentier R., Mikkelsen T., Wagner R., Lindelow P., Sjöholm M., and Enevoldsen K. (2009) Comparison of 3D turbulence measurements using three staring wind lidars and a sonic anemometer. *Meteorol. Z.*, **18**:135–140
- Mann J, Peña A., Bingöl F., Wagner R., and Courtney M. S. (2010) Lidar scanning of momentum flux in and above the surface layer. *J. Atmos. Oceanic Technol.*, **27**:792–806
- Monin A. S. and Yaglom A. M. (1975) *Statistical Fluid Mechanics*, volume 2. MIT Press,
- Motta M. and Barthelmie R. J. (2005) The influence of non-logarithmic wind speed profiles on potential power output at Danish offshore sites. *Wind Energy*, 219–236
- Peña A., Hasager C. B., Gryning S.-E., Courtney M., Antoniou I., Mikkelsen T. (2009) Offshore wind profiling using light detection and ranging measurements. *Wind Energy* **12**:105–124
- Peña A., Gryning S.-E., and Hasager C. B. (2010a) Comparing mixing-length models of the diabatic wind profile over homogeneous terrain. *Theor. Appl. Climatol.* **100**:325–335
- Peña A., Gryning S.-E., and Mann J. (2010) On the length scale of the wind profile. *Q. J. Royal Meteorol. Soc.*, **136**: 2119–2131
- Pichugina Y. L., Banta R. M., Kelly N. D., Jonkman B. J., S C. Tucker S. C., R K. Newsom B. J., and Brewer W. A. (2008) Horizontal-velocity and variance measurements in the stable boundary layer using Doppler lidar: Sensitivity to averaging procedures. *J. Atmos. Oceanic Technol.*, **25**:1307–1327
- Sathe A., Mann J., Gottschall J., and Courtney M. (2011) Can wind lidars measure turbulence? *Accepted for publication in the J Atmos. Oceanic Technol.*

- Sjöholm M., Mikkelsen T., Mann J., Enevoldsen K., and Courtney M. (2009) Spatial averaging-effects on turbulence measured by a continuous-wave coherent lidar. *Meteorol. Z.*, **18**:281–287
- Smalikho I., Kopp F., and Rahm S. (2005) Measurement of atmospheric turbulence by 2- $\mu\text{m}$  Doppler lidar. *J Atmos. Oceanic Technol.*, **22**:1733–1747
- Smith D. A., Harris M., Coffey A. S., Mikkelsen T., Jørgensen H. E., Mann J., and Danielian R. (2006) Wind lidar evaluation at the Danish wind test site in Høvsøre. *Wind Energy* **9**:87–93
- Sonnenschein C. M. and Horrigan F. A. (1971) Signal-to-noise relationships for coaxial systems that heterodyne backscatter from atmosphere. *Appl. Opt.*, **10**: 1600
- Wagner R., Mikkelsen T., and Courtney M. (2009) Investigation of turbulence measurements with a continuous wave, conically scanning lidar. Technical Report Risø-R-1682(EN), Risø DTU, 2009
- Wilson D. A. (1970) Doppler radar studies of boundary layer wind profiles and turbulence in snow conditions. In *Proc. 14<sup>th</sup> Conf. on Radar Meteorology*, 191–196,
- Wyngaard J. C. (1968) Measurement of small-scale turbulence structure with hot wires. *J. Sci. Instrum.*, **1**:1105–1108

# 11 Precision (and accuracy) for lidars

## Basics of a standardized testing of lidar profilers

**Julia Gottschall**

*Wind Energy Division, Risø DTU, Roskilde, Denmark*

---

The two key issues of this contribution are: the need for traceable lidar measurements, and the concept of a verification scheme defined for this purpose, respectively – both issues are briefly outlined below. For a comprehensive overview and discussion we refer to Gottschall et al. (2011).

### 11.1 Traceability for lidar measurements

The need for measuring wind speed and direction at greater heights and at several levels simultaneously gains in importance as wind turbines get larger and higher. For this purpose, remote sensing profilers become very attractive for disciplines like resource assessment and power performance testing. However, the existing standards only permit the use of cup anemometers as standard instruments. The main issue preventing the use of remote sensors in such standards is the need to maintain the traceability of the measurements in the international standard system.

Based on the results for a considerable number of commercial lidars tested at Risø DTU during the last years, we have defined a verification procedure that enables us to achieve the required traceability for lidar profilers. A significant limitation of the procedure is the considerable uncertainty introduced by the reference sensors. The decision as to whether to apply the derived lidar calibration or not therefore mainly depends on the interpretation of this reference uncertainty and the assumed and observed biases.

The work on lidar measurement traceability is directly connected to our more general activities on lidar testing – see e.g. Gottschall and Courtney (2010). However, an even stronger focus is put on the estimation of uncertainties and the necessary requirements for a standardization of the applied procedures.

### 11.2 General concept of verification scheme

The basic concept of the verification procedure proposed here is a direct comparison of measurements from a lidar profiler and reference sensors (cup anemometers and wind vanes) at different height levels. The results of the verification test are used in terms of both a calibration and a classification – based on the corresponding procedures for cup anemometers as described in IEC 61400-12-1 (IEC, 2005).

The comparison includes a statistical evaluation of the measurements, building the basis for the subsequent uncertainty estimation, but also a detailed check of the collected data with respect to outliers. Outliers, defined here as extreme deviations between the reference and lidar mean values, should be traced back either to the lidar or the reference sensors and their quantity minimized by means of appropriate filtering criteria.

Furthermore, the lidar to reference sensor comparison can provide the basis for correcting the lidar measurements with respect to the reference, i.e. a calibration of the lidar. The corresponding calibration function is found as the result of a regression analysis, for which different regression models can be assumed. The choice of the regression model is a trade-off between accuracy, flexibility and complexity, and the number of free parameters



is adjusted accordingly.

In this connection, possible error sources influencing the comparison of lidar and reference measurements and different error models differing in the number of free parameters that capture the error sources to a lesser or greater extent, have to be considered carefully – cf. (Lindelöw-Marsden, 2009).

The uncertainty related to the scatter between the recorded lidar and reference measurements, on the other hand, is found as the standard deviation of the deviations between the measurements in a bin-average analysis following the idea of a classification of cup anemometers according to IEC 61400-12-1. Classification here means to investigate the scatter in the data that is due to varying (internal and external) conditions and express this scatter as an uncertainty. Unlike for cup anemometers the conditions cannot be manipulated in a well-defined way but have to be taken as they arise under the verification test – that is why we refer to a limited classification.

Future standards allowing for the application of lidar profilers (as e.g. the revised version of IEC 61400-12-1 that is currently prepared) will in all likelihood involve this or a similar verification concept. An alternative to our approach – partly agreeing with our concept but partly also deviating from it – is e.g. proposed in Albers et al. (2010).

## References

- Albers A., Janssen A. W. and Mander J. (2010) How to gain acceptance for lidar measurements. (<http://www.windguard.de/ueber-uns/veroeffentlichungen/>)
- Gottschall J. and Courtney M. S. (2010) Verification test for three Windcube WLS7 LiDARs at the Høvsøre test site. Risø-R-1732(EN) (ISBN: 978-87-550-3819-6)
- Gottschall J., Wagner R., Courtney M. S., Jørgensen H. E., and Antoniou I. (2011) Lidar profilers in the context of wind energy – A verification procedure for traceable measurements. Wind Energy (submitted)
- IEC (2005) Wind Turbines – Part 12-1: Power performance measurements of electricity producing wind turbines (IEC 61400-12-1 International standard)
- Lindelöw-Marsden P. (2009) UpWind D1. Risø-R-1681(EN) (ISBN: 978-87-550-3735-9)

# 12 Derivation of the mixing-layer height by remote sensing including RASS

**Stefan Emeis**

*Institute for Meteorology and Climate Research,  
Atmospheric Environmental Research Division (IMK-IFU),  
Karlsruhe Institute of Technology, Garmish-Partenkirchen, Germany*

---

## 12.1 Introduction

This chapter gives an overview of the derivation of mixing-layer height (MLH) by surface-based remote sensing instruments. Sometimes the terms mixed-layer height or mixing height are used as well for MLH, but we will stick here to the most common term mixing-layer height. The detection of the vertical layering of the atmospheric boundary layer (ABL) is one of the principal tasks of experimental boundary-layer research. We must distinguish between the mixing-layer height, MLH (see section 12.2) and the boundary-layer height,  $z_i$  (see section 12.3). The boundary-layer height is the height up to which the influence of the presence of the lower surface is detectable. The mixing-layer height is the height up to which atmospheric properties (such as wind speed and turbulence) or substances originating from the surface are dispersed by turbulent vertical mixing processes. The mixing-layer – if it is present at all – is a part of the ABL. Thus, the mixing-layer height is usually shallower than the boundary layer, but it fills the whole ABL in deep convective boundary layers.

The next section describes methods to detect the mixing-layer height, while section 12.3 briefly mentions methods to capture the boundary-layer height. Acoustic (see Chapter 16) and optical (see the majority of the preceding chapters) sounding techniques have got a broad coverage in throughout this volume. RASS techniques are quite unusual in the assessment of wind resources. Therefore, a subsection on technical details of this instrumentation has been added in section 12.2. A more complete survey of remote sensing instrumentation is given in Emeis (2010a) and an overview of applications of ground-based remote sensing is presented in Emeis (2010b).

## 12.2 Mixing-layer height

The mixing-layer height is the height up to which atmospheric properties or substances originating from the Earth's surface or formed within this layer are dispersed almost uniformly over the entire depth of this layer by turbulent vertical mixing processes. Therefore, the existence and the height of a mixing layer can either be analyzed from a detection of the presence of the mixing process, i.e. turbulence, or from the verification that a given conservative atmospheric variable is distributed evenly over a certain height range. The level of turbulence can for instance be derived from fluctuations of the wind components or from temperature fluctuations. Suitable conservative atmospheric variables for the identification of the mixing layer and its height are, e.g., potential temperature, specific humidity or aerosol particle concentrations.

The latest rather complete overview of methods to determine MLH from in-situ measurements and surface-based remote sensing had been given by Seibert et al. (2000). Since then considerable development has taken place, especially concerning the usage of surface-based remote sensing methods (see the review paper by Emeis et al. (2008)). This chapter will mainly follow this latter review.

Optical methods for MLH detection may be used to illustrate this recent progress.

Seibert et al. (2000) still classified lidar methods as expensive, not eye-safe, with a high lowest range gate, limited range resolution, and sometimes subject to ambiguous interpretation. This has changed drastically in the last ten years when better lidars have been built and ceilometers have been discovered to be a nearly ideal boundary layer sounding instrument. Progress has been made in the field of acoustic sounding as well. Similarly, algorithms for the determination of MLH from vertical profiles of the acoustic backscatter intensity as described in Beyrich (1997) and Seibert et al. (2000) have been enhanced by using further variables available from sodar measurements such as the wind speed and the variance of the vertical velocity component (Asimakopoulos et al., 2004; Emeis and Türk, 2004). Such enhancements had been named as possible methods in Beyrich (1995) and Seibert et al. (2000) but obviously no example was available at that time.

A variety of different algorithms have been developed by which the MLH is derived from ground-based remote sensing data (see Table 17 for a short overview). We will mainly concentrate on acoustic and optical remote sensing because electro-magnetic remote sensing has too high lowest range gates for a good coverage of shallow MLH. The disadvantage of a too high lowest range gate can partly be circumvented by slantwise profiling or conical scanning if the assumption of horizontal homogeneity can be made.

*Table 17:* Overview of methods using ground-based remote sensing for the derivation of the mixing-layer height mentioned in this chapter (see right most column for section number).

method	short description	section
acoustic ARE	analysis of acoustic backscatter intensity	12.2-sodar
acoustic HWS	analysis of wind speed profiles	12.2-sodar
acoustic VWV	analysis of vertical wind variance profiles	12.2-sodar
acoustic EARE	analysis of backscatter and vertical wind variance profiles	12.2-sodar
optical threshold	detection of a given backscatter intensity threshold	12.2-ceilometer
optical gradient	analysis of backscatter intensity profiles	12.2-ceilometer
optical idealized backscatter	analysis of backscatter intensity profiles	12.2-ceilometer
optical wavelet	analysis of backscatter intensity profiles	12.2-ceilometer
optical variance	analysis of backscatter intensity profiles	12.2-ceilometer
acoustic/electro-magnetic	RASS	12.2-RASS
acoustic/electro-magnetic	sodar-RASS and windprofiler-RASS	12.2-RASS
acoustic/electro-magnetic/in situ	sodar-RASS plus surface heat flux data	12.2-RASS
acoustic/electro-magnetic	sodar plus windprofiler	12.2-further techniques
acoustic/optical	sodar plus ceilometer	12.2-further techniques

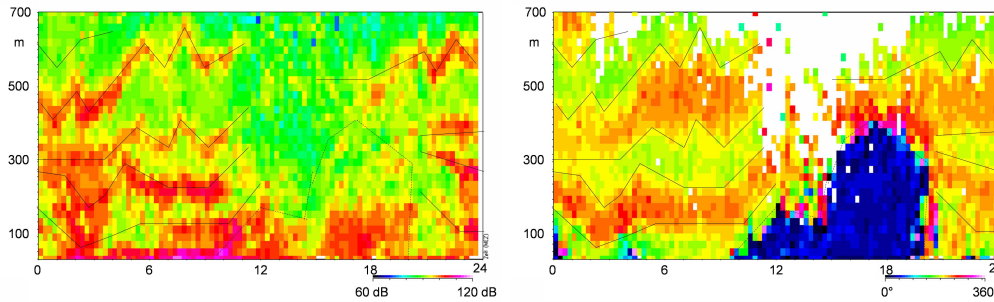


Figure 105: Sample time-height cross-section from acoustic sounding with a sodar. Left: acoustic backscatter intensity, right: horizontal wind direction. Thin black lines demark inversions.

### Sodar

Acoustic methods either analyze the acoustic backscatter intensity, or, if Doppler shifts in the backscattered pulses can be analyzed, features of vertical profiles of the wind components and its variances as well. The acoustic backscatter intensity is proportional to small-scale fluctuations in atmospheric temperature (usually generated by turbulence) or by stronger vertical temperature gradients. The latter feature may be an indication for the presence of temperature inversions, which can often be found at the top of the mixing layer.

Beyrich (1997) listed possible analyses which can mainly be made from acoustic backscatter intensities measured by a sodar. Later, Asimakopoulos et al. (2004) summarized three different methods to derive MLH from sodar data: (1) the horizontal wind speed method (HWS), (2) the acoustic received echo method (ARE), and (3) the vertical wind variance method (VWV). We will mainly follow this classification here and finally add a fourth method, the enhanced ARE method (EARE).

Figure 105, showing an acoustic sounding taken in an Alpine valley, gives an impression what wealth of detailed vertical information can be derived from acoustic boundary-layer sounding. The left-hand frame displays the acoustic backscatter intensity and the right-hand frame the wind direction as time-height sections over one day (from midnight to midnight) and over a height range of 700 m. The depicted wintry situation from a day in January exhibits a multiple layering of the air in that valley due to the very stable thermal stratification of the valley air over a snow-covered valley floor. The multiple layering originated from an interlacing of down-valley (wind direction around  $190^\circ$ ) and down-slope (wind direction around  $230^\circ$ ) flows. The layers are separated by temperature inversions and each higher layer is potentially warmer than the next lower layer. They persisted nearly the whole day because no vertical mixing took place in the stably stratified valley atmosphere.

**Acoustic received echo (ARE) method** The ARE method is the most basic method of determining MLH from acoustic remote sensing. Most of the methods listed in Beyrich (1997) belong to this method. The method does not require an analysis of the Doppler shift of the backscattered signals. The method makes use of the assumption that turbulence is larger in the mixing layer than in the atmosphere above, and that this turbulence is depicted in the intensity of the acoustic backscatter. MLH is analyzed either from the maximum negative slope or from the changing curvature of the vertical profile of the acoustic backscatter intensity or it is analyzed from the height where the backscatter intensity decreases below a certain pre-specified threshold value.

**Horizontal wind speed (HWS) method** The HWS method requires the analysis of the Doppler shift of the backscattered acoustic signals. The algorithm is based on the analysis of the shape of hourly-averaged vertical wind speed profiles using the assumption that wind speed and wind direction are almost constant within the mixing layer but approach gradually towards the geostrophic values above the mixing layer. Beyrich (1997) listed this method in his Tab. 2 but did not discuss it further. The applicability of the method is probably limited to the well-developed convective boundary layers (CBL) due to the underlying assumptions. Such CBLs are often higher than the maximum range of a sodar. Even if the CBL height is within the range of the sodar the algorithm for the analysis of the Doppler shift often fails above the inversion topping of the CBL due to too low signal-to-noise ratios.

**Vertical wind variance (VWV) method** The VWV method is also working only for CBLs. It is based on the vertical profile of the variance of the vertical velocity component  $\sigma_w$ . In a CBL  $\sigma_w$  reaches a maximum in a height  $az_i$ . Typical values for  $a$  are between 0.35 and 0.40. Thus, in principle, this is an extrapolation method. It has been tried for sodar measurements because it permits a detection of MLH up to heights which are 2.5 times above the limited maximum range (usually between 500 and 1000 m) of the sodar. Beyrich (1997) classified this method as not reliable.

**Enhanced acoustic received echo (EARE) method** The EARE algorithm has been proposed by Emeis and Türk (2004) and Emeis et al. (2007). The method is an enhancement of the ARE method in two ways. Firstly, it includes further variables into the MLH algorithm that are available from Doppler-sodars. The benefits of the additional usage of the variance of the vertical velocity component have been demonstrated by Emeis and Türk (2004). Secondly, it determines not only MLH from sodar measurements but also the heights of additional lifted inversions. Especially in orographically complex terrain, the vertical structure of the ABL can be very complicated. Emeis et al. (2007) have shown that several persistent inversions one above the other which form in deep Alpine valleys can be detected from sodar measurements (Fig. 105).

EARE determines three different types of heights based on acoustic backscatter intensity and the variance of the vertical velocity component. Because the horizontal wind information above the inversion is not regularly available from sodar measurements, horizontal wind data have not been included into this scheme. In the following a letter “ $H$ ” and an attached number will denote certain derived heights which are related to inversions and the MLH; while the variable  $z$  is used to denote the normal vertical coordinate. The EARE algorithm detects:

- the height ( $H1$ ) of a turbulent layer characterised by high acoustic backscatter intensities  $R(z)$  due to thermal fluctuations (therefore having a high variance of the vertical velocity component  $\sigma_w$ ),
- several lifted inversions ( $H2_n$ ) characterized by secondary maxima of acoustic backscatter due to a sharp increase of temperature with height and simultaneously low  $\sigma_w$  (like those depicted in the left-hand frame of Fig. 105), and
- the height of a surface-based stable layer ( $H3$ ) characterised by high backscatter intensities due to a large mean vertical temperature gradient starting directly at the ground and having a low variance of the vertical velocity component.

The height  $H1$  corresponds to a sharp decrease  $\partial R/\partial z < DR_1$  of the acoustic backscatter intensity  $R(z)$  below a threshold value  $R_c$  with height  $z$  usually indicating the top of a turbulent layer:

$$\begin{aligned}
 H1 = z, \quad \text{if} \quad (R(z) < R_c \quad \text{and} \quad R(z+1) < R(z) + zDR_1 \\
 \quad \quad \quad \text{and} \quad R(z+2) < R(z) + 2zDR_1). \quad (230)
 \end{aligned}$$

$R_c = 88$  dB and  $DR_1 = -0.16$  dB m<sup>-1</sup> have proven to be meaningful values in the above mentioned studies.  $R_c$  is somewhat arbitrary because the received acoustic backscatter intensities from a sodar cannot be absolutely calibrated. An absolute calibration would require the knowledge of temperature and humidity distributions along the sound paths for a precise calculation of the sound attenuation in the air.  $DR_1$  is, at least for smaller vertical distances, independent from the absolute value of  $R_c$ . An application-dependent fine-tuning of  $R_c$  and  $DR_1$  may be necessary.

Elevated inversions are diagnosed from secondary maxima of the backscatter intensity that are not related to high turbulence intensities. For elevated inversions increase in backscatter intensity below a certain height  $z = H2$  and a decrease above is stipulated while the turbulence intensity is low:

$$H2_n = z, \quad \text{if } (\partial R/\partial z|_{z+1} < -DR_2 \quad \text{and} \quad \partial R/\partial z|_{z-1} > DR_2 \\ \text{and } \sigma_w < 0.70 \text{ m s}^{-1}) \quad (231)$$

for  $n = 1, \dots, N$ . In Emeis et al. (2007)  $N$  was chosen to be five. A threshold value  $DR_2 = 0.08$  dB m<sup>-1</sup> has proven suitable. But again, an application-dependent tuning may be advisable.

The determination of the height of the stable surface layer  $H3$  is started if the backscatter intensity in the lowest range gates is above 105 dB while  $\sigma_w$  is smaller than 0.3 m s<sup>-1</sup>. The top of the stable layer  $H3$  is at the height where either the backscatter intensity sinks below 105 dB or  $\sigma_w$  increases above 0.3 m s<sup>-1</sup>,

$$H3 = z, \text{ if } (R(z) > 105 \text{ dB and } R(z+1) < 105 \text{ dB and } \sigma_w(z) < 0.3 \text{ m s}^{-1}) \text{ or} \\ \text{if } (\sigma_w(z) < 0.3 \text{ m s}^{-1} \text{ and } \sigma_w(z+1) > 0.3 \text{ m s}^{-1} \text{ and } R(z) > 105 \text{ dB})(232)$$

The  $\sigma_w$  values used in Eqs. (231) and (232) have been determined by optimizing the automatic application of the detection algorithm. In doing so it turned out that no lifted inversions occurred with a variance  $\sigma_w$  higher than 0.7 m s<sup>-1</sup> and that the variance  $\sigma_w$  in nocturnal stable surface layers was always below 0.3 m s<sup>-1</sup>. The first  $\sigma_w$  threshold made it possible to distinguish between inversions and elevated layers of enhanced turbulence. The latter  $\sigma_w$  threshold made it possible to differentiate between nocturnal stable surface layers and daytime super-adiabatic surface layers although both types of surface layers yield more or less the same level of backscatter intensity. Finally MLH from the acoustic remote sensing is determined as the minimum of  $H1$ ,  $H2_1$ , and  $H3$ :

$$\text{MLH}_{\text{ac}} = \min(H1, H2_1, H3). \quad (233)$$

## Ceilometer

Usually the aerosol content of the mixing layer is higher than in the atmospheric layer above, because the emission sources for aerosol are in most cases on the ground. Aerosol formation from precursors mainly takes place near the surface as well. Making the assumption that the vertical aerosol distribution adapts rapidly to the changing thermal structure of the boundary layer, MLH can be determined from the analysis of the vertical aerosol distribution. This also includes the assumption that the vertical aerosol distribution is not dominated by horizontally advected aerosol plumes or layers. The heights of the near surface aerosol layers ( $H4_n$ ) can be analysed from the optical vertical backscatter profile obtained from optical remote sensing. Several methods have been developed, the most prominent of these being: (1) the threshold method, (2) the gradient or derivative method, (3) the idealised gradient method, (4) the wavelet method, and (5) the variance method.

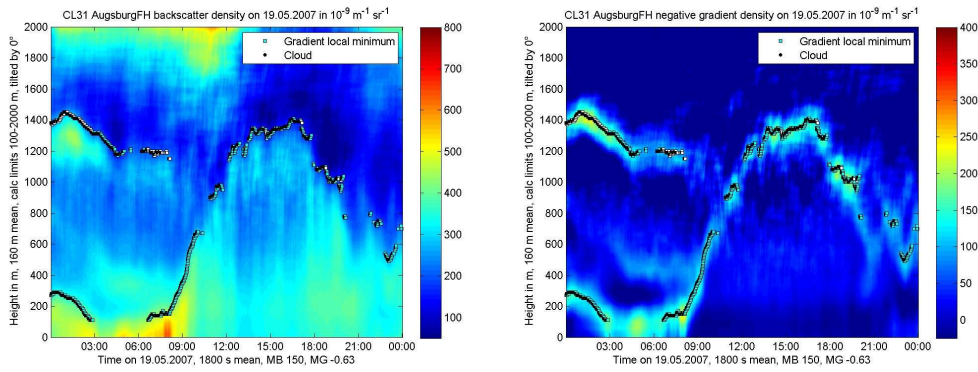


Figure 106: Sample time-height cross-section from optical sounding with a ceilometer. Left: optical backscatter intensity, right: vertical derivative of this backscatter intensity. Dots mark mixing-layer height derived from a gradient algorithm.

The application of optical remote sensing for MLH determination has focussed on the use of ceilometers in recent years. Ceilometers can be regarded as a small lidar. They are simpler and they have a much lower lowest range gate than lidars. For the detection of MLH below 150 to 200 m a ceilometer with one optical axis for the emitted and the received beam should be used. Due to the thin light beams the overlap of the emitted and received beam from a ceilometer with two parallel optical axes can be insufficient in this height range. Further on, Doppler shifts are not analyzed by ceilometers. Therefore, in contrast to acoustic remote sensing with Doppler-sodars, additional variables in addition to the backscatter intensity are not available from ceilometers for the design of determination schemes for MLH. Thus the schemes listed below all resemble to the ARE methods for acoustic remote sensing.

Figure 106 shows a sample measurement with a mono-axial ceilometer. The left-hand frame displays the optical backscatter intensity and the right-hand frame the negative vertical derivative of this intensity as time-height sections over one day (from midnight to midnight) and over a height range of 2000 m. The data was received on a clear day in spring and the vertical structure of the ABL was dominated by surface heating due to incoming solar radiation during daytime and radiative surface cooling during nighttime. In the morning hours until about 0900 LST a shallow stable nocturnal surface layer with a depth of about 200 m and a residual layer with a depth of about 1200 to 1400 m can be distinguished. From 0900 LST onwards the evolution of a daytime convective boundary layer with a maximum depth of about 1400 m can be clearly seen. The dots in both frames of Fig. 106 indicate the mixing-layer height determined with the gradient method described below. The right-hand frame in Fig. 106 demonstrates that the analysed MLH values indeed coincide with maxima of the negative vertical gradient of the optical backscatter intensity.

**Threshold method** Melfi et al. (1985) and Boers et al. (1988) used simple signal threshold values, though this method suffers from the need to define them appropriately (Sicard et al., 2006).  $H_4$  is defined here as the height within the vertical profile of the optical backscatter intensity where the backscatter intensity first exceeds a given threshold when coming downward from the free unpolluted troposphere. The determination of several heights  $H_{4n}$  would require the definition of several thresholds which probably cannot be done a priori to the analysis. Therefore this will always lead to a subjective analysis of MLH. The left-hand frame in Fig. 106 shows that the threshold value cannot be kept constant during the diurnal evolution of the boundary layer in order to get a result which is comparable to the one from the gradient method applied in Fig. 106.

**Gradient or derivative methods** Hayden et al. (1997) and Flamant et al. (1997)

proposed to use the largest negative peak of the first derivative of the optical attenuated backscatter intensity ( $B(z)$ ) for the detection of  $H4$  from LIDAR data (height of gradient minimum  $H4_{GM}$ ):

$$H4_{GM} = \min(\partial B(z)/\partial z). \quad (234)$$

The right-hand frame of Fig. 106 demonstrates that this is a very meaningful assumption. Likewise Wulfmeyer (1999) used the first minimum of the slope to detect the top of a convective boundary layer from DIAL data. Munkel and Räsänen (2004) and Schäfer et al. (2004, 2005) applied the gradient method to ceilometer data. Menut et al. (1999) took the minimum of the second derivative of  $B(z)$  as the indication for MLH:

$$H4_{IPM} = \min(\partial^2 B(z)/\partial z^2). \quad (235)$$

This method is called inflection point method (IPM). It usually gives slightly lower values for  $H4$  than the gradient method in Eq. (234). A further approach was suggested by Senff et al. (1996). They looked for the largest negative gradient in the logarithm of the backscatter intensity (height of logarithmic gradient minimum  $H4_{LGM}$ ):

$$H4_{LGM} = \min(\partial \ln B(z)/\partial z). \quad (236)$$

This approach usually gives the largest value for  $H4$ . According to Sicard et al. (2006)  $H4_{IPM}$  from Eq. (235) is closest to the MLH derived from radiosonde ascents via the Richardson method. The other two algorithms in Eqs. (234) and (236) give slightly higher values.

In Emeis et al. (2007) the gradient method in Eq. (234) has been further refined and extended to enable the calculation of up to  $n = 5$  lifted inversions. This algorithm, which has also been used for the MLH analysis shown in Fig. 106, is described in the following. Prior to the determination of gradient minima the overlap and range corrected attenuated backscatter profiles have to be averaged over time and height to suppress noise generated artefacts. Therefore the  $H4$  values are determined in a two-step procedure. Between 140 and 500 m height sliding averaging is done over 15 min and a height interval  $\Delta h$  of 80 m. In the layer between 500 and 2000 m  $\Delta h$  for vertical averaging is extended to 160 m. Two additional parameters have been introduced to further reduce the number of false hits. The minimum accepted attenuated backscatter intensity  $B_{\min}$  right below a lifted inversion is set to  $200 \times 10^{-9} \text{ m}^{-1} \text{ srad}^{-1}$  in the lower layer and  $250 \times 10^{-9} \text{ m}^{-1} \text{ srad}^{-1}$  in the upper layer. Additionally the vertical gradient value  $\partial B/\partial z_{\max}$  of a lifted inversion must be more negative than  $0.30 \times 10^{-9} \text{ m}^{-2} \text{ srad}^{-1}$  in the lower layer and more negative than  $-0.60 \times 10^{-9} \text{ m}^{-2} \text{ srad}^{-1}$  in the upper layer.

If  $B(z)$  denotes the measured attenuated backscatter intensity in the height  $z$  above ground averaged over time and height and  $\Delta h$  is the height averaging interval, then the gradient  $\partial B/\partial z$  in the height  $z$  is calculated as

$$\partial B/\partial z|_z = (B(z + \Delta h/2) - B(z - \Delta h/2)) / \Delta h. \quad (237)$$

A gradient minimum is characterized by a change of sign from minus to plus of the second derivative of  $B(z)$ . The height interval under examination is searched from bottom to top for these gradient minima  $H4_n$ .

The second derivative of  $B(z)$  in the height  $z$  is

$$\partial^2 B/\partial z^2|_z = (\partial B/\partial z|_{z+\Delta h/2} - \partial B/\partial z|_{z-\Delta h/2}) / \Delta h. \quad (238)$$

There is a gradient minimum  $H4_n$  in the height  $z$  if the second derivative of  $B(z)$  one range gate below  $z$  is not positive, if the second derivative of  $B(z)$  in the height  $z$  is positive, and if the false hit conditions mentioned above are fulfilled:



$$\begin{aligned}
H4_n = z, & \quad \text{if } \partial^2 B / \partial z^2|_{z-1} \leq 0 \text{ and } \partial^2 B / \partial z^2|_z > 0 \text{ and } B(z - \Delta h/2) \geq B_{\min} \\
& \quad \text{and } \partial B / \partial z|_z \leq \partial B / \partial z_{\max} \text{ for } n = 1, \dots, 5.
\end{aligned} \tag{239}$$

The MLH from optical remote sensing is taken as the lowest height  $H4_n$ :

$$\text{MLH}_{\text{op}} = H4_1. \tag{240}$$

**Idealised backscatter method** A parallel development by Eresmaa et al. (2006) using an idealised backscatter profile, originally described by Steyn et al. (1999), is also an extension of the gradient method. MLH is not determined from the observed backscatter profile, but from an idealised backscatter profile fitted to the observed profile. The robustness of this technique is founded on utilising the whole backscatter profile rather than just the portion surrounding the top of the mixing layer. In this method an idealized backscattering profile  $B_i(z)$  is fitted to measured profile by the formula

$$B_i(z) = ((B_m + B_u)/2 - (B_m - B_u)/2) \text{erf}((z - h)/\Delta h) \tag{241}$$

where  $B_m$  is the mean mixing layer backscatter,  $B_u$  is the mean backscatter in air above the mixing layer and  $\Delta h$  is related to the thickness of the entrainment layer capping the ABL in convective conditions. Two new parameters  $A1$  and  $A2$  are defined so that  $A1 = (B_m + B_u)/2$  and  $A2 = (B_m - B_u)/2$ . The value of  $A1$  is kept constant during the fitting procedure. A good estimation of  $A1$  based on an initial order-of-magnitude guess for the MLH is crucial for the quality of the result.

**Wavelet method** A Wavelet method has been developed for the automatic determination of mixing layer height from backscatter profiles of an LD-40 ceilometer by de Haij et al. (2006). Before that wavelet transforms have been applied in recent studies for MLH determination from LIDAR observations (Cohn and Angevine, 2000; Davis et al., 2000; Brooks, 2003; Wulfmeyer and Janjić, 2005). The most important advantage of wavelet methods is the decomposition of the signal in both altitude as well as vertical spatial scale of the structures in the backscatter signal.

The Wavelet algorithm in de Haij et al. (2006) is applied to the 10 minute averaged range and overlap corrected backscatter profile  $B(z)$  within a vertical domain of 90–3000 m. For each averaged profile the top of two significant aerosol layers are detected in order to detect MLH as well as the top of a secondary aerosol layer, like e.g. an advected aerosol layer or the residual layer. This Wavelet MLH method uses the scale averaged power spectrum profile  $W_B(z)$  of the wavelet transform with 24 dilations between 15 and 360 m and step size 15 m. The top of the first layer,  $H4_1$ , is detected at the first range gate at which the scale averaged power spectrum  $W_B(z)$  shows a local maximum, exceeding a threshold value of 0.1. This threshold value is empirically chosen, based on the analysis of several cases with both well pronounced and less clearly pronounced mixing layer tops.  $H4_2$  is optionally determined in the height range between  $H4_1$  and the upper boundary of detection. A valid  $H4_2$  is detected at the level with the strongest local maximum of  $W_B(z)$  provided that this maximum is larger than the  $W_B(z)$  of  $H4_1$ . MLH is set equal to  $H4_1$ .

However, problems with this method arise e.g. in case of multiple (well defined) aerosol layers, which renders the selection of the correct mixing layer top ambiguous. Furthermore, in spring and summer the detection of the MLH for deep (convective) boundary layers often fails. This is mostly due to the high variability of the aerosol backscatter signal with height which limits the range for MLH estimation in those conditions (de Haij et al., 2006).

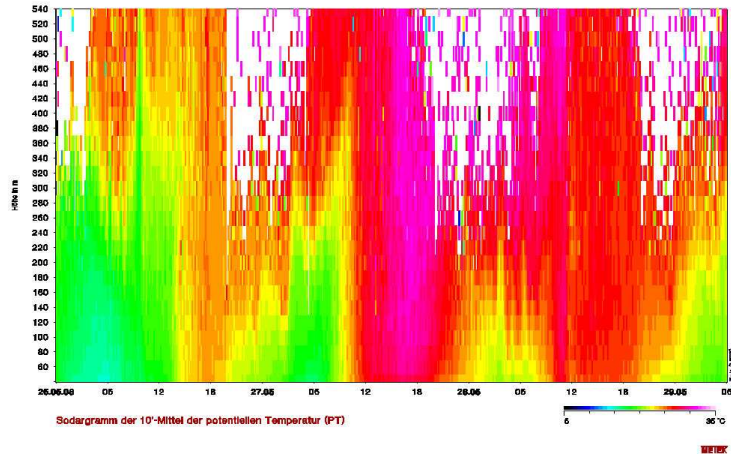


Figure 107: Sample time-height cross-section from a potential temperature sounding with RASS.

**Variance method** At the top of the CBL we have entrainment of clear air masses from the free troposphere into the ABL. The entrainment process is temporarily variable and leads locally to considerable fluctuations in the aerosol concentration. Therefore the maximum in the vertical profile of the variance of the optical backscatter intensity can be an indicator for an entrainment layer on top of a CBL (Hooper and Eloranta, 1986; Piironen and Eloranta, 1995). The method is called variance centroid method in Menut et al. (1999). The variance method for the CBL height is also described in Lammert and Bösenberg (2006). Due to the assumptions made this method is suitable for daytime convective boundary layers only. An elucidating comparison between the gradient method and the variance method can be found in Martucci et al. (2004) although they used a Nd:YAG LIDAR at 532 nm instead of a ceilometer and thus suffered from a high lowest range gate in the order of 300 m.

## RASS

The acoustic and optical methods for MLH determination, which have been described in the sections above, are all indirect methods that try to infer the mixing-layer height from other variables which usually adapt to the vertical structure of the ABL. The only direct and key variable for the analysis of the presence of a mixing layer is the vertical profile of virtual temperature. Temperature profiles can directly be measured with a radio-acoustic sounding system (RASS). Fig. 107 shows an example. We start here with a short description of the available RASS methods.

**Instrumentation** A radio-acoustic sounding system (RASS) operates acoustic and electro-magnetic sounding simultaneously (Marshall et al., 1972). This instrument is able to detect acoustic shock fronts of the acoustic pulses and to determine their propagation speed from the Doppler shift of the backscattered electro-magnetic waves. This propagation speed is equal to the speed of sound which in turn is a known function of air temperature and humidity. To different types of RASS have been realised (Engelbart and Bange, 2002): a Bragg-RASS and a Doppler-RASS.

**Bragg-(windprofiler) RASS** A Bragg-RASS (or windprofiler-RASS) is basically a windprofiler with an additional acoustic emitter. When the Bragg condition is fulfilled (Fig. 108), i.e. the wavelength of the sound waves  $\lambda_a$  is half the one of the electro-

electro-magnetic - acoustic frequency pairs for RASS devices

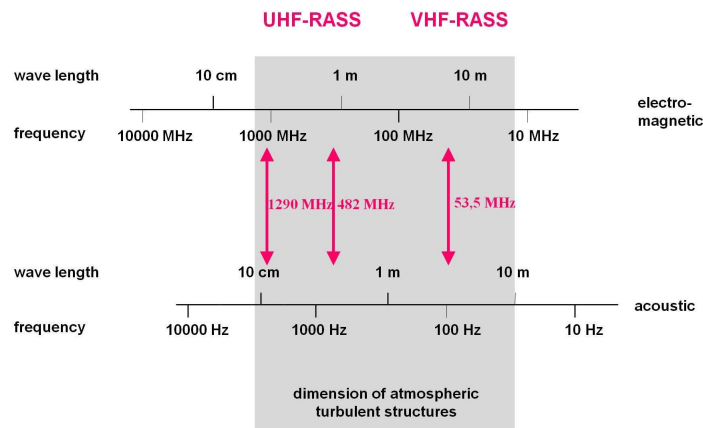


Figure 108: Bragg-related acoustic (below) and electro-magnetic (above) frequencies for RASS.

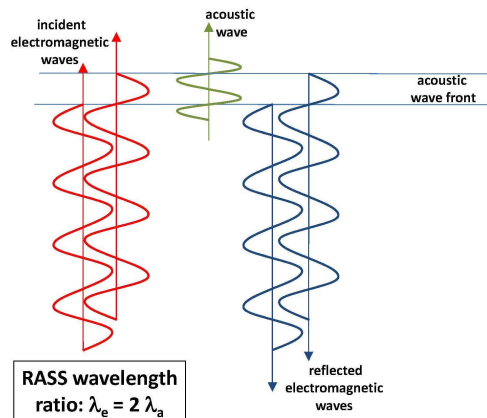


Figure 109: Bragg condition for RASS sounding.

magnetic waves  $\lambda_e$ , then there is optimal backscatter of the electro-magnetic waves from the acoustic waves (Fig. 109). The electro-magnetic signal is emitted at a fixed frequency, but the emitted sound signal is a chirp signal with varying frequency  $f_a$ . From the sound wave length  $\lambda_{a,B}$  at which optimal backscatter occurs the propagation speed of the sound signal can be determined via the following dispersion relation:

$$c_a = \lambda_{a,B} f_a / 2. \tag{242}$$

For a VHF windprofiler operating at 50 MHz a sound frequency of about 100 Hz is used, for a UHF windprofiler operating at 1 GHz a sound frequency around 2 kHz is most suitable to fulfil the Bragg condition. Because the attenuation of sound waves in the atmosphere is strongly frequency dependent, a UHF RASS can detect temperature profiles up to about 1.5 km height whereas a VHF RASS can observe temperature profiles throughout the troposphere.



Figure 110: Sodar-RASS. The acoustic antenna is in the middle, the electro-magnetic antennas to the left and right.

**Doppler-(sodar) RASS** A Doppler-RASS (or sodar-RASS) is a sodar with an additional electro-magnetic emitter and receiver (Fig. 110) operating at a frequency  $f_{e,0}$ . From the Doppler shift  $\Delta f_e$  of the electro-magnetic radiation which is backscattered at the density fluctuations caused by the sound waves the propagation speed  $c_a$  of the sound waves is determined:

$$c_a = -c\Delta f_e / (2f_{e,0}) \quad (243)$$

where  $c$  denotes the speed of light. A Doppler-RASS like a Bragg-RASS also emits a chirp sound signal in order to assure that the Bragg condition is optimally met due to the varying temperature over the entire height range.

The so determined propagation speed  $c_a$  is a sum of the speed of sound  $c_s$  and of the vertical movement of the air  $w$  within which the sound waves propagate:

$$c_a = c_s + w. \quad (244)$$

The vertical air speed component  $w$  can be determined separately from the Doppler shift of the backscattered electro-magnetic clear-air signal when operating a Bragg-RASS or from the Doppler shift of the backscattered acoustic signal when operating a Doppler-RASS. Using the definition of the acoustic temperature the height profile of  $c_s$  can then be converted in a height profile of the acoustic temperature  $T_a$ . For many purposes this acoustic temperature is a sufficiently accurate approximation of the virtual air temperature. The maximum range of a sodar-RASS is usually less than thousand metres so that such an instrument covers the lower part of the boundary layer. Due to the high vertical resolution and the low minimum range of about 30 to 40 m, which is comparable to the abilities of a sodar, a sodar-RASS is well suited for the detection of shallow nocturnal boundary layers.

**Algorithms** MLH can be determined from the lowest height where the vertical profile of potential temperature increases with height indicating stable thermal stratification of the air. The great advantage of RASS measurements is that the magnitude of stability (inversion strength) can be assessed quantitatively which is not possible from the acoustic and optical sounding devices described before. Fig. 107 displays a time-height cross-section of potential temperature over three days starting at midnight for a height range

of 540 m. On the afternoons of the second and the third day well-mixed boundary layers formed, which can be deduced from the vertically constant potential temperature. New surface layers form on the evenings of all three days at about 1800 LST. The depth of these new surface layers increase during the night to about 200 to 300 m. Above these nocturnal surface layers low-level jets (see below) form, indirectly visible from the white areas indicating missing data in Fig. 107. Stronger winds like those in low-level jets blow the sound pulses from the RASS out of the focus of the electro-magnetic antenna and hence lead to a failure of the temperature detection.

Ideally, thermal stratification of air should be analyzed from the virtual potential temperature ( $\Theta_v = \Theta(1 + 0.609q)$ , where  $q$  is specific humidity) in order to include the effects of the vertical moisture distribution on the atmospheric stability. Unfortunately, no active remote sensing device for the determination of high-resolution moisture profiles is available. Therefore, the acoustic potential temperature ( $\Theta_a = \Theta(1 + 0.513q)$ ), which actually is the temperature that is delivered by a RASS, is often used as a substitute. This is sufficient for cold and dry environments, but somewhat underestimates the virtual potential temperature in humid and warm environments. In case of larger vertical moisture gradients and small vertical temperature gradients this can lead to a switch in stability from stable to unstable or vice versa.

Engelbart and Bange (2002) have analyzed the possible advantages of the deployment of two RASS instruments, a sodar-RASS and a high-UHF windprofiler-RASS, to derive boundary-layer parameters. With these instruments, in principle, MLH can either be determined from the temperature profiles or from the electro-magnetic backscatter intensity. The latter depends on temperature and moisture fluctuations in the atmosphere. The derivation of MLH from the temperature profile requires a good vertical resolution of the profile which is mainly available only from the sodar-RASS. But even if the inversion layer at the top of the boundary layer is thick enough, due to the high attenuation of sound waves in the atmosphere, also the 1290 MHz-windprofiler-RASS used by Engelbart and Bange (2002) can measure the temperature profile only up to about 1 km. Therefore, in the case of a deeper CBL, MLH was determined from a secondary maximum of the electro-magnetic backscatter intensity which marks the occurrence of the entrainment zone at the CBL top. Thus, with this instrument combination the whole diurnal cycle of MHL is ideally monitored by interpreting the temperature profile from the sodar-RASS at night-time and by analyzing the electro-magnetic backscatter intensity profile from the windprofiler-RASS during daytime.

Hennemuth and Kirtzel (2008) have recently developed a method that uses data from a sodar-RASS and surface heat flux data. MLH is primarily detected from the acoustic backscatter intensity received by the sodar part of the sodar-RASS and verified from the temperature profile obtained from the RASS part of the instrument. Surface heat flux data and statistical evaluations complement this rather complicated scheme. The surface heat flux is used to identify situations with unstable stratification. In this respect this observable takes over an analogous role as the  $\sigma_w$  in the EARE algorithm (see above). The results have been tested against radiosonde soundings. The coincidence was good in most cases except for a very low MLH at or even below the first range gate of the sodar and the RASS.

### Further techniques

Beyrich and Görsdorf (1995) have reported on the simultaneous usage of a sodar and a wind profiler for the determination of MLH. For the sodar data the ARE method was used. From the wind profiler data MLH was likewise determined from the height of the elevated signal intensity maximum (Angevine et al., 1994; Grimsdell and Angevine, 1998; White et al., 1999). Good agreement between both algorithms was found for evolving CBLs. The vertical ranges of the two instruments (50 to 800 m for the sodar and 200 to 3000 m for the wind profiler) allowed following the complete diurnal cycle of MLH.

## Comparison of acoustic and optical MLH detection algorithms

There is an interesting difference between the schemes for the determination of MLH from acoustic and optical backscatter intensities which should be noted carefully. While the acoustic backscatter intensity itself is taken for the detection of  $H1$  and  $H3$  (see Eqs. (230) and (232)) and the first derivative of this backscatter intensity for the determination of  $H2$  (see Eq. (231)), the first and the second derivative of the optical backscatter intensity (but not the optical backscatter intensity itself) is used to determine  $H4$  (see Eq. (234)). This discrepancy in the processing of the two backscatter intensities is due to the different scattering processes for acoustic and optical waves: Acoustic waves are scattered at atmospheric refractivity gradients and thus at temperature gradients (Neff and Coulter, 1986) while optical waves are scattered at small particles. Therefore the optical backscatter intensity is proportional to the aerosol concentration itself. The MLH on the other hand, which we desire to derive from these backscatter intensities, is in both cases found in heights where we have vertical gradients of the temperature and of the aerosol concentration. Therefore, in principle, the vertical distribution of the acoustic backscatter intensity should look very much alike the vertical distribution of the vertical gradient of the optical backscatter intensity.

Simultaneous measurements with different remote sensing devices have mainly been made in order to evaluate one remote sensing method against the other (Devara et al., 1995). But one could also think of combining the results two or more remote sensing devices for determining the structure of the ABL. The analysis of the sodar data and the ceilometer data can be combined to one single piece of MLH information by forming the minimum from Eqs. (233) and (240):

$$\text{MLH} = \min(\text{MLH}_{\text{ac}}, \text{MLH}_{\text{op}}). \quad (245)$$

## 12.3 Boundary-layer height

Often, the boundary layer consists of more layers than just the mixing layer. For example, at night, a residual layer may persist over a newly formed near-surface stable surface layer. The deployment of sophisticated lidars (Bösenberg and Linné, 2002) may be a choice to detect such features as well as the combined deployment of a sodar and a ceilometer. Such a combination of parallel measurements of the vertical structure of the atmospheric boundary layer by a ceilometer and a sodar is described in Emeis and Schäfer (2006). Fig. 111, which is taken from this study, shows a daytime convective boundary layer, shallow nocturnal surface layers in the morning and the evening, and a residual layer above the nocturnal surface layers. The ceilometer detects the overall boundary layer height (blue triangles) whose height is partly modified by large-scale sinking motion in the anticyclone dominating the weather during the measurement period. Stable nocturnal surface layers with a depth of a few hundred metres can be detected underneath the black squares derived from the sodar soundings. The convective boundary layer during daytime fills the full depth of the boundary layer. This combination offers the same advantages as the combination of sodar and windprofiler presented in Beyrich and Görsdorf (1995). First results from a combined deployment of a RASS and a ceilometer are given in Emeis et al. (2009).

In such combined remote sensing measurements a sodar better detects the near-surface features such as nocturnal stable layers (a RASS instead of a sodar directly delivers the near-surface temperature profile) while the ceilometer is able to follow the diurnal variation of the daytime convective boundary layer and the top of the whole boundary layer. The residual layer then becomes visible as the layer between the new nocturnal surface layer below and the top of the boundary layer above.

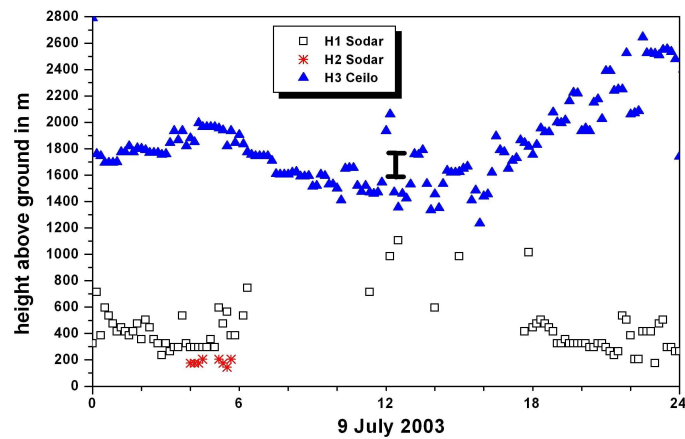


Figure 111: Combined sounding with a sodar (black squares and red asterisks) and a ceilometer (blue triangles) giving a complete view of the diurnal variation of the vertical structure of the ABL.

## 12.4 Summary

Wind resources depend on the large-scale weather conditions as well as on the local vertical structure of the atmospheric boundary layer. Ground-based remote sensing is now a viable technique to monitor the vertical structure of the atmospheric boundary layer. Three different techniques are presently available: acoustic sounding (sodars), optical sounding (lidars and ceilometers) and the combination of acoustic and electro-magnetic sounding (RASS). Direct detection of MLH from acoustic backscatter intensities is limited to the order of about 1 km due to the rather high attenuation of sound waves in the atmosphere. In contrast, optical remote sensing offers much larger height ranges of at least several kilometres, because the attenuation of light waves in the atmosphere is small unless there is fog, clouds or heavy precipitation. This now offers the possibility to introduce information on boundary layer structure such as mixing-layer height into the monitoring and description of wind resources.

## Notation

$a$	factor of proportionality
$A1$	$(B_M + B_U) / 2$
$A2$	$(B_M - B_U) / 2$
ABL	atmospheric boundary layer
ARE	acoustic received echo (method)
$B_{\min}$	threshold value for $B(z)$
$B_M$	mixing-layer mean of $B(z)$
$B_U$	value of $B(z)$ above the mixing layer
$B(z)$	optical backscatter intensity
$B_i(z)$	idealized optical backscatter intensity
$\partial B / \partial z_{\max}$	threshold value for the vertical derivate of $B(z)$
$c$	speed of light
$c_a$	RASS speed of sound ( $= c_s + w$ )
$c_s$	true speed of sound
CBL	convective boundary layer
$DR_1$	threshold value for the vertical gradient of $R(z)$

$DR_2$	threshold value for the vertical gradient of $R(z)$
EARE	enhanced acoustic received echo (method)
$f_a$	acoustic frequency
$f_e$	electro-magnetic frequency
$Hn$	analysed height ( $n$ is a one-digit number)
$H4_{GM}$	height of minimum of vertical gradient of $B(z)$
$H4_{IPM}$	height of minimum of second vertical derivate of $B(z)$
$H4_{LGM}$	height of minimum of logarithmic vertical gradient of $B(z)$
HWS	horizontal wind speed (method)
MLH	mixing-layer height
MLH <sub>ac</sub>	mixing-layer height from acoustic sounding
MLH <sub>op</sub>	mixing-layer height from optical sounding
$q$	specific humidity
$R_c$	threshold value for $R(z)$
$R(z)$	acoustic backscatter intensity
RASS	radio-acoustic sounding system
$T_a$	acoustic temperature
VWV	vertical wind variance (method)
$w$	vertical wind component
$W_B(z)$	scale averaged power spectrum profile
$z$	height above ground
$z_i$	boundary-layer height
$\Delta f_e$	Doppler shift of electro-magnetic frequency
$\Delta h$	height interval
$\Theta$	potential temperature
$\Theta_a$	acoustic potential temperature
$\Theta_v$	virtual potential temperature
$\lambda_a$	wavelength of sound wave
$\lambda_{a,B}$	wavelength of sound wave fulfilling the Bragg condition
$\lambda_e$	wavelength of electro-magnetic wave
$\sigma_w$	standard deviation of the vertical wind component

## References

- Angevine W., White A. B., and Avery S. K. (1994) Boundary layer depth and entrainment zone characterization with a boundary layer profiler. *Bound.-Layer Meteorol.* **68**: 375–385
- Asimakopoulou D. N., Helmig G., and Michopoulos J (2004) Evaluation of SODAR methods for the determination of the atmospheric boundary layer mixing height. *Meteorol. Atmos. Phys.* **85**: 85–92
- Beyrich F. (1995) Mixing height estimation in the convective boundary layer using sodar data. *Bound.-Layer Meteorol.* **74**: 1–18
- Beyrich F. (1997) Mixing height estimation from sodar data - a critical discussion. *Atmosph. Environ.* **31**: 3941–3954
- Beyrich F. and Görsdorf U. (1995) Composing the diurnal cycle of mixing height from simultaneous SODAR and Wind profiler measurements. *Bound.-Layer Meteorol.* **76**: 387–394
- Boers R., Spinhirne J. D., and Hart W. D. (1988) Lidar Observations of the Fine-Scale Variability of Marine Stratocumulus Clouds. *J. Appl. Meteorol.* **27**: 797–810
- Bösenberg J. and Linné H. (2002) Laser remote sensing of the planetary boundary layer. *Meteorol. Z.* **11**: 233–240
- Brooks I. M. (2003) Finding boundary layer top: application of a wavelet covariance transform to lidar backscatter profiles. *J. Atmos. Oceanic Technol.* **20**: 1092–1105
- Cohn S. A. and Angevine W. M. (2000) Boundary Layer Height and Entrainment Zone Thickness Measured by Lidars and Wind-Profiling Radars. *J. Appl. Meteorol.* **39**: 1233–1247
- Davis K. J., Gamage N., Hagelberg C. R., Kiemle C., Lenschow D. H., and Sullivan P. P. (2000) An objective method for deriving atmospheric structure from airborne lidar observations. *J. Atmos. Oceanic Technol.* **17**: 1455–1468
- de Haij M., Wauben W., and Klein Baltink H. (2006) Determination of mixing layer height from ceilometer backscatter profiles. In: Slusser J. R., Schäfer K., Comerón A. (eds) Remote Sensing of Clouds and the Atmosphere XI. *Proc. SPIE* Vol 6362: paper 63620R.



- Devara P. C. S., Ernest Ray P., Murthy B. S., Pandithurai G., Sharma S., and Vernekar K. G. (1995) Intercomparison of Nocturnal Lower-Atmospheric Structure Observed with LIDAR and SODAR Techniques at Pune, India. *J. Appl. Meteorol.* **34**: 1375–1383
- Emeis S. (2010a) Measurement methods in atmospheric sciences. In situ and remote. Vol. 1 of Quantifying the Environment. Borntraeger, Stuttgart, in print.
- Emeis S. (2010b) Surface-Based Remote Sensing of the Atmospheric Boundary Layer. Springer, Heidelberg etc., submitted.
- Emeis S. and Schäfer K. (2006) Remote sensing methods to investigate boundary-layer structures relevant to air pollution in cities. *Bound.-Layer Meteorol.* **121**: 377–385
- Emeis S. and Türk M. (2004) Frequency distributions of the mixing height over an urban area from SODAR data. *Meteorol. Z.* **13**: 361–367
- Emeis S., Jahn C., Münkler C., Münsterer C., and Schäfer K (2007) Multiple atmospheric layering and mixing-layer height in the Inn valley observed by remote sensing. *Meteorol. Z.* **16**: 415–424
- Emeis S., Schäfer K., and Münkler C (2008) Surface-based remote sensing of the mixing-layer height - a review. *Meteorol. Z.* **17**: 621–630
- Emeis S., Schäfer K., and Münkler C (2009) Observation of the structure of the urban boundary layer with different ceilometers and validation by RASS data. *Meteorol. Z.* **18**: 149–154
- Engelbart D. A. M. and Bange J. (2002) Determination of boundary-layer parameters using wind profiler/RASS and sodar/RASS in the frame of the LITFASS project. *Theor. Appl. Climatol.* **73**: 53–65
- Eresmaa N., Karppinen A., Joffre S. M., Räsänen J., and Talvitie H. (2006) Mixing height determination by ceilometer. *Atmos. Chem. Phys.* **6**: 1485–1493
- Flamant C., Pelon J., Flamant P. H., and Durand P. (1997) Lidar determination of the entrainment zone thickness at the top of the unstable marine atmospheric boundary-layer. *Bound.-Layer Meteorol.* **83**: 247–284
- Grimsdell A. W. and Angevine W. M. (1998) Convective Boundary Layer Height Measurement with Wind Profilers and Comparison to Cloud Base. *J. Atmos. Oceanic Technol.* **15**: 1331–1338
- Hayden K. L., Anlauf K. G., Hoff R. M., Strapp J. W., Bottenheim J. W., Wiebe H. A., Froude F. A., Martin J. B., Steyn D. G., and McKendry I. G. (1997) The Vertical Chemical and Meteorological Structure of the Boundary Layer in the Lower Fraser Valley during Pacific '93. *J. Atmos. Environ.* **31**: 2089–2105
- Hennemuth B. and Kirtzel H.-J. (2008) Towards operational determination of boundary layer height using sodar/RASS soundings and surface heat flux data. *Meteorol. Z.* **17**: 283–296
- Hooper W. P. and Eloranta E. (1986) Lidar measurements of wind in the planetary boundary layer: the method, accuracy and results from joint measurements with radiosonde and kytoon. *J. Clim. Appl. Meteorol.* **25**: 990–1001
- Lammert A. and Bösenberg J. (2006) Determination of the Convective Boundary-Layer Height with Laser Remote Sensing. *Bound.-Layer Meteorol.* **119**: 159–170
- Marshall J. M., Peterson A. M., and Barnes A. A. (1972) Combined radar-acoustic sounding system. *Appl. Opt.* **11**: 108–112
- Martucci G., Srivastava M. K., Mitev V., Matthey R., Frioud M., and Richner H. (2004) Comparison of lidar methods to determine the Aerosol Mixed Layer top. In: Schäfer K., Comeron A., Carleer M., Picard R. H. (eds.): Remote Sensing of Clouds and the Atmosphere VIII. *Proc of SPIE* 5235: 447–456
- Melfi S. H., Spinhirne J. D., Chou S. H., and Palm S. P. (1985) Lidar Observation of the Vertically Organized Convection in the Planetary Boundary Layer Over the Ocean. *J. Clim. Appl. Meteorol.* **24**: 806–821
- Menut L., Flamant C., Pelon J., and Flamant P. H. (1999) Urban Boundary-Layer Height Determination from Lidar Measurements Over the Paris Area. *Appl. Opt.* **38**: 945–954
- Münkler C. and Räsänen J. (2004) New optical concept for commercial lidar ceilometers scanning the boundary layer. *Proc. SPIE* Vol 5571: 364–374
- Neff W. D. and Coulter R. L. (1986) Acoustic remote sensing. In: Lenschow D. H. (ed) Probing the Atmospheric Boundary Layer. Amer. Meteorol. Soc., Boston, MA, 201–239

- Piironen A. K. and Eloranta E. W. (1995) Convective boundary layer depths and cloud geometrical properties obtained from volume imaging lidar data. *J. Geophys. Res.* **100**: 25569–25576
- Schäfer K., Emeis S. M., Rauch A., Münkler C., and Vogt S. (2004) Determination of mixing-layer heights from ceilometer data. In: Schäfer K., Comeron A. T., Carleer M. R., Picard R. H., and Sifakis N. (eds.): Remote Sensing of Clouds and the Atmosphere IX. *Proc. SPIE* Vol 5571: 248–259
- Schäfer K., Emeis S., Junkermann W., and Münkler C. (2005) Evaluation of mixing layer height monitoring by ceilometer with SODAR and microlight aircraft measurements. In: Schäfer K., Comeron A. T., Slusser J. R., Picard R. H., Carleer M. R., and Sifakis N. (eds) Remote Sensing of Clouds and the Atmosphere X. *Proc. SPIE* Vol 5979: 59791I-1–59791I-11
- Seibert P., Beyrich F., Gryning S.-E., Joffre S., Rasmussen A., and Tercier P. (2000) Review and inter-comparison of operational methods for the determination of the mixing height. *Atmosph. Environ.* **34**: 1001-1-027
- Senff C., Bösenberg J., Peters G., and Schaberl T. (1996) Remote Sensing of Turbulent Ozone Fluxes and the Ozone Budget in the Convective Boundary Layer with DIAL and Radar-RASS: A Case Study. *Contrib. Atmos. Phys.* **69**: 161–176
- Sicard M., Pérez C., Rocadenbosch F., Baldasano J. M., and García-Vizcaino D. (2006) Mixed-Layer Depth Determination in the Barcelona Coastal Area From Regular Lidar Measurements: Methods, Results and Limitations. *Bound.-Layer Meteorol.* **119**: 135–157
- Steyn D. G., Baldi M., and Hoff R. M. (1999) The detection of mixed layer depth and entrainment zone thickness from lidar backscatter profiles. *J. Atmos. Ocean Technol.* **16**: 953–959
- White A. B., Senff C. J., and Banta R. M. (1999) A Comparison of Mixing Depths Observed by Ground-Based Wind Profilers and an Airborne Lidar. *J. Atmos. Oceanic Technol.* **16**: 584–590
- Wulfmeyer V. (1999) Investigation of turbulent processes in the lower troposphere with water-vapor DIAL and Radar-RASS. *J. Atmos. Sci.* **56**: 1055–1076
- Wulfmeyer V. and Janjić T. (2005) 24-h observations of the marine boundary layer using ship-borne NOAA High-Resolution Doppler Lidar. *J. Appl. Meteorol.* **44**: 1723–1744

# 13 SAR for wind energy

Merete Badger<sup>1</sup>, Charlotte B. Hasager<sup>1</sup>, Donald Thompson<sup>2</sup>, and Frank Monaldo<sup>2</sup>

<sup>1</sup>*Wind Energy Division, Risø DTU, Roskilde, Denmark*

<sup>2</sup>*The Johns Hopkins University, Applied Physics Laboratory, USA*

This manuscript is an updated version of Chapter 2 in the book “Ocean Remote Sensing: Recent Techniques and Applications” Edited by R. Niclòs, Research Signpost, Karala, India, 2008.

---

## 13.1 Introduction

Modern, purpose-built wind sensors such as scatterometers and radiometers typically provide global wind products resampled to  $0.25^\circ$  latitude and longitude ( $\sim 25$  km at mid-latitudes). A coastal mask is applied to avoid mixed land-ocean pixels and coastal areas are therefore neglected. Scatterometer and radiometer products offer daily global coverage and are very useful for large-scale wind monitoring and weather forecasting. To resolve mesoscale wind variability associated with e.g. weather fronts, hurricanes, gap flows, or barrier jets more detailed spatial information is needed. Synthetic Aperture Radar (SAR) measurements are high-resolution observations of the Earth surface. Although no SAR sensor has been designed specifically for wind mapping, it has become clear that the data are very suitable for high-resolution wind retrievals over the ocean including near-shore areas. In contrast to optical sensors, radar sensors are independent of sunlight such that measurements may be obtained both day and night. A further advantage is the ability of microwaves to penetrate clouds and light rain. In the following, we review techniques for mapping of ocean wind fields from SAR in a historical context. We then focus on different applications in meteorology and wind energy where high-resolution ocean wind fields are useful. Recent advances and issues that remain to be solved are addressed for each of these applications. Finally, we discuss the potential of two newly launched SAR sensors and the future perspectives of SAR sensing of ocean winds.

## 13.2 Background

A SAR is an active microwave sensor capable of imaging the amount of backscattered signal per unit area - the normalised radar cross section (NRCS). NRCS depends on the size and geometry of roughness elements on the scale of the radar wavelength at the Earth surface. Over a calm ocean surface, the returned NRCS is limited because radar pulses are reflected away from the SAR at an angle equal to the angle of incidence. As the wind picks up, roughness in the form of capillary and short-gravity waves is generated by the surface wind stress. The dominant scattering mechanism is then diffuse and known as Bragg scattering (Valenzuela, 1978). The relation of NRCS to the local wind speed and direction and to the radar viewing geometry forms the key principle in ocean wind retrievals from SAR. High-frequency radars (X- or Ku-band) are generally the most sensitive to small-scale waves generated by the instantaneous local wind. Lower-frequency SAR sensors (L-band) are more sensitive to longer-period surface waves that, because of their longer growth time, are not so sensitive to local wind fluctuations. For further discussion how the sea surface roughness affects NRCS, see e.g. Thompson (2004).

Remote sensing measurements of the ocean were first collected from space by the SEASAT satellite in 1978 from a variety of onboard sensors including a radar altimeter (Brown et al., 1981), scatterometer (Wentz et al., 1984), and passive microwave radiometer systems (Wentz et al., 1986). A SAR, also on board SEASAT, not only demonstrated

the ability to measure the ocean surface wind field, but also revealed the presence of surface and internal waves, current and temperature boundaries, and shoaling bathymetry (Holt, 2004). A consistent NRCS-to-wind relationship could not be established from the SEASAT SAR data due to calibration issues and the fact that it looked at only a single incident angle. However, an important observation was that wind-aligned rows created periodic variations of the surface roughness and thus the image brightness. Gerling (1986) applied Fast Fourier Transformation (FFT) to extract the orientation of linear features in SEASAT SAR imagery. Comparisons with the SEASAT scatterometer demonstrated that these features are aligned with the wind direction with a  $180^\circ$  ambiguity.

In 1991, the European Space Agency (ESA) launched ERS-1 – a C-band ( $\sim 5$  cm) SAR operating at vertical polarization in transmit and receive ( $C_{VV}$ ). This mission was followed up by the nearly identical ERS-2 mission in 1995. ERS-1/2 SAR images covered a 100-km swath with a spatial resolution of 25 m. Due to the shorter wavelength of these sensors, compared to an L-band SAR, the sensitivity of NRCS to wind stress increased and wind signatures became more visible in the SAR imagery, especially at wind speeds less than  $5 \text{ m s}^{-1}$ . A renewed scientific interest emerged for the mapping of ocean wind fields from SAR.

The active microwave sensors aboard ERS-1/2 could also be operated as scatterometers with three antennae. Viewing of a given point at the surface from several different incidence and/or aspect angles allowed for unambiguous estimates of the wind speed and direction from a set of NRCS values at different aspect angles. Geophysical model functions (GMFs) were empirically developed to establish the wind-vector-to-backscatter relationship for the C-band scatterometer data. Scatterometer model functions have later proven to be suitable for SAR wind retrievals as well. SAR sensors operate with a single antenna and view each ground target from one angle only. As a consequence, several wind speed and direction pairs correspond to a given NRCS. The number of possible solutions may be reduced if a priori information about the wind direction is used to retrieve the wind speed.

A new era of SAR sensing began with the launch of Canadian RADARSAT-1 in 1995. RADARSAT-1 has ScanSAR capability and is by default operated with a swath width of 500 km and a spatial resolution of 75 m. The wider swath is very suitable for studying mesoscale meteorological phenomena at a resolution that is still far better than that of scatterometers and radiometers. RADARSAT-1 is designed mainly for ice monitoring and has a C-band SAR operating with horizontal polarization ( $C_{HH}$ ). A major challenge related to ocean wind retrievals has been the modification of existing GMFs (developed for vertical polarization measurements of ERS-1/2) to fit the  $C_{HH}$  measurements from RADARSAT-1. Rather than the construction of completely new C-band GMF for use with RADARSAT-1, some researchers have assumed that the C-band HH-pol cross section,  $C_{HH}$ , is simply equal to  $C_{VV}$  times a function that describes the ratio  $C_{HH}/C_{VV}$ ; the so-called polarization ratio. In general, this polarization ratio function should depend on the radar viewing geometry and the local wind vector. However, polarization ratio expressions proposed by Elfouhaily (1996), Thompson et al. (1998), and Vachon and Dobson (2000) over the past decade or so depend only on the radar incident angle and usually contain an adjustable parameter that can be tuned to fit the existing data. Recently, Mouche et al. (2005) proposed a more complete model for the C-band polarization ratio based on simultaneous measurements of  $C_{HH}$  and  $C_{VV}$  from an airborne radar.

Another ScanSAR sensor is ENVISAT launched by ESA in 2002. ENVISAT carries an advanced C-band SAR (ASAR) which may be operated in several different modes with co- or cross-polarization. The majority of ENVISAT's modes are suitable for ocean wind mapping. In ScanSAR mode, the ASAR sensor is capable of scanning in a 400 km wide swath with a spatial resolution of 100 m. A higher resolution over smaller areas may be achieved in the Stripmap mode. In recent years, the capacity of the SAR processing facilities has increased so that RADARSAT-1 and ENVISAT data are made available

for users in near-real-time; images can typically be downloaded via internet archives 1–3 hours after the data acquisition. This opportunity has opened up for operational SAR-based wind mapping.

A new C-band SAR sensor, RADARSAT-2 was launched in December 2007. This sensor is the first spaceborne C-band SAR to have fully polarimetric capabilities such that  $C_{VV}$ ,  $C_{HH}$ ,  $C_{VH}$ , and  $C_{HV}$  data can be acquired simultaneously. Polarimetric data have previously been collected from various airborne SAR missions and also from the three spaceborne systems ALOS PALSAR, TerraSAR-X, and COSMO SkyMed operating in L-band and X-band. ALOS was launched in 2006 by the Japanese Space Agency (JAXA) and TerraSAR-X was launched in 2007 by the German Aerospace Center (DLR). COSMO SkyMed is a constellation of four satellites launched in 2007, 2008, and 2010 by the Italian Space Agency (ASI). Altogether, the recent opportunity of using multipolarization and multifrequency SAR sensing is expected to provide new insight in oceanic and atmospheric processes including perhaps improving the retrieval of ocean wind fields.

### 13.3 Ocean wind retrievals from SAR

The most widely used GMFs for C-band SAR wind retrievals at low to moderate wind speeds are CMOD4 (Stoffelen and Anderson, 1997) and CMOD-IFR2 (Quilfen et al., 1998). These model functions are valid for wind speeds of 2–24 m s<sup>-1</sup> and have a nominal accuracy of  $\pm 2$  m s<sup>-1</sup>. A new model function, CMOD5, has been developed to improve the accuracy of wind retrievals at hurricane wind speeds (Hersbach, 2003). Generally, the empirical GMFs take the following form:

$$\sigma^0 = U^{\gamma(\theta)} A(\theta) [1 + B(\theta, U) + C(\theta, U) \cos 2\phi] \quad (246)$$

where  $\sigma^0$  is the NRCS,  $U$  is wind speed at the height 10 m for a neutrally-stratified atmosphere,  $\theta$  is the local incident angle, and  $\phi$  is the wind direction with respect to the radar look direction. The coefficients  $A$ ,  $B$ ,  $C$ , and  $\gamma$  are functions of wind speed and the local incident angle. Empirical model functions rely on the assumption that wind speed increases logarithmically with height above the sea surface. This is normally true if the atmospheric boundary layer is neutrally stratified. Stable stratification would typically lead to an underestimation and unstable stratification to an overestimation of the 10-m wind speed. Deviations from the logarithmic wind profile are mostly found in near-shore areas where the atmospheric boundary layer may be influenced by the land. GMFs can thus be expected to perform better over the open ocean than in near-shore areas. Several parameters other than the surface wind vector or wind stress can affect the sea surface roughness and thus the NRCS. For example, mineral oil (Gade and Alpers, 1999; Espedal and Johannessen, 2000) or biogenic slicks (Espedal et al., 1996, 1998; Gade et al., 1998a,b) have a damping effect on Bragg waves. Other oceanographic processes including fronts and eddies (Lyzenga, 1991; Johannessen et al., 1996; Kudryavtsev et al., 2005; Johannessen et al., 2005), internal waves (Thompson et al., 1988; Hogan et al., 1996), long-period surface waves (Alpers et al., 1981; Hasselmann et al., 1985; Vachon et al., 2004), and bathymetry (Alpers and Hennings, 1984; Romeiser and Alpers, 1997) can also alter the NRCS. For each of these processes, it is the modulation of the surface wave spectrum due to the surface current field induced by the particular process that is responsible for the modulation of the NRCS. A convenient “rule of thumb” to estimate the sign of the NRCS modulation is that a positive gradient of this induced surface current (i.e. a current convergence) will increase the NRCS whereas a negative gradient (current divergence) will decrease the NRCS. The detailed character of the modulation, of course, is more complicated and depends on the radar frequency and local wind velocity among other things (see e.g. Thompson et al. (1988) and references contained therein).

The Johns Hopkins University Applied Physics Laboratory (JHU/APL) has developed the APL/NOAA SAR Wind Retrieval System (ANSWRS) that is currently being used for near real-time wind field retrievals at NOAA, JHU/APL, the Alaska SAR

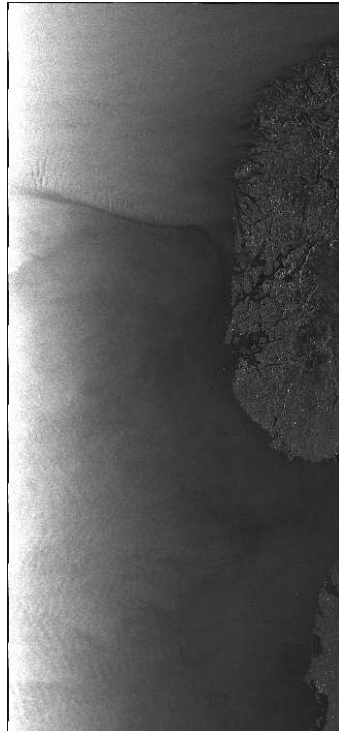


*Figure 112:* ENVISAT ASAR scene acquired over the North Sea on 30 October 2006

Facility (ASF), and Risø National Laboratory for Sustainable energy at the Technical University of Denmark (Risø DTU). To meet the requirements of processing in near real-time, the ANSWRS software produces high-resolution ( $< 1$  km) wind speed fields initialized using wind directions determined by the Navy Operational Global Atmospheric Prediction System (NOGAPS) models. At present, we have an extensive database of SAR wind maps derived mainly from the SAR systems on the Canadian RADARSAT-1 and the European ENVISAT satellites. The wind maps in our database date back to the launch dates of RADARSAT-1 and ENVISAT and can be viewed at the web site: [http://fermi.jhuapl.edu/sar/stormwatch/web\\_wind/](http://fermi.jhuapl.edu/sar/stormwatch/web_wind/). The maps in the database cover most areas of the globe, but are concentrated mainly in the Gulf of Alaska and coastal regions of continental US and Europe. Comparisons between the estimated wind speeds from these maps (mainly in the Gulf of Alaska and the US East coast) yield agreement with buoy measurements to within  $1.76 \text{ m s}^{-1}$  standard deviation (Monaldo et al., 2001) and with QuikSCAT wind speeds to within  $1.25 \text{ m s}^{-1}$  standard deviation (Monaldo et al., 2004).

Figure 112 shows an ENVISAT ASAR scene acquired over the North Sea on 30 October 2006. The scene is aligned according to the satellite orbit and shows a higher NRCS in near-range (left) compared to far-range (right). Several atmospheric features can be observed from the NRCS image. Dark streaks off the Norwegian coast indicate low-wind areas caused by shadowing from the land and a weather front is seen as an almost linear feature. Wave patterns are observed adjacent to this front and also towards the lower left image corner. The waves are most likely associated with atmospheric processes impacting the sea surface roughness. Their wavelength is several orders of magnitude larger than the Bragg wavelength. Figure 113 shows a wind field generated from the same ASAR image and mapped to geographical coordinates. The wind retrieval was initiated using wind directions from the NOGAPS model interpolated in time and space to match the satellite data. NOGAPS data are available at 6-hour intervals mapped to a  $1^\circ$  latitude/longitude grid. In this case, the model data capture very well the complex wind pattern associated with a weather front. To the north of the front, strong winds are

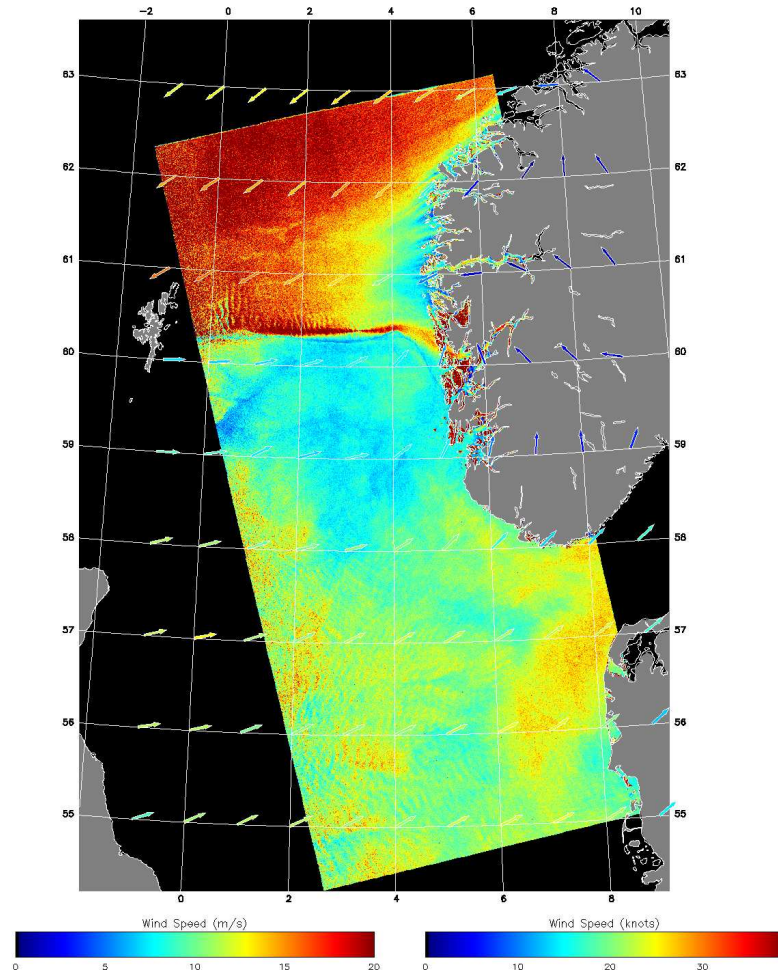


*Figure 113:* Wind field generated from the ENVISAT ASAR image in Figure 112 using the ANSWRS software from JHU/APL. Arrows indicate wind vectors from the NOGAPS model interpolated in time and space to match the satellite data. A weather front is captured by the satellite as well as the model data. There is a good overall agreement on wind speeds for this complex situation

coming from the northeast. To the south of the front, winds are from the southwest and weaker. On the lee side of Norway, wind speeds are reduced significantly. Wind speeds around  $5 \text{ m s}^{-1}$  are found near the coastline. The wind speed increases to more than  $15 \text{ m s}^{-1}$  over a distance of 100 km offshore. There is an excellent overall agreement between the satellite and model wind speeds.

It is also possible to estimate the wind direction directly from km-scale streaks in the SAR imagery, aligned approximately with the wind direction. The streaks originate from atmospheric roll vortices and other phenomena impacting the sea surface. Different image analysis techniques such as FFT (Gerling, 1986; Vachon and Dobson, 1996; Lehner et al., 1998; Furevik et al., 2002) and wavelet transformation (Fichaux and Ranchin, 2002; Du et al., 2002) have been exploited to obtain the direction of wind streaks in SAR imagery with a  $180^\circ$  ambiguity. An advanced algorithm for wind direction retrieval, developed at GKSS Research Center in Germany, yields a wind speed and direction accuracy of  $1.6 \text{ m s}^{-1}$  and  $20^\circ$  (Horstmann et al., 2000, 2003; Koch, 2004). This method examines the change in intensity of the SAR image at various spatial scales. The wind direction retrievals are made at  $\sim 6\text{-km}$  scales and the wind speeds are usually computed on a 500-m pixel scale with wind directions interpolated down to the pixel location. Figure 114

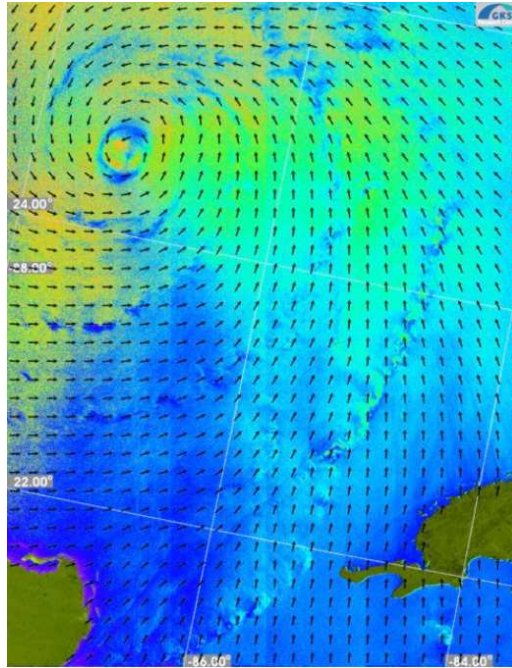


*Figure 114:* This image (provided by J. Horstmann from GKSS) shows the SAR wind vector retrieval over Hurricane Ivan in September 2004. The small arrows represent the SAR retrieved direction and the color indicates the extracted wind speed (dark blue  $\sim 3$  m s $^{-1}$ ; orange near the hurricane eye  $> 30$  m s $^{-1}$ )

shows an example of SAR wind vector retrieval over Hurricane Ivan in September 2004 where the wind direction was determined directly from features in the image (Horstmann et al., 2005).

Of course the two approaches for the determination of wind direction for use in SAR wind-speed retrievals have advantages and disadvantages. The use of model directions for the wind speed retrieval has the advantage that a dynamically consistent and unambiguous wind direction is always available. However, the direction associated with wind features at small spatial scales cannot be resolved by the numerical models. On the other hand, the use of linear features from the SAR image to infer direction has the inherent advantage that the entire wind vector (direction as well as magnitude) is obtained from the SAR image itself, independent of model estimates. The major disadvantage in this method lies in the fact that for a small fraction of cases, unique wind directions may not be found. In such cases, the directions must be interpolated from adjacent parts of the SAR image.

Finally, the possibility of obtaining wind directions from scatterometer data has been investigated (Monaldo et al., 2004; He et al., 2005). The method requires nearly simultaneous overpasses of a SAR and scatterometer, which becomes more practical with increasing latitudes. A solution to this time correlation issue may be a routine merging of the two data types (Monaldo and Beal, 2004). Estimation of the wind direction is among the largest sources of error in SAR wind speed retrievals. For offshore sites where high-quality meteorological data are available and used to provide the wind direction input, wind speeds may be retrieved with an standard deviation error as low as 1.1 m s $^{-1}$  (Hasager et al., 2004, 2005, 2006; Christiansen et al., 2006).

### 13.4 Meteorological applications of SAR wind fields

The ocean wind fields shown in Figures 113 and 114 have already indicated how SAR imagery is valuable for meteorological applications such as weather prediction and hurricane



monitoring. High-resolution SAR wind fields may also be used to provide measurements required in basic research efforts that are not available from other, more conventional instrumentation and sensors. An interesting example is to study the dynamics of coastal wind fields where terrain forcing can cause large gradients in the local wind over spatial scales on the order of a few kilometers or so. In the Gulf of Alaska, a combination of factors provides a nearly perfect location to study intense mesoscale meteorological phenomena. In addition to the meteorological forcing present in this region, excellent satellite coverage from polar-orbiting SAR satellites is available due to the high latitude. It is thus an excellent test bed for observing atmospheric phenomena with SAR.

### **Gap flows and barrier jets**

Two specific examples of mesoscale meteorological phenomena that occur frequently in the Gulf and are readily observable using SAR are gap flows and barrier jets. Gap flows occur when cold continental air spills through gaps in the complex mountainous coastal terrain that forms the boundary of most of the Gulf. Barrier jets occur when stable atmospheric flow encounters a barrier in the local terrain from a high mountain ridge or wall for example (Parish, 1982). If the flow is sufficiently statically stable (i.e. resistant to vertical motion), it is blocked from crossing the barrier and as mass piles up along the upwind side of the barrier, a local, positive pressure gradient parallel to the terrain barrier is induced. The atmosphere adjusts to this gradient by deflecting the onshore flow to the left (northern hemisphere) and accelerating it along the pressure gradient. When the horizontal extent of the barrier is sufficiently large, the flow becomes rotationally trapped against the barrier by the Coriolis force (Chen and Smith, 1987; Bell and Bosart, 1988).

Figure 115 shows six barrier jets in the region between Mount Fairweather and Prince William Sound. It is immediately evident from the figure that very sharp offshore wind speed gradients are associated with these structures. This morphology is not consistent with the exponential wind speed increase predicted by classical barrier jet theory. However barrier jets similar to those seen in this figure have been previously observed by research aircraft and have long been part of the experience of local mariners in Alaska (Neiman et al., 2004). Having access to SAR images in this region has served to confirm and provide context to these previous observations. Of course, such observations of sharp gradients prompt one to seek understanding of the governing dynamics that cause these features to form. Once these dynamics are understood, further questions concerning forecasting the strength and shape of these phenomena naturally arise. Such questions have led to a project funded by the US National Science Foundation to study barrier jets in the Gulf of Alaska using SAR imagery (Winstead et al., 2006).

### **Flow model validation**

A practical application of SAR wind fields in meteorology is the validation of mesoscale modeling over the ocean. Mesoscale models are widely used for operational prediction of atmospheric dispersion and also for wind resource assessment. The modeling of wind fields for a given domain is initiated with geostrophic wind and temperature profiles plus information about the terrain height and the surface roughness. Wind fields at different heights are typically modeled at a grid resolution of 5 km. The right-hand side of Figure 116 shows wind speeds for the height 70 m over the western part of the Baltic Sea predicted with the KAMM model using a geostrophic wind forcing of  $10 \text{ m s}^{-1}$  from the southeast. The spatial resolution is 2 km. Local effects of the land are clearly seen. For example, wind speeds are generally low on the lee side of Germany. Note also the very pronounced sheltering effect of the Danish and German islands. The best example is the small German island Rügen located around  $11.2^\circ$  east and  $54.5^\circ$  north. Other areas show an enhancement of the wind speed as the wind is forced between the different islands.

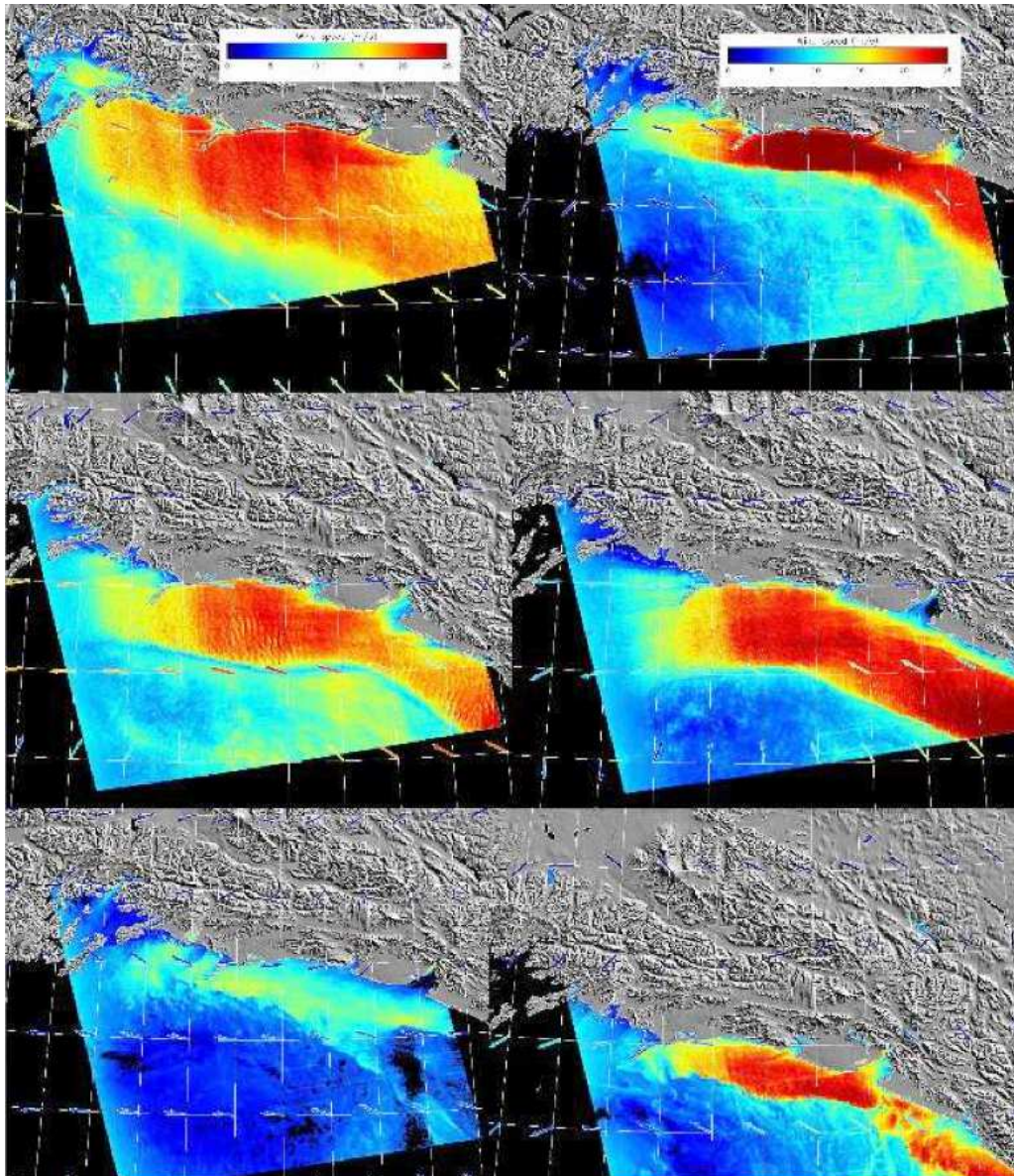


*Figure 115: SAR-wind maps showing the wind structure of Barrier Jets around the region of Yakutat, AK. The collection dates are as follows (from left to right, top to bottom): 0311 UTC 30 May 1999, 0310 UTC 18 February 2000, 0306 UTC 4 September 2000, 0306 UTC 22 October 2000, and 0302 UTC 24 October 2001, and 0310 UTC 27 November 2001. All six images were collected by the RADARSAT-1 SAR*

The left-hand side of Figure 116 shows a SAR wind field valid for a 10-m height. The SAR and the model wind fields cannot be compared quantitatively due to the difference in height and likely differences in the large scale forcing. However, it is interesting to compare the spatial variability of the wind speed, which is very similar for the two maps with identical color scaling. Work is in progress to model all the different wind situations that are found in our SAR data archive for Denmark and to quantify the differences between SAR and model wind fields. Ultimately, this analysis could provide valuable guidance for the improvement of mesoscale modeling results.

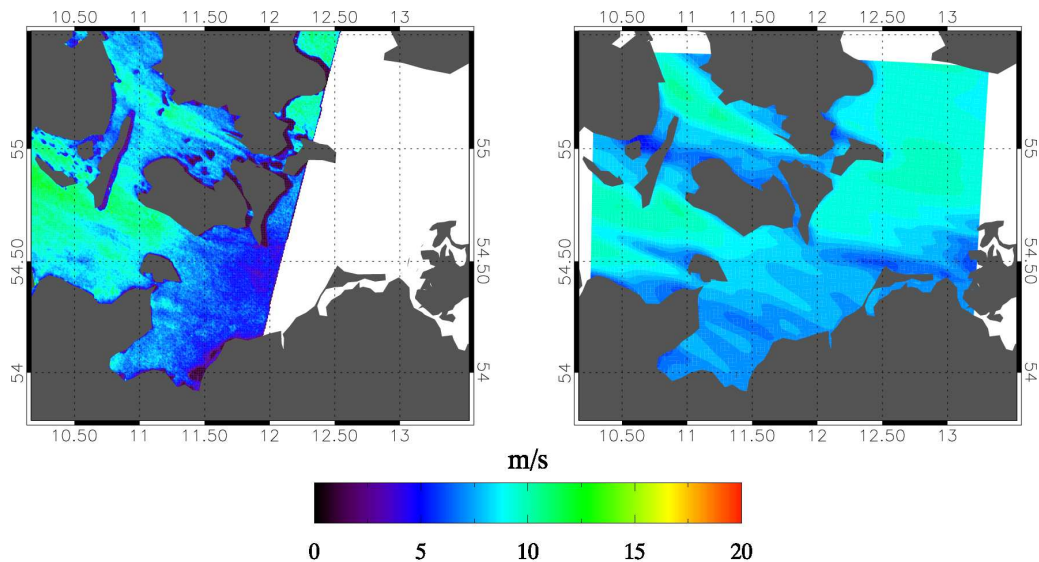


*Figure 116:* Ocean wind field over the western part of the Baltic Sea estimated from (left) an ENVISAT ASAR image acquired on 23 June 2004 at 09:46 UTC, and (right) the KAMM mesoscale model using a geostrophic wind forcing of  $10 \text{ m s}^{-1}$ . The wind is directed from the southeast ( $\sim 120^\circ$ ). Wind variability caused by the terrain of Denmark and Germany is visible in both maps. Modified from Badger et al. (2006)

### 13.5 Wind energy applications of SAR wind fields

Prior to wind farm installation the best location within a given region needs to be identified. This is to ensure an optimal power production and economical benefit from the wind farm. The potential wind power production is closely related to the prevailing wind climate. Wind turbines were first established on land. Observations from meteorological masts within the region typically would be used to assess the wind climate. The landscape effects were of great importance for the wind resource as described in the European Wind Atlas (Troen and Petersen, 1989). This wind atlas method developed for wind resource assessment is a de facto standard today and it is used worldwide through the Wind Atlas Analysis and Applications Program (WASP, [www.wasp.dk](http://www.wasp.dk)) (Mortensen et al., 2005). Wind resource assessment is based on observations of wind speed and wind direction for a least one year and local scale maps of the area of interest. These maps should hold details on topography and obstacles as well as a general characterization of the roughness classes of the terrain. Wind resource assessment in the coastal region offshore – where most offshore wind farms are located or are in development – is challenging as coastal wind systems are complicated and ocean wind observations are sparse compared to land-based wind data.

Large wind farms cover areas of several square-kilometers. As an example, the Horns Rev I wind farm in the North Sea covers  $\sim 25 \text{ km}^2$ . This wind farm is located between 14 and 21 km offshore from the closest coastal point. Future wind farms will be located much further from the coast. At Horns Rev, a second wind farm (Horns Rev II) has just been installed (in 2009) approximately 26 to 31 km offshore. Thus the coverage needed in offshore wind resource analysis is roughly from 5 to 50 km offshore and with a spatial resolution that resolves variations in the wind climate at the 1–2 km grid scale. SAR images from ERS-1/2, Radarsat-1 and ENVISAT cover the coastal zone at the desired spatial resolution. The SAR data archives contain observations from many years ( $\sim 16$ , 11 and 5 years, respectively).

## SAR-based wind statistics

Work was initiated in the EU WEMSAR project (2000–2003) to produce software for integration of SAR wind maps to standard wind resource mapping tools (e.g. WAsP). Further development has taken place within other projects and recently, cooperation between the institutions Risø DTU, JHU/APL, and GRAS A/S has resulted in the software Satellite-WAsP (S-WAsP) for SAR-based offshore wind resource assessment. In the following, we describe the key principles for treating a series of SAR-based wind maps and calculating wind resource statistics.

The collection of satellite SAR scenes for a given area of interest takes place at fixed times of the day. This introduces a bias in SAR-based wind climatologies. Another bias is associated with the relatively low number of available SAR samples compared to in situ measurements collected over e.g. 10-min intervals. A simulation study has been carried out to analyze the effect of these biases on statistical wind climate analyses (Barthelmie and Pryor, 2003; Pryor et al., 2004). The findings were relatively promising regarding estimates of the mean wind speed, which requires around 70 randomly sampled SAR images. To estimate the wind energy density, however, far more samples are needed ( $\sim 2000$ ). The conclusion of this work was that SAR-based wind resource estimations have a quality relevant in pre-feasibility studies. In other words, the SAR-based wind resource maps may be used as guide to site an offshore meteorological mast in a wind farm project. SAR-based wind resource maps provide quantification of relative wind resource variations in the spatial domain. In case offshore meteorological time series observations are already available, extrapolation using SAR-based wind statistics would be possible rather than erecting another meteorological mast nearby.

The software developed for SAR-based wind statistics takes care of several issues related to the nature of SAR-based wind maps. Firstly, grid cells upwind of the point of interest (any point in the selected domain) are averaged by a footprint-weighted function (Gash, 1986). Secondly, the samples available within each wind direction sector (bin) are used to calculate the Weibull shape and scale parameters. Finally, the fact that SAR-based wind mapping excludes winds below a certain threshold ( $2 \text{ m s}^{-1}$ ) and above a certain threshold ( $24 \text{ m s}^{-1}$ ) has made the choice of the maximum likelihood estimator relevant for Weibull fitting to SAR-based wind data (Nielsen et al., 2004; Hasager et al., 2007). Promising results on wind statistics based on  $\sim 100$  SAR images were found by Christiansen et al. (2006) using a preliminary version of the S-WAsP software at Horns Rev in the North Sea.

## Wind resource mapping for the Danish Seas

Wind resource mapping using a series of ENVISAT ASAR scenes acquired in wide swath mode (WSM) over the Danish seas has been performed. A total of 300 scenes were included in the study. Figure 117 (left) shows the number of overlapping samples. The orbital paths from ascending and descending frames are clearly visible. Most samples cover the inner Danish Seas whereas fewer cover the North Sea and the Baltic Sea. A first result on mean wind speed is shown in Figure 117 (right). The result shows much higher winds in the North Sea than in the inner Danish Seas. The very high mean wind speeds near the coast of Norway are likely caused by flow compression, as the wind is forced around the high-relief topography of southern Norway. For the near-coastal seas of Denmark and Sweden, the mean wind speed is seen to increase with distance offshore up to 50 km. It is possible to discern the orbital paths in the image but this artifact may be diminished or avoided in future image processing. The wind statistics are expected to improve in accuracy as our image archive continues to grow. The spatial coverage will be extended to include the entire North Sea, Baltic Sea, and Irish Sea as part of the project EU-NORSEWInD (2008–2012).

Wind resource assessment studies based on a relatively low number of SAR samples

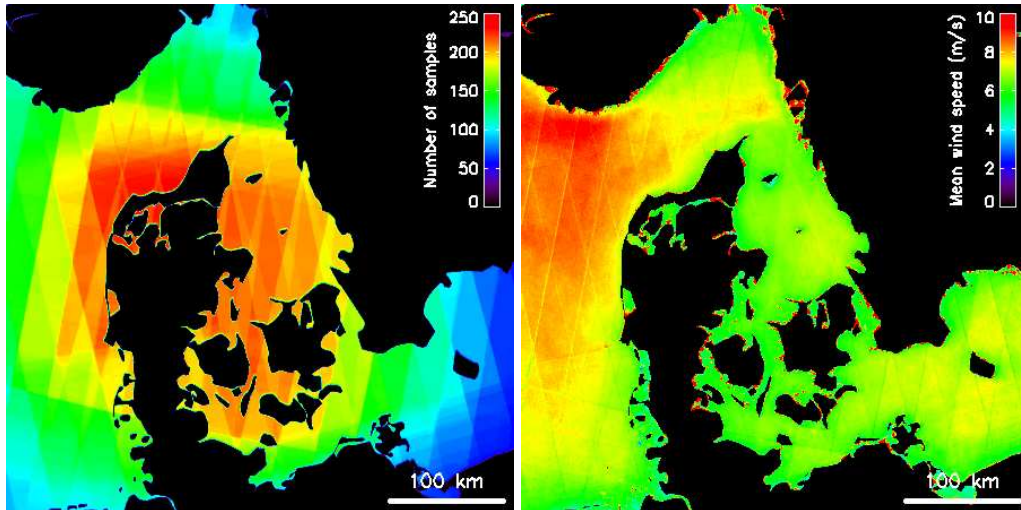


*Figure 117:* Left: Number of overlapping ENVISAT ASAR WSM images that are available for the Danish Seas. Right: Mean wind speed estimated from a total of 300 ENVISAT ASAR WSM satellite images covering the Danish seas

should take the directional distribution of the samples into account. This is particularly important in the vicinity of land where wind shadowing occurs. Our sampling strategy so far has simply been to collect as many random SAR samples as available from the image archives. Our ENVISAT ASAR image collection for the Danish seas contains several samples in each of 12 wind sectors. Figure 7 shows the directional distribution at Horns Rev, where the number of overlapping SAR scenes is 198 in total. Also shown is the directional distribution estimated from 7 years (1999–2006) of QuikSCAT data with 1–2 daily samples. Previous studies have shown an excellent agreement between QuikSCAT and high-frequency in situ measurements of the wind direction (Hasager et al., 2007, 2008). The wind distribution from SAR and QuikSCAT data agree well for most wind sectors, except the SAR dataset underestimates the contribution from westerly winds and overestimates the contribution from easterly winds. The prevailing wind direction found from the SAR data is thus east whereas it should be southwest. This type of error is likely to diminish as more SAR samples are collected for the Danish Seas. Another way to cope with the wind distribution problem is to implement a weighting function according to higher-frequency observations such as in situ measurements, atmospheric models, or scatterometer data. For sites where thousands of SAR scenes are available in the image archives, the weighting could be performed during the initial image selection. This option is currently being investigated further.

### Wind farm wake analysis

Wind resource assessment also includes an estimate on the wind reduction appearing within a wind farm – the so-called wind wake effect between wind turbines – or between wind farms in clusters. Typically, wind turbines and wind farms are located near each other to reduce the cost of cables from the turbines to the transform platform and from the transform to the electrical grid on land. The wind farm wake is characterized by lower wind speeds downstream of a wind turbine and higher turbulence level. Wind turbines in the wake of other turbines will thus produce less energy and suffer more wear due to the higher turbulence intensity.

Wind farm wake effects from two large offshore wind farms, Horns Rev wind farm in the North Sea and Nysted wind farm in the Baltic Sea, have been investigated from satellite and airborne SAR. The analysis showed – as expected – a significant reduction in wind speed downwind of the wind turbines. The magnitude of the wake near the wind farms

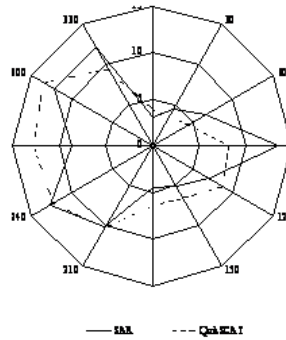


Figure 118: Directional distribution of winds at Horns Rev for a total of 198 overlapping SAR scenes (solid) and for QuikSCAT samples obtained 1–2 times daily for the period 1999–2006 (dashed)

was found to be similar to the wake effect predicted by state-of-the-art wake models and observed from meteorological masts. More surprisingly the study demonstrated that the wind farm wake may extend as far as 20 km downwind of a large offshore wind farm (Christiansen and Hasager, 2005, 2006). This is much longer than current wake models predict. Therefore the potential power production from wind farms in clusters may be more affected by wakes than it is assumed in general.

### 13.6 Future advances in ocean wind mapping from SAR

As already discussed in this chapter, two satellite SAR systems, RADARSAT-1 and ENVISAT (both operating at C-band;  $\sim 5.3$  GHz), are presently being used routinely to provide operational estimates of the near surface wind field at resolutions of  $\sim 500$  m or so. In fact, the SAR on board ENVISAT, using its alternating polarization mode, is capable of transmitting vertically polarized radiation (V-pol) followed by horizontally polarized radiation (H-pol) on successive pulses, and collecting the reflected radiation in one of three distinct (user-defined) pairs: HH and VV, HH and HV, or VV and VH. New satellites have been launched with fully polarimetric transmit/receive SAR capability: ALOS (L-band;  $\sim 1.2$  GHz), RADARSAT-2 (C-band  $\sim 5.3$  GHz), TerraSAR-X, and COSMO SkyMed (X-band;  $\sim 10$  GHz). The ability to collect multi-polarization SAR imagery at three different frequencies represents a significant advance in SAR acquisition technology. Similar refinement in the interpretation and processing of data from these new SAR sensors is required in order to fully utilize this new technology for remote-sensing applications.

In order to extract geophysical information from the data collected by microwave sensors, it is clear that one must understand not only the scattering physics, but also surface wave hydrodynamics and the structure of the marine boundary layer. In particular, a method for characterizing the shape of the sea surface (the surface roughness) is necessary in order to properly apply the electromagnetic boundary conditions. Since these boundary conditions depend on the polarization state of the incident field, the scattering of electromagnetic radiation will be different for different polarization even for a smooth flat surface (Jackson, 1997). These differences generally become more pronounced as the surface roughness characteristics become more complicated. However, if scattering measurements from two (or more) polarization states are available, it should be possible to utilize the polarization-dependent differences in the scattering to improve the accuracy of the parameter extraction and perhaps even to separate wind-induced cross section variations from those caused by oceanic processes such as internal waves or variable

bathymetry (Ufermann and Romeiser, 1999).

Although much has been learned over the last years about the physics that governs microwave scattering from the ocean surface, there are still a number of outstanding problems that need to be addressed. In particular, the measured polarization ratios (HH/VV) of the backscattered cross section at moderate incidence angles for L-, C-, and X-band are larger than those predicted by the rough-surface scattering and surface spectral models commonly in use. At 45° incidence for example, the measured HH/VV ratio for a 10 m s<sup>-1</sup> wind directed toward the radar is about -3 dB at X-band (Mazuko et al., 1986), about -5.0 dB or so at C-band (Mouche et al., 2005), and about -4 dB at L-band according to airborne E-SAR data from DLR acquired over the wind farm at Horns Rev, Denmark. Simple Bragg-based scattering models predict the HH/VV ratio to be about -9.5 dB; independent of radar frequency. Ratios predicted by composite-type scattering models that include the effects of long-wave tilt and hydrodynamic modulation yield frequency dependence and a somewhat large ratio (Romeiser et al., 1997), but the predicted polarization ratios remain significantly smaller than the measurement data.

Improved understanding of these discrepancies could yield significant improvement in the remote sensing of ocean processes, especially high wind events such as hurricanes. In particular, differences in the hurricane signatures observed by (roughly concurrent) SAR imagery collected by L-, C-, and X-band systems presently available could provide new insight into hurricane morphology and sea state as well as the rain rate since the influence of rain on the NRCS increases with increasing frequency. If such observations are collected at multiple polarizations, it may further be possible to estimate the foam or breaking wave coverage using techniques similar to those proposed by Kudryavtsev et al. (2003). Perspectives of mapping these properties of the ocean surface include not only an improved accuracy on ocean wind fields but also a possibility of using SAR-derived parameters for gas transfer parameterization and climate monitoring. Work by several international research groups is currently underway to begin to address these issues.

## Acknowledgements

It is a pleasure to acknowledge our colleagues Jake Badger, Jochen Horstmann and Nathaniel Winstead for providing us with details of their research as well as helpful comments concerning this manuscript. Funding from the EU WEMSAR project (ERK6-CT1999-00017), the ESA EOMD EO-windfarm project (17736/03/I-IW), the SAT-WIND project (Sagsnr. 2058-03-0006) and the SAT-WIND-SMV project (Sagsnr. 2104-05-0084) is much appreciated. Donald Thompson gratefully acknowledges support from the National Oceanic and Atmospheric Administration (NOAA). Satellite data provided by the European Space Agency (EO-3644) and the Canadian Space Agency through NOAA.

## Notation

$A$	function of wind speed and local incident angle in a GMF
ANSWRS	APL/NOAA SAR wind retrieval system
ASAR	advanced C-band SAR
ASF	Alaska SAR facility
ASI	Italian Space Agency
$B$	function of wind speed and local incident angle in a GMF
$C$	function of wind speed and local incident angle in a GMF
$C_{HH}$	C-band SAR operating at horizontal polarization in transmit and receive
$C_{HV}$	C-band SAR operating at horizontal polarization in transmit and vertical in receive
$C_{VH}$	C-band SAR operating at vertical polarization in transmit and horizontal in receive
$C_{VV}$	C-band SAR operating at vertical polarization in transmit and receive
DLR	German Aerospace Center
ESA	European Space Agency
FFT	fast Fourier transformation

GMF	geophysical model function
H-pol	horizontally polarized radiation
JAXA	Japanese Space Agency
JHU/APL	Johns Hopkins University Applied Physics Laboratory
NCRCS	normalised radar cross section
NOAA	National Oceanic and Atmospheric Administration
NOGAPS	navy operational global atmospheric prediction system
Risø DTU	Risø National Laboratory for Sustainable Energy at the Technical University of Denmark
SAR	synthetic aperture radar
S-WAsP	satellite WAsP
$U$	wind speed at 10 m height
V-pol	vertically polarized radiation
WAsP	Wind Atlas Analysis and Application Program
WSM	wind swath mode
$\gamma$	function of wind speed and local incident angle in a GMF
$\theta$	radar's local incident angle
$\sigma^0$	normalised radar cross section
$\phi$	wind direction with respect to the radar look direction

## References

- Alpers W. R. and Hennings I. (1984) A theory of the imaging mechanism of underwater bottom topography by real and synthetic aperture radar. *J. Geophys. Res.* **89**:529–546
- Alpers W. R., Ross D. B., and Rufenach C. L. (1981) On the detectability of ocean surface-waves by real and synthetic aperture radar. *J. Geophys. Res. Oceans* **86**:6481–6498
- Badger J., Barthelmie R., Frandsen S., and Christiansen M. (2006) Mesoscale modelling for an offshore wind farm. *Proc. of the European Wind Energy Conf.*, Athens
- Barthelmie R. J. and Pryor S. C. (2003) Can satellite sampling of offshore wind speeds realistically represent wind speed distributions. *J. Appl. Meteorol.* **42**:83–94
- Bell G. D. and Bosart L. F. (1988) Appalachian Cold-Air Damming. *Mon. Wea. Rev.* **116**:137–161
- Brown G. S., Stanley H. R., and Roy N. A. (1981) The Wind-Speed Measurement Capability of Spaceborne Radar Altimeters. *IEEE J. Oceanic Eng.* **6**:59–63
- Chen W. D. and Smith R. B. (1987) Blocking and Deflection of Air-Flow by the Alps. *Mon. Wea. Rev.* **115**:2578–2597
- Christiansen M. B. and Hasager C. B. (2005) Wake effects of large offshore wind farms identified from satellite SAR. *Rem. Sens. Environ.* **8**:251–268
- Christiansen M. B. and Hasager C. B. (2006) Using airborne and satellite SAR for wake mapping offshore. *Wind Energy* **9**:437–455
- Christiansen M. B., Koch W., Horstmann J., and Hasager C. B. (2006) Wind resource assessment from C-band SAR. *Rem. Sens. Environ.* **105**:68–81
- Du Y., Vachon P. W., and Wolfe J. (2002) Wind direction estimation from SAR images of the ocean using wavelet analysis. *Can. J. Rem. Sens.* **28**:498–509
- Elfouhaily T. M. (1996) Modèle couple vent/vagues et son application à la télédétection par micro-onde de la surface de la mer. PhD thesis. University of Paris, Paris
- Espedal H. A. and Johannessen O. M. (2000) Detection of oil spills near offshore installations using synthetic aperture radar (SAR). *Int. J. Rem. Sens.* **21**:2141–2144
- Espedal H. A., Johannessen O. M., Johannessen J., Dano E., Lyzenga D. R., and Knulst J. (1998) COASTWATCH'95: ERS 1/2 SAR detection of natural film on the ocean surface. *J. Geophys. Res. Oceans* **103**:24969–24982
- Espedal H. A., Johannessen O. M., and Knulst J. (1996) Satellite detection of natural films on the ocean surface. *Geophys. Res. Lett.* **23**:3151–3154
- Fichaux N. and Ranchin T. (2002) Combined extraction of high spatial resolution wind speed and direction from SAR images: a new approach using wavelet transform. *Can. J. Rem. Sens.* **28**:510–516
- Furevik B., Johannessen O., and Sandvik A. D. (2002) SAR-retrieved wind in polar regions - comparison with in situ data and atmospheric model output. *IEEE Trans. Geo. Rem. Sens.* **40**:1720–1732



- Gade M. and Alpers W. (1999) Using ERS-2 SAR images for routine observation of marine pollution in European coastal waters. *Sci. Total Environ.* **237–238**:441–448
- Gade M., Alpers W., Hühnerfuss H., Masuko H., and Kobayashi T. (1998) Maging of biogenic and anthropogenic ocean surface films by the multifrequency/multipolarization SIR-C/X-SAR. *J. Geophys. Res. Oceans* **103**:18851–18866
- Gade M., Alpers W., Hühnerfuss H., Wismann V. R., and Lange P. A. (1998) On the reduction of the radar backscatter by oceanic surface films: scatterometer measurements and their theoretical interpretation. *Rem. Sens. Environ.* **66**:52–70
- Gash J. H. C. (1986) A note on estimating the effect of a limited fetch on micrometeorological evaporation measurements. *Bound.-Layer Meteorol.* **35**:409–413
- Gerling T. W. (1986) Structure of the surface wind field from the SEASAT SAR. *J. Geophys. Res.* **91**:2308–2320
- Hasager C. B., Dellwik E., Nielsen M., and Furevik B. (2004) Validation of ERS-2 SAR offshore wind-speed maps in the North Sea. *Int. J. Rem. Sens.* **25**:3817–3841
- Hasager C. B., Nielsen M., Astrup P., Barthelmie R. J., Dellwik E., Jensen N. O., Jørgensen B. H., Pryor S. C., Rathmann O., and Furevik B. (2005) Offshore wind resource estimation from satellite SAR wind field maps. *Wind Energy* **8**:403–419
- Hasager C. B., Barthelmie R. J., Christiansen M. B., Nielsen M., and Pryor S. C. (2006) Quantifying offshore wind resources from satellite wind maps: study area the North Sea. *Wind Energy* **9**:63–74
- Hasager C. B., Astrup P., Nielsen M., Christiansen M. B., Badger J., Nielsen P., Sørensen P. B., Barthelmie R. J., Pryor S. C., and Bergström, H. (2007) SAT-WIND final report. Risø-R-1586(EN). Risø National Laboratory, Roskilde
- Hasager C. B., Peña A., Christiansen M. B., Astrup P., Nielsen M., Monaldo F., Thompson D., and Nielsen P. (2008) Remote sensing observation used in offshore wind energy. *IEEE J. Selected Topocs Appl. Earth Obs. Rem. Sens.* **1**:67–79
- Hasselmann K., Raney R. K., Plant W. J., Alpers W., Shuchman R. A., Lyzenga D. R., Rufenach C. L., and Tucker M. J. (1985) Theory of synthetic aperture radar ocean imaging - a marsen view. *J. Geophys. Res. Oceans* **90**:4659–4686
- He Y. J., Perrie W., Zou Q. P., and Vachon P. W. (2005) A new wind vector algorithm for C-band SAR. *IEEE Trans. Geo. Rem. Sens.* **43**:1453–1458
- Hersbach H. (2003) CMOD5. An improved geophysical model function for ERS C-band scatterometry. Reading, UK: ECMWF Technical Memorandum 395, 50 pp
- Hogan G. G., Chapman R. D., Watson G., and Thompson D. R. (1996) Observations of ship-generated internal waves in SAR images from Loch Linnhe, Scotland, and comparison with theory and in situ internal wave measurements. *IEEE Trans. Geo. Rem. Sens.* **34**:532–542
- Holt B. (2004) AR imaging of the ocean surface. In Jackson C. R. and Apel J. R. (Eds.), Synthetic aperture radar marine user's manual. Washington, DC: U.S. Department of Commerce, National Oceanic and Atmospheric Administration
- Horstmann J., Koch W., Lehner S., and Tonboe R. (2000) Wind retrieval over the ocean using synthetic aperture radar with C-band HH polarization. *IEEE Trans. Geo. Rem. Sens.* **38**:2122–2131
- Horstmann J., Schiller H., Schulz-Stellenfleth J., and Lehner S. (2003) Global wind speed retrieval from SAR. *IEEE Trans. Geo. Rem. Sens.* **41**:2277–2286
- Horstmann J., Thompson D. R., Monaldo F., Iris S., and Graber H. C. (2005) Can synthetic aperture radars be used to estimate hurricane force winds? *Geophys. Res. Lett.* **32**, L22801, doi:10.1029/2005GL023992
- Jackson J. D. (1997) Classical electrodynamics, John Wiley & Sons, 808 pp
- Johannessen J., Shuchman R. A., Digranes G., Lyzenga D. R., Wackerman C., Johannessen O. M., and Vachon P. W. (1996) Coastal ocean fronts and eddies imaged with ERS 1 synthetic aperture radar. *J. Geophys. Res. Oceans* **101**:6651–6667
- Johannessen J. A., Kudryavtsev V., Akimov D., Eldevik T., Winther N., and Chapron B. (2005) On radar imaging of current features: 2. Mesoscale eddy and current front detection. *J. Geophys. Res.* **110**, C07017, doi:10.1029/2004JC002802

- Koch W. (2004) Directional analysis of SAR images aiming at wind direction. *IEEE Trans. Geo. Rem. Sens.* **42**:702–710
- Kudryavtsev V., Hauser D., Caudal G., and Chapron B. (2003) A semiempirical model of the normalized radar cross-section of the sea surface - 1. Background model. *J. Geophys. Res.* **108**(C3), 8054, doi:10.1029/2001JC001003
- Kudryavtsev V., Akimov D., Johannessen J., and Chapron B. (2005) On radar imaging of current features: 1. Model and comparison with observations. *J. Geophys. Res.* **110**, C07016, doi:10.1029/2004JC002505
- Lehner S., Horstmann J., Koch W., and Rosenthal W. (1998) Mesoscale wind measurements using recalibrated ERS SAR images. *J. Geophys. Res. Oceans* **103**:7847–7856
- Lyzenga D. R. (1991) Interaction of Short Surface and Electromagnetic-Waves with Ocean Fronts. *J. Geophys. Res. Oceans* **96**:10765–10772
- Masuko H., Okamoto K. I., Shimada M., and Niwa S. (1986) Measurement of Microwave Backscattering Signatures of the Ocean Surface Using X-Band and Ka-Band Airborne Scatterometers. *J. Geophys. Res. Oceans* **91**:3065–3083
- Monaldo F. M. and Beal R. (2004) Wind speed and direction. In Jackson C. R. and Apel J. R. (Eds.), Synthetic aperture radar marine user's manual. Washington, DC: U.S. Department of Commerce, National Oceanic and Atmospheric Administration
- Monaldo F. M., Thompson D. R., Beal R. C., Pichel W. G., and Clemente-Colon P. (2001) Comparison of SAR-derived wind speed with model predictions and ocean buoy measurements. *IEEE Trans. Geo. Rem. Sens.* **39**:2587–2600
- Monaldo F. M., Thompson D. R., Pichel W. G., and Clemente-Colon P. (2004) A systematic comparison of QuikSCAT and SAR ocean surface wind speeds. *IEEE Trans. Geo. Rem. Sens.* **42**:283–291
- Mortensen N. G., Heathfield D. N., Myllerup L., Landberg L., and Rathmann O. (2005) Wind Atlas Analysis and Application Program: WAsP 8 Help Facility. Risø National Laboratory, Roskilde
- Mouche A. A., Hauser D., Daloz J. F., and Guerin C. (2005) Dual-polarization measurements at C-band over the ocean: Results from airborne radar observations and comparison with ENVISAT ASAR data. *IEEE Trans. Geo. Rem. Sens.* **43**:753–769
- Neiman P. J., Persson P. O. G., Ralph F. M., Jorgensen D. P., White A. B., and Kingsmill D. E. (2004) Modification of fronts and precipitation by coastal blocking during an intense landfalling winter storm in southern California: Observations during CALJET. *Mon. Wea. Rev.* **132**:242–273
- Nielsen M., Astrup P., Hasager C. B., Barthelmie R. J., and Pryor S. C. (2004) Satellite information for wind energy applications. Risø-R-1479(EN). Risø National Laboratory, Roskilde
- Parish T. R. (1982) Barrier winds along the Sierra-Nevada mountains. *J. Appl. Meteorol.* **21**:925–930
- Pryor S. C., Nielsen M., Barthelmie R. J., and Mann J. (2004) Can satellite sampling of offshore wind speeds realistically represent wind speed distributions? Part II Quantifying uncertainties associated with sampling strategy and distribution fitting methods. *J. Appl. Meteorol.* **43**:739–750
- Quilfen Y., Chapron B., Elfouhaily T., Katsaros K., and Tournadre J. (1998) Observation of tropical cyclones by high-resolution scatterometry. *J. Geophys. Res. Oceans* **103**:7767–7786
- Romeiser R. and Alpers W. (1997) An improved composite surface model for the radar backscattering cross section of the ocean surface. 2: Model response to surface roughness variations and the radar imaging of underwater bottom topography. *J. Geophys. Res. Oceans* **102**:25251–25267
- Romeiser R., Alpers W., and Wismann V. (1997) An improved composite surface model for the radar backscattering cross section of the ocean surface.1: Theory of the model and optimization/validation by scatterometer data. *J. Geophys. Res. Oceans* **102**:25237–25250
- Stoffelen A. and Anderson, D. L. T. (1997) Scatterometer data interpretation: Estimation and validation of the transfer function CMOD4. *J. Geophys. Res.* **102**:5767–5780
- Thompson D., Elfouhaily T., and Chapron B. (1998) Polarization ratio for microwave backscattering from the ocean surface at low to moderate incidence angles. *Proc. Int. Geosci. Rem. Sens. Symp.*, Seattle
- Thompson D. R. (1988) Calculation of Radar Backscatter Modulations from Internal Waves. *J. Geophys. Res. Oceans* **93**:12371–12380

- Thompson D. R. (2004) Microwave scattering from the Sea. In Jackson C. R. and Apel J. R. (Eds.), Synthetic aperture radar marine user's manual. Washington, DC: U.S. Department of Commerce, National Oceanic and Atmospheric Administration
- Thompson D. R., Gotwols B. L., and Sterner R. E. (1988) A comparison of measured surface-wave spectral modulations with predictions from a wave-current interaction-model. *J. Geophys. Res. Oceans* **93**:12339–12343
- Troen I. and Petersen E. L. (1989) European wind atlas. Risø National Laboratory, Roskilde
- Ufermann S. and Romeiser R. (1999) Numerical study on signatures of atmospheric convective cells in radar images of the ocean. *J. Geophys. Res. Oceans* **104**:25707–25719
- Vachon P. W. and Dobson E. W. (1996) Validation of wind vector retrieval from ERS-1 SAR images over the ocean. *Glob. Atmos. Ocean Sys.* **5**:177–187
- Vachon P. W. and Dobson E. W. (2000) Wind retrieval from RADARSAT SAR images: selection of a suitable C-band HH polarization wind retrieval model. *Can. J. Rem. Sens.* **26**:303–313
- Vachon P. W., Monaldo F. M., Holt B., and Lehner S. (2004) Ocean surface waves and spectra. In Jackson C. R. and Apel J. R. (Eds.), Synthetic aperture radar marine user's manual. Washington, DC: U.S. Department of Commerce, National Oceanic and Atmospheric Administration
- Valenzuela G. R. (1978) Theories for the interaction of electromagnetic and ocean waves – A review. *Bound.-Layer Meteorol.* **13**:61–85
- Wentz F. J., Peteherych S., and Thomas L. A. (1984) A Model Function for Ocean Radar Cross-Sections at 14.6 Ghz. *J. Geophys. Res. Oceans* **89**:3689–3704
- Wentz F. J., Mattox L. A., and Peteherych S. (1986) New Algorithms for Microwave Measurements of Ocean Winds – Applications to Seasat and the Special Sensor Microwave Imager. *J. Geophys. Res. Oceans* **91**:2289–2307
- Winstead N. S., Colle B., Bond N., Young G., Olson J., Loescher K., Monaldo F., Thompson D., and Pichel W. (2006) Using SAR remote sensing, field observations, and models to better understand coastal flows in the Gulf of Alaska. *B. Am. Meteorol. Soc.* **87**:787–800